MAGAZINE OF CIVIL ENGINEERING

Magazine of Civil Engineering

Online peer-reviewed open-access scientific journal in the field of Civil and Construction Engineering

Founder and Publisher: Peter the Great St. Petersburg Polytechnic University

This journal is registered by the Federal Service for Supervision of Communications, Information Technology, and Mass Media (ROSKOMNADZOR) in 2020. Certificate El No. FS77-77906 issued February 19, 2020.

Periodicity: 8 issues per year

Publication in the journal is open and free for all authors and readers.

Indexing: Scopus, Web of Sceince (ESCI, RSCI), DOAJ, Compendex, Google Academia, Index Copernicus, ProQuest, Ulrich's Serials Analysis System, CNKI

Corresponding address: 29 Polytechnicheskaya st., Saint Petersburg, 195251, Russia

Chief science editor: D.S. in Engineering, Galina L. Kozinetc

Deputy chief science editors:
D.S. in Engineering, Sergey V. Korniyenko

Executive editor: Ekaterina A. Linnik

Translator, editor: Irina Ye. Lebedeva

Proofreader: Philipp Chrysanthes S. Bastian

DT publishing specialist:
Anastasiya A. Kononova

Contacts:
E-mail: mce@spbstu.ru
Web: http://www.engstroy.spbstu.ru

Date of issue: 13.05.2024

Contents

Contents

Composite cement materials
for structures foundation strengthening

R.S. Fediuk[1,2] ✉ iD , *V.S. Lesovik*[2] iD , *S.V. Vavrenyuk*[3], *M.Ye. Zaiakhanov*[4], *A.V. Bituyev*[4],
S.V. Klyuev[2] iD , *K. Yu*[5], *Y.R. Lesovik*[2], *K.A. Bakatov*[2]

[1] *Far Eastern Federal University, Vladivostok, Russian Federation*

[2] *V.G. Shukhov Belgorod State Technological University, Belgorod, Russian Federation*

[3] *branch FGBU "TSNIIP Russian Ministry of Construction" DalNIIS, Vladivostok, Russian Federation*

[4] *East Siberia State University of Technology and Management, Ulan-Ude, Russian Federation*

[5] *Tongji University, Shanghai, China*

✉ *roman44@yandex.ru*

Keywords: operation, soil, reliability, seismic resistance, weakening, technology, injection mortar

Abstract. There was a development of composite cements (CC), that include aluminosilicates (AS), obtained by enrichment of ash-to-slag mixture (up to 65 wt. %), cement clinker, and gypsum. Based on the developed CC, wide range of injection mortars, including crushed granite, was created. Injection mortars are capable of effectively fixing of underground structures foundations soils, providing high strength (25.6 MPa) with deformation modulus 10.1 GPa. These materials have percentage of water separation from 22.5 % at W/B=1 to 36.5 % at W/B=2. Viscosity indicators of these materials indicate high penetrating ability, since time for mortars to flow through Marsh viscometer is 39 and 33 seconds at W/B=1.5 and W/B=2, respectively. Effect of increasing density of injection mortars at 28 days was maximum at AS dosage of 45 wt. %, then it decreased with aluminosilicate content increase. There are high ratios of strength values on second day to those in grade age: for compressive strength 0.24 (0.20–0.22 for additive-free clinker compositions), for flexural strength 0.16 (0.15 for additive-free compositions; with AS content increase above 45 %, this ratio decreases to 0.14). High early strength makes it possible to effectively use injection mortars for urgent fixing of soils during the repair of underground structures.

Citation: Fediuk, R.S., Lesovik, V.S., Vavrenyuk, S.V., Zaiakhanov, M.Ye., Bituyev, A.V., Klyuev, S.V., Yu, K., Lesovik, Y.R., Bakatov, K.A. Composite cement materials for structures foundation strengthening. Magazine of Civil Engineering. 2024. 17(3). Article no 12701. DOI: 10.34910/MCE.127.1

1. Introduction

As a result of the analysis of literature data and our own surveys, the emergency state of many underground structures was established [1–4]. There is an obvious importance of restoring the functional suitability of these facilities, including for the possibility of dual-use operation, which requires a set of repair measures using new building materials (including for fixing soils). It has been established that only the strengthening of load-bearing walls while maintaining weak foundation soils is not effective. Injection fixing

of soils with cementing compounds can significantly improve the technical characteristics of the foundations, which will contribute to the comprehensive repair of underground structures.

Strengthening of soils containing an underground object (plugging) consists in the formation of an injected volume that can effectively withstand external pressure [5, 6]. The dimensions of this volume are calculated taking into account the current bearing capacity of the structures of the underground facility and the type of injection mortars used [7, 8].

Harcenko et al. [7], Svintsov et al. [8], Salamanova et al. [9] were engaged in the development of materials and improvement of soil strengthening technologies. The classification of soil strengthening methods is shown in Fig. 1.

Constructive methods for strengthening soils are quite complex and time-consuming [10]. Injection solutions based on various composite binders [11–13] are very promising for consolidating soils. Soil reinforcement is carried out by introducing special reinforcing elements into the soil in the form of tapes or solid mats made of geotextiles (less often, metal reinforcement) [14]. Sheet piling is a solid wall composed of identical elements connected to each other. In this regard, big data is important in predicting the climate resistance of building materials, especially for air temperature and humidity [15]. The construction of embankments (lateral surcharges) is carried out, as a rule, from coarse-grained or sandy soils [16]. Gavrilov and Kolesnikov [17] studied evolving crack influence on the strength of frozen sand soils.

Mechanical methods of fixing soils are divided into surface and deep ones [18]. Deep compaction of soils by drilling holes (soil piles) consists in the fact that holes are pierced in the compacted massif with an impact projectile, with the soil displaced to the sides and the creation of compacted zones around them [19, 20]. Drilling wells with explosions allows for a higher degree of soil compaction, but at the same time, labor intensity and danger increase [21]. Deep vibration compaction (hydrovibrocompaction) is used for compaction of loose sandy soils of natural occurrence, as well as when laying bulk non-cohesive soils, backfilling, etc. [22]. Soil compaction by preliminary soaking and soaking with deep explosions is carried out in a pit with a depth of 0.8 m and a width equal to the thickness of the subsidence soil layer, but not less than 20 m [23, 24].

Physical methods of soil strengthening involve the use of complex and scarce equipment. Thermal fixing of the soil is a transformation of structural bonds in the soil under the influence of high temperatures [25]. Electrochemical fixation is based on the phenomenon of electroosmosis, which means that when a direct current is passed through clay soil, the latter loses cohesive water, which moves (migration) towards the negative electrode (cathode) [26]. The soaking method has limited application and is used only for loess bases [27, 28]. Preliminary soaking of loess bases destroys the loess structure and causes it to sag under its own weight, i.e. the compaction process takes place. Dewatering provides a decrease in the level of groundwater below the bottom of the future excavation [29].

Soil freezing is used in heavily water-saturated soils [30]. To fix dispersed soils with a filtration coefficient kf = 0.01–0.1 m/day, the electrosilication method is used [31–33].

The most effective way to fix soils is injection cementing compositions, which can significantly improve the technical characteristics of the bases. Unlike compaction methods and complex physical methods, injection fixing of soils does not significantly affect their structure. With injection fixing, the introduced compositions form strong structural bonds in the soil massif. As a result of this, an increase in the strength of soils, a decrease in their compressibility, a decrease in water permeability and sensitivity to changes in the external environment, especially humidity, are provided.

The aim of the work is the development of injection mortars and their study for fixing subsiding soils. To achieve this aim, the following tasks were solved:

1. Conduct a sedimentation analysis of mortars to determine the percentage of water separation and viscosity indicators.

2. Determine the effect of increasing the density of the injection solutions on composite cement.

3. Study the early strength of the injection mortars.

4. Determine the potential for consolidating the foundation soils of underground structures with the developed injection mortars.

2. Materials and Methods

2.1. Raw materials characterization

Portland cement clinker (Spasskcement, Spassk-Dalniy, Russia) served as the basis for composite cement (Fig. 2a, Table 1). As a component of composite cement (CS), aluminosilicates (AS) were used,

extracted from ash and slag mixtures (ASM) of the Primorskaya Thermal Power Plant by enrichment by flotation and magnetic separation (Fig. 2b). To regulate the setting time, ground gypsum stone (gypsum dihydrate) was added in an amount of 5 % by weight of the clinker (Fig. 2c).
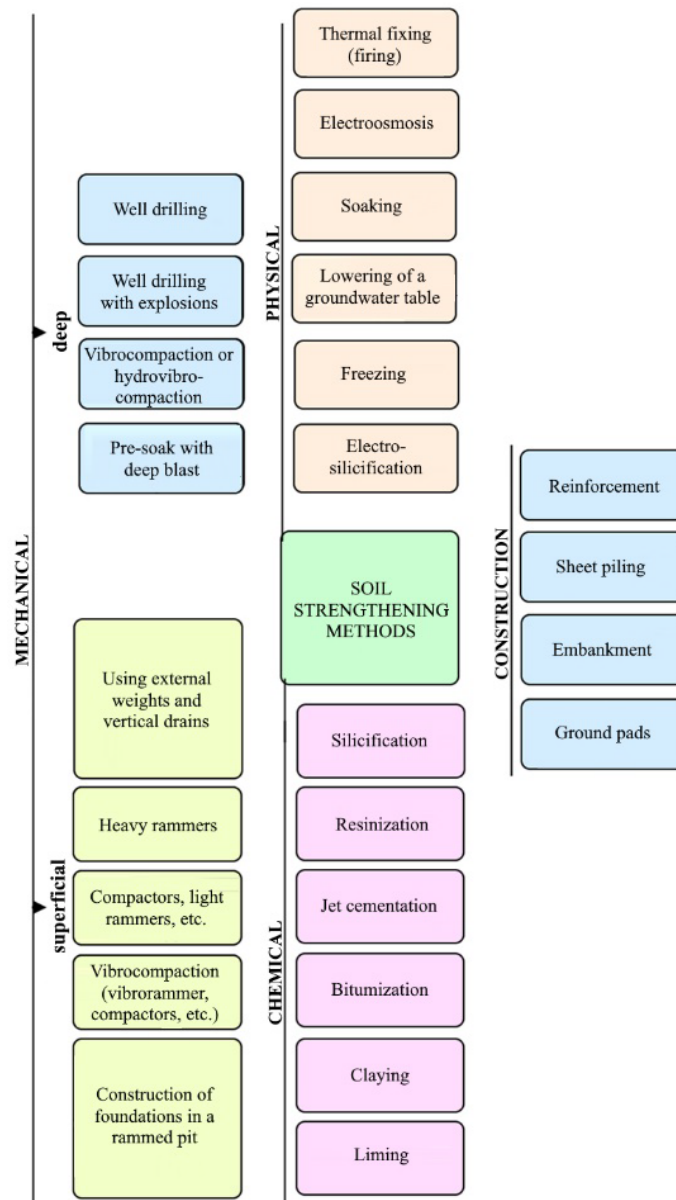
Figure 1. Soil strengthening methods.

a)

b)
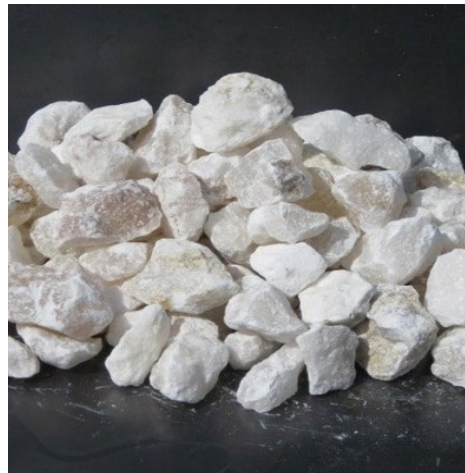
c)

Figure 2. CC components: a) Portland cement clinker, b) aluminosilicates, c) dihydrate gypsum.

Table 1. Composition of the clinker, % wt.

Chemical content						Mineral content			
CaO	SiO_2	Al_2O_3	Fe_2O_3	MgO	CaO_{free}	C_3S	C_2S	C_4AF	C_3A
64.5	22.6	6.4	3.8	1.8	0.9	57.5	23.6	16.8	2.1

The fine aggregate was used from screenings of crushed granite (GCS) (Vostokcement, Spassk-Dalniy, Russia) with fineness module 0.7 (Fig. 3).

Figure 3. Appearance of granite crushing screening.

Polycarboxylate superplasticizer (SP) used to reduce water-cement ratio.

Thus, the materials selected for research are local and often waste products, which is economically and environmentally promising.

2.2. Mix design

At the first stage, from the selected components listed in Fig. 1, a line of composite cements was created, obtained by joint grinding in a vibratory mill to a specific surface area of 450 m^2/kg (Table 2).

Table 2. Compositions and activity of composite cements.

Miz ID	Content				Activity, MPa 28 days	Increase in activity in relation to control, %
	Binder base, wt. %		Gypsum, % by weight of clinker	SP, % of CC wt.		
	Clinker	AS				
C1	100	–	5	–	45.9	–
C2	100	–	5	–	55.,2	17
CC-15*	85	15	5	0.25	56.7	24
CC-25	75	25	5	0.5	59.2	29
CC-35	**65**	**35**	**5**	**0.75**	**67.7**	**47**
CC-45	55	45	5	1	61.2	33
CC-55	45	55	5	1.25	56.1	22
CC-65	35	65	5	1.5	51.6	12

From the developed composite cements, a wide range of injection mortars from composite cements ground to a specific surface area of 450 m^2/kg was developed (Table 3). As a fine aggregate, polyfractional granite screenings with a fineness modulus of 0.7 were used. The level of replacement of clinker by the aluminosilicate component varied from 45 to 65 wt. %. The water-binder (W/B) ratio varied within 1.0–2.0. The ratio "binder : filler" was 1 : 3.

Table 3. The injection mortars.

Mix ID	Consumption, kg/m^3					W/B
	Clinker	AS	Gypsum	Water	GCS	
IM1(C2)	450	–	22,5	472.5	1350	1.0
IM2(C2)	450	–	22,5	708.8	1350	1.5
IM3(C2)	450	–	22,5	945	1350	2.0
IM4(CC-45)	247.5	202.5	12,4	464.4	1350	1.0
IM5(CC-45)	247.5	202.5	12,4	696.6	1350	1.5
IM6(CC-45)	247.5	202.5	12,4	928.8	1350	2.0
IM7(CC-55)	202.5	247.5	10,1	460.1	1350	1.0
IM8(CC-55)	202.5	247.5	10,1	690.1	1350	1.5
IM9(CC-55)	202.5	247.5	10,1	920.2	1350	2.0
IM10(CC-65)	157.5	292.5	7,9	457.9	1350	1.0
IM11(CC-65)	157.5	292.5	7,9	686.8	1350	1.5
IM12(CC-65)	157.5	292.5	7,9	915.8	1350	2.0

2.3. Equipment and methods

2.3.1. Materials morphology

To study the Portland cement mineral composition, a D8 Advance AXS X-ray powder diffractometer (Bruker, Billerick, USA) was used (wavelength λ = 1.5418 Å) using Rietveld refinement. The percentage of oxides and minerals in the Portland cement was determined by the standard method of X-ray fluorescence analysis.

2.3.2. Granulometry

The specific surface of bulk raw materials was studied using a PSH-11 device (Khodakov Devices, Moscow, Russia). The granulometry of the particles of the raw materials was evaluated using a laser analyzer Analysette 22 (Fritsch, Idar-Oberstein, Germany).

2.3.3. Fresh properties

The slump of the concrete mix is determined by laying a metal ruler with an edge on the top of the cone and measuring the distance from the lower edge of the ruler to the top of the concrete mixture with an error of up to 0.5 cm. The slump flow of the concrete mix is determined by measuring the diameter of the spread paste with a metal ruler in two mutually perpendicular directions with an error of not more than 0.5 cm. The viscosity was determined by the flow time of the mortar through a Marsh viscometer.

2.3.4. Physical and mechanical properties

The value of the average density of the samples was calculated by dividing the mass by the volume. The compressive strength was determined according to the standard method of the Russian standard on cubes with an edge of 70 mm. The flexural strength was determined by the three-point method on specimens of prismatic shape 40 × 40 × 160 mm.

2.3.5. Study of soil concrete

The mechanical properties of soil concrete (compressive strength and modulus of deformation) were evaluated on cylinder samples of soil concrete (sandy hard loam) with a diameter of 200 mm and a height of 400 mm with an artificial structure.

3. Results and Discussion

3.1. Fresh properties

Due to the high water-binding ratio, cast mortars were obtained, which are effective for the convenience of injection fixing of soils (Table 4).

Table 4. Indicators of viscosity and sedimentation of injection mortars.

Mix ID	Viscosity, s	Sedimentation over time in minutes, %							
		15	30	45	60	75	90	120	150
IM1	37	0	0.5	8.5	16.5	19.5	27.5	29.5	34.5
IM2	35	0.5	1.5	9.5	17.5	18.5	26.5	28.5	33.5
IM3	32	1	2	10	18	19	27	29	34
IM4	40	0.5	1	9.5	15.5	18.5	21.5	20.5	22.5
IM5	39	0	1.5	2	5.5	10.5	15.5	18.5	24.5
IM6	33	1	1.5	10.5	16	18.5	26.5	27.5	30.5
IM7	37	1	2	10	18	19	27	29	34
IM8	36	2	3	11	17	18	26	28	33
IM9	35	2.5	3.5	9.5	17.5	18.5	26.5	28.5	33.5
IM10	35	2.5	3.5	11.5	19.5	20.5	28	30	33
IM11	34	3	4	12	20	21	29	31	36
IM12	32	3.5	4.5	12.5	20.5	21.5	29.5	31.5	36.5

According to the sedimentation analysis of the mortars, it can be seen that these materials have a percentage of water separation from 22.5 % at W/B = 1 to 36.5 % at W/B = 2. At the same time, the viscosity indicators of these materials indicate a high penetrating ability, since the time of the expiration of solutions through the Marsh viscometer for mortars IM5 and IM6 is 39 and 40 seconds at W/B = 1.5 and W/B = 2, respectively.

An increase in the density of the mixed mixture with an increase in the content of the aluminosilicate component in the composite cement was established (Table 5). This picture is explained by the filling of voids formed in the process of volume reduction during hydration with finely dispersed particles of finely ground CC.

Table 5. Development of the injection mortars density.

Mix ID	Fresh mix average density, kg/m^3	Average density at 28 days, kg/m^3
IM1	2048	2062
IM2	2050 (+ 0.1 %)	2064 (+ 0.1 %)
IM3	2052 (+ 0.2 %)	2066 (+ 0.2 %)
IM4	2112 (+ 3.1 %)	2190 (+ 6.2 %)
IM5	2113 (+ 3.1 %)	2192 (+ 6.3 %)
IM6	2116 (+ 3.2 %)	2196 (+ 6.5 %)
IM7	2128 (+ 3.9 %)	2138 (+ 3.7 %)
IM8	2132 (+ 4.1 %)	2126 (+ 3.1 %)
IM9	2136 (+ 4.3 %)	2132 (+ 3.4 %)
IM10	2149 (+ 4.9 %)	2072 (+ 0.5 %)
IM11	2154 (+ 5.1 %)	2074 (+ 0.5 %)
IM12	2159 (+ 5.3 %)	2070 (+ 0.4 %)

The consequences of an increase in the density of injection mortars based on composite cement at the age of 28 days were maximum at a dosage of AS of 45 % by weight, then it decrease with an increase in the content of the aluminosilicate in the mixes.

3.2. Compressive and flexural strength

The effect of increase in compressive strength of injection mortars based on composite cement was maximum at an AS dosage of 45 % by weight, and at the same time it was the maximum effect for assessing early strength, in particular, at the age of 2 days, an increase in strength indicators during compression compared to the composition without additives was 25 %, and with a bend of 50 %. This also realizes high ratios of strength properties on the second day to comparable indicators at grade age: for compressive strength 0.24 (0.20–0.22 for clinker compositions without additives), for flexural strength 0.16 (0.15 in non-additive clinker compositions). High early strength allows to quickly apply injection mortars for urgent fixing of soils in the process of repairing underground structures (Table 6).

By day 7, the growth rate of strength properties stabilizes to some extent, however, it remains in comparison with the control composition: 6 % and 8 % for compressive and flexural strength. At the same

time, the ratio of flexural and compressive strength at this age (0.12) corresponds to a similar characteristic of additive-free compositions, despite the replacement of Portland cement clinker up to 65 wt. %. The ratio of flexural and compressive strengths at different ages can characterize the development of the material's crack resistance. For a rationally developed composition of IM5, it is: on the second day 0.16; in sevenths 0.12; at a grade age of 0.13, which is not only not lower than these characteristics for traditional Portland cement concretes but even exceeds them for some of the obtained materials.

As it was found, the strength development of cement materials based on composite cements is carried out more intensively than that of non-additive compositions due to the positive effect of the superplasticizer and polymineral components, helping to reduce water demand and intensify the hydration of clinker minerals and heat generation. Compaction of the microstructure leads to a decrease in capillary porosity and, accordingly, the permeability of the material for liquids and gases. In turn, this leads to an increase in the entire range of performance and durability.

Thus, the developed injection mortars are able to provide the necessary degree of strengthening of subsiding soils.

3.3. Strengthening of load-bearing structures with developed mixes

The main strength and deformation characteristics of the injection-fixed soils of the foundations of buildings and structures are the compressive strength and the deformation modulus.

To determine these characteristics, at first the properties of soil concretes obtained by injecting solutions into soil cylinder samples (sandy solid loams) with an artificial structure were to be determined. This is explained by the fact that when fixing soils, physical and chemical processes occur mainly in the microaggregate part of the soil. Moreover, the strength characteristics of soil-concrete specimens with natural and artificial structures are practically the same and comparable. It should be noted that it is easy and simple to manufacture samples with an artificial structure in any size and in large quantities, and it is also possible to model soil bases of various configurations, taking into account the requirements of the standard for testing artificial materials (Table 7).

Table 6. Mechanical properties of the developed shotcrete.

Properties	IM1	IM2	IM3	IM4	IM5	IM6	IM7	IM8	IM9	IM10	IM11	IM12
Compressive strength, MPa												
2 days	17.9	17.3	17.0	21.5	22.4	19.3	22.1	21.5	21.2	21.9	20.8	19.7
		(− 3%)	(− 5 %)	(+ 20%)	(+ 25 %)	(+ 8 %)	(+ 23 %)	(+ 20 %)	(+ 18 %)	(+ 22 %)	(+ 16 %)	(+ 10 %)
7 days	31.7	30.8	30.6	32.4	33.7	31.5	33.5	32.8	32.1	32.3	31.6	31.2
		(− 3 %)	(− 3 %)	(+ 2 %)	(+ 6 %)	(−1 %)	(+ 6 %)	(+ 3 %)	(+ 1 %)	(+ 2 %)	(− 1 %)	(− 2 %)
28 days	54.1	5.,8	55.0	61.2	68.1	63.3	67.0	67.4	69.1	61.3	67.3	65.2
		(− 1 %)	(− 2 %)	(+ 13 %)	(+ 26 %)	(+ 17 %)	(+ 24 %)	(+ 25 %)	(+ 28 %)	(+ 13 %)	(+ 25 %)	(+ 20 %)
R^2_{com} / R^{28}_{fl}	0.33	0,32	0.31	0.35	0.33	0.30	0.33	0.32	0.31	0.36	0.31	0.30
Flexural strength, MPa												
2 days	1.8	1.7	1,6	2.6	2.7	1.9	2.2	2.2	2.2	2.2	2.1	1.9
		(− 6 %)	(− 12 %)	(+ 44 %)	(+ 50 %)	(+ 6 %)	(+ 22 %)	(+ 22 %)	(+ 22 %)	(+ 22 %)	(+ 17 %)	(+ 6 %)
7 days	3.8	3.7	3,7	3.9	4.1	3.8	4.0	3.9	3,.9	3.9	3.8	3.7
		(− 1 %)	(− 1 %)	(+ 1 %)	(+ 8 %)		(+ 5 %)	(+ 1 %)	(+ 1 %)	(+ 1 %)		(− 1 %)
28 days	7.0	7.0	7,1	8.0	8.6	7.6	8.0	8.1	8.3	8.0	7.8	7.3
			(+ 1 %)	(+ 14 %)	(+ 23 %)	(+ 9 %)	(+ 14 %)	(+ 16 %)	(+ 19 %)	(+ 14 %)	(+ 11 %)	(+ 4 %)
$R_{fl}/R_{com.}$, 2 days	0.10	0.10	0.09	0.12	0.12	0.10	0.10	0.10	0.10	0.10	0.10	0.10
R^2_{fl} / R^{28}_{fl}	0.26	0.24	0.23	0.27	0.32	0.25	0.28	0.27	0.26	0.28	0.27	0.26
$R_{fl}/R_{com.}$, 7 days	0.12	0.12	0.12	0.12	0.12	0.12	0.12	0.12	0.12	0.12	0.12	0.12
$R_{fl}/R_{com.}$, 28 days	0.13	0.13	0.13	0.13	0.13	0.12	0.12	0.12	0.12	0.12	0.12	0.12

Table 7. Strength and deformation properties of soil concrete.

Mix ID	Compressive strength, MPa	Deformation modulus, MPa
IM1	10.1	2100
IM2	11.3	3200
IM3	12.4	3700
IM4	22.3	9300
IM5	25.6	10100
IM6	24.3	9700
IM7	19.1	7600
IM8	20.6	8100
IM9	18.7	7100
IM10	14.2	5800
IM11	15.3	6200
IM12	13.1	4200

Dependence of the deformation modulus on the strength of soil concretes of two different types (sandy hard loams and semi-solid loams fixed with the developed injection mortars) is shown in Fig. 4. The graph shows that the greater the strength index of soil concrete is, the higher its modulus of deformation is. At the same time, it should be noted that the most important factor influencing the strength and deformation properties of soil concrete is the percentage of AS and W/B of the mortars with which these soils are fixed.
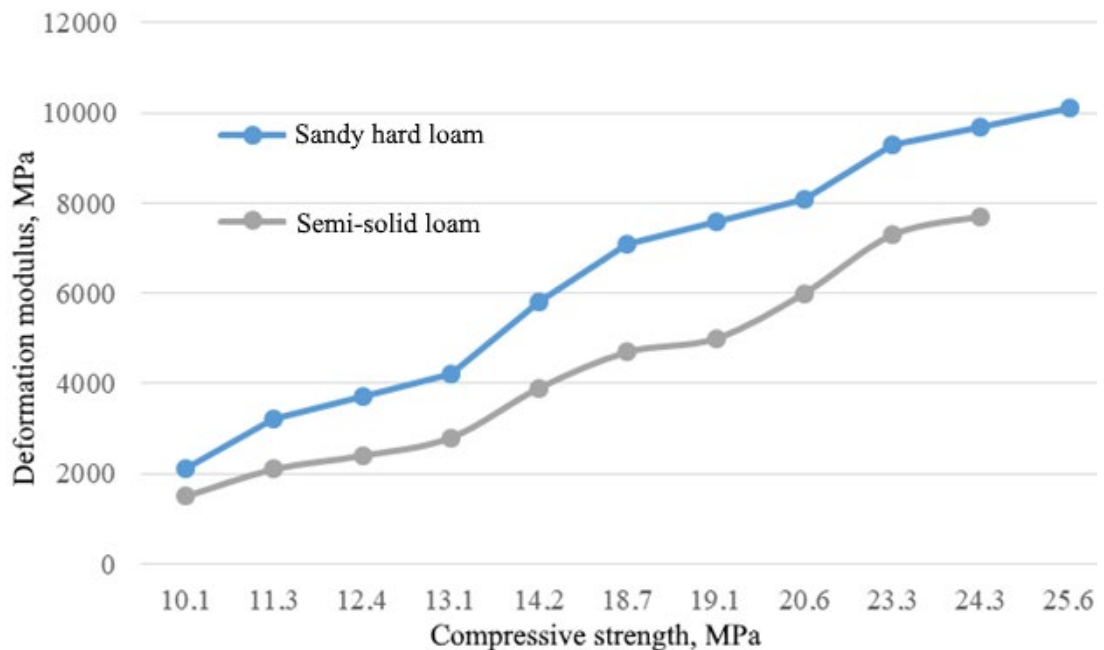
Figure 4. Dependence of the deformation modulus on the strength of soil concrete.

The mechanism of structure formation of fixed soils, which consists in the elimination of reversible transitional contacts that can quickly collapse in the process of wetting, with the formation of stronger phase contacts of the cementation type, leading to an increase in structural strength, has been studied.

Thus, the developed injection mortars are able to effectively fix the soils of the bases of underground structures, providing the strength of the soil-concrete mass up to 25.6 MPa with a deformation modulus of 10.1 GPa.

4. Conclusions

Consolidation of subsidence soils is an important practical scientific and technical task, which makes it possible to carry out construction and repair work on weak (subsidence) base soils. Injection mortars were developed and their research was carried out to strengthen underground structures, as a result of which the following conclusions were obtained:

1. According to the sedimentation analysis of mortars, it can be seen that these materials have a percentage of water separation from 22.5 % at W/B = 1 to 36.5 % at W/B = 2. At the same time, the viscosity indicators of these materials prove a high penetrating ability, since the time of the expiration of mortars through the Marsh viscometer for mortars IM5 and IM6 is 39 and 33 seconds at W/B = 1.5 and W/B = 2, respectively.

2. The effect of increasing the density of injection mortars on composite cement at the age of 28 days was maximum at an AS dosage of 45 % by weight, then it decreased with an increase in the content of the aluminosilicate component.

3. There are high ratios of the values of strength properties on the second day to those in the grade age: for compressive strength 0.24 (0.20–0.22 for additive-free clinker compositions), for bending strength 0.16 (0.15 for additive-free clinker compositions; at the same time, with an increase in the AS content above 45 %, this ratio decreases to 0.14). High early strength makes it possible to effectively use injection solutions for urgent fixing of soils during the repair of underground structures.

The developed injection mortars are capable of effectively fixing the foundation soils of underground structures, providing the strength of the soil-concrete mass up to 25.6 MPa with a deformation modulus of 10.1 GPa.

The developed injection solutions showed improved characteristics (by 15–35 %) in terms of percentage of water separation, viscosity, penetrating ability, density, strength, and deformation modulus compared to modern results of world-class authors [27–31].

References

1. Fan, H., Li, T., Gao, Y., Deng, K., Wu, H. Characteristics inversion of underground goaf based on InSAR techniques and PIM. International Journal of Applied Earth Observation and Geoinformation. 2021. 103. Article no 102526. DOI: 10.1016/j.jag.2021.102526

2. Guo, D., Chen, Y., Yang, J., Tan, Y.H., Zhang, C., Chen, Z. Planning and application of underground logistics systems in new cities and districts in China. Tunnelling and Underground Space Technology. 2021. 113. Article no 103947. DOI: 10.1016/j.tust.2021.103947

3. Hebbal, B., Marif, Y., Hamdani, M., Belhadj, M.M., Bouguettaia, H., Bechki, D. The geothermal potential of underground buildings in hot climates: Case of Southern Algeria. Case Studies in Thermal Engineering. 2021. 28. Article no 101422. DOI: 10.1016/j.csite.2021.101422

4. Volodchenko, A.A. Efficient Silicate Composites of Dense Structure Using Hollow Microspheres and Unconventional Aluminosilicate Raw Materials. Construction Materials and Products. 2023. 6(2). Pp. 19–34. DOI: 10.58224/2618-7183-2023-6-2-19-34

5. Lee, B., Wang, S.-Y., Lin, T.-C., Chang, H.-H. Underground pipeline explosions and housing prices: Quasi-experimental evidence from an urban city. Land Use Policy. 2021. 111. . Article no 105782. DOI: 10.1016/j.landusepol.2021.105782

6. Lu, W., Wu, Y., Choguill, C.L., Lai, S.-K., Luo, J. Underground Hangzhou: The challenge of safety vs. commerciality in a major Chinese city. Cities. 2021. 119. Article no 103414. DOI: 10.1016/j.cities.2021.103414

7. Harcenko, I.Ya., Panchenko, A.I., Piskunov, A.A., Harcenko, A.I., Mirzoyan, M. Mineral Injection Mixtures for Construction and Operation of Underground Structures under Dense Urban Development Conditions. Zhilishchnoe Stroitel'stvo [Housing Construction]. 2020. 10. Pp. 53–60. DOI: 10.31659/0044-4472-2020-10-53-60

8. Svintsov, A.P., Shchesnyak, E.L., Galishnikova, V.V., Fediuk, R.S., Stashevskaya, N.A. Effect of nano-modified additives on properties of concrete mixtures during winter season. Construction and Building Materials. 2020. 237. Article no 117527. DOI: 10.1016/j.conbuildmat.2019.117527

9. Salamanova, M.Sh., Murtazaev, S.-A.Yu., Alaskhanov, A.Kh., Ismailova, Z.Kh. Development of Multicomponent Binders Using Fine Powders. Proceedings of the International Symposium "Engineering and Earth Sciences: Applied and Fundamental Research" dedicated to the 85th anniversary of H.I. Ibragimov (ISEES 2019). Atlantis Press. 2019. Pp. 524–528. DOI: 10.2991/isees-19.2019.58

10. Huang, J., Kogbara, R.B., Hariharan, N., Masad, E.A., Little, D.N. A state-of-the-art review of polymers used in soil stabilization. Construction and Building Materials. 2021. 305. Article no 124685. DOI: 10.1016/j.conbuildmat.2021.124685

11. Fediuk, R.S., Lesovik, V.S., Liseitsev, Yu.L., Timokhin, R.A., Bituyev, A.V., Zaiakhanov, M.Ye., Mochalov, A.V. Composite binders for concretes with improved shock resistance. Magazine of Civil Engineering. 2019. 851. Pp. 28–38. DOI: 10.18720/MCE.85.3

12. Wu, T., Zhang, Y., Sun, H., Galindo, R., Wu, W., Cai, Y. Dynamic response of sheet-pile groin under tidal bore considering pile-pile mutual interaction and hydrodynamic pressure. Soil Dynamics and Earthquake Engineering. 2023. 164. Article no 107568. DOI: 10.1016/j.soildyn.2022.107568

13. Fediuk, R.S., Smoliakov, A.K., Timokhin, R.A., Batarshin, V.O., Yevdokimova, Yu.G. Using thermal power plants waste for building materials. IOP Conference Series: Earth and Environmental Science. 2017. 87(9). Article no 092010. DOI: 10.1088/1755-1315/87/9/092010

14. Ibragimov, R., Fediuk, R.S. Improving the early strength of concrete: Effect of mechanochemical activation of the cementitious suspension and using of various superplasticizers. Construction and Building Materials. 2019. 226. Pp. 839–848. DOI: 10.1016/j.conbuildmat.2019.07.313

15. Nizina, T.A., Nizin, D.R., Selyaev, V.P., Spirin, I.P., Stankevich, A.S. Big data in predicting the climatic resistance of building materials. I. Air temperature and humidity. Construction Materials and Products. 2023. 6(3). Pp. 18–30. DOI: 10.58224/2618-7183-2023-6-3-18-30

16. Kiliç, R., Küçükali, Ö., Ulamiş, K. Stabilization of high plasticity clay with lime and gypsum (Ankara, Turkey). Bulletin of Engineering Geology and the Environment. 2016. 75(2). Pp. 735–744. DOI: 10.1007/s10064-015-0757-2

17. Gavrilov, T.A., Kolesnikov, G.N. Evolving crack influence on the strength of frozen sand soils. Magazine of Civil Engineering. 2020. 94(2). Pp. 54–64. DOI: 10.18720/MCE.94.5

18. Li, W., Yi, Y., Puppala, A.J. Effects of curing environment and period on performance of lime-GGBS-treated gypseous soil. Transportation Geotechnics. 2022. 37. Article no 100848. DOI: 10.1016/j.trgeo.2022.100848

19. Vorona-Slivinskaya, L.G. Regional plans for solid waste management: distinctive features of practice in Russia and EU countries. Construction Materials and Products. 2023. 6(3). Pp. 98–118. DOI: 10.58224/2618-7183-2023-6-3-98-118

20. Ebailila, M., Kinuthia, J., Oti, J., Al-Waked, Q. Sulfate soil stabilisation with binary blends of lime-silica fume and lime-ground granulated blast furnace slag. Transportation Geotechnics. 2022. 37. Article no 100888. DOI: 10.1016/j.trgeo.2022.100888

21. Ghanitoos, H., Goharimanesh, M., Akbari, A. Prediction of drill penetration rate in drilling oil wells using mathematical and neurofuzzy modeling methods. Energy Reports. 2024. 11. Pp. 145–152. DOI: 10.1016/j.egyr.2023.11.006

22. Mavlyanova, N.G., Ismailov, V.A., Larionova, N.A. Comparative assesment of influence of loess soils soaking and silication methods on changes of their seismic properties in regional comdtions of Uzbekistan. Engineering Geology. 2017. 4. Pp. 72–80. DOI: 10.25296/1993-5056-2017-4-72-80

23. Cheng, Y., Wang, Z., Liang, S., Zheng, A., Liu, K. Analysis of macro and micro freezing characteristics of gravelly soil. Environmental Research. 2023. 216(2). Article no 114600. DOI: 10.1016/j.envres.2022.114600

24. Fang, R., Wang, B., Pan, J., Liu, J., Wang, Z., Wang, Q., Ling, X. Effect of concrete surface roughness on shear strength of frozen soil-concrete interface based on 3D printing technology. Construction and Building Materials. 2023. 366. Article no 130158. DOI: 10.1016/j.conbuildmat.2022.130158

25. Lyu, Q., Dai, P., Zong, M., Zhu, P., Liu, J. Plant-germination ability and mechanical strength of 3D printed vegetation concrete bound with cement and soil. Construction and Building Materials. 2023. 408. Article no 133587. DOI: 10.1016/j.conbuildmat.2023.133587

26. Mezhgosudarstvennyj standart GOST 310.4-81. Cementy. Metody opredeleniya predela prochnosti pri izgibe i szhatii [Cements. Methods of bending and compression strength determination]. Izdatel'stvo standartov. 1981. Pp. 12–22.

27. Castel, A., Foster, S.J. Bond strength between blended slag and Class F fly ash geopolymer concrete with steel reinforcement. Cement and Concrete Research. 2015. 72. Pp. 48–53. DOI: 10.1016/j.cemconres.2015.02.016

28. Zhao, G., Zhu, Z., Ren, G., Wu, T., Ju, P., Ding, S., Shi, M., Fan, H. Utilization of recycled concrete powder in modification of the dispersive soil: A potential way to improve the engineering properties. Construction and Building Materials. 2023. 389. Article no 131626. DOI: 10.1016/j.conbuildmat.2023.131626

29. Chen, J.-Y., Feng, D.-L., Liu, J.-H., Yu, S.-Y., Lu, Y. Numerical modeling of the damage mechanism of concrete-soil multilayered medium subjected to underground explosion using the GPU-accelerated SPH. Engineering Analysis with Boundary Elements. 2023. 151. Pp. 265–274. DOI: 10.1016/j.enganabound.2023.03.003

30. Liu, S.-w., Zhang, Q.-q., Ma, B., Li, Z.-b., Yin, W.-p., Lou, Q.-g. Study on surface roughness effect on shear behavior of concrete-soil interface. Engineering Failure Analysis. 2023. 145. Article no 107050. DOI: 10.1016/j.engfailanal.2023.107050

31. Fehervari, A., MacLeod, A.J.N., Gallage, C., Collins, F., Callahan, D., Gates, W.P. Suitability of remediated heat-treated soil in concrete applications. Journal of Environmental Management. 2023. 329. Article no 117076. DOI: 10.1016/j.jenvman.2022.117076

32. Prakash, R., Divyah, N., Srividhya, S., Avudaiappan, S., Amran, M., Raman, S.N., Guindos, P., Vatin, N.I., Fediuk, R.S. Effect of Steel Fiber on the Strength and Flexural Characteristics of Coconut Shell Concrete Partially Blended with Fly Ash. Materials. 2022. 15. Article no 4272. DOI: 10.3390/ma15124272

33. Makul, N., Fediuk, R., Amran, M., Zeyad, A.M., Klyuev, S., Chulkova, I., Ozbakkaloglu, T., Vatin, N., Karelina, M., Azevedo, A. Design Strategy for Recycled Aggregate Concrete: A Review of Status and Future Perspectives. Crystals. 2021. 11. Article no 695. DOI: 10.3390/cryst11060695

Information about authors:

Roman Fediuk, *Doctor of Technical Sciences*
ORCID: *https://orcid.org/0000-0002-2279-1240*
E-mail: *roman44@yandex.ru*

Valeriy Lesovik, *Doctor of Technical Sciences*
ORCID: *https://orcid.org/0000-0002-2378-3947*
E-mail: *naukavs@mail.ru*

Svetlana Vavrenyuk, *Doctor of Technical Sciences*
E-mail: *trusanova2014@mail.ru*

Mikhail Zaiakhanov, *Doctor of Technical Sciences*
E-mail: *roman44@ya.ru*

Aleksandr Bituyev, *Doctor of Technical Sciences*
E-mail: *office@esstu.ru*

Sergey Klyuev, *Doctor of Technical Sciences*
ORCID: *https://orcid.org/0000-0002-1995-6139*
E-mail: *Klyuyev@yandex.ru*

Kequan Yu, PhD
E-mail: *12yukequan@tongji.edu.cn*

Yaroslav Lesovik,
E-mail: *lesovik@ya.ru*

Konstantin Bakatov,
E-mail: *bakatov@ya.ru*

Mechanical behavior and eco-efficiency of sisal fiber reinforced cement composites containing husk rice ash

K.G. Calazans[1] iD , *P.R.L. Lima[1]* ✉ iD , *R.D. Toledo Filho[2]* iD

[1] State University of Feira de Santana, Bahia, Brazil

[2] Federal University of Rio de Janeiro, Rio de Janeiro, Brazil

✉ *prllima@uefs.br*

Abstract. The use of cementitious composites reinforced with plant fibers in construction elements has emerged as a promising alternative to mitigate the environmental impact of the construction industry. The challenge of chemical incompatibility between plant fibers and the matrix has been addressed through the incorporation of mineral additives, with metakaolin being the most commonly used despite its high energy consumption during production and CO_2 generation. An alternative to this industrial additive is rice husk ash (RHA), a pozzolanic material derived from agricultural waste. The research aims to evaluate the influence of a high RHA content replacing cement on the mechanical properties and sustainability indicators of composites reinforced with 4 % and 6 %, by mass, of sisal fibers. Composites incorporating 50 % RHA exhibited higher compressive strength, multiple cracks, and increased toughness under flexion compared to composites with metakaolinite, fly ash, and silica of fume. Sustainability assessments indicated that replacing metakaolin with RHA resulted in reduced CO_2 emissions and embodied energy, contributing to the enhanced eco-efficiency of the composites. This improvement was particularly notable in terms of increased compressive strength and toughness.

1. Introduction

One of the primary challenges in civil construction is aligning with the United Nations' Sustainable Development Goals, particularly in the context of establishing inclusive, sustainable, and resilient cities. To attain this objective, a pivotal step for civil engineering is the utilization of sustainable materials that not only curtail greenhouse gas emissions but also exhibit lower energy consumption during their production. In this context, the incorporation of waste materials from other industrial sectors into the construction industry offers an advantage over traditional materials because they are ready for use after minimal processing operations, which have a lower environmental impact. In the case of utilizing agro-industrial waste, such as rice husk, there is an added benefit of it originating from plant sources that sequester carbon during their growth, thus contributing to minimizing environmental harm caused by transformation processes required to make them suitable for construction materials.

Rice husk ash (RHA) has emerged as a promising mineral addition in cement-based material production [1], offering various benefits that enhance the sustainability and performance of construction materials. In recent years, several studies have demonstrated the positive effects of incorporating RHA in

concrete, leading to increased compressive strength, improved durability, and a reduced environmental impact in the construction industry. It can be used in the production of normal concrete [2], contributing to the widespread use of this sustainable additive in standard construction practices. Additionally, RHA has shown promise in producing lightweight concrete for use in bricks [3], concrete containing recycled aggregates [4], and self-compacting concrete for highway pavements [5]. By replacing a portion of cement with RHA, the construction industry can significantly enhance its sustainability profile, since cement production is a major contributor to greenhouse gases emissions and energy consumption in the civil construction sector. Therefore, integrating RHA into concrete formulations helps mitigate the environmental impact, reduce CO_2 emissions, and conserve energy resources, contributing to a greener and more eco-friendly construction sector.

The utilization of RHA in cementitious matrices for cement-based composites reinforced with plant fibers was initially explored in the 1980s, with researchers studying its potential benefits [6–8]. The natural fiber reinforced cement composites offer the opportunity to produce robust and durable construction elements, suitable for various applications, such as blocks for precast slabs [9], sandwich panels [10], lightweight tiles, which enhance the thermal comfort of buildings in urban and rural areas [11] or ultra-high-performance concrete [12]. Plant fibers, being renewable resources, hold a sustainability advantage over steel and polymeric fibers. However, their successful application as reinforcement in cement-based composites requires overcoming the potential chemical incompatibility between the fibers and the hydrated cement compounds. To address this, two main approaches have been employed by researchers: application of chemical treatment to the fiber [13] or developing calcium hydroxide-free (CH-free) matrices, which are responsible for a mineralization process of the vegetable fiber [14].

To create CH-free cementitious matrices, researchers have successfully replaced a portion of the cement with mineral additions that exhibit excellent pozzolanic reactivity. These mineral additions, such as fly ash, silica of fume, and metakaolinite, react with calcium hydroxide produced during cement hydration to form additional cementitious compounds. This process not only improves the strength and durability of the cementitious matrix but also reduces the potential for chemical incompatibility with vegetable fibers [14]. Despite the advantages of using RHA as a mineral addition to improve cement-based composites reinforced with plant fibers [15], the development of constructive elements using these materials has primarily employed silica of fume [9] or metakaolinite [10].

Certainly, rice husk ash offers numerous advantages over industrial mineral additions like metakaolinite, particularly in terms of enhancing sustainability in construction materials. RHA is a byproduct obtained from the combustion of plant biomass, making it both renewable and readily available. For use in construction, RHA undergoes a grinding and drying process, resulting in equivalent CO_2 emissions ranging from 103.2 to 157 kg CO_2/t [16, 17], as well as energy consumption in the range of 200 to 2070 MJ/t [17–19]. In contrast, industrial mineral additives, such as metakaolinite, are manufactured using energy-intensive processes and are non-renewable, resulting in a greater environmental impact and depletion of finite resources. The substantial equivalent CO_2 emissions associated with metakaolinite, which can vary from 236 to 840 kg CO_2/t [16, 20–22], stem from the energy-intensive processes, with energy consumption ranging from 2720 to 3300 MJ/t [18, 23]. These processes involve calcination and grinding operations during its production. Despite this environmental impact, metakaolin is extensively used due to its ability to enhance mechanical strength. This highlights the need for studies that assess the relationship between mechanical efficiency and sustainability, as will be presented in this article.

The aim of this study is to perform a comparative analysis of the influence of various mineral additions, used as substitutes for cement, on the mechanical properties and sustainability of sisal fiber reinforced cement composites (SFRCC). To achieve this, SFRCC were produced and reinforced with 4 % and 6 %, in mass, of sisal fiber, incorporating rice husk ash, metakaolinite, fly ash, and silica of fume. They were then subjected to direct compression and bending tests. Additionally, this research assesses the CO_2 emissions, energy consumption, and eco-efficiency of composites reinforced with 4 % sisal fibers.

2. Materials and Methods

2.1. Materials

The sisal fibers were sourced from Valente, Brazil. A pre-treatment procedure involved immersing the fibers in water at 50° C for 1 hour to eliminate residues adhering to their surface. Following this, the fibers were manually aligned and cut to a length of 40 mm. An alkaline treatment based on calcium hydroxide was applied to the fibers in order to improve their adhesion with the matrix. The procedure was performed with immersion of the fibers in a solution of calcium hydroxide – $Ca(OH)_2$, at a concentration of 0.73 %. After 50 minutes of immersion, the fibers were removed, placed in sieves for drying in the open air. After treatment, the fibers showed a lower rate of water absorption and higher tensile strength, comparative to natural fibers.

To produce the cementitious matrix of the composites, natural quartz sand with particles smaller than 600 μm and density of 2.67 g/cm^3 was used. The binder was formed by a combination of high initial strength Portland cement, metakalonite (MK), silica, fly ash, and rice husk ash. The rice husk ash used in this work, commercially known as amorphous rice husk silica (SILCCA NOBRE), is produced by controlled combustion via fluidized bed of rice husk agricultural waste from the food industry. The chemical composition and density of these materials is shown in Table 1 while in Fig. 1 the particle size curves are shown.

According to ASTM C618, all binders can be classified as pozzolanic material since the sum of three oxides from their chemical analyses, $SiO_2 + Al_2O_3 + Fe_2O_3$, was higher than 70 %. The granulometry of the binders, represented in Table 1 by the D50 diameter, corresponding to cumulative passing at 50 %, confirms that the rice husk ash has a fineness compatible with cement and metakaolinite, which enhances its chemical reactivity.
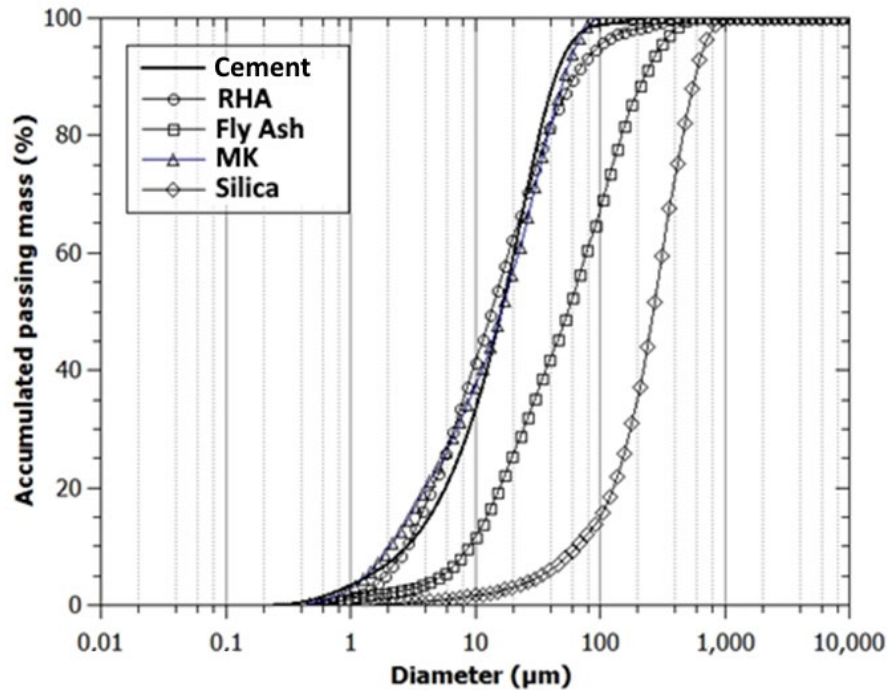

Figure 1. Granulometric curves of binders.

Table 1. Chemical composition, density and medium diameter of binders.

Major chemical component (%)	Cement	Fly ash (FA)	Silica of fume (SF)	Rice husk ash (RHA)	Metakaolin
CaO	68.97	1.94	0.52	0.78	–
SiO$_2$	14.95	52.24	94.90	94.95	51.85
Al$_2$O$_3$	4.70	33.80	1.91	–	41.69
SO$_3$	4.29	1.79	1.59	1.25	1.09
Fe$_2$O$_3$	3.50	4.91	0.10	0.07	1.91
K$_2$O	0.98	3.44	0.86	2.37	1.89
Density (g/cm^3)	3.18	2.16	2.39	2.24	2.81
D50 (μm)	17.4	60.2	275.4	15.1	17.4

The cement matrices, in the proportion of 1 : 1 : 0.5 (binder : sand : water/binder ratio, by weight), were prepared with the use of different binders in three combinations, as shown in Table 2. The cement content was 50 % of the total mass of binder in all mixtures. The mix 30MK has, in addition to cement, 30 % metakaolinite ash, 10 % fly ash, and 10 % silica of fume. The mix 30RHA had the objective of evaluating the replacement of metakaolinite by 30 % of the rice husk ash, keeping the cement and the other mineral additions. The mix 50RHA replaces all mineral additions with rice husk ash; the binder being made up of 50 % cement and 50 % rice husk ash. With these three matrices, SFRCC were produced with the addition of 4 % and 6 %, by mass, of sisal fiber randomly distributed in the mixture.

Table 2. Mix proportions of the composites (kg/m³).

Components		30MK4%	30RHA4%	30RHA6%	50RHA4%	50RHA6%
Binder	Cement	389.4	381.4	374.3	381.1	374.0
	Metakaolin	233.7	–	–	–	–
	Rice husk ash	–	228.8	224.6	381.1	374.0
	Fly ash	77.9	76.3	74.9	–	–
	Silica of fume	77.9	76.3	74.9	–	–
Aggregate	Sand	778.9	762.8	748.6	762.2	748.0
Additives	Plasticizer	7.8	7.6	7.5	7.6	7.5
	Viscosity agent	3.9	3.8	3.7	3.8	3.7
Water		389.4	381.4	374.3	381.1	374.0
Fiber		31.1	30.5	44.9	30.5	44.9

2.2.   Methods

A third-generation superplasticizer with a solid content of 31 % and density of 1.06 g/cm³ was added to the mixtures to ensure a self-compacting behavior for all matrices. The viscosity modifier admixture Rheomac UW 410, with density of 0.7 g/cm³, at a dosage of 0.05 % relative to the binder, by mass, was also used to avoid segregation of composites during molding. The composites were produced in a bench mortar with a capacity of 20 dm³ and their flowability was tested using a flow table.

The uniaxial compression test was carried out on a 100 kN Shimadzu machine at a rate of axial displacement of 0.2 mm/min. The static-elastic chord modulus of elasticity was calculated from the stress-strain diagram, as recommended by ASTM C 469.

For the 4-point bending test, three plates were cut in prismatic specimens with dimensions of 400 mm × 80 mm × 15 mm and tested over a span of 300 mm at a displacement rate of 0.3 mm/min with a 100 kN Shimadzu machine, with the load cell of 1 kN. From the load–deflection curves three parameters were calculated to evaluate the fiber reinforcement effect: a) the first-cracking flexural stress $\left(\sigma_{fc}\right)$, determined from the load correspondent to first crack; b) the maximum stress post-cracking of the composite $\left(\sigma_{pc}\right)$, determined from the maximum load supported by the composite after the first crack; and c) the toughness, defined as the area under stress–deflection curves. The evaluation of the cracking pattern was performed through the analysis of images obtained from different displacement stages. A CANON D90 digital camera with Macro Lens and 10 megapixel resolution was used, which captured high resolution images every 30 seconds.

3.   Results and Discussion

3.1.   Mechanical behaviour of SFRCC

3.3.1. Mechanical behavior under compression

Fig. 2 illustrates typical stress-strain curves for the composites under compression at curing times of 7, 28, and 56 days. The curves allowed us to determine the compressive strength values, corresponding to the maximum tension reached during the test, and the modulus of elasticity.
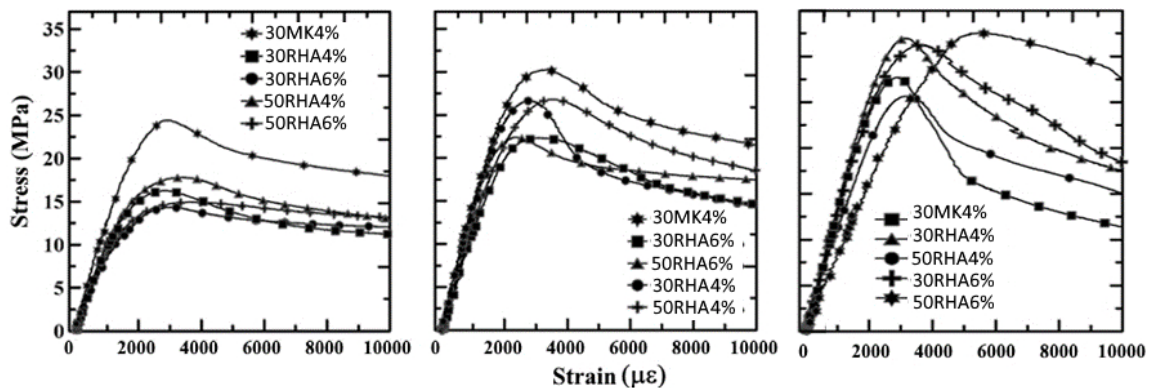

Figure 2. Typical stress x strain curves of composites under axial compression:
a) 7 days; b) 28 days; c) 56 days.

The results presented in Table 3 demonstrate that the composites exhibited compressive strength values, at 28 days, ranging from 23.18 MPa to 29.12 MPa and modulus of elasticity values ranging from 13.68 GPa to 15.80 GPa. These mechanical properties indicate that the composites possess sufficient strength and stiffness for use in building elements without structural function.

Table 3. Compressive strength and modulus of elasticity of composites.

Composite	Compressive strength (MPa)			Elastic Modulus (GPa)		
	7 days	28 days	56 days	7 days	28 days	56 days
30MK4%	24.10 (0.87)	29.12 (3.41)	30.30 (5.09)	13.41 (12.40)	15.34 (3.60)	15.80 (3.23)
30RHA4%	16.08 (1.44)	25.55 (4.96)	27.69 (11.72)	11.86 (1.44)	12.21 (0.11)	14.11 (10.75)
30RHA6%	14.45 (1.10)	23.24 (5.02)	25.33(10.22)	10.32 (7.64)	11.94 (10.54)	14.02 (12.16)
50RHA4%	16.72 (8.93)	25.25 (9.88)	32.27 (9.20)	10.83 (3.34)	14.41 (6.36)	14.84 (11.36)
50RHA6%	14.69 (1.66)	23.18 (4.47)	31.64 (1.73)	9.91 (2.63)	13.11 (7.11)	13.68 (7.96)
Coefficient of variation, in % (in parentheses)						

By evaluating the replacement of metakaolinite with rice husk ash, a reduction of 33.3 % and 20.4 % in compressive strength was observed at ages of 7 days and 28 days, respectively. This finding confirms the hypothesis that higher reactivity additions lead to increased mechanical strength. Specifically, for similar levels of replacement of the mineral addition with cement, using metakaolinite results in greater compressive strength than using rice husk ash at 28 days, as reported by [24].

In Fig. 3, the evolution of the compressive strength and elastic modulus of the composites is presented over a 7-day period.
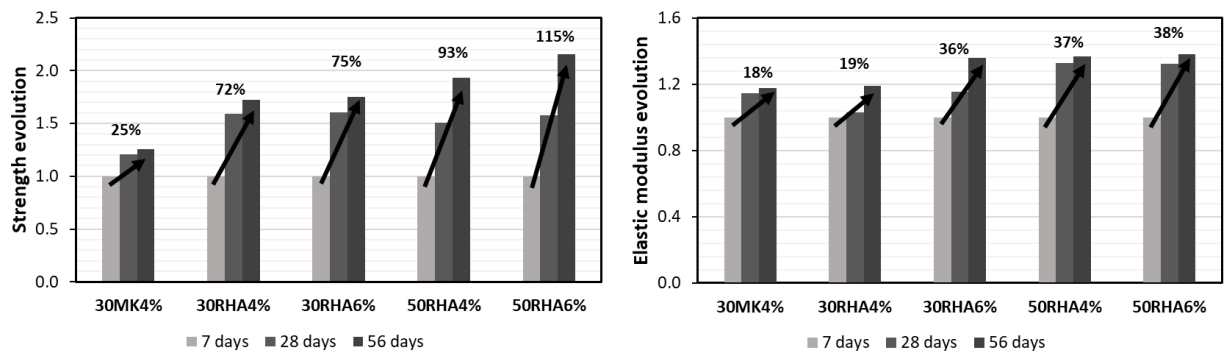

Figure 3. Evolution of mechanical properties in relation to the 7 days of curing.

For the 30MK4% and 30RHA4% composites, the strength evolution from 7 days to 56 days was 25 % and 72 %, respectively. However, for the 50RHA4% composite, where all mineral additions are replaced by rice husk ash, the strength evolution reached 93 % at 56 days, achieving an absolute mechanical strength greater than that of the 30MK4% composite. The strength evolution of the 50RHA composite, reaching 115 % at 56 days of age, indicates that rice husk ash exhibits slower reactivity compared to metakaolinite, which is consistent with the findings of [25]. The observed results suggest that the complete replacement of mineral additions with rice husk ash led to a favorable and continuous strength development over time.

Regarding the elastic modulus, the incorporation of rice husk ash led to a reduction in comparison to the mixtures with metakaolinite. Specifically, the reductions were 20 % and 6 % for the 30RHA4% and 50RHA4% composites, respectively, when compared to the 30MK4% composite. However, it is noteworthy that over time, specifically at an age of 56 days, the composite with 50 % rice husk ash exhibited a more significant evolution in the elastic modulus, as illustrated in Fig. 3. This indicates that the rice husk ash composite demonstrated an improved rate of stiffness development during the later stages of curing, which compensated for the initial reduction in modulus compared to the 30MK4% composite.

In general, fiber cement-based composites often experience a reduction in mechanical strength as the fiber content increases. This is attributed to the challenge of homogenizing and placing the fresh composite, especially with higher fiber volumes [26]. However, in the composites produced in this study, the increase in fiber content did not significantly impact the compressive strength at 28 days for the 30RHA and 50RHA composites. The variations in compressive strength ranged from 9.0 % to 8.2 % with a change in fiber content from 4 % to 6 % for the respective composites. Similarly, the modulus of elasticity showed minor variations, ranging from 2.2 % to 9.0 % for the same composites.

This behavior can be attributed to two factors. First, the use of a self-compacting mortar with a suitable gradation of fine content and higher superplasticizer content contributed to good workability and maintained compressive strength and modulus of elasticity even with an increase in fiber content. Second, the treatment of the fibers with calcium hydroxide contributed to the reduced water absorption of the fibers, further enhancing the overall performance of the composite [26, 29].

3.3.2. Flexural behavior and cracking of composites

The inclusion of fibers in cement-based composites offers significant advantages to counteract the inherent brittleness of cementitious materials under tensile stress. Fibers contribute by sustaining load capacity even after the first crack appears, allowing the composite to undergo greater deformations under direct tension or bending, resulting in enhanced ductility. Additionally, the presence of fibers significantly increases the material's energy absorption capacity, leading to improved toughness and resilience.

Fig. 4 shows the stress-displacement curves obtained for the composite containing metakaolinite. The mechanical behavior can be defined by five distinct phases [26] depending on the cracking process of the matrix. After the beginning of loading, the stress-displacement behavior of the composite is linearly elastic during Phase I, until the emergence of internal cracks in the matrix, which results in a loss of stiffness and deviation from the linearity of the stress-displacement curve. These cracks are microscopic and barely visible. With the increase in loading, there is the formation of a macrocrack, called the first visible crack, which results in an abrupt loss of tension in the composite, and which characterizes the end of Phase II. The stress in the composite at the end of Phase II is called the first crack stress $\left(\sigma_{fc}\right)$. After an initial abrupt drop, there is a transfer of stress between the cracked matrix and the fibers, and the stress in the composite grows again, until the appearance of a new macrocrack, which results in a new stress drop. This process, called the multiple cracking (Phase III), is influenced by fiber content and fiber-matrix adhesion.
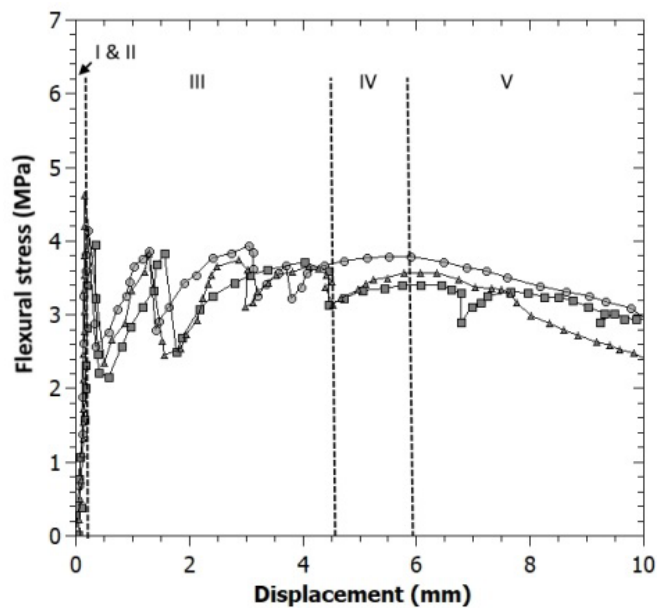

Figure 4. Flexural behavior of composites with metakaolinite.

Phase IV represents the end of multiple cracking, in which stress transfer in the cracked matrix is not sufficient for new cracks to appear in the matrix; the crack spacing remains constant and the increase in stress is accompanied by an increase in crack opening until coalescence of a main crack. In Phase V, the mechanical behavior of the composite is governed by the opening of this main crack. The gradual pulling out of the fibers from within the matrix in the region of the crack leads to a progressive loss of tension, and the composite's behavior becomes controlled by the frictional adhesion between the fibers and the matrix. Fig. 5 illustrates the stress-displacement curves in bending for the composites containing rice husk ash, showing a behavior similar to that observed in Fig. 4.

Table 6 presents the mean values and coefficients of variation in percentage (%) for the first crack stress $\left(\sigma_{fc}\right)$ and maximum post-cracking stress $\left(\sigma_{pc}\right)$ of the composite, which correspond to the highest stress level endured by the cracked composite in either Phase III or Phase IV. Additionally, the Table 6 includes the toughness, which was calculated as the area under the stress-displacement curve up to a displacement of 2 mm, equivalent to a span/150 ratio.

Table 4. Experimental results of the four-point bending test.

Composite	σ_{fc}, MPa	σ_{pc}, MPa	Toughness (N/mm)
30MK4%	4.24 (8.1)	3.88(2.0)	5.52 (6.5)
30RHA4%	4.01 (11.7)	4.15 (11.7)	6.17 (9.2)
30RHA6%	4.09 (7.1)	4.14 (3.6)	6.27 (3.8)
50RHA4%	5.02 (6.4)	4.78 (12.1)	7.03 (9.5)
50RHA6%	3.44 (10.6)	3.33 (18.50)	5.37 (14.8)
Coefficient of variation, in % (in parentheses)			

Upon evaluating the replacement of metakaolinite with rice husk ash in the composites, it is verified that the 30RHA4% composite displayed a 5.4 % reduction in first crack strength compared to the 30MK4% composite, showing a proportional relationship to the reduction observed in compressive strength. For 50RHA4%, an increase of 18.4 % is verified, in relation to 30MK4%, which can be attributed to the better interaction of the matrix with the fiber and microcrack control in Phase II, which presents greater tension gain than the other composites, as shown in Fig. 5.
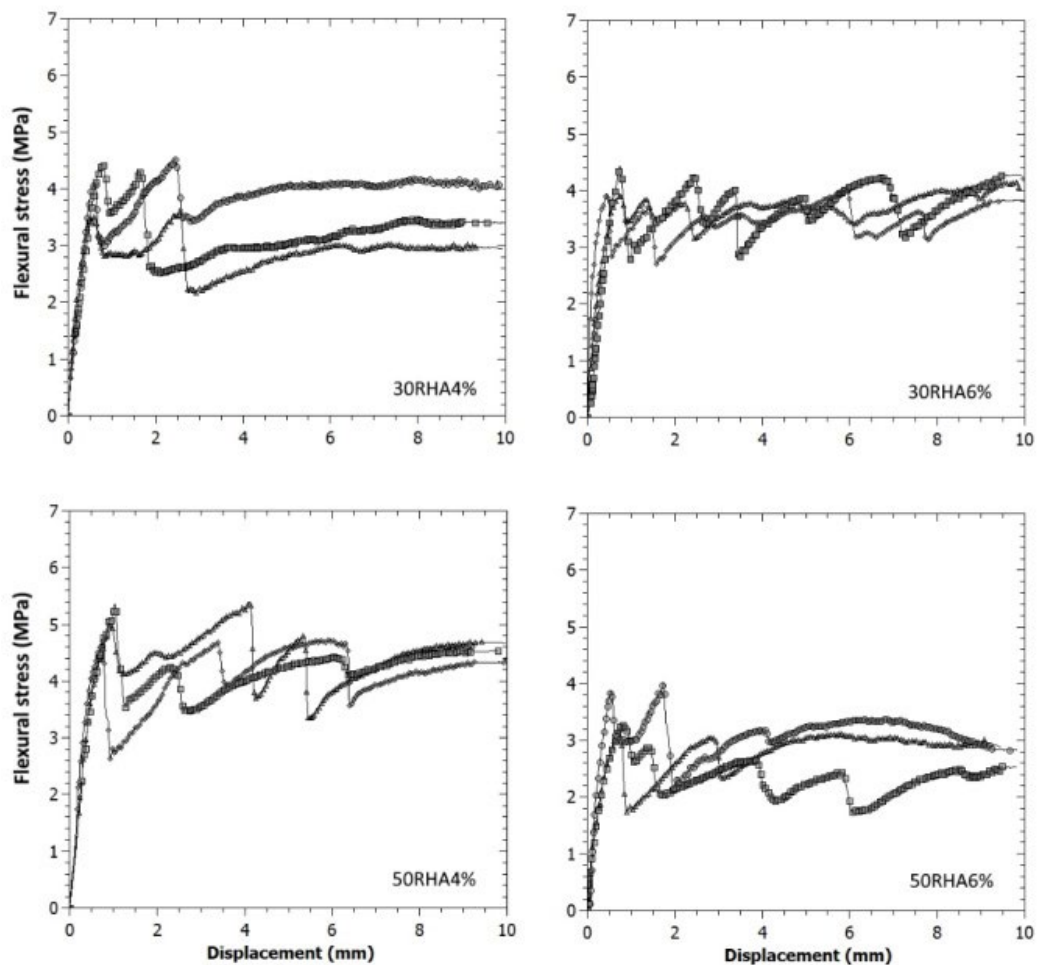
Figure 5. Flexural behavior of composites with RHA.

After cracking, the composites present a maximum stress that varies from 92 % to 103 % of the first crack stress, depending on the type of pozzolan and fiber content. For composites with 4 %, it appears that the use of RHA resulted in improved toughness, compared to 30MK4%. Notably, all composites demonstrated a toughness greater than 5 N/mm, indicating their superior energy absorption capacity compared to the matrix capacity of about 1.8 N/mm, with the highest toughness observed in the 50RHA4% composite. This enhanced toughness is attributed to the fibers' role in effectively transmitting stresses between cracks and, consequently, hindering the propagation of unstable cracks.

Fig. 6 presents the cracking map of the composites at 10 mm displacement, displaying the distribution of cracks and their spacing at varying fiber contents. Notably, a higher fiber content leads to a

more widespread distribution of cracks with smaller spacing between them. As the composite displacement increases, there is a notable increase in crack opening. The crack opening values range from a minimum of 0.34 mm at a displacement of 2 mm to a maximum of 1.73 mm when the displacement reaches 10 mm. It's important to note that the extent of crack opening varies based on the type of matrix and fiber content used in the composites.

Crack spacing in the composites was influenced by mineral addition and fiber content. Specifically, for the 30RHA composites, an increase in fiber content resulted in a reduction of crack spacing from 33.3 mm to 25.0 mm. However, in the 50RHA composites, the crack spacing remained constant at 25 mm for both fiber contents. Generally, smaller crack spacing indicates stronger interfacial bonding stress for composites with the same fiber content [27], underscoring its significance in understanding the composites' mechanical properties.

The behavior of the 50RHA6% composite exhibited a distinctive pattern. Instead of featuring parallel cracks, this composite demonstrated cracking characterized by the branching of small cracks around a central crack. This unusual behavior might be attributed to non-homogeneity in the distribution of fibers. Notably, this composite displayed lower workability in its fresh state, resulting in lower mechanical strength values.
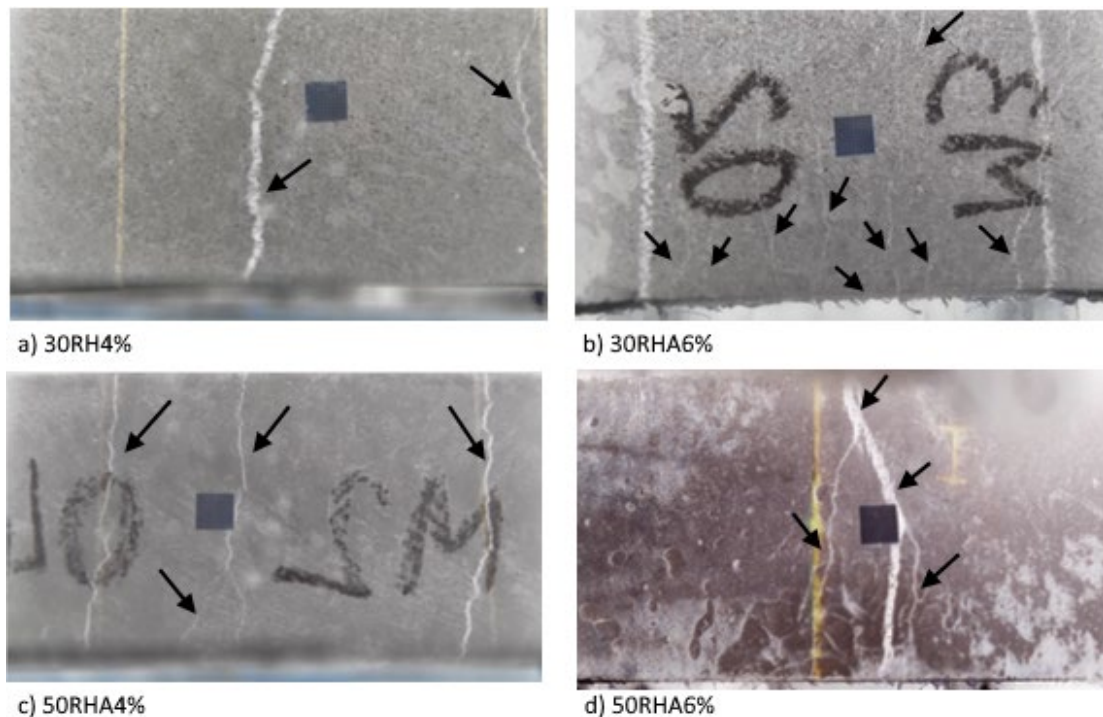

a) 30RH4% b) 30RHA6% c) 50RHA4% d) 50RHA6%

Figure 6. Crack patterns of composites with RHA.

3.2. Assessment of the eco-efficiency

The results of mechanical tests indicate that, by using mineral additives to replace cement, it is possible to produce composites with appropriate mechanical strength and toughness for use in construction elements. However, with the need for sustainable building construction, it is essential that material choices are based on the environmental impact of their production. This includes considering the consumption of raw materials, energy, waste generation, and, notably, greenhouse gas emissions, known as equivalent CO_2 emissions (ECO2e).

Table 7 provides an overview of the materials used in composite production, including details about raw materials and primary production processes. It also presents data on ECO2e and energy (EE) consumption during material manufacturing. Conventional materials like cement and metakaolin are derived from non-renewable minerals and have substantial ECO2e and EE during their production. In the studied composites, these materials were partially or completely replaced by RHA, silica of fume, and fly ash, which are waste materials from different industrial sectors. This substitution contributes to a global effort to reduce the environmental impact of civil engineering. RHA is a byproduct of rice husk combustion for energy generation, originating from a renewable source material, and exhibits lower ECO2e and EE compared to metakaolin.

Considering the material consumption for each mix presented in Table 2, it was possible to calculate the CO_2 emissions and EE per volume (1 m³) of composite during production as follows:

$$ECO2e = \sum_i m_i ECO2e_i;$$

$$ECO2e = \sum_i m_i EE_i,$$

where $ECO2e_i$ is the CO$_2$ emission equivalent per unit mass of constituent i, EE_i is the embodied energy per unit mass of constituent i and m_i corresponds to the mass of composite ingredient i per unit volume of composite. The value adopted to calculate $ECO2e_i$ and EE_i was the average obtained with the maximum and minimum values presented in Table 7.

Table 5. Sustainability aspects of the materials.

Material	Raw material		Main production operations	ECO2e (kg CO₂e/ton)	EE (MJ/t)
Cement	Limestone, clay	Non-renewable	Extraction, burning, milling	750 – 1300 [17, 19, 21, 28]	3000 – 11800 [19, 29, 30]
Metakaolin	Kaolinite clay	Non-renewable	Extraction, burning, milling	236 – 840 [16, 20–22]	2720 – 3300 [18, 23]
Rice husk ash	Husk rice combustion residuals	Renewable	Grinding, drying	103.2 – 157.0 [16–17]	20 – 2070 [17–19]
Fly ash	Coal combustion residuals	Non-renewable	Grinding, drying	4 – 93 [16, 31–32]	33 – 100 [30, 32]
Silica of fume	Co-product of ferrosilicon production	Non-renewable	Grinding, drying	14 – 28 [16, 19, 21]	36 – 100 [29–30, 32]
Sand	Quartz	Non-renewable	Extraction, separation	2.4 – 13.9 [16, 19-20]	80 – 340 [29, 33]
Water	Water	Non-renewable	Extraction, treatment	0.6 – 1.3 [18–19, 29, 33]	0– 200 [18–19, 29, 33]
Plasticizer	Éter policarboxilato	Non-renewable	Chemical operations	510 – 944 [29, 34]	11470 – 16260 [29–30, 35]
Natural Fiber	Vegetable plant	Renewable	Decortification, brushing, balling	182.8 – 311.0 [36–38]	4200 [38]

Fig. 7 and 8 illustrate the ECO2e and EE values for the studied composites, along with the influence of each constituent material. When replacing metakaolin (30MK4%) with rice husk ash (30RHA4%), there is a reduction of 21.0 % in ECO2e and 13.4 % in EE, indicating an increase in the sustainability of the composite. Conversely, when replacing all supplementary materials with rice husk ash (50RH4%), there is an increase of 3.7 % and 4.3 % in ECO2e and EE, compared to the 30RHA4% mixture. This suggests that there is an increase in sustainability when using RHA in conjunction with residual supplementary materials. Nonetheless, it is important to consider that RHA is derived from a renewable plant-based source, and it has the capacity to sequester carbon during the growth of rice plants.
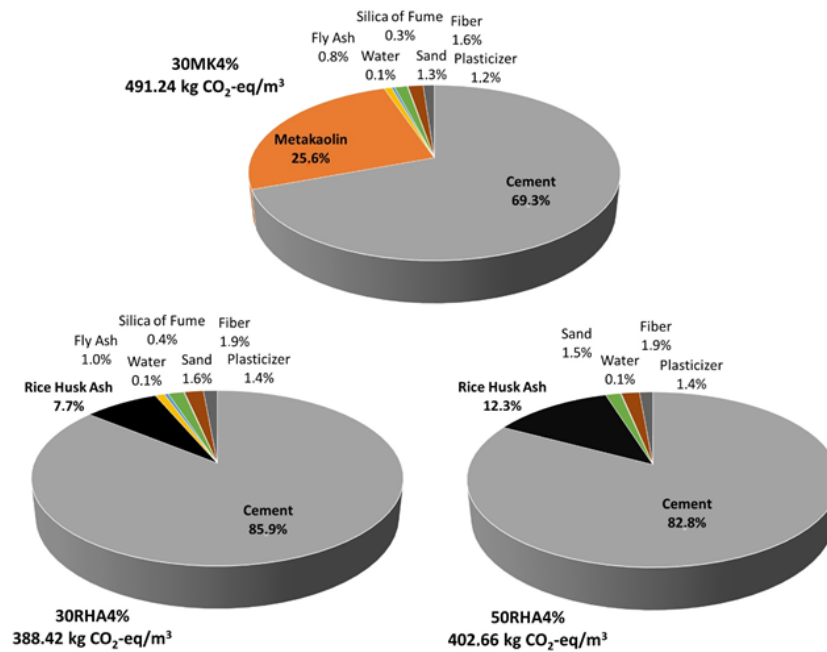
Figure 7. Emission of CO$_2$-eq of composites reinforced with 4 % of sisal fiber.
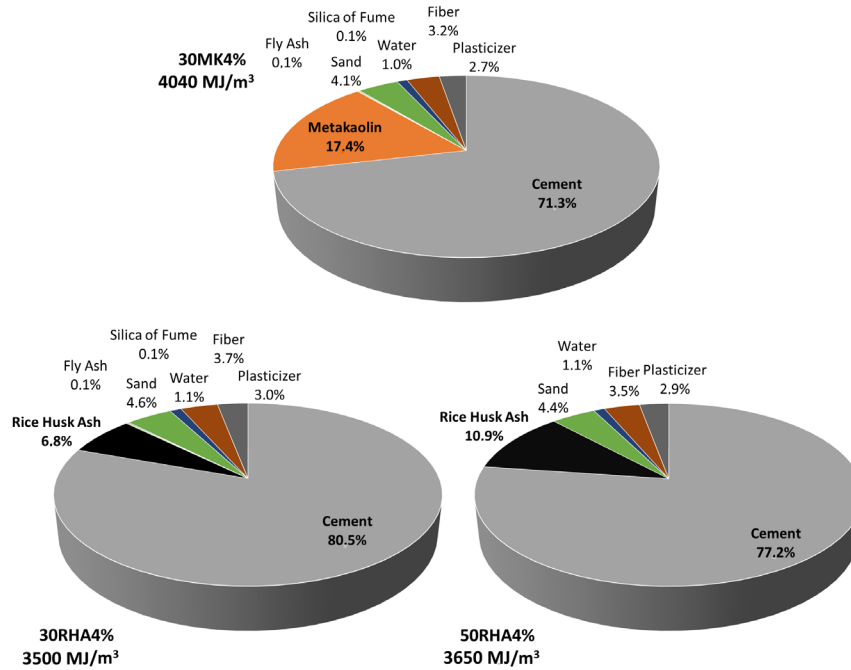
Figure 8. Embodied energy of composites reinforced with 4 % of sisal fiber.

Even though vegetable fibers originate from plants, they still require processing. Consequently, they represent the second-largest environmental impact in composite production, following the binder, despite their maximum contribution being 1.9 % to ECO2e and 3.7 % to EE. Nevertheless, the environmental impact of using vegetable fibers as reinforcement in cement matrices remains lower than that of using manufactured fibers. In the case of conventional concrete, Ali et al. [39] found that 1 % of steel fibers contributed to 36.7 % of the ECO2e in concrete. According to the authors, glass and polymeric fibers contributed 13.0 % and 4.5 %, respectively. Additionally, the emission impact of sisal fiber could be even lower if carbon sequestration during the growth of sisal plants is considered.

The evaluation of sustainability should also consider the concept of eco-efficiency, which connects the parameters ECO2e and EE with material performance indicators. As per Hasan et al. [40], this parameter is calculated using:

$$Ci = \frac{ECO2e}{Cs},$$

where Ci represents the emission-performance efficiency and Cs is this performance requirement. According Damineli et al. [41], in most cases Cs represents the compressive strength, but this indicator will depend of application of material. In this study, Cs was used to denote compressive strength at 7, 28, and 56 days, as well as the toughness of the composites at 28 days.

Similarly, a coefficient Ei represents the energy-performance efficiency and was established in accordance:

$$Ei = \frac{EE}{Cs}.$$

Fig. 9a illustrates the emission-strength efficiency for the composites considering compressive strength. At 7 days, the mixture with metakaolin exhibits higher efficiency, as a lower Ci value corresponds to fewer ECO2e per MPa. As the hydration process of mixtures containing rice husk ash progresses slowly, there is a reduction in the Ci efficiency index. Considering the 28-day strength, which serves as a reference for the design of reinforced concrete structures, there is a reduction of 10.0 % and 5.6 % in the Ci value for the 30RHA4% and 50RHA4% mixtures, respectively, compared to the 30MK4% mixture.

The Ci values for compressive strength at 28 days ranged from 15 to 17 kg CO2e/m³-MPa, which are consistent with the values reported by Hasan et al. [42] for concrete reinforced with 4 % areca nut husk fiber, which were approximately 16.62 kg CO2e/m³-MPa. It is worth noting that the authors used a different matrix and factored in transportation emissions (30 %) in their calculations. However, it's important to highlight that the authors did not account for emissions related to the processing of the fibers, which were done manually and involved sun-drying.

The values, obtained for emission-toughness efficiency, shown in Fig. 9b, demonstrate even greater efficiency for the mixtures containing rice husk ash, with a reduction of 29.3 % and 35.7 % in the Ci value for the 30RHA4% and 50RHA4% mixtures, respectively, in comparison to the 30MK4% mixture.
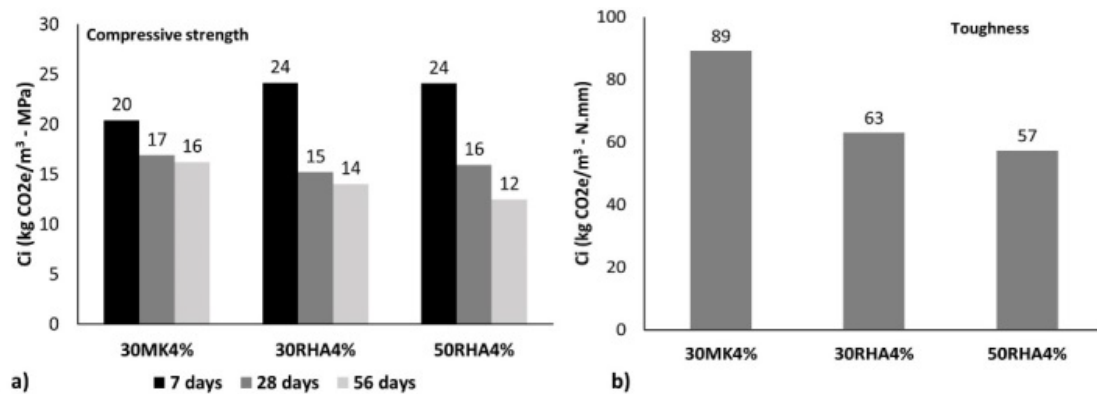

**Figure 9. Emission efficiency of composites reinforced with 4 % of sisal fibers:
a) compressive strength; b) toughness.**

The energy efficiency, denoted as Ei, shown in Fig. 10, also signifies the higher sustainability of mixtures containing RHA in comparison to the mixture with metakaolin. However, when it comes to compressive strength, the best results are achieved when considering a longer hydration period. For a curing age of 56 days, the 30RHA4% and 50RHA4% mixtures exhibit reductions of 5.0 % and 15.1 %, respectively, in the Ei value compared to the 30MK4% mixture. The energy efficiency Ei concerning toughness, even at 28 days of age, shows reductions of 22.3 % and 29.0 % for the same mixtures.
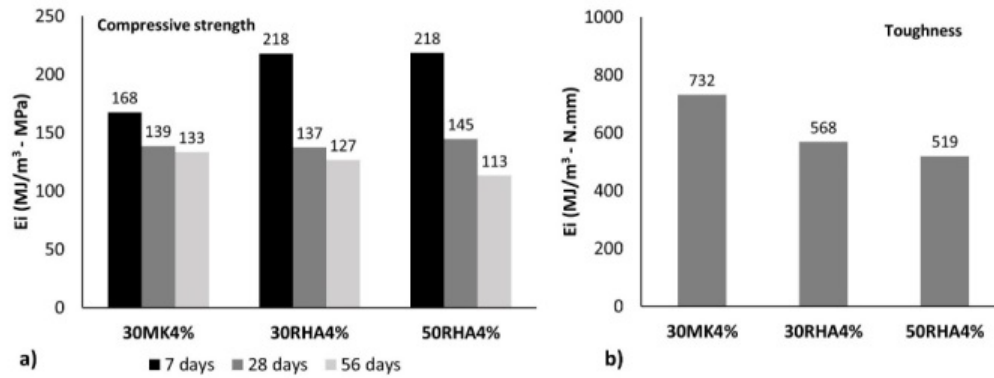
**Figure 10. Energy efficiency of composites reinforced with 4 % of sisal fibers:
a) compressive strength; b) toughness.**

4. Conclusions

This study examined how the composition of the cementitious matrix affects the mechanical performance and sustainability of the sisal fiber reinforced cement composites. The research primarily focused on investigating the feasibility of employing rice husk ash as an environmentally sustainable alternative to industrial mineral additives in the development of cementitious matrices for composites containing vegetable fibers.

It was verified that composites using metakaolin, which is a more reactive pozzolanic addition, exhibit higher mechanical strength and modulus of elasticity at 7 and 28 days. Composites, produced with 50 % RHA, exhibited the highest compressive strength at 56 days when compared to composites produced with metakaolin, fly ash, and silica of fume. This can be attributed to the slower reactivity of RHA in comparison to metakaolin.

Under flexural loading, SFRCC with 4 % and 6 % fiber content exhibited good post-cracking performance, with increased toughness due to a process of multiple cracking that maintained residual stress even at large deformations. The use of 50 % RHA as a substitute for cement resulted in a reduction in crack width and increased toughness.

The calculated values of CO_2 emissions and embodied energy per volume (1 m^3) of the composite indicated that cement and metakaolin are the components with the highest environmental impact. As a result, mixtures containing RHA as a substitute for metakaolin showed a reduction of 21.0 % in CO_2 emissions and 13.4 % in embodied energy, indicating an increase in the sustainability of the composite. The assessment of eco-efficiency, concerning the compressive strength and toughness of the SFRCC, revealed higher efficiency in terms of CO_2 emissions and embodied energy consumption for the mixtures incorporating rice husk ash compared to the mixture containing metakaolin.

The incorporation of rice husk ash into cement-based composites not only improves material properties but also aligns with global initiatives to mitigate environmental impact and address climate change. This is achieved by reducing CO_2 emissions and embodied energy consumption compared to conventional sisal fiber-reinforced cement composites that contain metakaolinite.

References

1. Sharifi, N.P., Jafferji, H., Reynolds, S.E., Blanchard, M.G., Sakulich, A.R. Application of lightweight aggregate and rice husk ash to incorporate phase change materials into cementitious materials. Journal of Sustainable Cement-Based Materials. 2016. 5(6). Pp. 349–369. DOI: 10.1080/21650373.2016.1207576

2. Ahsan, M.B., Hossain, Z. Supplemental use of rice husk ash (RHA) as a cementitious material in concrete industry. Construction and Building Materials. 2018. 178. Pp. 1–9. DOI: 10.1016/j.conbuildmat.2018.05.101

3. Ling, I.H., Teo, D.C.L. Properties of EPS RHA lightweight concrete bricks under different curing conditions. Construction and Building Materials. 2011. 25. Pp. 3648–3655. DOI: 10.1016/j.conbuildmat.2011.03.061

4. Liu, C., Zhang, W., Liu, H., Zhu, C., Wu, Y., He, C., Wang, Z. Recycled aggregate concrete with the incorporation of rice husk ash: Mechanical properties and microstructure. Construction and Building Materials. 2022. 351. Article no. 128934. DOI: 10.1016/j.conbuildmat.2022.128934

5. Kannur, B., Chore, H.S. Low-fines self-consolidating concrete using rice husk ash for road pavement: An environment-friendly and sustainable approach. Construction and Building Materials. 2023. 365. Article no. 130036. DOI: 10.1016/j.conbuildmat.2022.130036

6. Ranasinghe, A. Rice husk and rice straw ashes can prevent cracks in natural fibre reinforced concrete roofing elements. Engineer. 1986. 14. Pp. 9–32.

7. Gram, H.E., Nimityongskul, P. Durability of natural fibres in cement-based roofing sheets. Journal of Ferrocement. 1987. 17(4). Pp. 321–327.

8. Shafiq, N., Robles-Austriaco, L. Nimityongskul, P. Durability of natural fibers in RHA mortar. Journal of Ferrocement. Journal of Ferrocement. 1988. 18(3). Pp. 249–262.

9. Lima, P.R.L., Barros, J.A., Roque, A.B., Fontes, C.M., Lima, J.M. Short sisal fiber reinforced recycled concrete block for one-way precast concrete slabs. Construction and Building Materials. 2018. 187. Pp. 620–634. DOI: 10.1016/j.conbuildmat.2018.07.184

10. Frazão, C., Barros, J.A., Toledo Filho, R.D., Ferreira, S., Gonçalves, D. Development of sandwich panels combining sisal fiber-cement composites and fiber-reinforced lightweight concrete. Cement and Concrete Composites. 2018. 86. Pp. 206–223. DOI: 10.1016/j.cemconcomp.2017.11.008

11. Tonoli, G.H.D., Santos, S.F.D., Rabi, J.A., Santos, W.N.D., Savastano Junior, H. Thermal performance of sisal fiber-cement roofing tiles for rural constructions. Scientia Agricola. 2011. 68. Pp. 1–7. DOI: 10.1590/S0103-90162011000100001

12. Feng, S., Lyu, J., Xiao, H., Feng, J. Application of cellulose fibre in ultra-high-performance concrete to mitigate autogenous shrinkage. Journal of Sustainable Cement-Based Materials. 2023. 12(7). Pp. 842–855. DOI: 10.1080/21650373.2022.2119618

13. Ezugwu, E.K., Calabria-Holley, J., Paine, K. Physico-mechanical and morphological behavior of hydrothermally treated plant fibers in cementitious composites. Industrial Crops and Products. 2023. 200. Aricle no. 116832. DOI: 10.1016/j.indcrop.2023.116832

14. Toledo Filho, R.D., Ghavami, K., England, G.L., Scrivener, K. Development of vegetable fibre–mortar composites of improved durability. Cement and Concrete Composites. 2003. 25(2). Pp. 185–196. DOI: 10.1016/S0958-9465(02)00018-5

15. Wei, J., Meyer, C. Utilization of rice husk ash in green natural fiber-reinforced cement composites: Mitigating degradation of sisal fiber. Cement and Research. 2016. 81. Pp. 94–111. DOI: 10.1016/J.CEMCONRES.2015.12.001

16. Ozturk, E., Ince, C., Derogar, S., Ball, R. Factors affecting the CO_2 emissions, cost efficiency and eco-strength efficiency of concrete containing rice husk ash: A database study. Construction and Building Materials. 2022. 326. Article no. 126905. DOI: 10.1016/J.CONBUILDMAT.2022.126905

17. Hu, L., He, Z., Zhang, S. Sustainable use of rice husk ash in cement-based materials: Environmental evaluation and performance improvement. Journal of Cleaner Production. 2020. 264. Article no. 121744. DOI: 10.1016/J.JCLEPRO.2020.121744

18. Arrigoni, A., Panesar, D.K., Duhamel, M., Opher, T., Saxe, S., Posen, I.D., MacLean, H.L. Life cycle greenhouse gas emissions of concrete containing supplementary cementitious materials: cut-off vs. substitution. Journal of Cleaner Production. 2020. 263. Article no. 121465. DOI: 10.1016/J.JCLEPRO.2020.121465

19. Selvaranjan, K., Navaratnam, S., Gamage, J.C.P.H., Thamboo, J., Siddique, R., Zhang, J., Zhang, G. Thermal and environmental impact analysis of rice husk ash-based mortar as insulating wall plaster. Construction and Building Materials. 2021. 283. Article no. 122744. DOI: 10.1016/J.CONBUILDMAT.2021.122744

20. Chandar, S.P., Raganathan, S., Ramachandran, R. CO_2 emission analysis of metakaolin and alccofine replaced cement in M40 grade concrete. Environmental Science and Pollution Research. 2023. 30(47). Pp. 104408–104414. DOI: 10.1007/s11356-023-29771-4

21. Maddalena, R., Roberts, J.J., Hamilton, A. Can Portland cement be replaced by low-carbon alternative materials? A study on the thermal properties and carbon emissions of innovative cements. Journal of Cleaner Production. 2018. 186. Pp. 933–942. DOI: 10.1016/J.JCLEPRO.2018.02.138

22. Asghari, Y., Mohammadyan-Yasouj, S.E., Koloor, S.S.R. Utilization of metakaolin on the properties of self-consolidating concrete: A review. Construction and Building Materials. 2023. 389. Article no. 131605. DOI: 10.1016/J.CONBUILDMAT.2023.131605

23. Tasiopoulou, T., Katsourinis, D., Giannopoulos, D., Founti, M. Production-Process Simulation and Life-Cycle Assessment of Metakaolin as Supplementary Cementitious Material. Eng. 2023. 4(1). Pp. 761–779. DOI: 10.3390/ENG4010046

24. Kannan, V., Ganesan, K. Chloride and chemical resistance of self compacting concrete containing rice husk ash and metakaolin. Construction and Building Materials. 2014. 51. Pp. 225–234. DOI: 10.1016/J.CONBUILDMAT.2013.10.050

25. Langaro, E.A., Santos, C.A. dos, Medeiros, M.H.F., Jesus, D.S., Pereira, E. Rice husk ash as supplementary cementing material to inhibit the alkali-silica reaction in mortars. Revista IBRACON de Estruturas e Materiais. 2021. 14(4). Article no. e14404. DOI: 10.1590/S1983-41952021000400004

26. Silva, F.A., Mobasher, B., Toledo Filho, R.D. Cracking mechanisms in durable sisal fiber reinforced cement composites. Cement and Concrete Composites. 2009. 31(10). Pp. 721–730. DOI: 10.1016/J.CEMCONCOMP.2009.07.004

27. Mobasher, B., Peled, A., Pahilajani, J. Distributed cracking and stiffness degradation in fabric-cement composites. Materials and Structures. 2006. 39(3). Pp. 317–331. DOI: 10.1007/S11527-005-9005-8

28. Josa, A., Aguado, A., Heino, A., Byars, E., Cardim, A. Comparative analysis of available life cycle inventories of cement in the EU. Cement and Concrete Research. 2004. 34(8). Pp. 1313–1320. DOI: 10.1016/J.CEMCONRES.2003.12.020

29. Yu, J., Lu, C., Leung, C.K.Y., Li, G. Mechanical properties of green structural concrete with ultrahigh-volume fly ash. Construction and Building Materials. 2017. 147. Pp. 510–518. DOI: 10.1016/J.CONBUILDMAT.2017.04.188

30. Jones, R., McCarthy, M., Newlands, M. Fly ash route to low embodied CO_2 and implications for concrete construction. Proceedings of World of Coal Ash (WOCA) Conference. Denver. 2011. Pp. 1–14.

31. Han, Y., Lin, R.S., Wang, X.Y. Compressive Strength Estimation and CO2 Reduction Design of Fly Ash Composite Concrete. Buildings. 2022. 12(2). Pp. 139. DOI: 10.3390/BUILDINGS12020139

32. Hammond, G.P., Jones, C.I. Embodied energy and carbon in construction materials. Proceedings of the Institution of Civil Engineers-Energy. 2008. 161(2). Pp. 87–98. DOI: 10.1680/ENER.2008.161.2.87

33. Long, W.J., Li, H.D., Wei, J.J., Xing, F., Han, N. Sustainable use of recycled crumb rubbers in eco-friendly alkali activated slag mortar: Dynamic mechanical properties. Journal of Cleaner Production. 2018. 204. Pp. 1004–1015. DOI: 10.1016/J.JCLEPRO.2018.08.306

34. Zhang, Y.R., Liu, M.H., Xie, H.B., Wang, Y.F. Assessment of CO_2 emissions and cost in fly ash concrete. Proceedings of the 2014 3rd International Conference on Frontier of Energy and Environment Engineering. Taiwan, 2014. Pp. 327–331.

35. Zheng, H. Concrete for Sustainability. [Online] System requirements: AdobeAcrobatReader. URL: https://www.devb.gov.hk/filemanager/en/content_680/7_dr_herbert_zheng_concrete_for_sustainability.pdf (date of application: 26.01.2024)

36. De Beus, N., Carus, M., Barth, M. Carbon Footprint and Sustainability of Different Natural Fibres for Biocomposites and Insulation Material. 2019, Accessed: Jan. 23, 2024. [Online]. Available: www.nova-institut.eu

37. Dellaert, S.N.C. Sustainability assessment of the production of sisal fiber in Brazil. 2014, Accessed: Jan. 23, 2024. [Online]. Available: https://studenttheses.uu.nl/handle/20.500.12932/17383

38. Broeren, M.L.M., Dellaert, S.N.C., Cok, B., Patel, M.K., Worrell, E., Shen, L. Life cycle assessment of sisal fibre – Exploring how local practices can influence environmental performance. Journal of Cleaner Production. 2017. 149. Pp. 818–827. DOI: 10.1016/J.JCLEPRO.2017.02.073

39. Ali, B., Qureshi, L.A., Kurda, R. Environmental and economic benefits of steel, glass, and polypropylene fiber reinforced cement composite application in jointed plain concrete pavement. Composites Communications. 2020. 22. Article no. 100437. DOI: 10.1016/J.COCO.2020.100437

40. Hasan, N.M.S., Shaurdho, N.M.N., Sobuz, M.H.R., Meraz, M.M., Basit, M.A., Paul, S.C., Miah, M.J. Rheological, Mechanical, and Micro-Structural Property Assessment of Eco-Friendly Concrete Reinforced with Waste Areca Nut Husk Fiber. Sustainability. 2023. 15(19). Article no. 14131. DOI: 10.3390/SU151914131

41. Damineli, B.L., Kemeid, F.M., Aguiar, P.S., John, V.M. Measuring the eco-efficiency of cement use. Cement and Concrete Composites. 2010. 32(8). Pp. 555–562. DOI: 10.1016/J.CEMCONCOMP.2010.07.009

Contacts:

Kaline Guerra Calazans,
ORCID: https://orcid.org/0000-0002-4963-6216
E-mail: kaline.guerracalazans@hotmail.com

Paulo Roberto Lopes Lima, *PhD*
ORCID: https://orcid.org/0000-0003-2937-9520
E-mail: prllima@uefs.br

Romildo Dias Toledo Filho, *PhD*
ORCID: https://orcid.org/0000-0001-5867-4452
E-mail: toledo@coc.ufrj.br

Research article

Obtaining and using synthetic fluorite for Portland cement clinker production

B.P. Kulikov, N.V. Vasyunina (iD) **, I.V. Dubova** ✉ **, A.S. Samoilo, N.V. Merdak**

Siberian Federal University, Krasnoyarsk, Russian Federation

✉ *idubova@mail.ru*

Abstract. The given paper deals with the issues of natural raw fluorite material replaced by synthetic fluorite. Natural raw fluorite material is used as a mineralizer during clinker production (by means of roasting). The article studies fluorite synthesis from fluorocarbon-containing waste of aluminium production. Moreover, the article focuses on Portland cement clinker application in production. We analysed the studies of the influence of fluorine-containing additives on the efficiency of Portland cement clinker production. The chemical and phase composition of raw material and caustification products were analysed with the help of X-ray fluorescence analysis, X-ray spectroscopy analysis, chemical titration method. Granulometric composition of solid products, obtained by caustification, was studied with the help of laser particle analyser with reverse design of Fourier lenses ANALYSETTE 22 MicroTec. Pills were pressed using raw mixtures and roasted in laboratory furnace: the raw mixture was heated up to 1100–1450° C at the rate 10° C/min. The results of the laboratory research are given. The final product contains from 20.7 % up to 60.5 % of synthetic fluorite. Empirical dependencies of optimal liquid-solid ratio were obtained. Our solution of the task is to enlarge particle size of synthetic fluorite and to reduce alkalescence. A brief characteristic of hardware and technological scheme of waste caustification is given. The paper also gives an assessment of mineralizing effect of synthetic fluorite, obtained by fluorocarbon-containing waste from aluminium production caustification. We proved the mineralizing effect of the additive based on synthetic fluorite and carbon to be correct. Samples containing synthetic fluorite are characterized by higher shrinkage and lower content of CaO_{free} at equal temperatures.

1. Introduction

Efficiency of cement industry is specified by the choice and application of fluor-containing additives (mineralizers) during Portland cement clinker production.

The most efficient mineralizers in cement industry are fluorine substances based on natural fluorite, in the form of ore or concentrate. The sources of natural fluorite are located far away from prospective consumers. This is one of the factors, which holds the wide application of natural fluorite back. The main deposits of fluorite ore are located in Siberia, the Far East and Mongolia as well. Significant transport component in natural fluorite (fluorspar) cost decreases the advantages of the mineralizer use for cement plants, located in Ural and the European part of Russia.

Intensification of clinker production increases efficiency of rotary furnaces by 3–5 % due to the use of mineralizers, decreases specific fuel consumption for clinker production up to 3 %, improves operation of furnaces due to stabilization of material coating, improves the quality of clinker and cement [1–3].

The issues, which have to do with theoretical explanation and practice of fluorine-containing mineralizers use, have been studied in our country and abroad [4–6].

It has been established, that addition of small amounts of fluorine salts leads to the increase of reactive capability during all stages of clinker production, though to different extent [7, 8].

Fluorine salts interact with calcium carbonate in the process of heating up to 1100° C, which result in intermediate compounds (such as binary salt). These compounds are distinguished by comparably low melting temperatures. Therefore, materials interact involving liquid phase in the process of clinker production in preparation areas. It makes interaction of lime and silicon oxide easier. Fluorides react on crystalline lattice of calcium carbonate, it may result in the opening of lattice. What is more, there are intermediate compounds within the surface [8–10].

When fluorides interact with SiO_2 we get the compound SiF_4. It hydrolyzes under the influence of water vapour. As the result we get bulk and very active cristobalite. The most effective use of fluorine salts is marked during the production of hard-sintering clinkers with a high saturation coefficient (SC). Clinkers also contain a small amount of melt and mixtures with a high content of alkaline oxides. Intensive sublimation of alkali involving fluorine accelerates the binding of CaO and increases the activity of a clinker [10].

The production of Portland cement starts with a reaction between thoroughly mixed solid materials. There is synthesis of main cement compounds in the later stages of clinker production, when the liquid phase is formed. The monograph [11] shows that the processes of clinker formation depend on three factors: chemical composition of the mixture, physico-chemical properties of raw materials, temperature and duration of clinker production. The fourth condition that affects the formation of a clinker is the cooling rate. It has to do with the cases when only a small part of the mixture turns into liquid. According to some scientists [11–13], the reactions, which result in the formation of clinker minerals start at 600 °C. Despite the fact, that the maximum clinker production temperature is 1400–1500 °C, only 20 to 30 % of the roasted material melts.

Fluorocarbon-containing waste of aluminium production [13–22] are the alternative of natural fluorine mineralizers. Fluorocarbon-containing waste is considered to be cheap technology-related product. Scientists of Siberian federal university (Krasnoyarsk) have carried out the research on obtaining synthetic fluorite made of waste of aluminium production. As a result of fluorocarbon-containing waste of aluminium production treatment with milk of lime in an aqueous solution with stirring and at elevated temperature, sodium aluminium fluoride (cryolite and chiolite) are converted into fluorite [23–25].

Nowadays, obtaining cheap fluorite is an extremely topical issue. Firstly Russia doesn't meet needs for fluorspar at the expense of its own sources of raw materials completely. Secondly, fluorite synthesis with the help of processing of fluorocarbon-containing industrial waste has an obvious environmental and resource-saving orientation.

Modes of synthetic fluorite obtaining at caustification of fluorocarbon-containing waste are developed, mechanism and kinetics of sodium-aluminium fluorides transformation into synthetic fluorite are studied in the article [25]. On the other hand, the research must be continued, as the fundamental hardware and technological scheme of synthetic fluorite obtaining from fluorocarbon-containing waste from aluminium production should be developed and suggested. What is more, it is necessary to try out obtained materials and get the data, which approve the efficient impact of obtained mineralizer on clinker production.

Therefore, further research is aimed at the assessment of mineralizing effect of synthetic fluorite, obtained by fluorocarbon-containing waste from aluminium production caustification.

Main tasks of the current study are as follows:

The research of the impact of synthetic fluorite obtaining conditions on the composition and the product granulometric composition, the development of technological recommendations in order to improve the composition and granulometric composition;

The development of fundamental hardware and technological scheme of synthetic fluorite obtaining from fluorocarbon-containing waste of aluminium production;

The experimental tests of the obtained synthetic fluorite usage in Portland cement clinker production.

2. Methods

The current research studies phase composition of coal froth flotation tailings (CFFT), electrostatic precipitation dust (EPD) as well as gas purification sludge (GPS). These wastes are generated due to the Soderberg anode electrolysis technology, which takes place at the public joint-stock company "Rusal Bratsk aluminium smelter" (samples were taken on 06.03.2023). The caustification data are shown by the example of CFFT. Sample collection for the experiment was carried out with averaging by the means of the squaring method. In order to achieve the goals outlined, we used theoretical methods (study and analysis of literature on the research problem), modern physical and chemical methods of analysis, as well as methods established by GOST. We also employed equipment of the Center for collective use "scientifically advanced methods and methods of analysis of new materials, nano materials and mineral raw materials" of Siberian Federal University.

Major types of fluorocarbon-containing waste of aluminium production are used in order to obtain synthetic fluorite. The waste includes electrostatic precipitators dust, gas purification sludge, coal froth flotation tailings. The aluminium production waste includes coal froth (CF) of aluminium electrolyte production. he monograph [23] gives the most complete description of composition and properties of fluorocarbon-containing waste of aluminium production.

Fluorocarbon-containing waste of aluminium production underwent treatment using milk of lime, containing active CaO = 96.0 % in aqueous solution at elevated temperature with stirring. Milk of lime is aqueous suspension of solid calcium hydroxide $Ca(OH)_2$ containing small amount of dissolved lime.

In experiments with the removal of kinetic dependencies, pulp samples were taken after a certain time period with a 20 ml syringe for the entire duration of the experiment. The caustification was carried out during 60 minutes. At first, samples were taken in 1.0–2.5 minutes within 15 minutes, next samples were taken every 15 minutes. Samples were necessary in order to check the composition.

After caustification, the pulp was filtered through a blue tape filter on the vacuum line for a specified time. The filtrate was analyzed by titrimetric analysis for the content of total, carbonate and caustic alkali (GOST31957), for the content of aluminium (GOST 2542.4-97). The cake was dried to a constant mass at a temperature of 120° C, the dried product was weighed and given for analysis by XRF.

In order to identify phases of X-ray pattern, we registered using X-ray diffraction analysis and X-ray spectroscopic analysis with the help of X-ray diffractometer XRD-6000 Shimadzu, featuring CuK radiation. In order to get the most careful phase identification we used information data system (RetrieveQQPA) and data bank PDFICDD [26, 27]. Photography of sample spectrum for X-ray spectroscopic analysis was carried out using X-ray automated fluorescence spectrometer Shimadzu XRF-1800 (equipped with Rh-anode).

Granulometric composition of solid products, obtained by caustification, was studied with the help of laser particle analyzer with reverse design of Fourier lenses ANALYSETTE 22 MicroTec.

The mineralizing effect was assessed using the product, obtained by coal froth flotation tailings caustification during the laboratory research.

Pills of the following specifications (d = 40 mm, h = 7,0 mm) were pressed using raw mixtures. The pills were roasted in laboratory furnace, raw mixture was heated up to 1100, 1200, 1300, 1400, 1450 °C at the rate 10 °C/min.
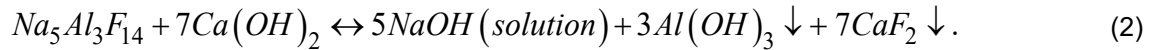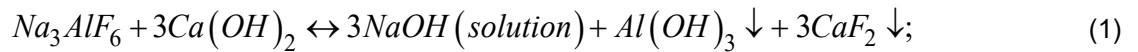
3. Results and Discussion

Phase composition of fluorocarbon-containing waste from aluminium production (Table 1).

Table 1. Phase composition of waste and aluminium industrial waste

Waste types	Na_3AlF_6	$Na_5Al_3F_{14}$	K_2NaAlF_6	Al_2O_3	Na_2SO_4	C	CaF_2	$AlF_30,5H_2O$	The rest
EPD	58.3	0.67	3.80	3.48	4.06	25.7	0.29	–	3.70
GPS	17.1	14.77	–	7.79	–	50.8	0.85	7.46	1.23
SCFFT	15.87	3.47	0.60	1.25	–	74.2	0.21	–	4.40
CF	47.4	12.7	3.73	9.54	–	24.3	2.18	–	0.15

Note. The rest means the following compounds: $NaAl_{11}O_{17}$, Al_{met}, SiO_2, Fe_2O_3, $AlF_3 \cdot 3H_2O$, $Na_2Ca_3Al_2F_{14}$.

As the authors have already mentioned in the early works [24], cryolite and chiolite interfere with lime, which is a part of the solution:

$$Na_3AlF_6 + 3Ca(OH)_2 \leftrightarrow 3NaOH\,(solution) + Al(OH)_3 \downarrow + 3CaF_2 \downarrow; \qquad (1)$$

$$Na_5Al_3F_{14} + 7Ca(OH)_2 \leftrightarrow 5NaOH\,(solution) + 3Al(OH)_3 \downarrow + 7CaF_2 \downarrow. \qquad (2)$$

As dissolved $Ca(OH)_2$ is used, the solution is fed with new servings of lime. They interact with sodium aluminium fluoride. Therefore, caustification of fluoride contains gradual dissolution of solid $Ca(OH)_2$. As the result it breaks into resultants of reaction: CaF_2, $Al(OH)_3$, and $NaOH$.

The carbon contained in waste and industrial products does not undergo changes during lime treatment and transits into a solid product. Thus, the resulting solid product contains synthetic fluorite and carbon. Aluminium oxide and hydroxide are present as impurities in the product. Also, an excess of lime-containing reagent may be present in the product. Sodium from cryolite and chiolite passes into a solution in the form of caustic soda $NaOH$, in which aluminium hydroxide is partially dissolved to form sodium aluminate.

Treatment conditions and a brief characteristics of obtained solid and liquid caustification products are given in the Table 2.

Table 2. Characteristics of original reagents, conditions and caustification products

Waste and AIW	Waste and APP weight	CaO, g	Weight H_2O, g	Temperature, °C	Mixing time, min.	Solid product		Filtrate		
						Cake weight, g	Solid product weight, g	pH	Na_2O general, g/dm^3	Na_2O caust., g/dm^3
GPS	50.00	24.43	600	40	60	168.64	55.69	13.15	18.6	12.09
EPD	50.00	20.69	501	50	30	139.0	72.6	12.10	4.75	1.27
CFFT	50.00	9.04	247	50	15	98.2	55.49	13.05	15.4	10.39
CF	50.00	26.06	600	80	30	110.61	61.98	13.23	20.15	14.16

Note. Rotation frequency of the tempering mill in all the experiments is 270 rotations per minute.

Average molecular composition of waste caustification products and aluminium industrial waste is given in the Table 3.

Table 3. Content of caustification solid products [25]

Waste and AIW	CaF_2	C	$Ca(OH)_2$	Al_2O_3	$Al(OH)_3$	$3Ca(OH)_2 \cdot 2Al(OH)_3$	The rest
GPS	47.9±2.6	32.2±3.6	2.06±0.5	10.3±1.2	-	2.58±0.4	4.96
EPD	33.4±2.1	44.4±3.1	1.24±0.4	10.7±1.5	7.13±1.4	1.3±0.35	1.83
CFFT	20.7±1.6	70.1±4.2	1.20±0.4	3.43±0.6	0.98±0.3	2.51±0.5	1.08
CF	60.5±3.4	22.3±2.3	1.22±0.3	9.3±1.8	2.75±0.6	3.27±1.1	0.66

The maximum composition of synthetic fluorite contains product of coal froth (CF) caustification 60.5 %, the minimum composition contains product of flotation tailings caustification 20.7 %. All solid products are practically free from sodium. It can be found in the solution in the form of caustic soda. The minimum sodium content in solid caustic products removes restrictions on the use of synthetic fluorite during clinker production as an additional source of alkali.

In order to carry out industrial caustification of fluorocarbon-containing waste of aluminium production, you need a simple process flow diagram. Moreover, the diagram can be implemented in continuous or periodic mode of operation. The approximate composition of the main equipment of the diagram includes the following items:

- agitator machine, which is used in order to make milk of lime;
- buffer mixer tank, which is used in order to store and dose suspension of fluorocarbon-containing waste of aluminium production;
- pumps and mud channel, which are used in order to feed milk of lime and waste suspension in chemical reactor;
- continuous or batch reactor, which is heated by indirect or direct steam;
- round basin-thickener, which is used in order to separate the main part of the caustic soda solution from the condensed solid caustic product;

- rotary-drum vacuum filter or band vacuum filter;
- tumble dry;
- bucket elevator;
- storage bunker for finished products.

Hardware configuration is tied round with pipes and pumps, which are used in order to pump over suspensions.

You need to take into consideration the following process-related moments before you start implementing industrial caustification of fluorocarbon-containing waste of aluminium production.

The choice of liquid to *solid (L:S) optimal ratio*

The increase of alkaline intensity of solution due to NaOH recovery reduces solubility of $Ca(OH)_2$ during the process of waste treatment by milk of lime. Therefore, the rate of chemical reactions slows down (1, 2). If the concentration of NaOH in the solution is high enough, the dissolution of $Ca(OH)_2$ may stop completely. Therefore reactions will stop (1, 2). In such a way, concentration of NaOH in products of interaction is a factor, which influences the rate and the totality of the interaction of sodium aluminium fluoride and calcium hydroxide. It has been established experimentally, that caustification of sodium aluminium fluoride slows down when the concentration of NaOH in the solution is more than 25 g/dm^3. Therefore, the concentration of NaOH in the solution depends on the content of sodium and fluorine in waste and industrial products, as well as on the weight ratio of liquid to solid *(L:S)* in the reaction mixture. The higher the fluorine content in waste and industrial products is, the greater the ratio of *L:S* in the reaction mixture should be. The reason is to prevent excessive increase of the concentration of NaOH in solution and slow down the rate of interaction of reagents. Dependency of the optimal ratio of *L:S* in reaction mixture has been established experimentally [28]:

$$L:S = \left[1 + (M.R. - 2.4) : 4.8\right] \times \left[-0.0028 \times F^2 + 0.3074 \times F + 0.2229\right], \tag{3}$$

where $L:S$ is weight ratio of liquid to solid, S = 1; $M.R.$ is molar ratio of NaF : AlF_3 in waste; F is fluoride concentration in waste, % mass.

Dependency (3) establishes the initial ratio of $L:S$ in the reaction mixture. Solid in the reaction mixture is taken as the total and stoichiometric weight of waste, for the formation of CaF_2, the weight of $Ca(OH)_2$, excluding excess of $Ca(OH)_2$ and the weight of lime impurities.

High content of caustic solution in filter cake

It is the result of fine granulometric composition of initial waste and obtained synthetic fluorite. Fig. 1 and table 4 show granulometric composition of solid products, obtained by GPS, EPD and CFFT caustification. These data demonstrate, that the average size of the product, obtained by GPS caustification is 7.19 micron, EPD caustification is 8.96 micron. Granulometric composition of solid products made of CFFT is represented by two distribution curves. Fine fraction of the product, which includes synthetic fluorite, has an average particle size of 10.48 microns. Coarse fraction is mainly carbon and aluminum oxide particles obtained by grinding coal foam.

Fine granulometric composition of solid products of caustification makes filtration more difficult and increases energy consumption while drying. What is more, it contaminates synthetic fluorite with sodium compounds. Therefore, it is necessary to search for solutions in order to enlarge the granulometric composition of caustification products. For example, the introduction of a catalyst into the reaction mixture, which is going to be the source of CaF_2 crystallization. In order to reduce the sodium concentration in synthetic fluorite, it is possible to use cake washing with water from a caustic soda solution.
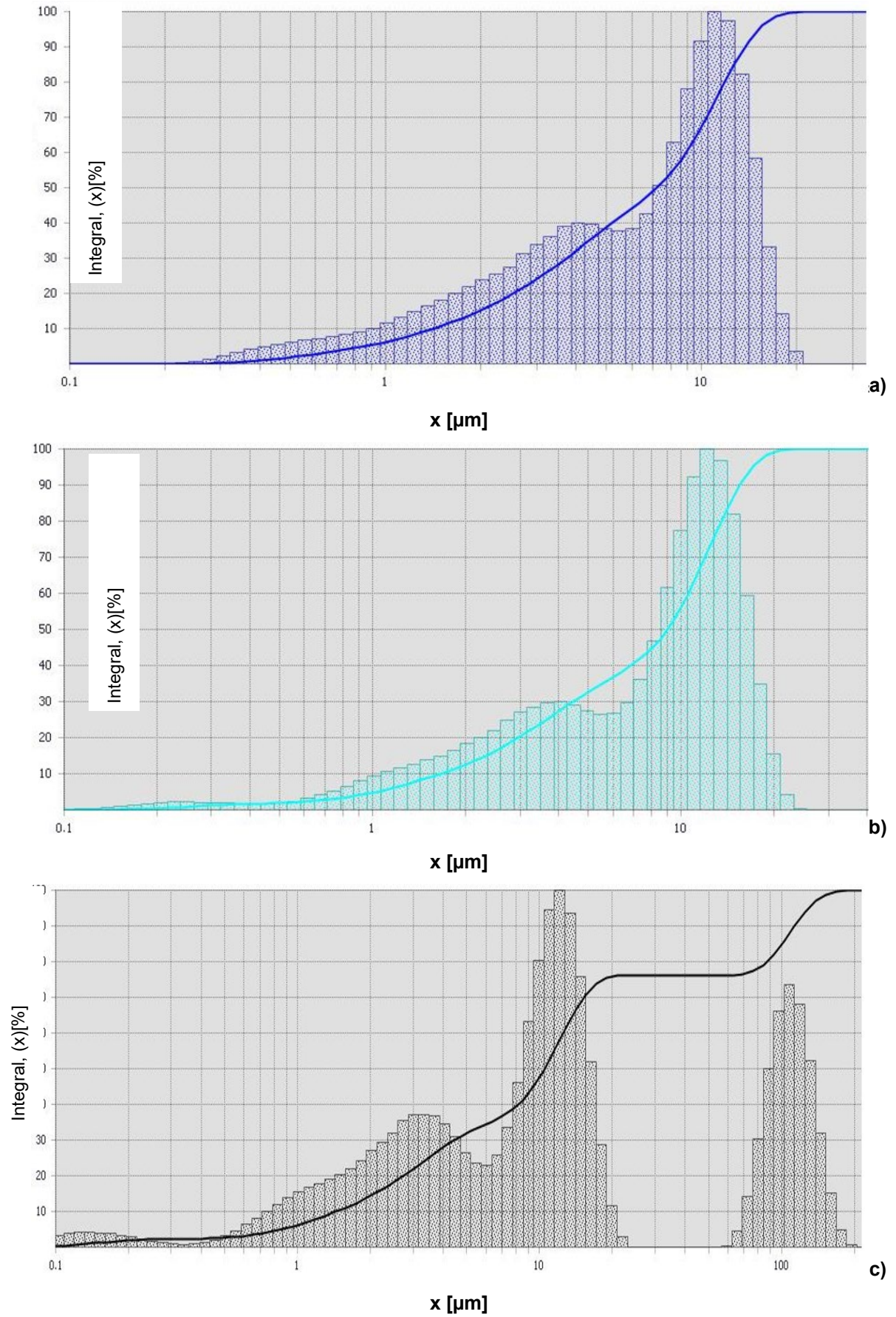
Figure1. Diagram of particles size distribution of solid products, obtained with the help of:

a) GPS; b) EPD; c) CFFT caustification [25]

Table 4. Granulometric composition of solid products, obtained by GPS, EPD and CFFT caustification [25]

| x [μm]	GPS	EPD	CFFT
0.10	0.00	0.01	0.32
0.20	0.00	0.49	1.84
0.30	0.26	1.20	2.27
0.50	1.92	1.97	2.66
0.70	3.70	2.82	3.78
1.00	6.23	4.85	6.30
1.50	10.79	8.82	10.49
2.00	15.34	12.66	14.36
3.00	24.02	20.28	21.90
5.00	38.89	32.73	32.02
7.00	49.03	40.59	36.80
10.00	67.55	56.46	47.71
20.00	99.88	99.04	75.73
30.00	100.00	100.00	76.20
40.00	100.00	100.00	76.20
50.00	100.00	100.00	76.20
60.00	100.00	100.00	76.21
70.00	100.00	100.00	76.61
80.00	100.00	100.00	78.17
90.00	100.00	100.00	81.02
100.00	100.00	100.00	84.78
150.00	100.00	100.00	100.00

Preparation of synthetic fluorite in the form of pellets and grains

There are many dusty materials in cement production. Therefore, synthetic fluorite, obtained from fluorocarbon-containing waste from aluminium production, should be shaped as granules or pellets. Synthetic fluorite, which looks like powder shouldn't be used. A drum rotary dryer should be used in order to dry the cake of synthetic fluorite. The product should be dried to a residual humidity of 8–10 % mass, which will ensure the production of pellets and granules of 5–50 mm [28].

There is sodium aluminate in the caustic soda solution

It has been established, that a solution, which is separated from solid caustification products, the concentration of Na_2O_{total} is generally greater than $Na_2O_{caust.}$, while treating fluorine-containing waste and industrial products with a lime-containing reagent. The graph (Fig. 2) shows the dynamics of the concentration change of CaF_2 in the solid product, Na_2O_{total} and $Na_2O_{caust.}$ in solution during the treatment of cryolite (Na_3AlF_6) with lime milk. The experimental data obtained indicate that part of the Na_2O in solution is associated with Al_2O_3 in sodium aluminate $NaAlO_2$.

If the solution is rich in $NaAlO_2$, it means, that it can be used in a limited way at wet gas purification system of aluminium smelters. Absorption of electrolysis gases by a mixture of caustic and aluminate solutions will lead to crystallization of cryolite in wet gas purification system of aluminium smelters (reaction 4). Electrolysis gases contain hydrogen fluoride.
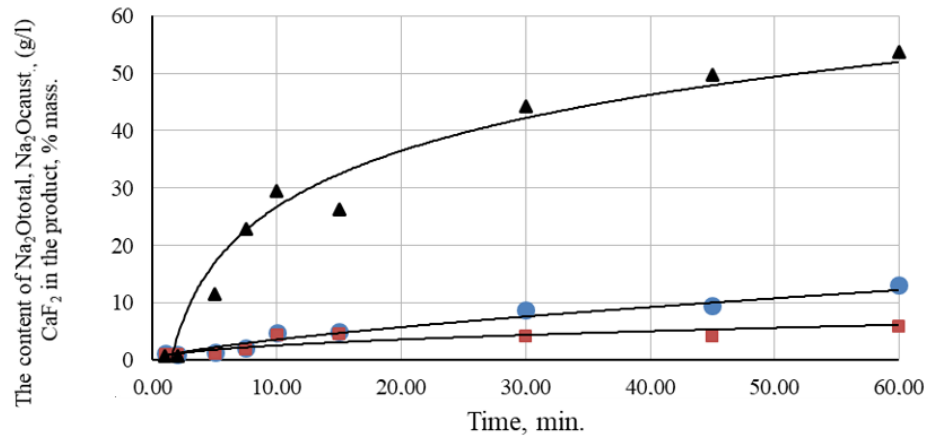
$$6HF + NaAlO_2 + 2NaOH = Na_3AlF_6 \downarrow + 4H_2O. \tag{4}$$
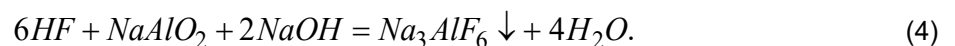
Figure 2 Change of CaF₂ (■), Na₂O_total (▲) and Na₂O_caust.(●) concentration at cryolite caustification [25]

The loss of fluorides and GPS will follow as well as mud channel will be filled with cryolite precipitation.

It is proposed to introduce an additional amount of lime into the reaction mixture in order to exclude the formation of an aluminate solution. Excess of lime binds forming aluminum hydroxide into the insoluble compound named katoite $3Ca(OH)_2 \cdot 2Al(OH)_3$:

$$2Al(OH) + 3Ca(OH)_2 = 3Ca(OH)_2 \cdot 2Al(OH)_3 \downarrow. \tag{5}$$
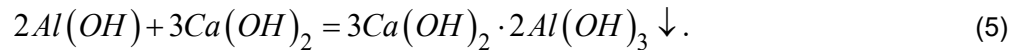
As the result we get the solution of caustic alkali free of sodium aluminate. Moreover solid products of caustification are enriched with calcium hydroxide and aluminium hydroxide.

Empirical dependency of recommended dosage of active lime $Ca(OH)_2$ was obtained during the experiments. $Ca(OH)_2$ is used in order to treat sodium-fluorine-carbon-containing waste and semiproducts of aluminium electrolytic production:

$$Ca(OH)_2 = (1 \pm 0.02) \times [1.95 \times F + 4.11 \times Al], \tag{6}$$

where $Ca(OH)_2$ is the amount of active lime (% mass.), which is added to 100 % of waste and aluminium industrial waste; F is fluor concentration in fluorocarbon-containing waste from aluminium production, which is a part of NaF and AlF₃, % mass.; Al is aluminium concentration in fluorocarbon-containing waste from aluminium production, which is a part of AlF₃, % mass.; (1 ± 0.02) is confidence interval, which 95 % safe fits experiment results.

Next step of the research is focused on the assessment of mineralizing effect of synthetic fluorite. The experimental research on clinker production was carried out using the product, obtained by coal froth flotation tailings caustification (the mineralizer). CFFT are characterized by the minimum fluorine concentration. It is represented mostly by cryolite Na₃AlF₆ and chiolite Na₅Al₃F₁₄ as well as maximum content of graphitized carbon. CFFT were used at the experiments on clinker production. CFFT are considered to be the best product, which fit for industrial implementation of the developed technology. Upgrading is being carried out, it will cause the reduction of EPD and GPS formation until they totally vanish. Upgrading implies the substitution of wet gas purification equipment by dry gas purification equipment. Dry gas purification equipment includes metallurgical alumina as an adsorbing material. Coal froth is an aluminium production waste, which is processed nowadays at aluminium smelters by reverse flotation technology. The given technology results in flotation cryolite obtaining (which can be recycled) and CFFT. CFFT is the only waste which is difficult to be recycled. The mineralizer contained 20.7 % of synthetic fluorite and 70.1 % of carbon (Table 3). A comparative assessment was made, based on the results of clinker production of a specific raw material mixture and a mixture with the addition of a mineralizer based on synthetic fluorite and carbon. The composition of basic oxides in the raw mixture is given in Table 5. The mineralizer was added to the composition of the raw mixture more than 100 %. The concentration of CaF₂ in the raw mixture with the mineralizer is 0.28 % mass.

The data given below in tables 5–8 shows the work of mineralizer and confirms the data by authors [4–8] on the impact of fluorite on reactive capability of raw materials.

Table 5. Composition of initial raw cement mixtures containing synthetic fluorite and free of it

Composition of compounds, % mass.													
Ignition loss	SiO_2	Al_2O_3	Fe_2O_3	CaO	MgO	SO_3	Na_2O	K_2O	TiO_2	P_2O_5	Σ	CaF_2	C
33.42	13.86	3.61	2.65	42.9	2.40	0.26	0.28	0.30	0.20	0.12	100.0	–	–
33.42	13.86	3.61	2.65	42.9	2.40	0.26	0.28	0.30	0.20	0.12	100.0	0.28	1.0

Note. Modular characteristics of raw mixture: $SC = 0.93$; $n = 2.21$; $p = 1.36$.

Shrinkage level and free calcium oxide CaO_{free} content were assessed in sintered samples. The results are presented in Tables 6, 7 down below.

Table 6. Shrinkage of samples, mm at temperatures of clinker production

№	Sample	1100°C	1200°C	1300°C	1400°C	1450°C
1	free of fluorite	39×6.8	37.5×6.4	35.3×5.9	33.6×5.6	31.7×5.5
2	containing fluorite	39×6.5	37.5×6.2	34.8×5.8	32.8×5.4	31.2×5.2

Table 7. Content in samples of CaO_{free} (% mass.) at temperatures of clinker production

№	Sample	1100°C	1200°C	1300°C	1400°C	1450°C
1	free of fluorite	35.5	34.1	17.8	4.2	0.20
2	containing fluorite	31.0	26.3	12.1	1.9	0.0

Table 8 shows the results of the study of obtained clinkers composition.

Table 8. Mineralogical composition of burnt mixtures, % mass

№	Clinker	1400°C					1450°C				
		C_3S	C_2S	C_3A	C_4AF	CaO_{free}	C_3S	C_2S	C_3A	C_4AF	CaO_{free}
1	free of fluorite	46.1	27.0	14.0	8.6	4.2	63.8	15.4	11.1	9.5	0.2
2	containing fluorite	52.1	22.8	13.0	10.2	1.9	64.7	14.4	10.4	10.5	0

Note. C_3S – $3CaO·SiO_2$, C_2S – $2CaO·SiO_2$, C_3A – $3CaO·Al_2O_3$, C_4AF - $4CaO·Al_2O_3·Fe_2O_3$.

The given research confirms the study [17]. Synthetic fluorite additive leads to the full binding of calcium oxide compared to other samples. Samples containing synthetic fluorite are characterized by higher shrinkage and lower content of CaO_{free} at equal temperatures. Therefore, if we add synthetic fluorite, it will stimulate clinker sintering.

4. Conclusion

As the result of research, we obtained a mineralizer for Portland cement clinker production by means fluorocarbon-containing waste caustification. Because of the mineralizer content (20.7–60.5 % of synthetic fluorite, the minimum sodium content) it may be used as a mineralizer for Portland cement clinker production.

It was determined that the average size of the mineralizer containing synthetic fluorite after caustication of GPS, EPD and CFFT makes up 7.19; 8.96; 10.48 microns. It has been established that the fine granulometric composition causes increased alkalinity. In order to reduce the sodium concentration in synthetic fluorite, it is proposed to introduce an inoculation into the reaction mixture for crystallization of CaF_2 and rinsing the cake with water to get rid from caustic soda. It is recommended to dry the cake of synthetic fluorite to a residual humidity of 8–10 % by weight in a drum rotary dryer in order to obtain pellets and granules of 5–50 mm in size.

The fundamental hardware and technological scheme of aluminium production waste caustification was developed. The final result is synthetic fluorite. The scheme may be implemented in continuous and periodic mode. There is an exemplary list of basic equipment.

We assessed the mineralizing effect of CFFT caustifification product. The mineralizing effect of the additive based on synthetic fluorite and carbon was proved correct experimentally. The additive was obtained with the help of coal froth flotation tailings treatment. Samples containing synthetic fluorite are characterized by higher shrinkage and lower content of CaO_{free} at equal temperatures. Therefore, the additive causes clinker production.

References

1. Dahhou, M., Hamidi, A., Moussaouiti, M., Arshad, M. Synthesis and characterization of belite clinker by sustainable utilization of alumina sludge and natural fluorite (CaF_2). Materialia. 2021. 20. 101204.

2. Kulikov, B.P., Vasyunina, N.V., Dubova, I.V., Samoilo, A.S. Balanev, R.O., Ivanova, I.K., Sysoeva, Ya.S. Effektivnaya dobavka na osnove sinteticheskogo flyuorita i grafitirovannogo ugleroda iz othodov alyuminievogo proizvodstva dlya sinteza klinkernyh soedinenij [Effective additive based on synthetic fluorite and graphitized carbon from aluminum production waste for the synthesis of clinker compounds]: scientific publication. Cement and its application. 2023. 2. Pp. 74–78.

3. Maruthupandian, S., Chaliasou, A., Kanellopoulos A. Recycling mine tailings as precursors for cementitious binders – Methods, challenges and future outlook. Construction and Building Materials. 2021. 312. 125333. DOI: 10.1016/j.conbuildmat.2021.125333

4. Sit'ko, M.K., Starodubenko, N.G. Issledovanie vliyaniya mineralizatorov na obzhig portlandcementnogo klinkera. [Researching of effect of mineralizers on the roasting process of Portland cement clinker]. Proceedings of BSTU. 2016. 3. Pp. 106–110.

5. Boughanmi, S., Labidi, I., Megriche, A., El Maaoui, H., Nonat, A. Natural fluorapatite as a raw material for Portland clinker. Cement and Concrete Research. 2018. 105. Pp. 72–80. DOI: 10.1016/j.cemconres.2018.01.006

6. Al-Anweh, A.M., El-Enein, S.A., Abu-Zeid, M. M., El-Anbaawy, M. I., Al-Akhaly, I. A. Influence of Corrective and Additive Raw Materials on Clinker Composition and Cement Properties: A Case Study from Yemen. Iranian Journal of Science and Technology, Transactions of Civil Engineering. 2023. Pp. 1–20. DOI: 10.1007/s40996-022-01012-7

7. Martínez-Martínez, S., Pérez-Villarejo, L., Eliche-Quesada, D., Sánchez-Soto, P.J. New Types and Dosages for the Manufacture of Low-Energy Cements from Raw Materials and Industrial Waste under the Principles of the Circular Economy and Low-Carbon Economy. Materials. 2023. 16(2). 802. DOI: 10.3390/ma16020802

8. Ostrovsky, S.V., Starostin, A.G., Potapov, I.S., Tumanov, V.V., Kuzminikh, K.G. Sintez ftorida kalciya po suhomu sposobu iz karbonata kal'ciya i ftorida ammoniya [Synthesis of calcium fluoride by dry method from calcium carbonate and ammonium fluoride]. Izv. Vyssh. Uchebn. Zaved. Khim. Khim. Tekhnol. [Russ. J. Chem. & Chem. Tech.]. 2020. 63(8). 8189.

9. Voitov, V., Ankuda, M. K., Kuzmenkov, M. I. Application of man-made products for energy saving purposes in the production of Portland cement clinker. Cement and its application. 2022. 3. Pp. 56–58.

10. Brial, V., Tran, H., Sorelli, L., Conciatori, D., Ouellet-Plamondon, C.M. Effect of fluorite addition on the reactivity of a calcined treated spent pot lining in cementitious materials. Cement. 2023. 12. 100070. DOI: 10.1016/j.cement.2023.100070

11. Makridin, N.I., Maksimova, I.N. Struktura i mekhanicheskie svojstva cementnyh dispersnyhsistem [Structure and mechanical properties of dispersed cement systems]: monograph. PGUAS. Penza. 2013. 340 p.

12. Kovalev, S.V., Mishin, D.A., Neverova, E.V. The effect of separate input of the mineralizer on the whiteness and strength characteristics of white cement. International Scientific Conference on Innovations and Technologies in Construction. Springer International Publishing. 2020. Pp. 318–324.

13. Anuarova, A., Shaikezhan, A. Belite-containing clinkers from phosphoric slags for refractory materials. Magazine of Civil Engineering. 2022. 110(2). 11010.

14. Kuz'min, M.P., Larionov, L.M., Kuzmina, M.Yu., Kuzmina, A.S., Ran, J.Q., Burdonov, A.E., Zenkov, E.V. Production of Portland cement using fluorine gypsum – hydrofluoric acid waste. Magazine of Civil Engineering. 2022. 111(3). Article No. 11113. DOI: 10.34910/MCE.111.13

15. Tobón, J.I., Ramírez, J.H. Use of industrial wastes for the synthesis of belite clinker. Materiales de Construcción. 2020. 70(339). 226. DOI: 10.3989/mc.2020.14219

16. Petrovskiy, A.A., Nemchinova, N.V., Tyutrin, A.A., Korepina N.A. Use of leaching cake from refractory lining of dismantled electrolysers in cement production. iPolytech Journal. 2022. 26(4). Pp. 697–708. DOI: 10.21285/1814-3520-2022-4-697-708

17. Novosyolov, A.G., Dreer, Yu.I., Novoselova, I.N., Vasina, Yu. A. Efficiency of using a technogenic product of electrolytic production of aluminum as a mineralizer when firing portland cement clinker. Bulletin of BSTU named after V.G. Shukhov. 2022. 7(5). Pp. 71–80. DOI: 10.34031/2071-7318-2022-7-5-71-80

18. Endzhievskaya, I. G., Demina, A. V., Lavorenko, A. A. Synthesis of a mineralizing agent for Portland cement from aluminum production waste. IOP Conference Series: Materials Science and Engineering. IOP Publishing. 2020. 945(1). 012062. DOI: 10.1088/1757-899X/945/1/012062

19. Chen, Y., Li, P., Bu, Kh., Chelgani, S., Kong,Y., Liang, X. Resource utilization strategies for spent pot lining: A review of the current state. Separation and Purification Technology. 2022. 300. 121816. DOI: 10.1016/j.seppur.2022.121816

20. Shepelev, I.I., Golovnykh, N.V. Kompleksnyj recikling othodov alyuminievogo proizvodstva [Integrated recycling of aluminum production waste. Scientific principles and practice of processing ores and technogenic raw materials]. Materialy XXV Mezhdunarodnoj nauchno-tehnicheskoj konferencii "Nauchnye osnovy i praktika pererabotki rud i tehnogennogo syrya". 7–10 aprelya 2020 g. [Proceedings of the XXV International Scientific and Technical Conference "Scientific foundations and practice of processing ores and man-made raw materials", April 07–10, 2020]. Tails KO. Ekaterinburg. 2020. Pp. 104–109.

21. Tropenauer, B., Klinar, D., Samec, N., Golob, J., Kortnik, J. Sustainable waste-treatment procedure for the spent potlining (SPL) from aluminium production. Materials and technology. 2019. 53(2). Pp. 277–284. DOI: 10.17222/mit.2018.147

22. Li, X., Liu, Y., Zhang, T. A comprehensive review of aluminium electrolysis and the waste generated by it. Waste Management & Research. 2023. 41(10). Pp. 1498–1511. DOI: 10.1177/0734242X231164321

23. Kulikov, B.P., Istomin, S.P. Recycling of aluminum production waste. LLC "Classic Center". Krasnoyarsk. 2004. 480 p.

24. Kulikov, B., Vasyunina, N., Dubova, I., Samoylo, A., Balanev, R., Kutovaya. A. Portland Cement Slinker Production Using Synthetic Fluorite and Graphitic Carbon Based Additives. Ecology and Industry of Russia. 2023. 27(10). Pp. 42–47. DOI: 10.18412/1816-0395-2023-10-42-47

25. Kulikov, B.P., Vasyunina, N.V., Dubova, I.V., Balanev, R.O., Sysoeva, Y.S., Ivanova, I.K. Processing of fine waste from aluminum production to obtain a fluorite-containing product. Metallurgy of non-ferrous, rare and noble metals: Proceedings of the XVI International Conference named after corresponding member of the Russian Academy of Sciences Gennady Leonidovich Pashkov. Krasnoyarsk. 2023. Pp. 180–189. DOI: 10.47813/sfu.mnfrpm.2023.180-189

26. Yakimov, I.S., Dubinin, P.S., Zaloga, A.N., Piksina, O.E., Yakimov, Ya.I. Regularization of methods of a standardless X-ray phase analysis. Journal of Structural Chemistry. 2011. 52. Pp. 319–325.

27. Gates-Rector S., Blanton T. The Powder Diffraction File: a quality materials characterization database. 2019. 34. 4. Pp. 352–360. DOI:10.1017/S0885715619000812

28. Patent No. 2291208 C2 Russian Federation, IPC C22B 1/245. Method for producing pelletized material: No. 2005104913/02: application. 02/22/2005: publ. 01/10/2007 / B. P. Kulikov, I. A. Tarasov, V. A. Nechaev; applicant Limited Liability Company "Engineering and Technology Center".

Information about authors:

Boris Kulikov, *Doctor of Technical Sciences*
E-mail: kulikov-boris@yandex.ru

Natalia Vasyunina, *PhD in Technical Sciences*
ORCID: https://orcid.org/0000-0002-4334-3914
E-mail: nvvasyunina@yandex.ru

Irina Dubova, *PhD in Technical Sciences*
E-mail: idubova@mail.ru

Aleksandr Samoilo,
E-mail: x_lab@rambler.ru

Nadezhda Merdak,
E-mail: nadya.merdak.92@mail.ru

Performance of geosynthetics-strengthened unconnected piled raft foundations under seismic loading

A.G. Jihad[1,2], M. Karkush[1] iD

[1]*Civil Engineering Department, University of Baghdad, Baghdad, Iraq*

[2]*Road and Transport Engineering Department, Al-Qadisiyah University, AL-Qadisiyah, Iraq*

✉ *mahdi_karkush@yahoo.com*

Keywords: unconnected piled raft, geosynthetics, foundations, seismic loading

Abstract. Over the past 20 years, geosynthetic reinforcement has been widely used in earthen constructions. For constrained building projects and challenging ground conditions, geosynthetic-reinforced-pile-supported (GRPS) embankments are regarded as dependable options. There has been significant research into ways to improve the stability of pile foundations, and there has also been some research into the viability of using unconnected piled raft under seismic load. This study investigates the use of geosynthetics to improve the performance of unconnected pile foundations under seismic load. A series of reduced-scale physical model experiments conducted on a shaking table was used to assess the seismic soil-structure interaction behaviors of geosynthetics-reinforced pile foundation systems. The study makes use of disconnected, closed-end aluminum piles with different thicknesses of cushion layers of sand soil and different spacing between piles are used in the study. The performance of disconnected footing was examined using a shaking table to determine the impact of the geosynthetics reinforced. These model findings are used to identify and thoroughly describe the contradictions in the present design methodologies. This study shows the settlement of the foundation under seismic loading decreased by reinforcing the cushion layer with one and two layers of geogrid materials, increasing the thickness of the cushion layer led to increasing the settlement of the foundation under seismic loading, where the settlement decreases with decreasing the value of spacing between piles. However, with further increases in either the cushion thickness or cushion stiffness or both, the effect of improvement would decrease.

1. Introduction

One of the key functions of geotechnical engineering is the design of the foundation system. A safe, effective, and cost-effective project will undoubtedly result from the proper selection and design of the foundation system. A foundation system can use piles for two main reasons: to increase bearing capacity and/or to limit predicted settlements to acceptable levels. The general assumption made by traditional pile foundation design techniques is that the piles would support the entire weight of the superstructure. Over the past few decades, a more modern strategy has been used, one that uses piles as settlement reducers in what is known as a piled raft foundation. Davis and Poulos [1] introduced the concept of piled raft foundation in 1972. After that, many researchers have been involved in the design and analysis of such type of foundation. Among those [2–8] and others, the foundation of a piled raft should only contain the minimum number of piles necessary to make the settlement at a reasonable level. A portion of the loads that are transmitted from the superstructure to them via the raft is also carried by these piles. In other words, the loads are shared between the raft and piles. High axial stress concentration at the pile head may occur [9, 10].

In addition, if the foundation is planned as a structurally connected piled raft in seismically active zones or places prone to high winds, large shear forces in addition to overturning moments may arise in the pile's head due to the lateral dynamic load. For all of that, the ultimate capacity may be governed by the structural capacity of the pile rather than the geotechnical capacity. In these situations, more likely than soil failure is the structural failure of a foundation. Therefore, to avoid structural damage to the foundation, the dimensions of piles should be increased and the result is an uneconomical design of the foundation. The use of disconnected piles and the use of an intervening compacted fill layer known as a cushion layer between the raft and the piles have recently been suggested as alternatives to the traditional method for dealing with constraint responses. The piles in such a foundation system are considered soil reinforcement members rather than structural components [11–13]. In unconnected piles, the carrying loads could be much higher than that carried by structurally connected piles, and still, the economic benefits have been gained. Moreover, there should be no possible damage to structural connections. In addition, because of the mobilized adhesion force along the soil-raft interface, the horizontal loads can be effectively transmitted as shown in Figure 1 [11,14,15].

In this study, the propagation and degradation of the sandy soil in the cushion layer that separates the raft and unconnected piles were investigated in detail by conducting several tests using a shaking table. The cushion layer used in this study was reinforced by several layers of geosynthetic materials at a different cushion layer thickness and change the space between piles, all the raft footing was tested under seismic load.
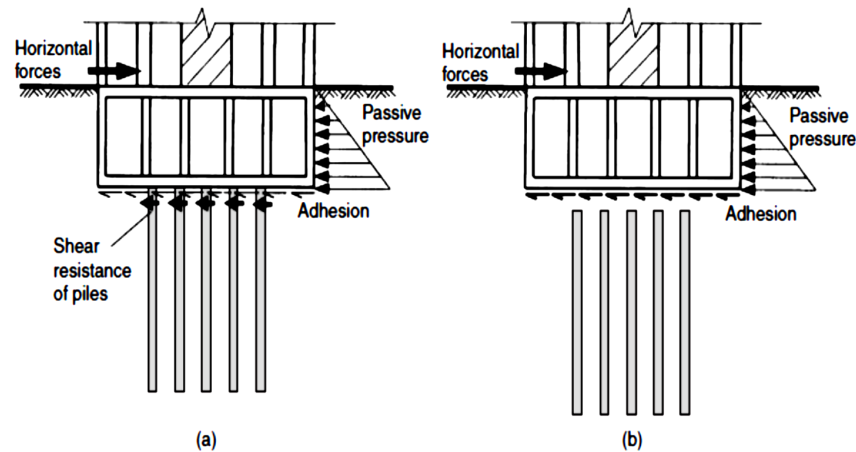

Figure 1. Transfer mechanism for horizontal loads: a) piles structurally connected to raft and b) piles structurally unconnected from raft [11].

2. Materials and Methods

2.1. Shaking Table

Using a shaking table device, the uniaxial sinusoidal motion was adopted with various frequencies as shown in Fig. 2. The shaking table was produced in the local market which has a dimension of 1×1 m size with 1.25 tons loading capability. It was supported by a heavy-duty steel frame that had 4 rollers that could move smoothly in one direction. All parts of the shaking plate were fixed to a rigid steel frame by 8 bolts to ensure rigidity and eliminate any motion, vibration, or sliding of the shaking table during the controlled seismic loading. In addition, the AC driver is contacted by the computer to control the time and frequency of the shaking. To adjust the exact frequency magnitude a calibration process must be done, this process was executed as follow: for a specific period, the number of cycles was recorded compared to the AC frequency, and using the accelerometer in the base of the shaking table the results were recorded, the result is the frequency in Hz by change the velocity of the motion a new value of frequency would appear as shown in Fig. 3. Thus, for a specific value of frequency, it is easy to select the correct number in the AC drive to determine the speed of the motor to get the required acceleration in the base of the shaking table.
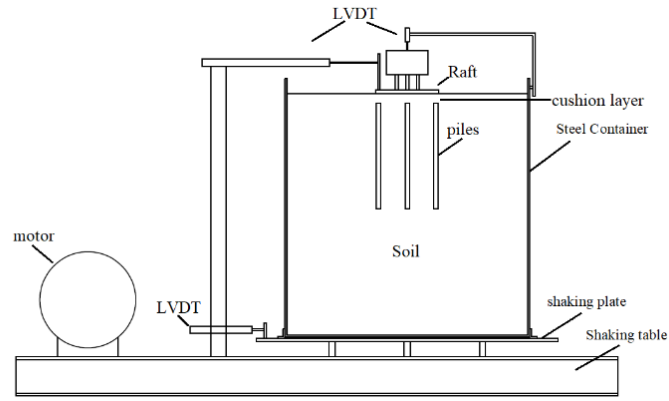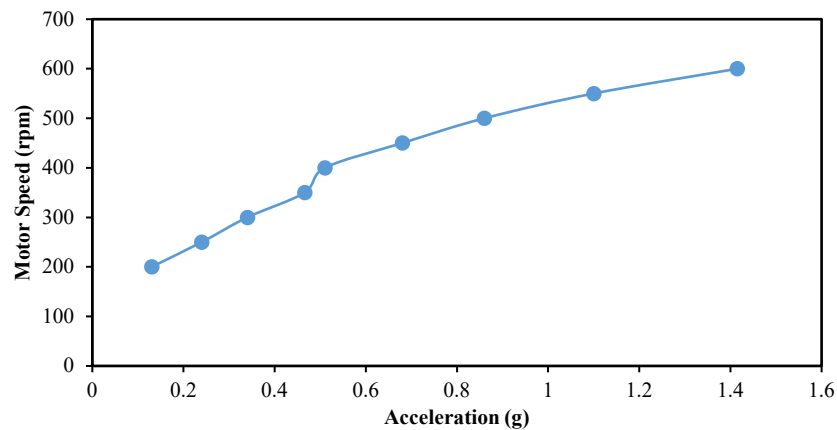
Figure 2. Testing model scheme.

Figure 3. The calibration of the motor speed (rpm) and the acceleration.

2.2. Steel Container

A steel container had a depth of 850 mm and 800×700 mm cross-section and was made of a 5 mm plate thickness. The steel container was set up on a mobile frame base. In every test, the container's side dimension was greater than three times that of the raft side. The piles' end tips were about 25D or more above the container's base. It was made out of a steel frame of L-shape steel angles of 75x75 mm in size. Three sides of the steel container were covered with a steel plate 5 mm thick, and the fourth side was covered with strengthened transparency glass which help to watch the behavior of the foundation during the test. One of the improvements applied was the flexible rubber joints at the box corners which permit motion within a specific limit, this movement was limited to 20 mm and could occur at the same time alternately for each opposite side. The purpose of this flexible joint was to lessen the effect of the fixed joint on the behavior of the soil sample during shaking, which resulted in unanticipated behavior by wave reversals, damping, and other factors.

2.3. Pile Model

The pile model used in the current study was made of aluminum alloy of hollow square section of 14 mm in outside dimension and 11 mm inside dimension. The embedded pile length of 350 mm was used in all experimental model tests. The slenderness ratio (length to diameter ratio (L/d)) was 22.15.

2.4. Raft Model

The square steel plate with side dimensions 210×210 mm and a thickness of 12 mm was used as a model raft. The modulus of elasticity (E_r) and Poisson's ratio (v_r) of the steel plate were 210×10⁶ kPa and 0.30, respectively. The total weight of the suggested footing was 18 kg which is equivalent to the ordinary building weight.
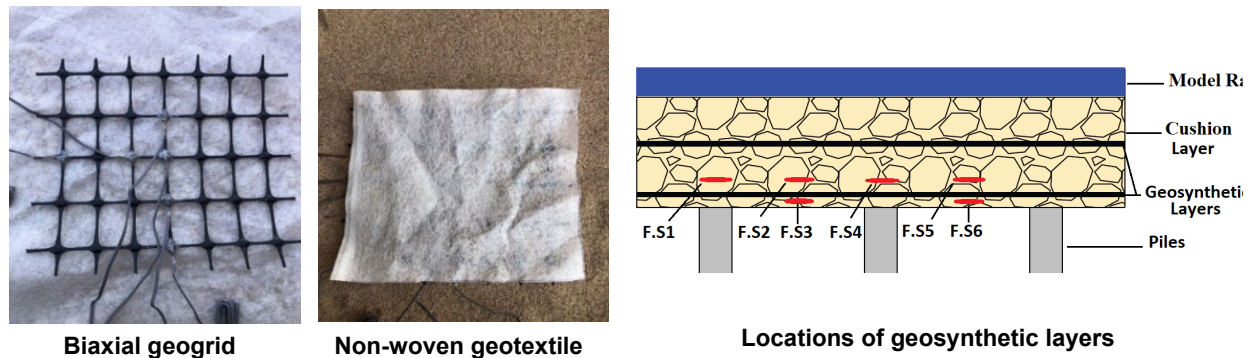
2.5. Geosynthetics

This study looked into how soil degradation was affected by geosynthetic reinforcement. A non-woven geotextile sheet was laid on top of a biaxial geogrid in the reinforced fill tests. The geosynthetic characteristics and forms and its location are presented in Table 1 and Fig. 4, respectively. Given that the fill material was sand, the non-woven geotextile was used over the geogrid to both transmit the load from the foundation to the geogrid and prevent sand from flowing through the geogrid apertures.

Table 1. Physical characteristics and geometry of geosynthetic materials.

Geosynthetic	Properties	Units	Values
Biaxial geogrid	Aperture dimensions	mm	25×33
	Minimum rib thickness	mm	0.76
	Tensile strength @ 2% strain	kN/m	6.6
	Tensile strength @ 5% strain	kN/m	13.4
	Ultimate tensile strength	kN/m	19
Non-woven geotextile	Mass/unit area	gm/m^2	96
	Thickness	mm	1.04
	Wide-width tensile strength	kN/m	7.23
	Wide-width tensile elongation	%	54
	Puncture strength (CBR)	N	1218
	Opening size	mm	0.15

Note: geosynthetic properties are based on the manufacturer-provided datasheet.

**Biaxial geogrid**   **Non-woven geotextile**   **Locations of geosynthetic layers**

Figure 4. Geosynthetic materials used in the experimental work.

2.6. Instruments

A 25 mm accurate LVDT (Linear Variable Differential Transformer) was placed on the center of the foundation system to measure the vertical settlements of the foundation model. Through metal rods fixed to the horizontal beam at the top of the box. The system was supported by metal rods and fixed to the base of the shaking table. The horizontal movement for the foundation and the shaking table was measured by LVDTs of lengths (400 and 500 mm) respectively shown in Fig. 5.

The acceleration of the shaking table, inside the soil, and on the plate and the foundation was measured by using an analog accelerometer sensor ADXL335, which can measure three directions of acceleration excitation as shown in Fig. 5. Five sensors were used; one on the shaking table, three within the soil column at different depths (each 20 cm depth apart), and the last one was fixed on the foundation. The selected sensor ADXL335X was a simple breakout board that allows easy, direct, and rapid evaluation of the performance of the ADXL335 accelerometer. The used sensor was a 3-axis analog-output accelerometer with a ±3 measurement range. The small size (25.4×25.4 mm) of the accelerometer made it easy to maneuver and fix on the different systems without needing additional hardware. All the accelerometers were connected to the data acquisition system channel.
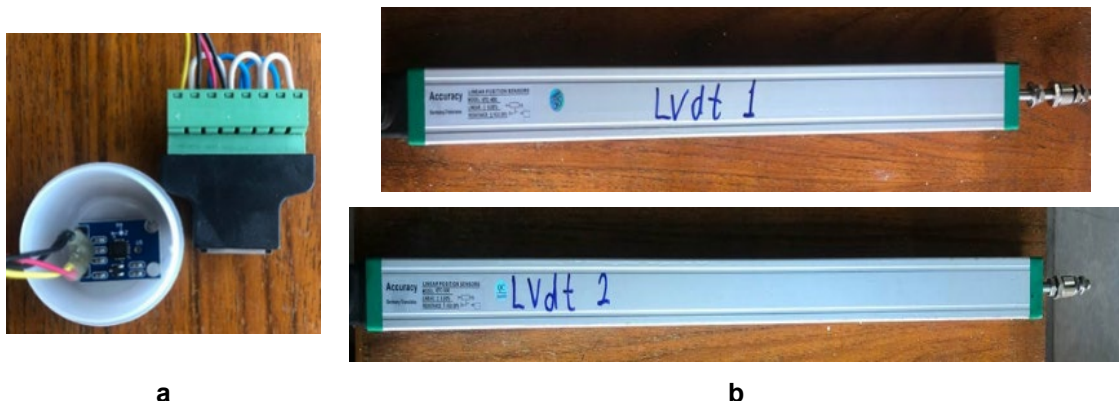
a   **b**

Figure 5. a) Accelerometer and b) LVDTs used in the tests.

Data acquisition with LabVIEW Application was used to record and save all the readings of LVDTs and accelerometer. LabVIEW (Laboratory Virtual Instrumentation Engineering Workbench) is a platform and development environment for a visual programming language from National Instruments. It is commonly used for data acquisition, instrument control, and industrial automation on a variety of platforms including Microsoft Windows, various flavors of UNIX, Linux, and Mac OS X. The data logger is supplied with 32 channels for connecting the transducers for all the instruments where 5 channels are used for accelerometers and 3 channels are used for LVDTs, as well 4 channels are used for AC drive control and internal connecter. The problem was represented by disturbance of the instrument's signals by the magnetic radiations from the motors of the shaker leading to incorrect readings. To solve this problem, two actions were adopted as described in the following points. First using ground connections for all the equipment and connecting them to a copper rod that has been previously installed in the ground soil to ensure the removal of any charges generated that may cause noise in the reading, the second use of a transformer for electricity equipped for all equipment to ensure the elimination of any noise caused by the electric current on the readings.

2.7. Soil Box Model and Bedding Soil

A relatively uniform dry sand of grain size between 0.35 and 1.18 mm was utilized in this investigation as foundation soil. The maximum and minimum dry unit weight of the tested sand were found 17.44 kN/m^3 and 15.17 kN/m^3, respectively. Table 2 shows the physical properties of the used soil. According to the Unified Soil Classification System (USCS), the soil is classified as poorly graded sand (SP).

Table 2. Physical Properties of the tested soil.

Property	Value	Standard Specification
Specific gravity	2.64	[16]
Sand (0.35–1.18 mm), %	100	
Coefficient of curvature	1.05	
Coefficient of uniformity	1.52	
D_{10}, mm	0.5	[17,18]
D_{30}, mm	0.6327	
D_{60}, mm	0.7597	
USCS soil type	SP	
Maximum dry unit weight, kN/m^3	17.44	[19]
Minimum dry unit weight, kN/m^3	15.17	[20]
Used dry unit weight, kN/m^3	16.627	
Relative density, %	50	

To reconstitute or prepare the sand samples for experimental model tests, several ways were used such as raining, vibration, or tamping. In general, as it was reported by [21–25], to provide relatively homogenous sand samples and to get the required relative density, the raining procedure is considered the best. The adopted raining technique consisted of a steel hopper of 35 cm height with a valve at the bottom to control sand raining manually. A sieve of 4.75 mm opening size was attached to the bottom via a funnel connected to a hopper to distribute the sand uniformly. The hopper was hanging by a pulley to adjust the height of the rain. Many trials were performed to draw a relationship between the falling height and the corresponding dry density as shown in Fig. 6. From the curve, it is clear that the falling height should be about 200 mm to get the required dry density of 16.627 kN/m^3.

The inside walls of the steel container were divided into 8 intervals 10 cm each to ensure that the desired dry density was obtained properly. To produce a homogenous sample overall in the container, the required quantity of sand for each layer was weighted such that the designed dry density could be obtained. After the completion of the raining of the soil for each layer, the sand layer was equalized by a steel plate of section area (175×200 mm) to an average of one blow per unit area for grain fixation and insurance of the required layer height. However, the target relative density of the sand sample was 50% ± 2%.
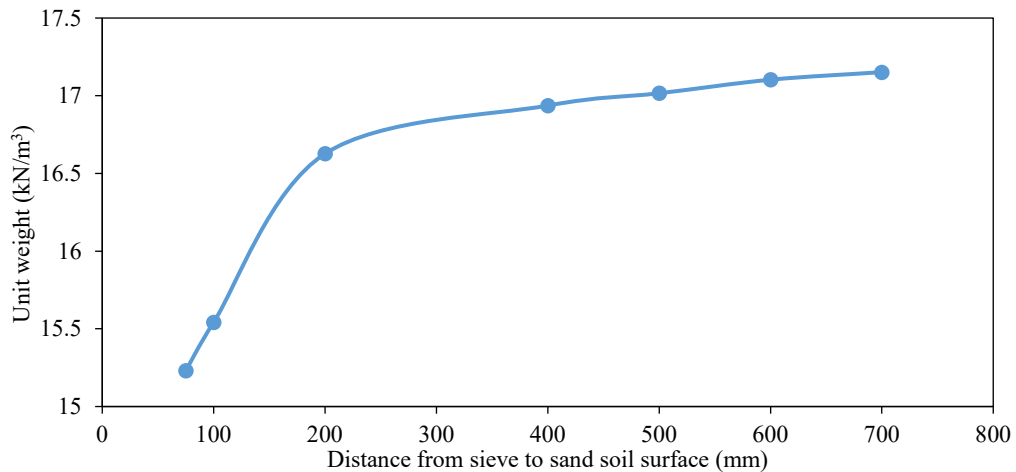
Figure 6. The relationship between the height of falling and dry density of sandy soil.

2.8. Seismic loading

Seismic loading, which is known as an application of seismic oscillation to a structure, can be considered one of the most essential basics of earthquake engineering. It depends on seismic hazard, geotechnical site parameters, and structural natural frequency which occurs at the surface of the structure and in contact with the ground or an adjacent structure. In the years 2017 and 2018, seismic activities were recorded with different strengths in Iraq. During the last two months of the year 2017, more than seventy earthquakes hit Iraq. As shown in Table 3, the magnitude of these earthquakes ranged from 4.0 to 7.3 on the Richter scale, with depths ranging from 6.21 to 42.32 km.

Table 3. History of some earthquakes in Iraq.

Year	Magnitude (Richter scale)	Location
1960	6.0 to 6.7	Halabja City which locates at northeast of Baghdad
1967	6.1	100 km south of Halabja City
2013	5.6 and 5.8	Two earthquakes hit about 60 km south of Halabja City, northeast of Baghdad
2017	7.3	Series of earthquakes 30 km south of Halabja City, northeast of Baghdad, Iraq
2018	4.0 to 4.5	A series of earthquakes hit northeast of Baghdad

Halabja City is located northeast of Baghdad (Iraq) and near the international border between Iraq and Iran. Halabja earthquake was used in this study. The acceleration of this earthquake was 0.24 g, and seismic loading conditions have been applied to the model as acceleration is shown in Fig. 7.
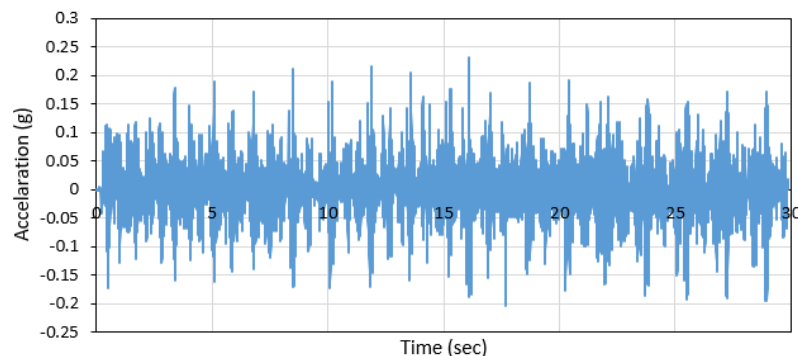

Figure 7. The acceleration time history of the applied Halabja earthquake.

2.9. Testing procedure

The test procedure followed in this investigation consisted of many steps such as:

1. The preparation of each model test was commenced by weighing the required quantity of sand to get the target density, then it was poured into the container by rainfall method into 8 layers each of 100 mm thickness.

2. Sand raining was paused when reaching the level above the pile tip by 50 mm. The pile was inserted 50 mm into the soil bed. This level was calculated previously to ensure proper seating of piles into the sand. The reached sand surface was leveled with a straight edge, and the steel mesh of square spaces of 70 mm was used to support the piles and ensure their verticality as shown in Fig. 8.
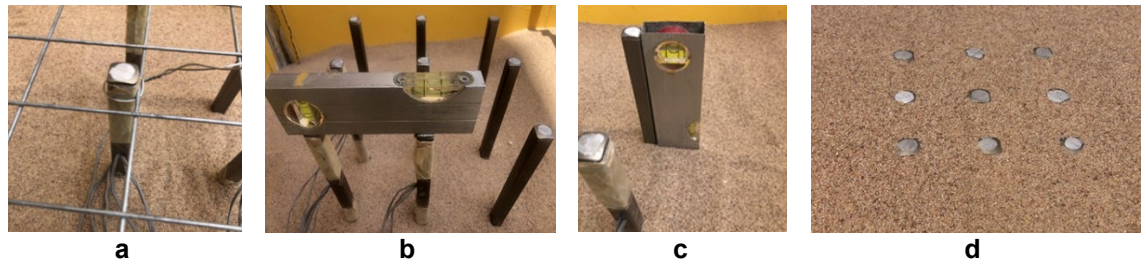

| a | b | c | d |

**Figure 8. a) Piles fixation by steel mesh, and b) horizontal leveling of
upper head of piles, c) vertical leveling of piles, and d) final level of soil and unconnected piles.**

3. Continuing the raining of soil to reach the middle of the pile level, stop the raining work and remove the steel mesh because the pile was fixed by the soil, through that the top level and side of the unconnected piles checked carefully by water bubble in longitudinal, transverse, and diagonal directions as shown in Fig. 9. Although the pile installation method utilized in this study is not the same as in practice, it was chosen instead of the pushing or driving method because using these methods may affect the unit weight of the nearby soil of the piles and consequently, the modulus of elasticity and the wires of the strain gauges in the pile affected the soil in the pushing method.

4. Through the last steps, the instruments fixed in their location. The accelerometer number one in the base plate of the shaking table and the numbers two, three, and four was put at three levels in the body of soil every 200 mm apart as shown in Fig. 9.

5. Sand surface should be leveled carefully such that it should be at the same level as the top pile's head in order to ensure that the applied cushion was definitely at one level with both the top head of the piles and the sand surface as shown in Fig. 9.

6. The cushion layer is raining in a special mold, the special mold used in this step depends on the dimension side and the thickness of the cushion. After that, the soil around the cushion prepared by raining to the level required and then carefully lifting the plate mold to ensure the density did not change.

7. In the reinforcement cushion layer tests, the geosynthetic (biaxial geogrid and non-woven geotextile) was added to the cushion layer in single or double layers. The first layer was at the head piles level and in case of double reinforcement the second layer was in the medium of the cushion layer.

8. The raft was placed on the cushion and the special loading was seated on it; the accelerometer number 5 was fixed in the raft previously.

9. The LVDTs were placed in the designated location, LVDT number one was fixed on the plate of the shaking table to determine the horizontal movement of the shaking plate, while LVDTs number two and three are fixed on the raft to measure the horizontal and vertical movement of the raft as shown in Fig. 9. To prevent the inclination in the LVDT2 that may be happened because of the vertical displacement of the raft, therefore sliding channel was used to allow vertical and horizontal movement at the same time.

10. After that, the instruments were connected to the data acquisition including all the instruments such as accelerometers and LVDTs. The wires extend through the piles and within the soil at the least possible effect on the test.

11. After assurance that all the measurement devices were connected correctly to the data acquisition system and connected to the computer in order to record and save all the readings automatically.

12. Starting the test by operating the computer and starting the shaking table work, the computer recorded and save all the readings automatically.

13. Removing the raft model and all the instruments, discharging sand from the model box, and keeping it in containers (water withdrawal and air drying the soil in case of saturated test).

14. Repeating the procedure mentioned above points to make another test.
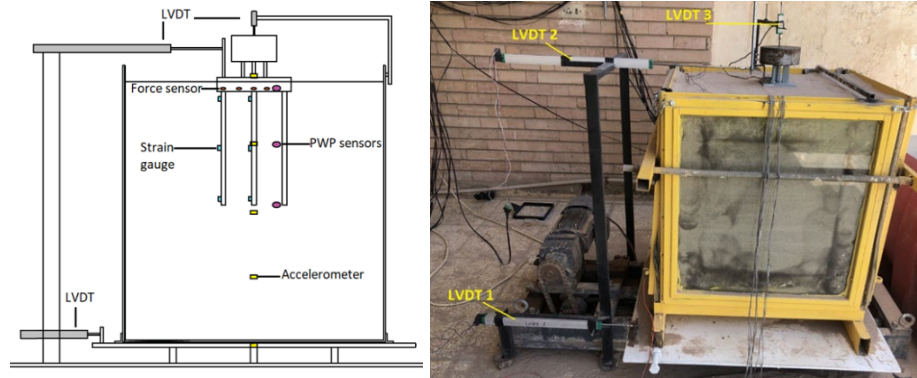
Figure 9. Schematic diagram of model test and instrument's location.

3. Results and Discussion

In this study, the settlement of the unconnected pile was experimentally measured by changing the thickness of the cushion layer, spacing between the piles, and reinforcement of the cushion layer by geosynthetics (biaxial geogrid and non-woven geotextile) using one and two layers. The thickness of the cushion used in the study was 2d, 3d, and 4d where d is the pile diameter. The spacing between piles used was 3d, 4.5d, and 6d. The settlement was determined at the end of the test after 30 seconds after starting the seismic load. The notations of conducted tests in this study are shown in Table 4.

Table 4. Notations and description of conducted shaking table tests.

Test no	Cushion thickness	Spacing between piles	Reinforcement
T1	2d		
T2	3d	3d	
T3	4d		
T4	2d		Without
T5	3d	4.5d	reinforcement
T6	4d		
T7	2d		
T8	3d	6d	
T9	4d		
T10	2d		One layer consists
T11	3d	3d	of
T12	4d		biaxial geogrid and
T13	2d		non-woven
T14	3d	4.5d	geotextile
T15	4d		
T16	2d		Two layers, each
T17	3d	3d	consisting of
T18	4d		biaxial geogrid and
T19	2d		non-woven
T20	3d	4.5d	geotextile
T21	4d		

The results of experimental tests showed that the interposed cushion layer between the raft and piles had caused a downward relative displacement of the soil-pile system. This relative displacement is maximum at the pile heads and extends to a certain depth below the pile heads. The relative displacement becomes zero at a certain depth which is known as the depth of the neutral plane. Initially, the surrounding soil and the raft settle greater than the piles which produce negative skin friction along the upper part of the piles (above the neutral plane). Thus, the piles loaded through their heads as well as through the negative skin friction. Because of the load on the pile head and the negative skin friction, the pile is settling and a mobilized positive skin friction occurring at the lower part of the pile shaft, as well as resistance at the lower tip. It is found that this mechanism was governed by the thickness and stiffness of the cushion layer.

Fig. 10 shows the variation of settlement of the tested soil models without reinforcement for several spacings between piles 3d, 4.5d, and 6d where d is the equivalent pile diameter. Also, the thickness of the cushion layer varies from 2d to 4d. The settlement increases with increasing the thickness of the cushion layer for a small spacing ratio of 3d but increasing the spacing between piles to 4.5d reflects a different trend of behavior. For this ratio of spacing (4.5d), increasing the thickness of the cushion layer to 3d reduces settlement more than 2d, but still, 4d gives higher settlement than the foundation with cushion layers of 2d and 3d. In case of spacing between piles is 6d, the settlement is decreased with increasing the thickness of the cushion layer, but still cushion layer of thickness 4d gives settlement higher than 3d. Generally, reducing the spacing between piles increases the stresses in the foundation and consequently increases the settlement, therefore the thickness of the cushion layer must be matched with spacing between piles to get the optimum benefit of cushion layer thickness. The difference in measured settlement due to changing the thickness of the cushion layer ranged between 0.19 to 9.75%.

To study the effects of changing the spacing between piles on the variation of settlement with time three ratios (3d, 4.5d, and 6d) have been studied as shown in Fig. 11. In each case, the thickness of the cushion layer is assumed constant. The settlement increased with increasing the spacing between piles, but the variation in the final value of settlement after 30 seconds of shaking ranged from 12.75 to 14.56%. Generally, the trend of settlement variation with time is almost the same for all tested cases. It can be seen that most of the settlement 90% occurred during the first 20 seconds of dynamic loading, then a slight increase noticed in the value of the settlement continues to the end of the loading period.

The stiffness of the cushion layer has an important role in increasing the efficiency of the unconnected piled raft foundation in reducing the settlement. However, if the stiffness of the cushion layer is not high enough, the performance of the unconnected piled raft in reducing the settlement is lower but it's better than the unconnected piled raft without reinforcement. Increasing the thickness of the cushion layer without reinforcement led to increasing the value of settlement because the seismic load decreases the angle of internal friction of soil used in the cushion layer and that makes the cushion layer creeps out from the cushion space, but this case is reversed in case of using reinforcement in the cushion layer whether using one or two layers of geogrid, so the settlement decreases with increasing the thickness of reinforced cushion layer. The geosynthetic materials used in reinforcing the cushion layer helps in the redistribution of the load between the pile and increases the stiffness of the cushion layer. Fig. 12 shows the effect of using reinforcement in the cushion layer on the variation of settlement with time for tested soil models. The efficiency of using reinforcement appears significantly when the thickness of the cushion layer is 3d and more and for any spacing between piles. Also, using one layer of reinforcement reduces the settlement of footing better than the cushion layer without reinforcement, and using two layers of reinforcement in the cushion layer reduces the settlement better than using one layer of reinforcement as shown in Fig. 12.
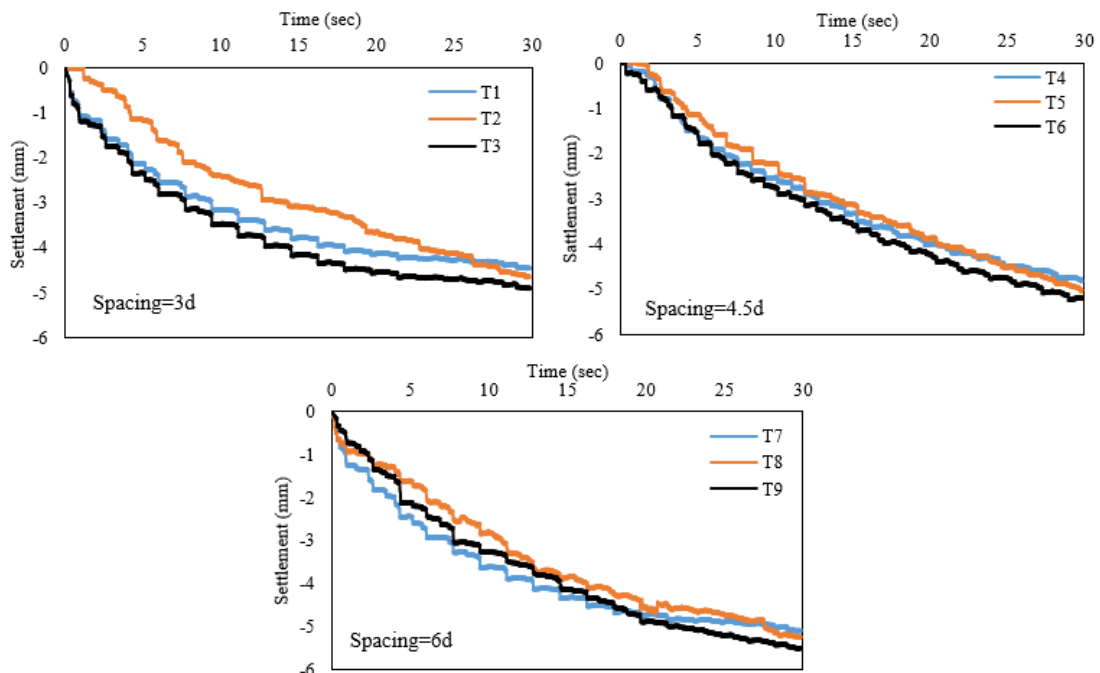

Figure 10. Variations of the settlement with time for soil samples without reinforcement of cushion and change cushion thickness.
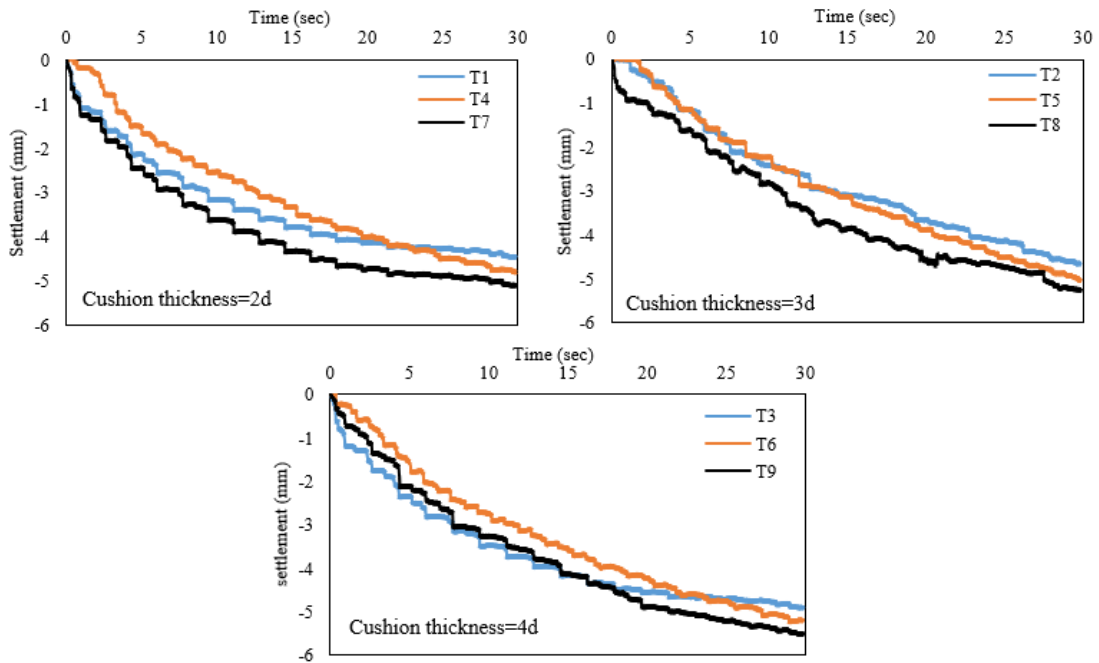
**Figure 11. Variations of the settlement with time for soil samples
without reinforcement of cushion and change spacing between piles.**

The mechanisms of the geosynthetic material in soil work as a tensioned membrane and help to stabilize the soil. The interlocking of geosynthetic-soil particles applied additional horizontal stress to the soil particles under loading and in turn increased the soil shear strength thus creating more stable soil. The vertical component of the tensioned membrane reduced the pressures on the soil between the piles and subsequently increased the pressures on the stationary supports (piles), so the tensioned membrane effect was more effective at the displacement. Fig. 13 and 14 show the effects of using one and two layers of geogrid on the settlement of soil model subjected to dynamic loading with constant spacing between piles. The results presented in these figures exhibited decreasing the settlement with increasing the number of reinforcement layers and this reduction was associated with increasing the thickness of the cushion layer.
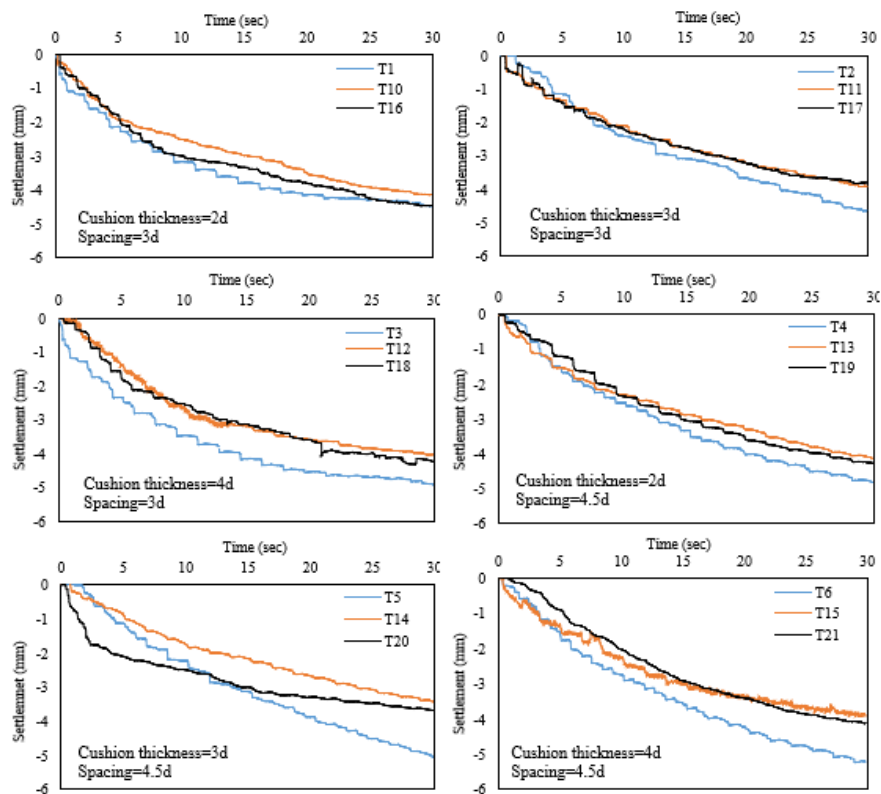

**Figure 12. Variations of the settlement with time for soil samples
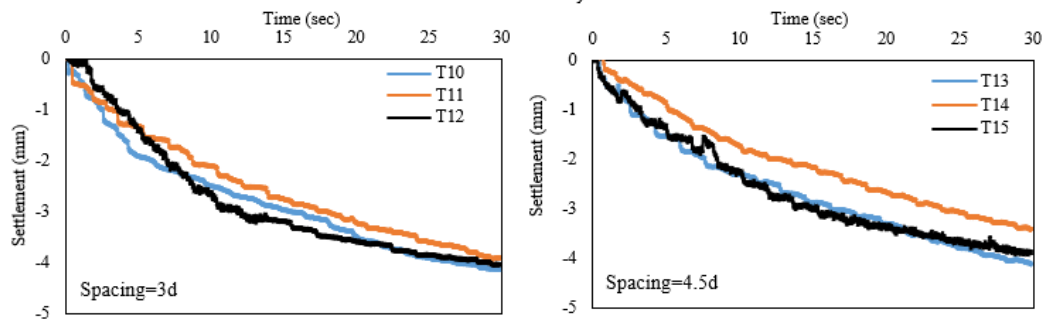with changing the number of reinforcement layers.**

**Figure 13. Variations of the settlement with time for soil samples
of cushion layer reinforced with one layer of geogrid.**
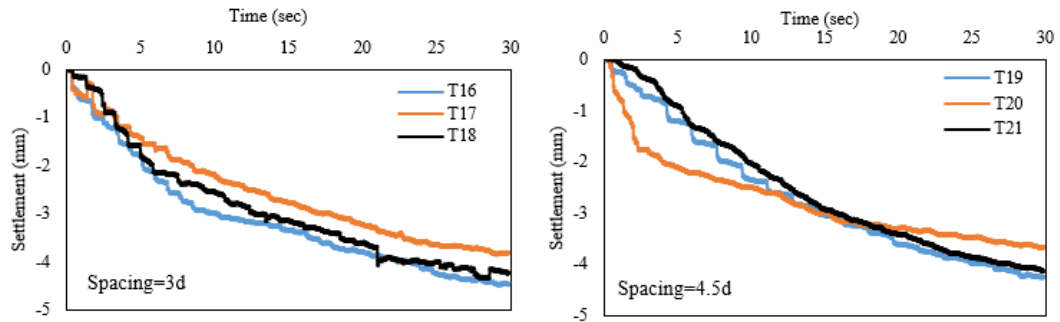

**Figure 14. Variations of the settlement with time for soil samples
of cushion layer reinforced with two layers of geogrid.**

4. Conclusions

This work is devoted to investigating the effects of improvement of the cushion layer in unconnected piles subjected to seismic loading using one and two layers of geogrid. The lateral restraint and the tensioned membrane effect of geosynthetic materials helped transfer the more vertical load onto the supports. The following points can be concluded from the results of the experimental work conducted in this study:

- The settlement of the foundation under the seismic loading decreased by reinforcing the cushion layer with one and two layers of geogrid materials. The improvement in settlement by reinforcement of the cushion layer was between 8 and 27%. There is no significant difference between using one and two layers of reinforcing the cushion layer but using two layers of reinforcement is better than using one layer.

- The reinforcement and the thickness of the cushion layer govern the amount of settlement. Increasing the thickness of the cushion layer led to increasing the settlement of the foundation under seismic loading in the case of using a cushion layer without reinforcement, the settlement increased between 4 and 10% with an increase in the thickness of the cushion from 2d to 3d and 4d. Especially in the case of the small thickness of the cushion layer and spacing between piles.

- The variation of the spacing between piles led to a change in the settlement, where the settlement had decreased with decreasing the value of spacing, the value of the settlement had decreased between 7 and 14% when decreasing the spacing from 6d to 4.5d and 3d. Reduction of the distance between piles makes the foundation system works as a block and that reduces the settlement.

- For a constant thickness of the cushion layer using geosynthetic materials in the reinforcement of the cushion layer reduces the settlement of the unconnected piled raft system.

- The results of tests indicated that there had been a considerable role for the thickness and the stiffness of the cushion layer on the loading sharing ratio between soil, raft, and piles. However, with further increases in either the cushion thickness or cushion stiffness or both the effect of adjustment will decrease.

- It was observed the variation of the spacing between piles led to a change in the settlement, where the settlement had decreased with decreasing the spacing between piles which had made the foundation system work as a block consequently leading to reduce the settlement.

References

1. Davis, E.H., Poulos, H.G. The analysis of Piled Raft Systems. Australia Geotechnique Journal. 1972. 2(1). Pp. 21–27.

2. Cooke, R.W. Piled raft foundations on stiff clays – a contribution to design philosophy. Géotechnique. 1986. 36(2). Pp. 169–203. DOI: 10.1680/geot.1986.36.2.169

3. Chow, Y.K. Iterative analysis of pile-soil-pile interaction. Géotechnique. 1987. 37(3). Pp. 321–333. DOI: 10.1680/geot.1987.37.3.321

4. Randolph, M.F. Design methods for pile groups and piled rafts. Thirteenth International Conference on Soil Mechanics and Foundation Engineering. 1994. 5. Pp. 61–82.

5. Karkush, M.O., Aljorany, A.N. Analytical and Numerical Analysis of Piled-raft Foundation of Storage Tank. Construction in Geotechnical Engineering. Lecture Notes in Civil Engineering. 2020. Vol. 84. Pp. 373–384.

6. Karkush, M.O., Ala, N.A. Numerical Evaluation of Foundation of Digester Tank of Sewage Treatment Plant. Civil Engineering Journal. 2019. 5(5). Pp. 996–1006. DOI: 10.28991/cej-2019-03091306

7. Ta, L.D, Small, J.C. Analysis of piled raft systems in layered soil. International Journal for Numerical and Analytical Methods in Geomechanics. 1996. 20(1). Pp. 57–72. DOI: 10.1002/(SICI)1096-9853(199601)20:1<57::AID-NAG807>3.0.CO;2-0

8. Horikoshi, K., Randolph, M.F. Centrifuge modelling of piled raft foundations on clay. Géotechnique. 1996. 46(4). Pp. 741–752. DOI: 10.1680/geot.1996.46.4.741

9. Poulos, H.G. 16. Practical design procedures for piled raft foundations. Design applications of raft foundations. 2000. Pp. 425–467. DOI: 10.1680/daorf.27657.0016

10. Kim, K.N., Lee, S.H., Kim, K.S,, Chung, C.K., Kim, M.M., Lee, H.S. Optimal pile arrangement for minimizing differential settlements in piled raft foundations. Computers and Geotechnics. 2001. 28(4). Pp. 235–253. DOI: 10.1016/S0266-352X(01)00002-7

11. Wong, I.H., Chang, M.F., Cao, X.D. 17. Raft foundations with disconnected settlement-reducing piles. Design applications of raft foundations. 2000. Pp. 469–486. DOI: 10.1680/daorf.27657.0017

12. Burghignoli, A., Jamiolkowski, M., Viggiani, C. Geotechnics for the preservation of historic cities and monuments: components of a multidisciplinary approach. Proceedings of the 14th European Conference on Soil Mechanics and Geotechnical Engineering. 2007. Pp. 24–27.

13. Alhassani, A.M.J., Aljorany, A.N. Parametric Study on Unconnected Piled Raft Foundation Using Numerical Modelling. Journal of Engineering. 2020. 26(5). Pp. 156–171. DOI: 10.31026/j.eng.2020.05.11

14. Al-Saidi, A. Correction Factor for Methods of Installation of Piles Group in Sandy Iraqi Soils. Journal of Engineering. 2016. 22(9). Pp. 172–181. DOI: 10.31026/j.eng.2016.09.11

15. Jebur, M.M., Ahmed, M.D., Karkush, M.O. Numerical Analysis of Under-Reamed Pile Subjected to Dynamic Loading in Sandy Soil. IOP Conference Series: Materials Science and Engineering. 2020. 671(1). Article no 012084. DOI: 10.1088/1757-899X/671/1/012084

16. American Society of Testing and Materials (ASTM). Standard test method for specific gravity of soil solids by water pycnometer. ASTM D854. 2006.

17. American Society of Testing and Materials (ASTM). Standard test method for classification of soils for engineering purposes (Unified Soil Classification System). ASTM D2487–06. 2006.

18. American Society of Testing and Materials (ASTM). Standard test method for particle size-analysis of soils. ASTM D422–63 (2002). 2006.

19. American Society of Testing and Materials (ASTM). Standard test method for direct shear test of soils under consolidated drained conditions. ASTM D3040–04. 2006.

20. American Society of Testing and Materials (ASTM). Standard test method for minimum index density and unit weight of soils and calculation of relative density. ASTM D4254–00 (2006). 2006.

21. Karkush, M.O., Ali, S.D., Saidik, N.M., Al-Delfee, A.N. Numerical Modeling of Sheet Pile Quay Wall Performance Subjected to Earthquake. Geotechnical Engineering and Sustainable Construction. 2022. Pp. 355–365. DOI: 10.1007/978-981-16-6277-5_28

22. Karkush, M.O., Jafar, G.S. Effects of Surcharge on the Behavior of Passive Piles in Sandy Soil. International Journal of Scientific & Engineering Research. 2015. 6(10). Pp. 392–397.

23. Karkush, M.O., Resol, D.A. Remediation of Sandy Soil Contaminated with Industrial Wastewater. International Journal of Civil Engineering. 2017. 15(3). Pp. 441–449. DOI:10.1007/s40999-017-0195-6

24. Jihad, A., Karkush, M. Behavior of Geosynthetics-Strengthened Saturated Cushion Layer in Disconnected Piled-Raft System under Seismic Loading. Indian Geotechnical Journal. 2024. DOI: 10.1007/s40098-024-00877-x

25. AlSaadi, K.A., Almurshedi, A.D., Karkush, M. Effect of Geosynthetics-Reinforced Cushion on the Behavior of Partial Connected Piled Raft Foundation in Dry and Saturated Sandy Soil Using Shaking Table. Indian Geotechnical Journal. 2024. DOI: 10.1007/s40098-024-00890-0

Information about authors:

Mahdi Karkush, *Doctor of Technical Sciences*
ORCID: https://orcid.org/0000-0003-1304-0303
E-mail: mahdi_karkush@yahoo.com

Amer G. Jihad,
E-mail: amer.ghani@qu.edu.iq

Research article

Non-combustible composite materials for fire curtains: thermal analysis and microscopy

M.V. Gravit [iD] *, I.L. Kotlyarskaya* ✉ [iD] *, D.I. Abdulova*

Peter the Great St. Petersburg Polytechnic University, St. Petersburg, Russian Federation

✉ *vasilieva_il@spbstu.ru*

Abstract. Fire protection systems are used to prevent fires and the spread of combustion products from one room to another. The systems include screens, curtains, drapes, etc. The article is devoted to the study of fire resistance and thermoanalytical properties of non-combustible materials used in passive fire protection system. Samples based on silica mat (No. 1); ultrafine basalt fiber (No. 2); quartz aerogel (No. 3), and ceramic mat (No. 4) were studied. Sample No. 1 was covered with carbon impregnated fabric. Samples No. 2, 3, 4 were covered with silica fabric with vermiculite coating. During standard fire test, all samples showed fire resistance limit (FRL) E 60. In terms of thermal insulation capacity, sample No. 2 turned out to be the best with the FRL I 30. Thermoanalytical study showed that the maximum weight loss (12.7 %) was recorded in sample No. 1. The minimum weight loss (0.823 %) was recorded in sample No. 2 in a nitrogen atmosphere. Thus, the material filled with ultrafine basalt fiber showed the best results, and it is recommended to be used as part of fire barriers to create fire-resistant casings, covers and fire-resistant curtains.

1. Introduction

With population growth and urbanization, the problem of fire safety of buildings is becoming more acute. 21st century buildings are characterized by a variety of geometries, large volume of rooms, high heights, open spaces, dynamic and glass facades, etc., but these complex elements and structures can be a weak point in terms of fire safety. In the last decade, there is a trend towards underground construction of shopping malls, warehouses, subway lobbies, and parking lots, from where timely evacuation in case of fire is quite difficult [1, 2]. In this regard, when designing buildings, it is necessary to take into account all measures to prevent fire and be able to manage the growth and consequences of accidental or intentional fires. In the regulatory aspect, fire safety of buildings is ensured through a combination of active and passive fire protection systems. Active fire protection systems (sprinklers, heat and smoke sensors, etc.) are designed to detect and control or extinguish a fire at its initial stage [3, 4]. Passive fire protection systems (load and non-load bearing elements of the building) are designed to ensure the stability of the building

during fire exposure and to contain its spread. The main purpose of a passive fire protection system is to provide sufficient time for extinguishing fire and rescue operations, as well as to minimize monetary losses [5]. Transformable fire barriers (TFBs) are the most innovative and advanced fire protection solution and combine both systems. For the effective functioning of flexible TFBs, the correct choice of materials and design solutions is of great importance. The fire barrier must meet the required fire resistance parameters, have a low density (light weight) and a small thickness so that it can be easily rolled up and rolled out.

Such products are a type of building structures that have a standardized fire resistance limit (FRL) and a class of structural fire hazard, and their main feature is the ability of the enclosing part of the structure to roll up and roll out. TFBs are adaptive structures, as they are able to adapt to changing conditions and come into action automatically after the fire alarm is activated. These structures are installed in wall openings as partitions and ceilings, effectively separating rooms from each other and providing protection from the spread of fire and combustion products (Fig. 1).

For example, they are actively used in large shopping malls because they do not block the view of goods, unlike stationary massive fire barriers [6].
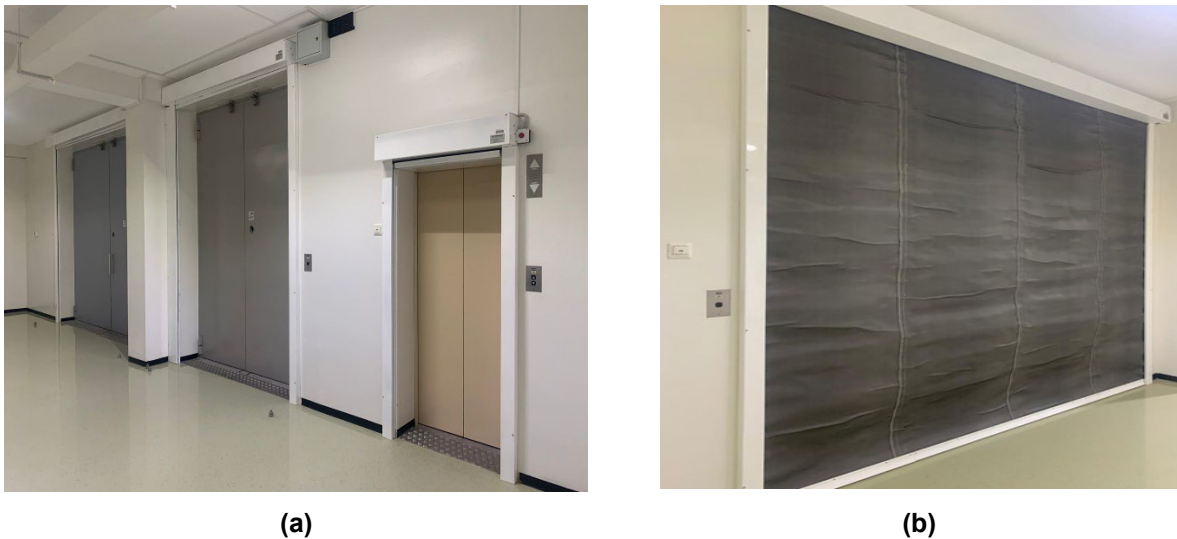

| (a) | (b) |

Figure 1. Fire curtains (a) rolled up (b) rolled out. Photo by the authors.

Fire barriers are also used in rooms where, for one reason or another, there is no possibility of emergency evacuation. One example of such premises is hospital wards, where patients are in different states of health, which affects their ability to move quickly [7]. Fire barriers are effectively used in a road tunnel in Moscow to divide it into fire compartments and organize smoke zones [8], as well as in public buildings, such as shopping malls and hotels [9, 10].

According to paragraph 2 of Article 88 of Federal Law No. 123-FZ [11], "fire resistance limits and types of building structures that perform the functions of fire barriers, the corresponding types of filling of openings and airlocks are given in Table 23 of the appendix to this Federal Law".

According to paragraph 3 of Article 88 of the Federal Law No. 123-FZ [11], "fire resistance limits for the corresponding types of filling of openings in fire barriers are given in Table 24 of the appendix to this Federal Law".

Fire curtains, according to Table 24 of the appendix of the Federal Law No. 123-FZ, belong to the first type of filling openings in fire barriers, therefore their FRL must be at least EI 60. Blinds and screens can be of types 1, 2, 3 and their FRL can be, respectively, E 60, E 30, E 15.

The article [12] presents a version of fireproof curtain with the following composition: fiberglass, mesh with intumescent composition, foil material (total thickness of the curtain is 12 mm), with FRL when exposed to standard temperature conditions E 60 (loss of integrity) and I 15 (loss of thermal insulation capacity) according to the national standard of the Russian Federation GOST R 53307–2009 "Elements of building constructions. Fire doors and gates. Fire resistance test method" [13].

Fire curtains should not be a source of smoke and toxic gaseous substances, so the use of non-combustible materials for fire curtains is a great advantage [14, 15].

The article [16] describes an experiment with curtain walling, which are designed to prevent the spread of fire, as well as to ensure the safe evacuation of people. Four panels with overall dimensions of 1000 × 1000 mm and a thickness of about 30 mm each were installed as a thermal insulation sheathing on the heated side of the structure. Each of the panels consisted of two layers of rolled, foil-coated basalt fire-

retardant material MBOR-5F, glued together (with non-foil sides) with a fire retardant compound OVPF-1M. Fire retardant consumption is 8.0–8.7 kg/m^2.

In our article we would like to discuss passive fire protection measures using non-combustible materials based on silica mat, basalt ultrafine fiber, quartz aerogel, and ceramic mat. Each of these materials is unique. The disadvantages of such materials include relatively high cost, high adsorption of dust and gases, and relatively large thickness (for example, in comparison with thin-layer coatings).

A distinctive feature of silica materials is their good stability at high temperatures and under oxidizing conditions, therefore they are effectively used in the construction industry as electrolytes [17], adsorbents of hazardous pollutants [18], fire-resistant aggregates [19] and in thermal insulation mortars [20].

The main advantages of ultrafine basalt fiber include: production exclusively from basalts without admixtures of other minerals, good thermal insulation properties, lack of combustibility, high thermal and chemical resistance, preservation of its characteristics and geometric shape under sudden temperature changes and durability of operation, even in a humid environments [21].

One of the promising developments in the construction market is a non-combustible nanomaterial aerogel and materials based on it. In its natural form it is transparent (Fig. 2a, 2b), and then with special processing it is applied to fabric (fiberglass, basalt or carbon) and delivered to the construction site already in the form of a roll (Fig. 2c). Aerogel in its natural form has a low coefficient of thermal conductivity 0.014 W/m·K at 10 °C [22]. Aerogel as a thermal insulating material was used in the "Space Shuttle" orbital craft, "Mars Pathfinder," and "Spirit" rovers [23]. Aerogel-based roll materials are used as heat insulators of steel pipelines, buildings and structures [24, 25].
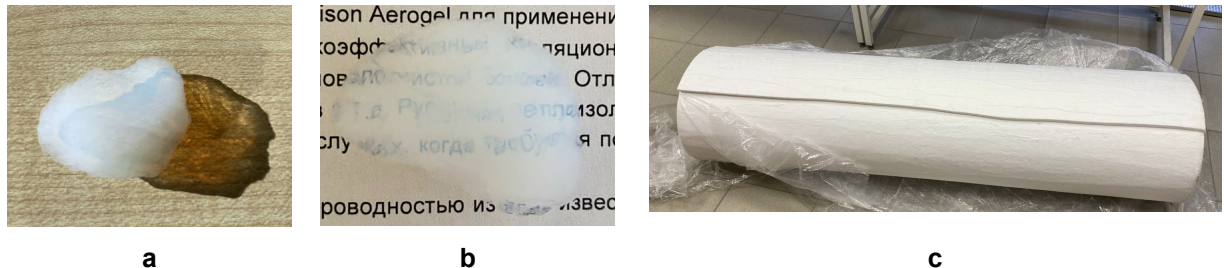

a **b** **c**

Figure 2. Aerogel (a) (b) in its natural state (c) on fabric material as a roll. Photo by the authors.

Ceramic fibers are promising materials as reinforcement materials for composite materials in the industry of high-temperature structural materials [26, 27].

The listed non-combustible materials in combination with non-combustible lining fabric, usually silica [12], form a fire-resistant fabric and can be part of fire curtains, screens, covers, caps, etc.

The purpose of this work is to FRL of the materials under study when the temperature changes by an average of 140 °C for 60 minutes on an unheated surface.

To achieve this goal, the following tasks were solved:

− standard fire tests for four thermal insulation non-combustible materials were conducted;

− thermoanalytical dependencies and microscopic photography of material samples before and after fire tests were obtained.

It is expected that the minimal mass loss during thermal analysis and the preservation of physical characteristics visible under microscopy in micro-samples will be reflected in the fire resistance characteristics of compositions made from such materials for fire curtains.

2. Method and Materials

2.1. Materials

All materials were commercially available technical products. Characteristics of the tested samples are shown in Table 1. Sample No. 1 consists of silica fabric from the company "Beltekhnolit" [28], and the filler is a mat "Supersilica" from "RLB Silica" [29]. Sample No. 2 consists of a lining silica fabric with vermiculite coating PS-1000V from the manufacturer "Polotsk-Steklovolokno" [30], and as a filler a layer of fire retardant material OBM-5 from "Votkinsk plant of thermal insulation materials VZTM" [31] is used. In samples No. 2, 3, 4, the same lining fabrics were used. The filler in sample No. 3 is a silica-based aerogel Insuflex 650 from the Chinese manufacturer NINBO EAS MATERIAL TECHNOLOGY CO., LTD (official representative in Russia of ETS Korda LLC [32]), and in sample No. 4, the filler is refractory ceramic material

in a roll from "Sukholozhsky Refractory Plant" [33]. The fabric and the filler are connected to each other by an aramid thread with a metal core [34].

Table 1. Characteristics of fillers of tested samples.

Samples	Filler	Thickness, mm	Weight, kg/m^2
No. 1	Silica mat Supersilica S	6.5–7	2.9
No. 2	Basalt superfine fibers OBM-5	6.5–7	2.5
No. 3	Silica-based aerogel Insuflex 650	11.5–12	4
No. 4	Ceramic mat	6.5–7	2.8

For sample No. 1, the fabric contained dressed carbon fibre in black color. Finishing of carbon fibers is carried out in order to increase its strength, as well as to improve its compatibility with the binder and increase the physical and mechanical characteristics of composite materials obtained from fibers, which can be used in various industries to create products and structural elements exposed to elevated temperatures [35]. The filler in sample No. 1 is silica needle-punched mat Super Silica S (with thickness of 4–6 mm), which is produced from silicon oxide fibers (96 %) without chemical binder. The innovative technology of silica materials production is based on the aerodynamic method of fiber layout, which ensures uniform weaving of canvas by needle-punching matrixes, without binders and additives. The thread is aramid with a metal core.

Samples No. 2, 3 and 4 were reinforced by V-spraying of an aqueous dispersion of vermiculite to the fabric. Heat resistance of the fabric is 900 °C, at short-term use is 1350 °C. In sample No. 2, as a filler with thickness of 5 ± 1.9 mm the fireproof material OBM-5 made of basalt superfine fiber was used. In the sample No. 3, the aerogel based on quartz Insuflex 650 was used. The thickness of the layer is equal to 10 mm. Sample No. 4 consists of silica fibers compressed into roll of fabric, with the density of 96 kg/m^3, produced by Sukholozhsky Refractory Plant, with vermiculite coating PS-1000V. The main characteristics of the materials are shown in Tables 2 and 3. This information is extracted from the official websites of material manufacturers.

Table 2. Material characteristics of the tested samples [29, 31–33].

Characteristics	Sample No. 1	Sample No. 2	Sample No. 3	Sample No. 4
Filler density, kg/m^3	160	70–100	200	96
Chemical composition of lining fabric, %	Na_2O (0.33–0.8), Si_2O (94–95.9)	SiO_2(98)	SiO_2(98)	SiO_2(9)
Heat resistance, °C	1200–1700	900–1350	900–1350	900–1350

Table 3. Thermal conductivity of filler material, W/(m·K) [29, 31–33].

Temperature, °C	25	125	200	300	400	600	800	1000
Sample No. 1								0.34
Sample No. 2	0.035	0.055		0.095				
Sample No. 3			0.022	0.025	0.029		0.065	
Sample No. 4			0.05		0.07	0.12	0.18	0.27

2.2. Methods

2.2.1. Thermal analysis tests

According to the national standard of the Russian Federation GOST 53293–2009 "Fire hazard of substances and materials. Materials, substance and fire protective means. Identification by thermal analysis methods" [36], thermal analysis includes the following methods:

– thermogravimetric analysis (TGA);
– thermogravimetric by derivative (derivative thermogravimetry (DTG));
– differential thermal analysis (DTA) or differential scanning calorimetry (DSC).

The STA 6000 synchronous thermal analyzer was used for thermal analysis (PerkinElmer, USA) [37]. The thermal analyzer is a measuring complex that combines the functions of a differential scanning calorimeter and highly sensitive analytical scales. This design solution allows to carry out simultaneously in one experiment and one sample measurements of calorimetric values at different thermodynamic transitions, to measure the temperature of these transitions and to register at the same time changes in the sample mass. The main technical characteristics of the STA 6000 analyzer are shown in Table 4 [38].

Table 4. Technical Specifications STA 6000.

Temperature range	15 °C to 1000 °C
Weight measurement range / sensitivity	1500 mg / 0.1 µg
Calorimetric accuracy / reproducibility	± 2 %
Scanning speed	0.1 °/min to 100 °/min
Cooling time	1000 °C to 100 °C – less than 12 min
Sample crucibles	Al_2O_3, 180 µl
Cooling	air, liquid
Gas flow controller	for 2 gases, automatic switching

The following study conditions were chosen for thermogravimetric analysis: atmosphere (air or nitrogen), initial temperature 30 °C, final temperature 900 °C, gas flow rate – 60 ml/min, heating rate 20 °C/min. Samples of materials before and after the fire test were subjected to the study.

2.2.2. Microscopy

To conduct a microscopic examination of the fillers, an Altami SM0745 stereomicroscope (Russian Federation) was used. The device is designed to observe three-dimensional images of objects in reflected or transmitted light.

The images were taken under the following conditions: without heating (25 °C) and with heating the sample to a temperature of 1050 °C and maintaining it for 30 minutes.

2.2.3. Fire tests

Elements of fire curtains were tested according to the national standard of the Russian Federation GOST 53307–2009 "Elements of building constructions. Fire doors and gates. Fire resistance test method" [13];

The limiting state of loss of integrity (E) is achieved as a result of the formation of through cracks or holes (slits) in the structure through which the products of combustion or flame penetrate, namely:

- the appearance of a stable flame on the unheated surface of the prototype lasting 10 seconds or more;
- fire or smoldering with glow of a cotton swab as a result of exposure to fire or hot gases within 10 seconds after being brought to the prototype;
- formation of through holes in the construction of the prototype with dimensions that ensure penetration of a probe with a diameter of 6 mm and movement along the hole to a distance of at least 150 mm or unhindered penetration of a probe with a diameter of 25 mm into the through hole;
- falling out of the sample mesh from the box or the box itself from the enclosing structure.

Achieving the limiting state for loss of thermal insulation capacity (I) occurs due to an increase in the temperature on the unheated surface of the samples by an average of more than 140 °C compared to the temperature of the surface of the prototype (taking into account the temperature at the beginning of the test) [13].

The samples were tested using a vertical firing furnace (installation) with fuel supply and combustion system (Fig. 3a). The size of the furnace opening was 2.45 × 2.5 m and provided the possibility of simultaneous testing of four samples with design dimensions of 1 × 1 m. Before installation, the combined fabric was assembled from samples No. 1–4 on the stand and mounted on the frame (Fig. 3b).

a   b

Figure 3. Preparation for the test: a) furnace; b) assembly of the combined web on the stand.

The temperature regime in the firing chambers of the furnace was ensured by burning natural gas. The temperature of the medium in the fire chamber of the furnace was measured by thermoelectric converters (thermocouples). The average temperature on the unheated surface of the enclosing structure samples was determined as the arithmetic mean of the thermocouple readings. The experiment used sensors (thermocouples) TPL011–0.5/1.5, which were located on the surface of the fabric according to the following principles:

a) a thermocouple in the center of the fabric section(s) of the prototype;

b) a thermocouple in the center of each quarter of the fabric section(s) of the prototype.

For every 1.5 m^2 of furnace opening intended for testing enclosing structures, at least one thermocouple must be installed. After installing the sensors, the frame with the combined sheet was placed in the furnace opening for fire test (Fig. 4).

a   b

Figure 4. Installation of the combined sheet in the furnace opening:
(a) appearance of the sheet before testing with attached thermocouples (b) side view.

A standard temperature regime was created in the furnace, characterized by the following relationship:

$$T - T_0 = 345 \cdot \log_{10}\left(8t + 1\right),$$ (1)

where T is temperature in the furnace corresponding to time t, °C; T_0 is temperature in the furnace before the start of heat exposure t, °C; t is time calculated from the beginning of the test, min.

The test conditions are shown in Table 6.

Table 6. Test conditions.

Parameter	Value
Ambient temperature, °C	23
Atmospheric pressure, kPa	99.8
Relative air humidity, %	49.6
Air velocity, m/sec	0.1

3.   Results and Discussion

3.1.   Results of thermal analysis before fire tests

The results of thermal analysis of samples No. 1–4 before the fire tests are shown in Fig. 5–8. The thermoanalytical curves in the figures are designated as follows: DSC – red, DTG – blue and TG – blue, going down. The images are arranged in the following order: air atmosphere tests (top), nitrogen atmosphere tests (bottom).
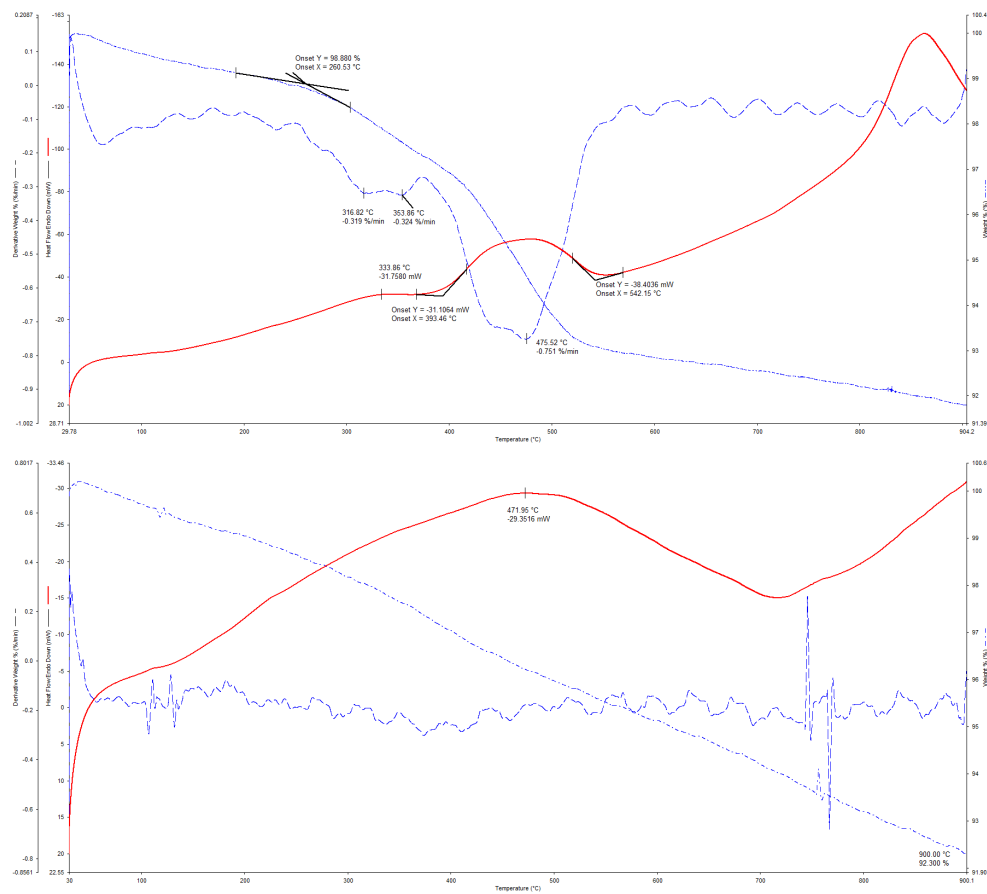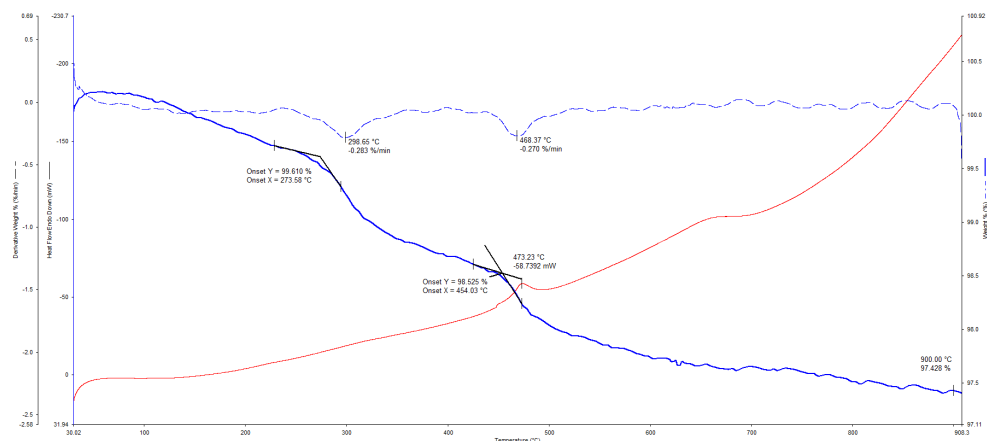

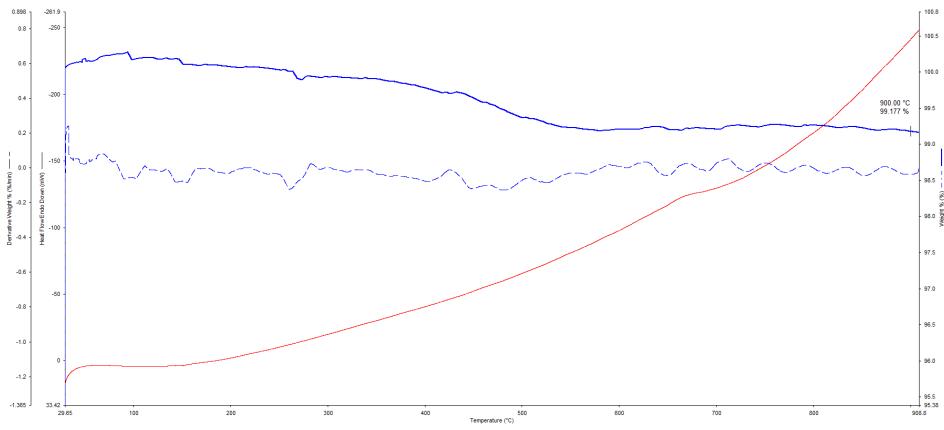**Figure 5. TA-curves for sample No.1: in air atmosphere and in nitrogen atmosphere.**

Figure 6. TA-curves for sample No. 2: in air atmosphere and in nitrogen atmosphere.
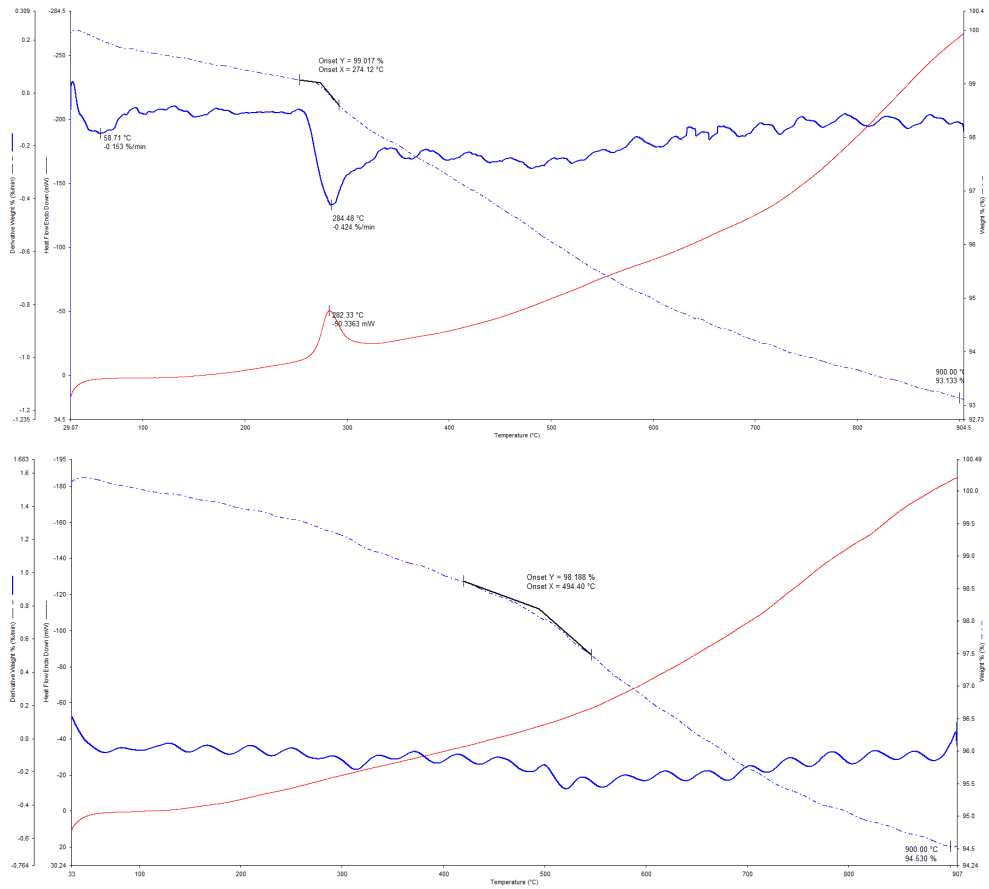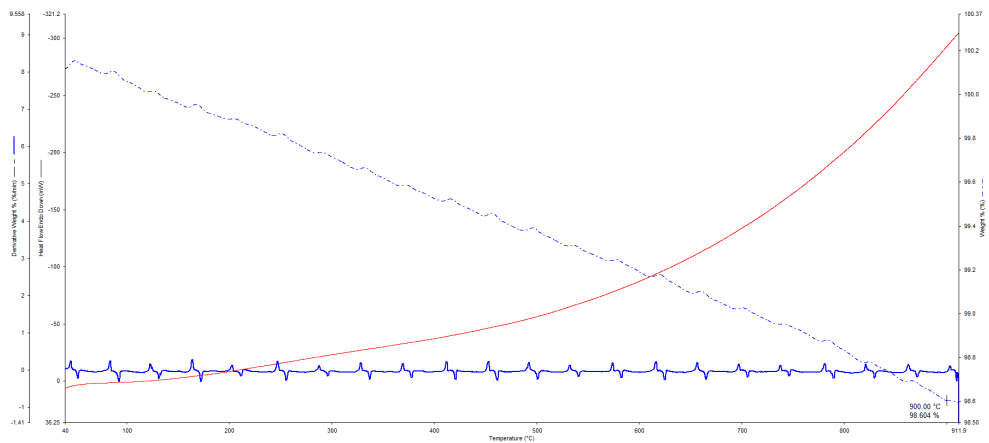

Figure 7. TA-curves for sample No. 3: in air atmosphere and in nitrogen atmosphere.
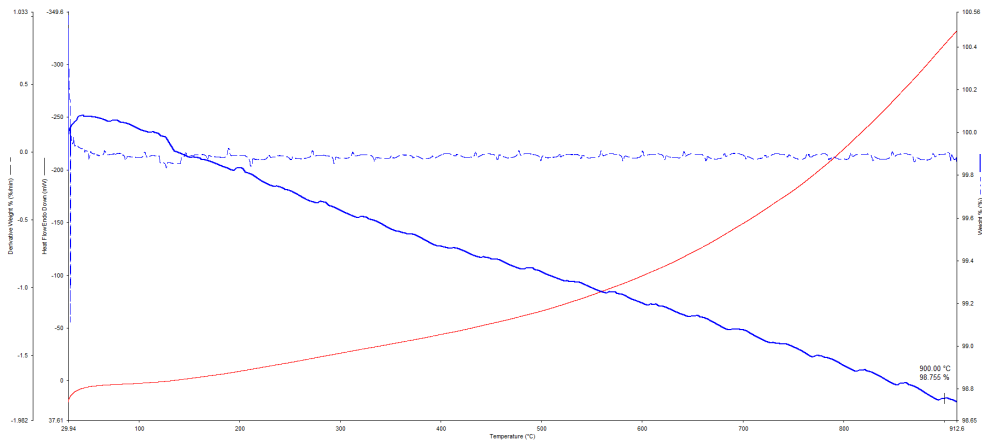
Figure 8. TA-curves for sample No. 4: in air atmosphere and in nitrogen atmosphere.

At constant linear heating to 900 °C, the maximum weight loss was recorded for sample No. 1 in nitrogen atmosphere (7.7 %). In air atmosphere, the greatest weight loss was recorded for sample No. 3 (6.8 %). The weight loss indicates that intensive reactions occurred in the samples, which led to the destruction of the samples. The smallest weight loss was recorded for sample No. 2 in nitrogen atmosphere. It amounted to only 0.823 %. In air atmosphere, the least weight loss was recorded for sample No. 4 (1.3 %).

Peaks of exothermic reactions were detected on DSC-curves only for samples in an air atmosphere, which indicates the occurrence of oxidative processes in the samples. Oxidative decomposition of the binder occurs. For sample No. 3, taken prior to the fire test, the exothermic peak on the DSC-curve occurs at a temperature of 282.33 °C. The best performance during standard tests was predicted for sample No. 2.

3.2. Results of microscopic examination of sample fillers prior fire tests

Before the fire test, the fillers of the studied samples No. 1–4 were examined using an Altami SM0745T microscope (Fig. 9–12). Magnification 30x.
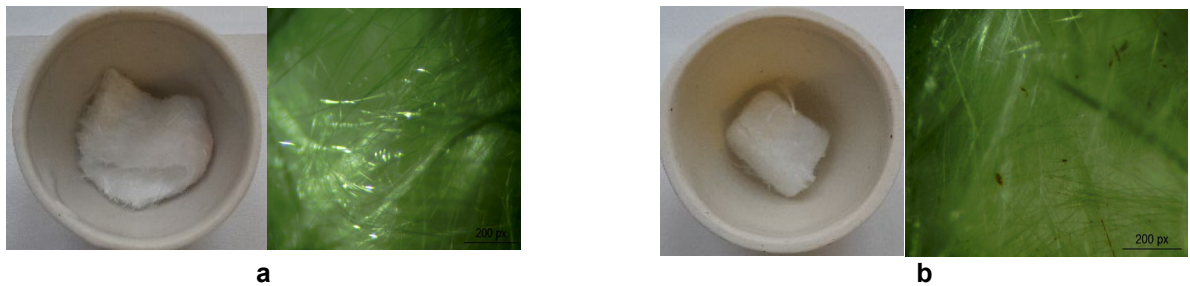

a   b
Figure 9. Sample No. 1: 25 °C (a) and 1050 °C, 30 min (b).

a   b
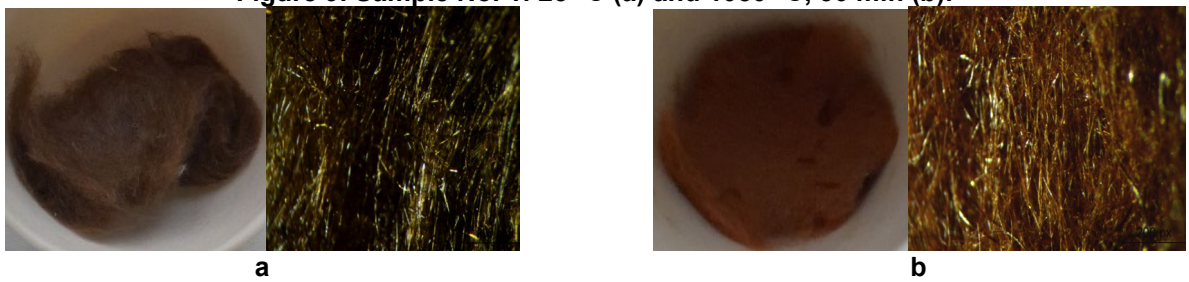**Figure 10. Sample No. 2: 25 °C (a) and 1050 °C, 30 min (b).**

a   b
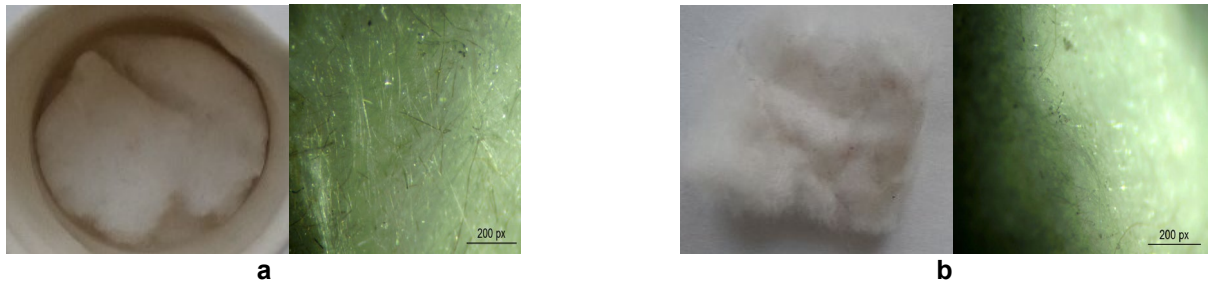**Figure 11. Sample No. 3: 25 °C (a) and 1050 °C, 30 min (b).**

a **b**
Figure 12. Sample No. 4: 25 °C (a) and 1050 °C, 30 min (b).

As follows from the physicochemical characteristics of basalt [39] and ceramic fibers (Table 1), up to a temperature of 1200 °C only softening of the mineral phases of basalt and ceramic fibers can be observed. As follows from Fig. 9–12, the structure under the microscope has not undergone visible changes. The following transformations were recorded: small inclusions appear, the samples become green and brown, and small phenocrysts of the incipient melt are clearly visible against the background of the total mass of the glass-fibrous structure. Oven temperatures during standard tests reach 900–950 °C for 60 minutes, and therefore discoloration is expected on composite sheets containing these thermal insulation materials.

3.3. Results of fire tests

During the testing, all possible changes in the appearance and condition of the samples were recorded. At the 21st minute, smoke from sample No. 3 was noticed. At the 25th minute, the smoke stopped, and barely noticeable green stripes and areas began to appear on samples No. 2 and 3 (Fig. 13a); over time, the stripes and areas became brighter and larger (Fig. 13b). At the 34th minute, the green area on sample No. 2 became more significant, it occupied the upper right corner, the green area on sample No. 3 grew more slowly. At the 34th minute, a brown area and a stripe also appeared on samples No. 2 and No. 4. At 45 minutes, the brown areas became larger. The test was stopped at the 60th minute on instructions from the technical customer, but observation continued. At the 65th minute, the upper right corner of sample No. 2 turned brown, and almost the entire rest of the canvas became green. Sample No. 4 also became almost entirely green, except for a wide brown stripe in the central part of the canvas. The upper half of sample No. 3 also became light green (Fig. 13c). At the 73rd minute, there were more brown areas on samples No. 2 and 4; on sample No. 3 the green area began to occupy two-thirds of the sample area (Fig. 13d).
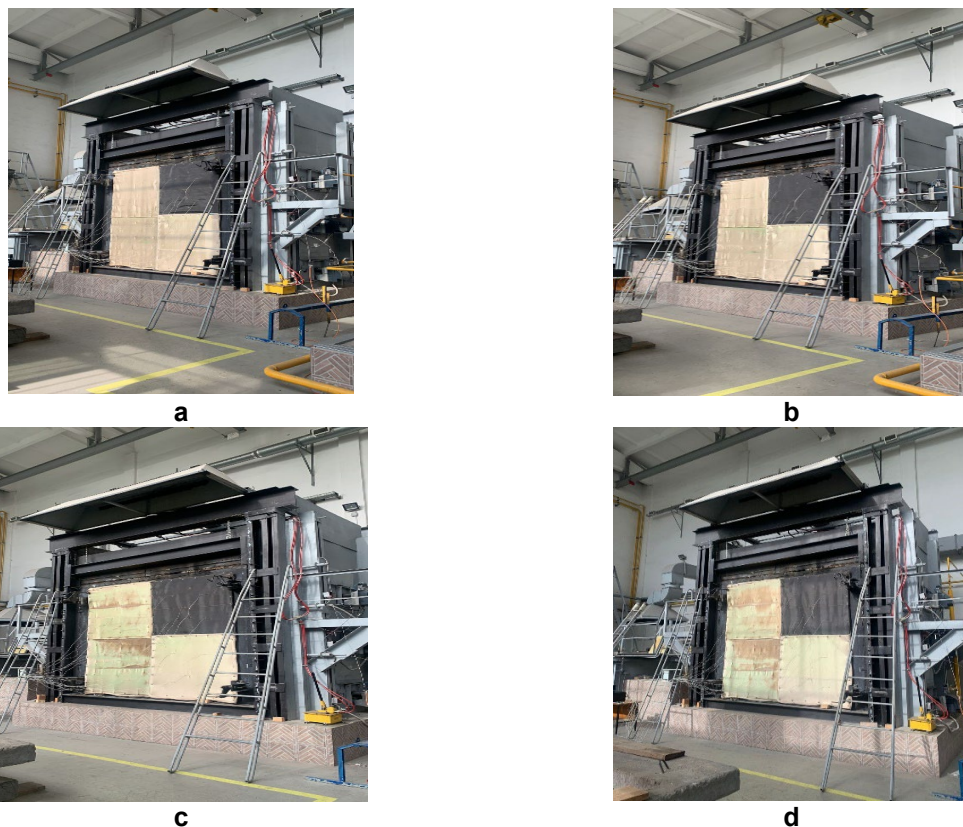

a **b**

c **d**

Fig. 13. Testing of samples: a) at the 25th minute of fire exposure; b) at the 29th minute of fire exposure; c) at the 65th minute of fire exposure; d) at the 73rd minute of fire exposure.

No through cracks, holes, or stable flames were found on the surface of the samples during testing, i.e. all samples retained their integrity, and the integrity FRL of E 60 was achieved.

Based on the results of recorded temperatures from sensors, graphs of temperature versus time were constructed (Fig. 14). The initial temperature of the samples was 23 °C.
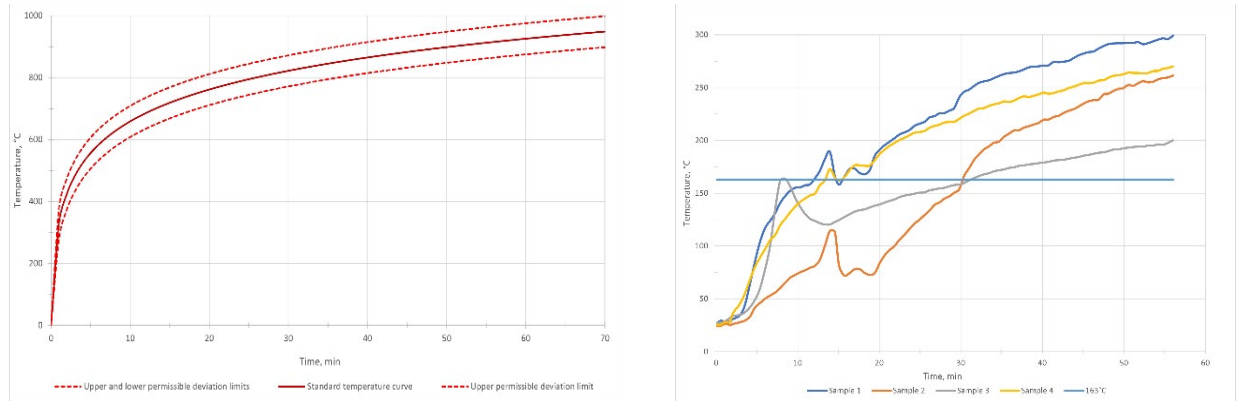

**Figure 14. Temperature curves for heating the medium in the furnace (left)
and experimental temperature curves for samples No. 1–4 (right).**

According to Fig. 14, sample No. 2, consisting of a PS-1000V vermiculite-coated silica lined fabric with basalt filler, showed the best value of thermal insulation capacity FRL I 30 (the specimen reached a temperature of 163 °C at the 1863rd second, i.e. 31st minute). Sample No. 3, consisting of a PS-1000V vermiculite-coated silica cladding fabric with aerogel filler, performed the worst; it lost its thermal insulation capacity at the 496th second, i.e. 8th minute.

Looking at the temperature values from each thermocouple individually, rather than the arithmetic average, the same conclusion can be drawn. Sample No. 2 reached 163 °C later than the other samples, and sample No. 3 reached 163 °C correspondingly earlier than all other samples.

After dismantling the structure, each sample was examined individually, and small pieces of the tested webs were taken for further studies of the properties of fire protection materials based on silica mat, basalt superfine fiber, quartz aerogel, and ceramic mat (Fig. 15).

| a | b | c | d |
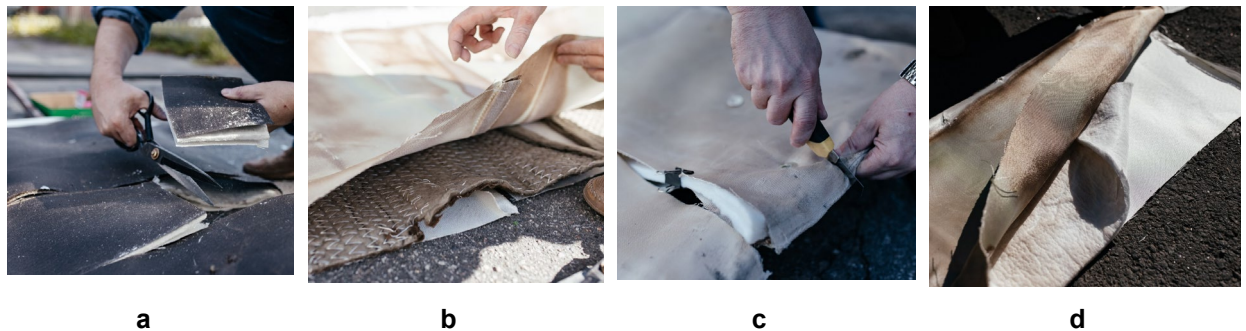
**Figure 15. Inspection of samples after testing: a) sample No. 1; b) sample No. 2; c) sample No. 3;
d) sample No. 4.**

3.4. Results of thermal analysis after the fire tests

The results of thermal analysis of samples No.1–4 after the fire tests are shown in Fig. 16–19. The thermoanalytical curves in the figures are designated as follows: DSC – red, DTG – blue and TG – blue going down. The images are arranged in the following order: air atmosphere tests (top), nitrogen atmosphere tests (bottom).

**Figure 16. TA-curves for sample No. 1 after the fire test:
in air atmosphere and in nitrogen atmosphere.**

**Figure 17. TA-curves for sample No. 2 after the fire test:
in air atmosphere and in nitrogen atmosphere.**

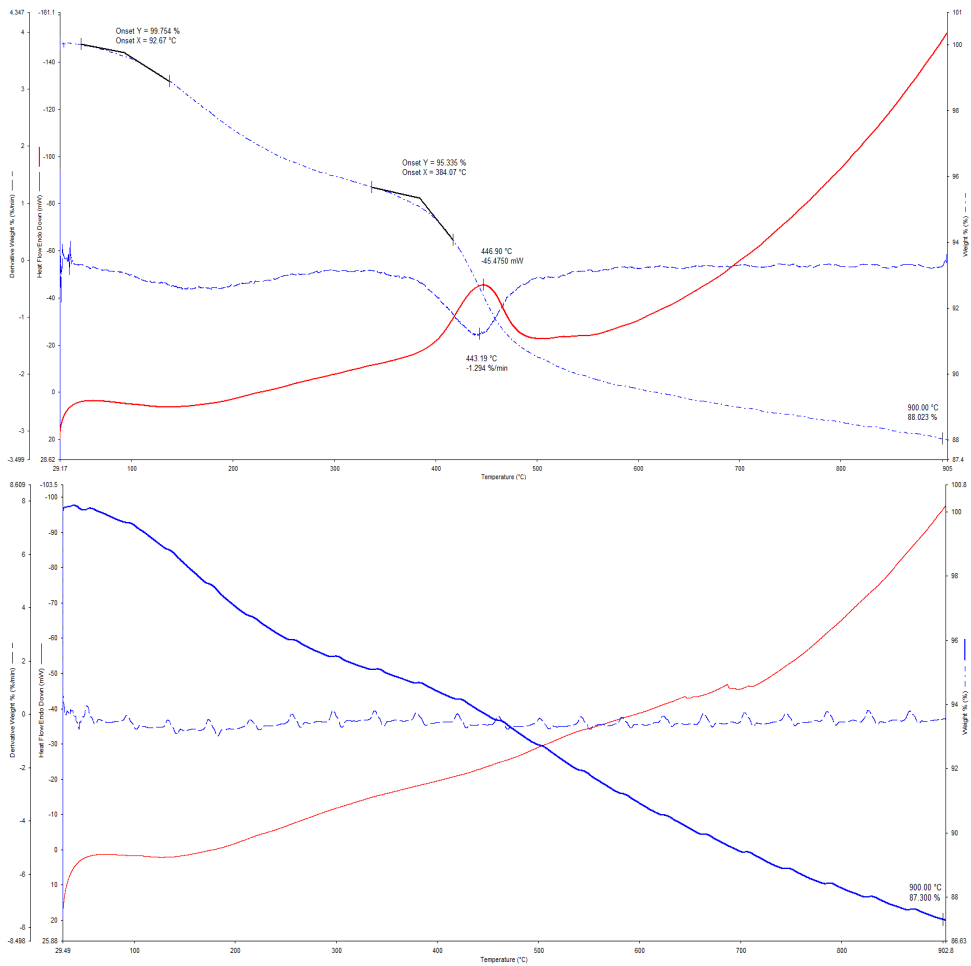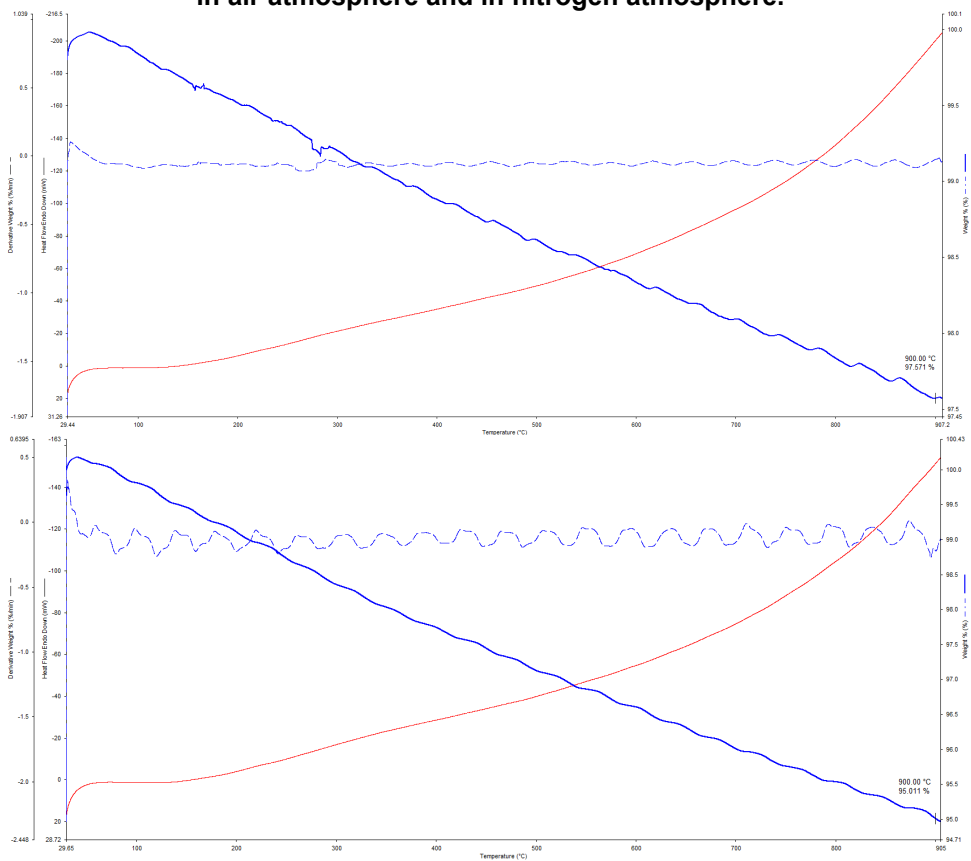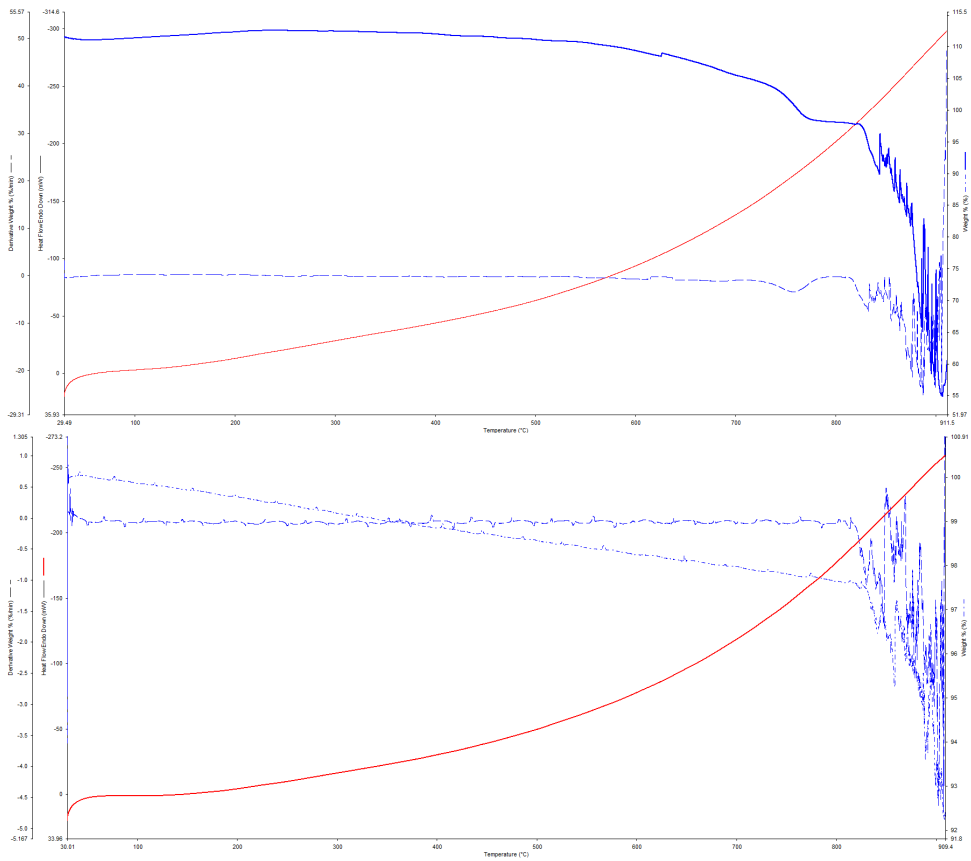**Figure 18. TA-curves for sample No. 3 after the fire test:
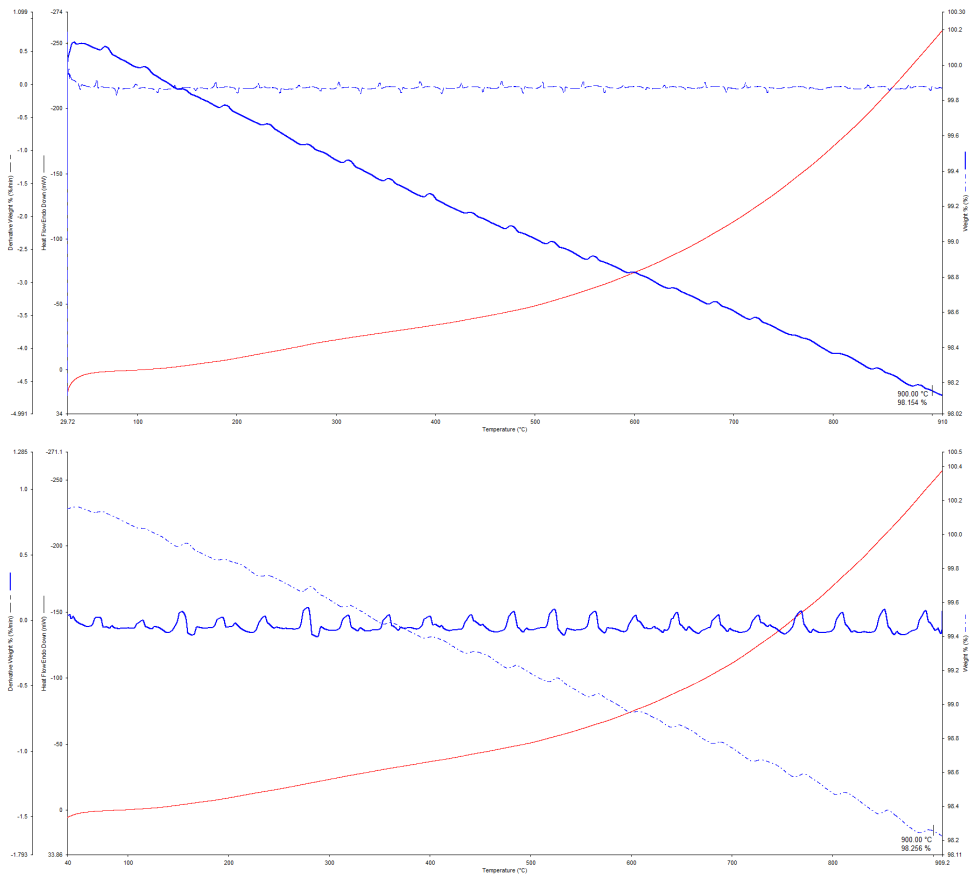in air atmosphere and in nitrogen atmosphere.**

**Figure 19. TA-curves for sample No. 4 after the fire test:
in air atmosphere and in nitrogen atmosphere.**

The samples studied earlier in the fire test were subjected to linear heating, i.e. re-tested at high temperatures. Linear heating showed that all specimens had also reduced their mass. Compared to the heating of samples not previously fire tested (paragraph 3.1), the weight of samples had changed more significantly the second time. The maximum weight loss was shown by sample No. 1 in nitrogen atmosphere. Its weight decreased by 12.7 %. In air atmosphere it also showed the highest weight reduction (11.9 %). After the fire test, thermogravimetric analysis showed the least weight loss in sample No. 4 at 1.744 % in nitrogen atmosphere. In air atmosphere it also showed the lowest value of weight reduction (1.8 %).

Thus, the fire-tested samples show greater weight loss on heating, but the weight loss values are similar for both air and nitrogen atmospheres.

4. Conclusions

Modern thermal insulation materials with the minimum possible technological thickness (5–7 mm) have been studied to obtain satisfactory characteristics for loss of integrity and thermal insulation capacity of a fire-resistant fabric. Such composite fabrics can be used for fire-resistant curtains, covers, casings in fire barriers and protecting products from fire. It is necessary that, with the required fire resistance, such composite materials can be rolled up and rolled out, i.e. would not be very thick.

Before the fire test, the maximum weight loss during thermal analysis during heating was shown by sample No. 1 in a nitrogen atmosphere, and the smallest minimum was shown by sample No. 2. During linear heating after the fire test, the masses of the samples decreased more significantly in percentage terms. The greatest weight loss was again recorded in sample No. 1, and the smallest in sample No. 4.

As a result of fire tests, it was established that after 60 minutes the presented fire-retardant materials based on silica mat (Sample No. 1), basalt ultrafine fiber (Sample No. 2), silica aerogel (Sample No. 3), and ceramic mat (Sample No. 4) retained their integrity. Thus, samples No. 1–4 have an FRL of E 60. During the fire test, sample No. 1 visually did not undergo any changes, unlike samples No. 2–4. The lining fabric of the listed samples began to change color starting from the 25th minute. Green and brown areas began to appear on the samples. Sample No. 1, in general, showed the worst characteristics both in terms of thermal analysis studies and in terms of loss of thermal insulation capacity.

The best, from the point of view of the obtained thermoanalytical characteristics (minimum mass loss) and further from the point of view of thermal insulation capacity, was sample No. 2, consisting of a lining silica fabric with a vermiculite coating and a basalt filler 7 mm thick. FRL for thermal insulation capacity is I 30. This material is recommended to be used in the future to create fire-resistant enclosures, covers, and fire curtains.

References

1. Yang, F., Qian, X., Huang, P. Fire Safety Assessment of Underground Buildings based on Grey Relational Analysis. Procedia Engineering. 2012. 45. Pp. 89–95. DOI: 10.1016/J.PROENG.2012.08.126

2. Lyu, H.F., Wang, C.P., Deng, J., Xiao, Y., Wang, W.F. Human behaviour and evacuation time for large underground comprehensive buildings during fire risk process. Journal of Loss Prevention in the Process Industries. 2023. 84. Article no. 105134. DOI: 10.1016/J.JLP.2023.105134

3. Kim, T. Optimization of fire sprinkler design for uniform water flux distribution using a micro-genetic algorithm. Fire Safety Journal. 2024. 144. Article no. 104090. DOI: 10.1016/J.FIRESAF.2024.104090

4. Tang, Z., Wang, Z., Chen, R., Fang, Z., Mou, Y., Wei, J., Zhang, C., Wang, Z., Feng, D., Zhang, M., Nie, Y. Experiment study of fire characteristics in full-scale bedrooms under different vents and sprinkler conditions. Fire Safety Journal. 2023. 141. Article no. 103927. DOI: 10.1016/J.FIRESAF.2023.103927

5. Bradley, I., Willoughby, D., Royle, M. A review of the applicability of the jet fire resistance test of passive fire protection materials to a range of release scenarios. Process Safety and Environmental Protection. 2019. 122. Pp. 185–191. DOI: 10.1016/J.PSEP.2018.12.004

6. Chung, D.H., Wang, T.C., Tsai, M.J., Lin, T.H., Lee, S.K. To Enhance the Fire Resistance Performance of High-Speed Steel Roller Door with Water Film System. Advances in Materials Science and Engineering. 2015. Article no. 436406. DOI: 10.1155/2015/436406

7. Kobes, M., Helsloot, I., de Vries, B., Post, J.G. Building safety and human behaviour in fire: A literature review. Fire Safety Journal. 2010. 45(1). Pp. 1–11. DOI: 10.1016/J.FIRESAF.2009.08.005

8. 8. Sokolov, V.P. The Present and the Future of Flexible Mechanical Transformable Smoke Barriers in the Automated Control System of Active Fire Protection. Grani bezopasnosti. 2004. 11. Pp. 36–39.

9. Prisadkov, V.I., Konstantinova, N.I., Muslakova, S. V., Abashkin, A.A. Classification of hotels taking into account fire risks. Pozharovzryvobezopasnost [Fire and Explosion Safety]. 2022. 31(3). Pp. 75–83. DOI: 10.22227/0869-7493.2022.31.03.75-83

10. Muslakova, S.V., Konstantinova, N.I., Prisadkov, V.I. Possibility of using a risk-based approach for accounting fire safety of the hotels when assigning a category. Occupational Safety in industry. 2022. 6. Pp. 75–80. DOI: 10.24000/0409-2961-2022-6-75-80

11. The Federal Law-123 „Technical regulations on fire safety requirements". Available at: https://legalacts.ru/doc/FZ-Teh-reglament-o-trebovanijah-pozharnoj-bezopasnosti/ (accessed 20.03.2024).

12. Gravit, M., Shabunina, D., Nedryshkin, O. The Fire Resistance of Transformable Barriers: Influence of the Large-Scale Factor. Fire. 2023. 6(8). 294. DOI: 10.3390/FIRE6080294

13. Russian State Standard GOST 53307–2009. Elements of building constructions. Fire doors and gates. Fire resistance test method. Available at: https://docs.cntd.ru/document/1200071942 (accessed 06.02.2024).

14. Konstantinova, N.I., Smirnov, N.V., Krivoshapkina, O.V., Molchadskiy, O.I. On the issue of safe use of fiber cement materials in the buildings and structures. Occupational Safety in Industry. 2021. 7. Pp. 31–37. DOI: 10.24000/0409-2961-2021-7-35-41

15. Zuban, A.V., Konstantinova, N.I., Poedintsev, E.A., Smirnov, N.V. Features of fire hazard assessment and selection of thermal insulation materials for pipelines and equipment in the buildings and structure. Occupational Safety in Industry. 2022. 12. Pp. 71–77. DOI: 10.24000/0409-2961-2022-12-71-77

16. Eremina, T.Y., Fadeev, V.E. To the assessment of the possibility of the introduction of curtain walling on objects with mass stay of people. Pozharovzryvobezopasnost [Fire and Explosion Safety]. 2018. 27(2–3). Pp. 57–66. DOI: 10.18322/PVB.2018.27.02-03.57-66

17. Seeber, R., Terzi, F., Zanardi, C. Silica-Based Materials and Derivatives. 2014. Pp. 183–220. DOI: 10.1007/978-3-662-45103-8_7

18. Zdarta, J., Jesionowski, T. Silica and Silica-Based Materials for Biotechnology, Polymer Composites, and Environmental Protection. Materials. 2022. 15(21). Article no. 7703. DOI: 10.3390/MA15217703

19. Najafi, P., Kohnehpooshi, O., Hedayatnasab, A., Parhizkar, T. Fire-resistance behavior of concrete columns produced with recycled ceramic and silica aggregates: An experimental and numerical approach. Construction and Building Materials. 2023. 390. Article no. 131774. DOI: 10.1016/J.CONBUILDMAT.2023.131774

20. Ding, C., Xue, K., Cui, H., Xu, Z., Yang, H., Bao, X., Yi, G. Research on fire resistance of silica fume insulation mortar. Journal of Materials Research and Technology. 2023. 25. Pp. 1273–1288. DOI: 10.1016/J.JMRT.2023.06.004

21. Batiz – Basalt thermal insulation. Available at: http://batis.ru/kompaniya/eto-interesno/30-sravnitelnaya-kharakteristika-teploizolyatsionnoj-vaty-poluchennoj-iz-razlichnogo-syrya/ (accessed 24.01.2024).

22. Vasileva, I., Nemova, D., Kotov, E., Andreeva, D., Ali, M. Al. The Use of Aerogel in Building Envelopes. Lecture Notes in Civil Engineering. 2020. 70. Pp. 793–802. DOI: 10.1007/978-3-030-42351-3_69

23. Ivanov, N.N., Ivanov, A.N. A sensor for the spatial registration and measurement of particles parameters in near and deep space – Experimental investigation of SiO2-aerogel characteristics. Solar System Research. 2014. 48(7). Pp. 549–554. DOI: 10.1134/S0038094614070090/METRICS

24. Kotlyarskaya (Vasileva), I.L., Vatin, N.I., Nemova, D.V. Thermal conductivity of aerogel thermal insulation under stationary thermal conditions. Construction of Unique Buildings and Structures. 2022. 104(5). Pp. 10303–10303. DOI: 10.4123/CUBS.103.3

25. Almeida, M., Kotov, E.V., Nemova, D., Sergeev, V., Dontsova, A., Koriakovtseva, T., Andreeva, D. Thermal Performance Assessment of Aerogel Application in Additive Construction of Energy-Efficient Buildings. Sustainability. 2024. 16(6). Article no. 2398. DOI: 10.3390/SU16062398

26. Ishikawa, T. Ceramic Fibers and Their Applications. Ceramic Fibers and Their Applications. New York: Jenny Stanford Publishing, 2019. DOI: 10.1201/9780429341885

27. Amir, N., Othman, W.M.S.W., Ahmad, F. Fire resistance properties of ceramic wool fiber reinforced intumescent coatings. AIP Conference Proceedings. 2015. 1669 (1). DOI: 10.1063/1.4919200

28. Beltekhnolit product catalog. Available at: http://bellit.ru/katalog-produktsii.php (accessed 6.02.2024).

29. SuperSilika, production of fire-resistant fabrics and mats. Available at: https://supersilika.ru/ (accessed 6.02.2024).

30. Open Joint Stock Company "Polotsk-Steklovolokno" is a manufacturer of fiberglass in Belarus. Polotsk-Steklovolokno. Available at: https://www.polotsk-psv.by/ (accessed 6.02.2024).

31. Votkinsk Thermal Insulation Materials Plant. Available at: https://www.vztm.ru/ (accessed 6.02.2024).

32. Thermal insulation. Fire protection. Refractories. Construction Materials. Corda. Available at: https://www.rosizol.com/ (accessed 6.02.2024).

33. JSC Sukholozhsky Refractory Plant. Available at: https://slsoz.ru/ (accessed 6.02.2024).

34. Zhang, B., Jia, L., Tian, M., Ning, N., Zhang, L., Wang, W. Surface and interface modification of aramid fiber and its reinforcement for polymer composites: A review. European Polymer Journal. 2021. 147. Article no. 110352. DOI: 10.1016/J.EURPOLYMJ.2021.110352

35. The Patent No. RU2694030C2. Dressed carbon fiber and method for production thereof. Application date: 31.10.2017. Publication date: 08.07.2019. Bulgakov, B.A., Babkin, A.V., Kepman, A.V., Avdeev, V.V., Korotkov, R.F. Application filed by Institut novyh uglerodnyh materialov i tekhnologij.

36. Nacional'nyj Standart Rossijskoj Federacii GOST 53293–2009. Fire hazard of substances and materials. Materials, substance and fire protective means. Identification by thermal analysis methods. 2011. Available at: https://docs.cntd.ru/document/1200071912 (accessed: 2.02.2024).

37. STA 6000 Simultaneous Thermal Analyzer Brochure – PerkinElmer – PDF Catalogs | Technical Documentation | Brochure. Available at: https://pdf.directindustry.com/pdf/perkinelmer/sta-6000-simultaneous-thermal-analyzer-brochure/14711-629925.html (accessed 3.01.2024).

38. Synchronous thermal analyzer STA 6000 (PerkinElmer, USA). Available at: https://techob.ru/katalog/katalog-priborov/kalorimetriya,-termoanaliz/termogravimetricheskie-analizatoryi-perkinelmer/analizator-sta-6000.html (accessed 6.02.2024).

39. The Patent No. RU2297986C1. Method of the basaltic raw melting. Application date: 21.02.2006. Publication date 27.04.2007. Babievskaja, I.Z., Gavrichev, K.S., Dergacheva, N.P., Drobot, N.F., Ermakov, V.A., Krenev, V.A., Kuznetsov, N.T., Novotortsev, V.M. Application filed by Kurnakov Institute of General and Inorganic Chemistry of the Russian Academy of Sciences (IGIC RAS).

Information about authors:

Marina Gravit, *PhD in Technical Sciences*
ORCID: https://orcid.org/0000–0003–1071–427X
E-mail: marina.gravit@mail.ru

Irina Kotlyarskaya,
ORCID: *https://orcid.org/0000–0002–8396–4870*
E-mail: *vasilieva_il@spbstu.ru*

Dalia Abdulova,
E-mail: *abdulova.dahlia@gmail.com*

Magazine of Civil Engineering

journal homepage: http://engstroy.spbstu.ru/

On the use of constrained modulus for soil settlement analysis

M.M. Al-Moadhen ✉ iD , **M.M. Abdullah**, **M.S. Oleiwi**

Middle Technical University, Technical Institute - Anbar, Iraq

✉ *m.m.almoadhen@mtu.edu.iq*

Abstract. Soil settlement is a key parameter in engineering design of geotechnical structures. Two approaches have been used for the characterization of soil behaviour under one dimensional compression: the linear - nonlinear, the traditional approach, and the modulus-based approach, the constrained modulus. The constrained modulus approach requires the knowledge of effective stress (σ'), stress exponent (d), and soil modulus number (m). In the current study, the constrained modulus approach was adopted in the settlement analysis. Compressibility data of 130 fine and mixed soils with a variety of composition and mineralogy was used in the analysis. In addition, three common clays, bentonite, sepiolite and attapulgite, was experimentally tested using one-dimensional oedometer compression test and the results were included in the analysis. The analysis shows that the approach of constrained modulus can be effectively used to calculate the settlement of fine and intermediate mixed soils, and the stress exponent (d) varies from 0 for clayey soils to 0.3–0.6 for intermediate silty and clayey sand soils depending on the soil plasticity and particle size distribution. Also, there is a simple relationship with $R^2 = 0.83$ between the soil modulus number, m , and the liquid limit, $IL.$ in that the higher the liquid limit, $IL.$ the lower the soil modulus number, m .

1. Introduction

Loads of engineering earth structures are transferred down by foundations to underlaying soils and distributed as a stress over the affected layers. Generally, stresses compress soil particles quickly at a small rate without any moisture loose at immediate stage. With a stress increase, a reduction in soil volume occurs due to the expulsion of water from interconnected voids, quickly and insignificant in coarse soils, but slowly and significant in fine-grained soils depending on the soil thickness and the permeability. At the end of the process, that is, when dissipation of excess pore water pressure is all completed, some compression (so-called secondary compression) takes place due to the plastic status of soil mass fabrics. In design, it is necessary to assess the suitability of a soil against both excessive settlement failure and allowable bearing capacity. While stability issues of structures in soil mechanics can often be defined satisfactorily, it is still difficult to estimate settlements and deformations accurately in advance [1]. In spite of the growth of knowledge in the past years, the variation of displacements measured is still to be significantly larger, and sometimes much smaller, than those calculated. This is because of the inappropriate selection of stiffness parameters in characterization of soil settlement [1]. The linear elastic

theory was the base of solutions in characterization of settlement $\left(\varepsilon\right)$ of coarse-grained soils, which depends on the elastic modulus of a soil $\left(E\right)$ and the flexibility of the resting foundation as:

$$\varepsilon = \frac{\Delta\sigma}{E}. \tag{1}$$

Most soils behave non-linearly under compression upon subjected to a stress change. As such, the linear elastic theory cannot be suitable, especially when dealing with compressible soils such as fine-grained soils (more specifically clays). In this case, the settlement can be found by:

$$\varepsilon = \frac{C_c}{1+e_o}\log\frac{\sigma'_f}{\sigma'_o}, \tag{2}$$

where σ'_o and σ'_f represent the initial and final effective stress, respectively.

The equation (2) shows that the settlement of a fine soil due to primary consolidation is a function of two key parameters; the compression index C_c, and the initial void ratio e_o, which can be determined from the traditional one-dimensional compression laboratory test. A range of theoretical, empirical, and semi-empirical relationships for C_c have been developed (e.g. [2]–[8]) depending on one (e.g. liquid limit, water content, field void ratio) or more soil properties. However, most civil engineers and soil researchers often report the values of C_c only, ignoring the magnitude of e_o. Sometimes, the reported e_o is determined from a soil sample different to that used in determining the C_c, which is not acceptable. The challenge of using two compression parameters is avoided by using soil modulus, the constrained modulus, the slope of stress-strain relationship which was first introduced by N. Janbu [9], using two non-dimensional parameters; a stress exponent, d, and a modulus number, m, as follows:

$$\frac{d\sigma}{d\varepsilon} = m\sigma_o\left(\frac{\sigma'}{\sigma_r}\right)^{1-d} = M, \tag{3}$$

where M is, σ' is an effective stress (kPa); and σ_r is a reference stress equal to (100 kPa).

Soil moduli have been used by several researchers as a measure of soil stiffness (e.g. [10]–[16]). Measurements of soil modulus by means of laboratory tests are quite difficult and often inaccurate because of the significant disturbance [17]. Therefore, correlations were always required to estimate the specific soil modulus. The constrained modulus approach for settlement, equation 3, is used where is no strain in the perpendicular direction which is the case of the soil behavior under one-dimensional compression. It combines the principles of linear and non-linear behavior [9]. It is also applicable for all types of soils even intermediate soils (e.g. silty sand, clayey sand) that exhibit transitional behavior which are not addressed properly by the traditional approaches (equation 1 and 2) [9] and [18]. According to Byington [19], the traditional approaches are limited and cannot be used with silt containing 15 % or less clay content. The interaction and arrangement of the fine and coarse particles in these soils affects the compressibility behavior such that they can be expected to exhibit behaviors and modes associated with clay and sands soils.

Despite the applicability of the constrained modulus approach, the approach is not commonly used in soil mechanics for soil compressibility and settlement. Very few studies were undertaken and provided preliminary information. N. Janbu [9] was the first who used the modulus approach to describe the compressibility behavior of rock, sand, silt and clay soils tested by oedometer and triaxial. He showed that the approach can describe the compressibility behavior provided that the accurate values of soil modulus number and stress exponent are selected. Schanz and Vermeer [1] tested the stiffness of three types of sands – Toyoura, Karlsruhe and Hostun sands – using the oedometer and triaxial modulus and showed that both normalized moduli have nearly same values.

The modulus number and stress exponent are of high importance in modulus-based settlement calculation. According to N. Janbu [9], the stress component (d) and the modulus number (m) both varies with soil initial porosity (n), the coarser the soil, the larger the stress exponent and modulus numbers assumed that, d = 1 for non-plastic soils, and d = 0 for plastic soils. The variation range of the modulus number, m, is really quite wide, from 6 orders of magnitude between coarse- and fine-grained soils.

According to the Canadian Foundation Engineering Manual 1992, the value of m for coarse soils, gravels and sands, ranges between 100 and 400 and for fine soils, silts, and clays, it is between 5 and 200. These values of m are approximate, and for intermediate soils such as silty clays or sandy clays, the values will be different as the compressibility behavior is different to that in pure soils. Therefore; the objective of this study is to determine both the modulus number, m, and the stress component, d, of 133 fine and mixed soils using the constrained modulus-based approach, and also to establish a new empirical relationship for the modulus number, m.

1.1 Soil settlement determination

With the knowledge of soil modulus number, m, stress exponent, d, and effective stress, σ', soil settlement can be determined. If, by the assumptions of N. Janbu [9], the stress exponent is fixed to unity for very coarse soils, rocks and gravels, and integrating the equation (3) gives:

$$\varepsilon = \frac{\sigma'_f - \sigma'_o}{100m}.$$ (4)

For fine soils, it equals to zero and equation (3) be:

$$\varepsilon = \frac{1}{m} ln\left(\frac{\sigma'_f}{\sigma'_o}\right).$$ (5)

However, for intermediate, composite, and transitional soils such as sandy clays, sandy silts and silty sands that are not covered properly by the traditional approaches, an intermitted value corresponds to 0.5 can be used which lies in an agreement with the fact that for each stress increment, the strain of a soil gets gradually smaller

$$\varepsilon = \frac{1}{5m}\left(\sqrt{\sigma'_f} - \sqrt{\sigma'_o}\right).$$ (6)

To estimate the modulus number, m, the normal compression curves $\left(e - log\,\sigma'\right)$ of soils were first converted to constrained modulus $\left(M - \sigma'\right)$ using the definition of volume compressibility $\left(m_v\right)$ as:

$$M = \frac{1}{m_v} = \frac{\delta\sigma'}{\delta e}\frac{\left(1+e\right)}{1000}.$$ (7)

Then, applying the best fit to the equation (3).

2. Materials and Methods

It is known that soil type, stress history and magnitude of effective stress play an important role in compressibility behavior of soils so a range of data from different sources varying in geological origin, soil type, sample preparation and index properties was selected in analysis. Published data of [5–7, 20–31] was included in the analysis. The soil samples in these sources are natural, remolded, and reconstituted samples prepared with an initial water content of 1–2 times of liquid limit. The standard one-dimensional oedometer test was used in these papers to assess the compression characteristics with a stress varying between (2.5–40000 kPa). Table 1 summarizes the soil data used in the analysis.

Table 1. Data used in analysis.

No.	Soil type	IL	m	d	Sources
1	Sail soil	158.3	5	0	
2	Black cotton soil	97.3	5.14	0	
3	Red soil	45.3	10.16	0	[5]
4	Vienna clay	47	9.8	0	
5	Silty clay	56.7	11.9	0.01	
6	Silty sand	36.2	16.4	0.01	
7	10 % bentonite + 90 % brown soil	68	8.5	0.13	
8	20 % bentonite + 80 % brown soil	77	8.2	0.25	
9	10 % bentonite + 90 % black cotton	88	5.8	0.18	
10	20 % bentonite + 80 % black cotton	93	4.97	0.15	
11	30 % bentonite + 70 % brown soil	95	4.58	0.15	[20]
12	30 % bentonite + 70 % black cotton	104	4.79	0.17	
13	49 % bentonite + 51 % sand	162	3.6	0.19	
14	59 % bentonite + 41 % sand	195	3.77	0.24	
15	100 % bentonite	330	3	0.28	
16	Lower Cromer Till	25	14.5	0.15	
17	Boulder clay	28	18.8	0.13	
18	Silty clay	28	17.5	0.10	
19	Magnus Clay	35	9.68	0.11	
20	Grangemouth	35	10.7	0.1	
21	Ton V	36	10.33	0.1	
22	Weald clay	39	10.95	0.08	
23	Boston blue clay	39	12.7	0.07	
24	Red soil	45.3	9.8	0.06	
25	River Severn alluvium	46	12.7	0.05	
26	Wiener Tegel	46.7	9.3	0.04	
27	Oxford clay	53	9.7	0.03	[21]
28	Ton IV	58	9.14	0.02	
29	Residual clay	58	8.91	0.01	
30	London Clay	62.3	7.3	0.02	
31	London Clay	67.5	6.68	0.03	
32	Ganges delta clay	69	7.8	0	
33	Gosport clay	76	6.8	0.02	
34	London Clay	77	6.9	0.02	
35	Brown London Clay	88	6.1	0.03	
36	Black cotton clay	97.3	5.8	0.04	
37	Kleinbelt Ton	127	5.1	0.06	
38	Argile plastique	128	6.3	0.03	
39	SAIL	159.3	5.3	0.05	
40	Red earth 1	37	12.867	0.03	
41	Silty soil	39	13.797	0.12	
42	Kaolinite 1	48	9.88	0	
43	Red earth 2	48	9.88	0	
44	Kaolinite 2	55	12.449	0.13	
45	Cochin clay	56.4	10.57	0.18	[6]
46	Brown soil 1	58.5	8.23	0.1	
47	Illatic soil	73.4	10.81	0.13	
48	BC soil	73.5	5.39	0	
49	Glacial sity clay	28	21.625	0.16	
50	Boulder clay	28	19.493	0	

No.	Soil type	IL	m	d	Sources
51	Sandy delta mud	36	8.195	0	
52	Weiner tegel	46.7	9.775	0.02	
53	Vienna clay	47	10.5	0.04	
54	Oxford clay	53	10.465	0	
55	Residual clay	58	9.82	0.08	
56	London clay	77	7.3	0.03	
57	Kleinbelt Ton	127	5.57	0.01	
58	MX80 clay	520	1	0	
59	Kunigel clay	474	1.2	0	[22]
60	Fourges clay	112	3.9	0.04	
61	96 sand + 4 clay	33	20.4	0.24	
62	92 sand + 8 clay	37.5	16.7	0	[23]
63	75 sand + 25 clay	47	10.39	0	
64	55 sand + 45 clay	61	9.8	0.16	
65	Na-Ca MX80	520	1	0	[24]
66	Na-Kunigel	474	1.2	0	
67	Atchafalaya	101	6.2	0.1	
68	Attapulgite	202	5	0	[25]
69	Boston blue clay	45	13.9	0.05	
70	Kaolinite	42	15.8	0	
71	Kaolinite (Ca 0.01 M)	81	7.4	0.2	[26]
72	Bentonite (Ca 0.001 M)	102	3.8	0.1	
73	SPV200 WB	354	1.7	0	[27]
74	Dunkettle silt 1	36	18	0.14	
75	Dunkettle silt 2	40	16	0.36	
76	Sligo sandy silt	61	12	0.24	[28]
77	Dunkettle silt 3	22	24	0.3	
78	Dunkettle silt 4	20	27	0.5	
79	0 sand + 100 clay (bentonite 9 : kaolin 1)	260	3.6	0.1	
80	0 sand + 100 clay (bentonite 7 : kaolin 3)	198.4	3.9	0.13	
81	30 sand + 70 clay (bentonite 9 : kaolin 1)	155	4.4	0.28	
82	0 sand + 100 clay (bentonite 5 : kaolin 5)	157.2	4	0.1	
83	40 sand + 60 clay (bentonite 9 : kaolin 1)	127.7	4.8	0.2	[29]
84	30 sand + 70 clay (bentonite 7 : kaolin 3)	123.7	4.9	0.26	
85	40 sand + 60 clay (bentonite 7 : kaolin 3)	106.3	4.78	0.26	
86	30 sand + 70 clay (bentonite 5 : kaolin 5)	101.2	5.15	0.2	
87	50 sand + 50 clay (bentonite 5 : kaolin 5)	68.8	5.94	0.17	
88	Kaolinite	29.1	13.2	0.13	
89	95 % kaolinite + 5 % bentonite	43.9	9.2	0.11	[7]
90	90 % kaolinite + 10 % bentonite	53.3	7.8	0.06	
91	85 % kaolinite + 15 % bentonite	61.7	4.9	0	
92	Lianyungang clay	74	5.5	0	
93	Baimahu clay	91	4.6	0	[30]
94	Kemen clay	61	7.6	0.04	
95	Kaolinite	56	9.55	0.44	
96	10 fine sand – 90 kaolinite	52.1	10.91	0.48	
97	20 fine sand – 80 kaolinite	48.2	11.40	0.50	
98	30 fine sand – 70 kaolinite	43.4	11.69	0.50	[31]
99	40 fine sand – 60 kaolinite	38.7	12.91	0.51	
100	50 fine sand – 50 kaolinite	33.2	14.80	0.57	
101	60 fine sand – 40 kaolinite	27.9	15.98	0.62	

No.	Soil type	IL	m	d	Sources
102	Kaolinite	56	9.55	0.10	
103	10 medium sand – 90 kaolinite	51.6	10.24	0.48	
104	80 medium sand – 20 kaolinite	47.3	10.02	0.53	
105	70 medium sand – 30 kaolinite	42.6	10.37	0.57	
106	60 medium sand – 40 kaolinite	37.8	12.59	0.52	
107	50 medium sand – 50 kaolinite	32.2	13.39	0.58	
108	60 medium sand -40 kaolinite	26.9	15.18	0.60	
109	10 fine sand – 90 bentonite	97.1	5.06	0.03	
110	20 fine sand – 80 bentonite	87.9	4.99	0.12	
111	30 fine sand – 70 bentonite	78.1	5.01	0.22	
112	40 fine sand – 60 bentonite	67.5	5.50	0.33	
113	50 fine sand – 50 bentonite	58.2	6.16	0.42	
114	60 fine sand – 40 bentonite	47.3	7.65	0.53	
115	10 medium sand – 90 bentonite	95	4.90	0.05	
116	20 medium sand – 80 bentonite	85.8	4.99	0.14	
117	30 medium sand – 70 bentonite	76.5	4.97	0.24	
118	40 medium sand – 60 bentonite	65.7	5.75	0.34	
119	50 medium sand – 50 bentonite	56	7.08	0.44	
120	60 medium sand – 40 bentonite	45.3	11.22	0.55	
121	10 medium sand – 90 sepiolite	104.9	5.50	0.00	
122	20 medium sand – 80 sepiolite	92.9	6.31	0.07	
123	30 medium sand – 70 sepiolite	81.5	6.61	0.19	
124	40 medium sand – 60 sepiolite	70	7.59	0.30	
125	50 medium sand – 50 sepiolite	58.5	7.94	0.42	
126	60 medium sand – 40 sepiolite	48	8.43	0.52	
127	70 medium sand – 30 sepiolite	36.5	12.59	0.56	
128	Illlite	37.6	12.70	0.57	
129	20 fine sand – 80 Illite	31.5	12.38	0.59	
130	40 fine sand – 60 Illite	26	13.22	0.6	
131	Bentonite 1	112	3.7	0.04	Present study
132	Sepiolite 1	125	5	0.14	
133	Attapulgite 1	217	4.5	0.12	

In addition, three common commercially clays; bentonite, sepiolite, and attapulgite were chosen in the present study which covers a range of plasticity (105 % ≤ IL ≤ 220 %). The index properties, determined by ASTM D4318–17e1 [32], D854–14 [33], and D2487–17 [34] of the materials are shown in Table 2. The plasticity chart of the data used is shown in Fig. 1. As per Fig. 1, the classification of clays is high plasticity silts (MH). Also, the used data covers a range of clayey, silty, and intermediate soils with high and low plasticity which is very important as to cover a range of soils for settlement analysis.

The clays were prepared in a blender as slurry by adding de-aired water using 1.75 times of liquid limit ensuring a fully saturated and homogeneous sample. The mixture was poured into a rigid stainless steel consolidometer tube with a 14 cm diameter and 25 cm height and then consolidated to the desired stress. The compressibility test was conducted using the standard oedometer equipment following ASTM D2435/D2435M-11 [35] procedures. The internal area of the consolidation ring was lubricated with silicon grease so that the side friction can be minimized, and the test was carried out at maintained room temperature of 20 °C. The ring was inserted into the consolidated sample to bring the target sample. The assembled cell was mounted and placed on the platform of the oedometer equipment with an adjusted dial gage of a 0.001 mm resolution. Before applying loads, the soil sample was kept in saturated condition by submerging it in de-aired water for the whole test period. Increments of load increments were applied up to maximum stress of 1280 kPa and each increment was doubled when the primary compressibility for the current load was completed.

Table 2. The properties of materials used.

Clays	Atterberg limits	Specific gravity (G_s)	Classification
Bentonite 1	IL = 112 % PI = 52 %	2.64	MH
Sepiolite 1	IL = 125 % PI = 29 %	2.38	MH
Attapulgite 1	IL = 217 % PI = 101 %	2.12	MH
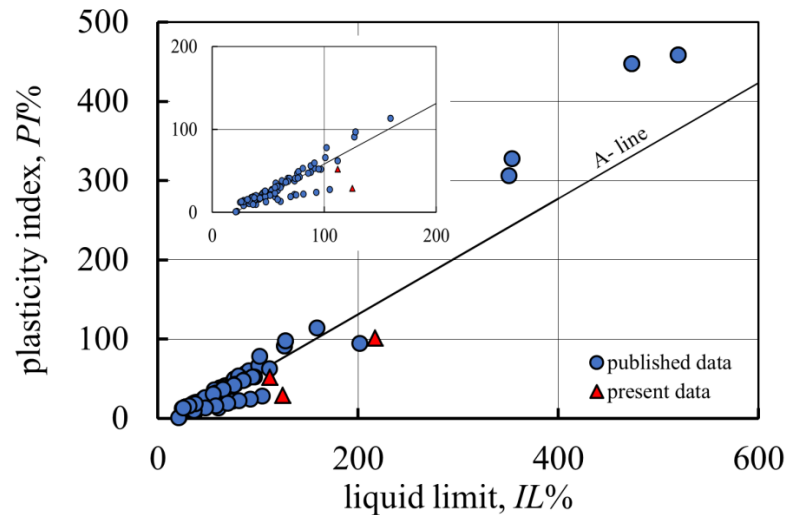
Figure 1. The plasticity chart of present clays and data used.

3. Results and Discussion

Fig. 2 shows the normal compression curves of the bentonite, sepiolite and attapulgite clays that were tested in the present study. It can be seen that the curves are slightly concave up for the stresses larger than 10 kPa which is the most common.
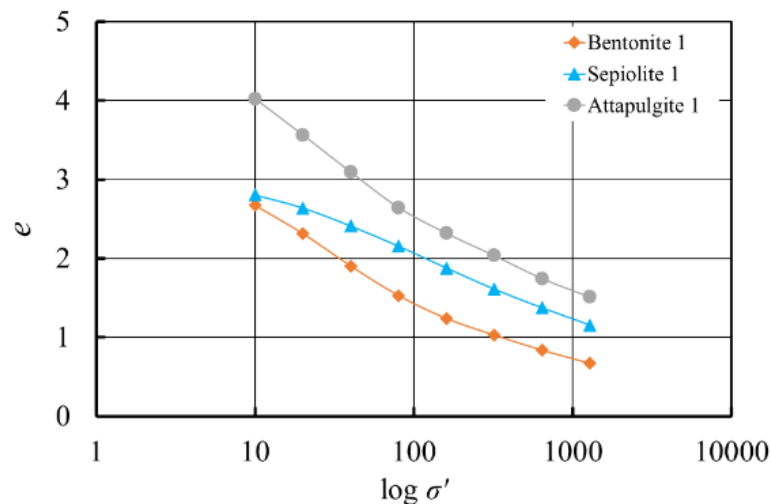
Figure 2. Normal compression curves of clays (bentonite, sepiolite, and attapulgite).

The normal compression curves in the preset study (Fig. 2) and in previous selected studies were replotted in terms of the constrained modulus, M, versus effective stress, σ' (as seen in Fig. 3). It can be seen that the constrained modulus is a function of effective stress, stress history, and soil type. The modulus increases when the stress increases.

The modulus number, m, and stress exponent, d, were determined using the best-fit of the equation (3). The values are presented in Table 2 and correlated in Fig. 4 and 5 with liquid limit, IL. It can be observed that there is a good relationship for m with IL with $R^2 = 0.83$ in the form:

$$m = 264.11(IL)^{-0.841}. \tag{8}$$

This is acceptable because the liquid limit is a material property that is relied on soil composition, particle size and surface characteristics. This single relationship has an advantage of the fact that liquid limit test is easy to conduct in lab.
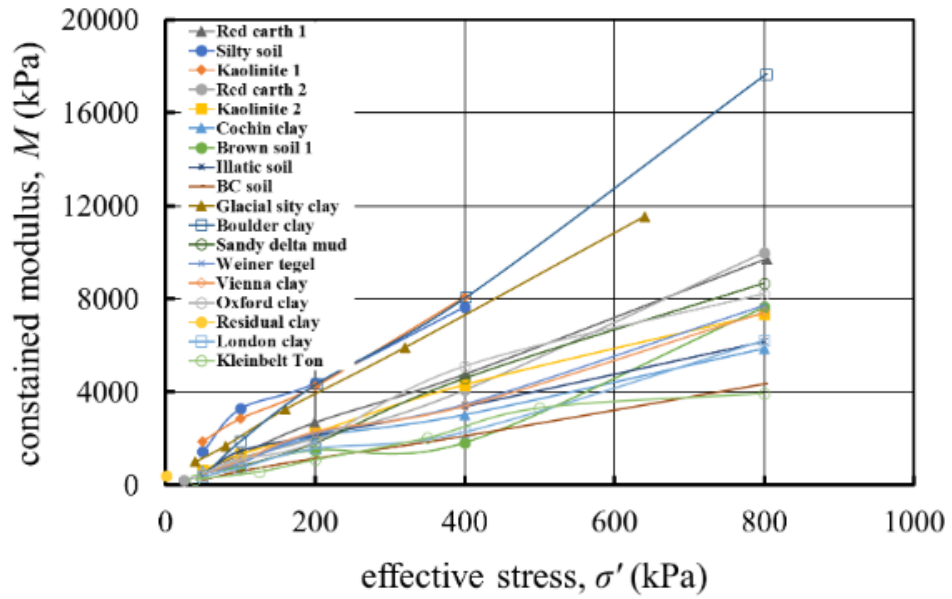
The stress exponent, d, shows a scatter as it depends on soil plasticity and particle size distribution and varies from 0 for clayey soils to 0.3–0.6 for silty and clayey sand soils. This is similar to the assumptions of N. Janbu [9] for normal consolidated clays and intermediate soils.
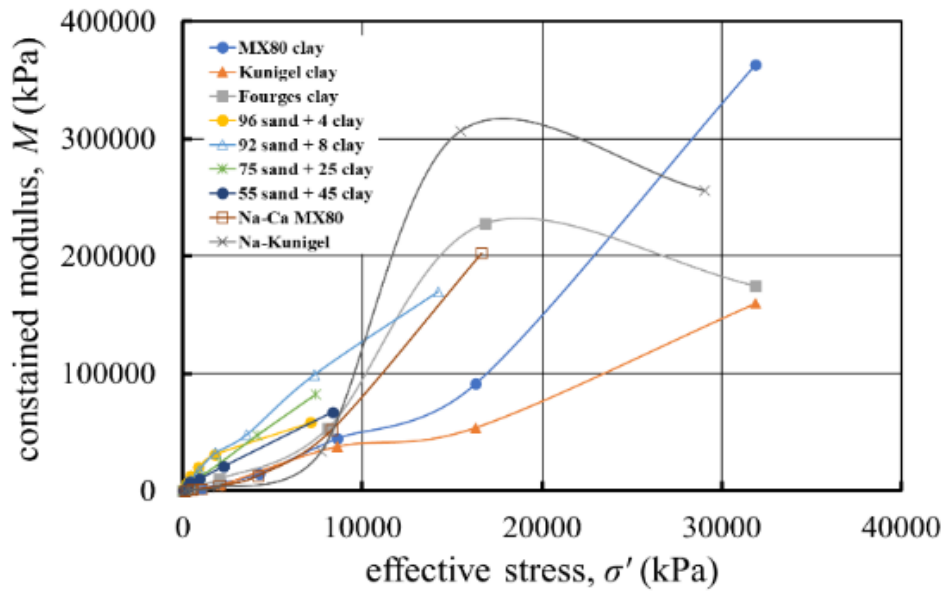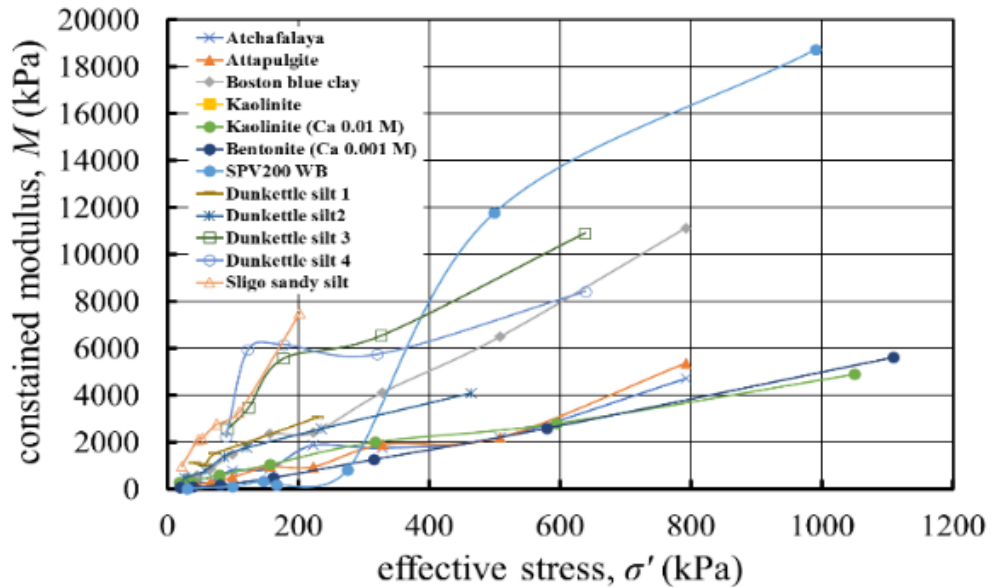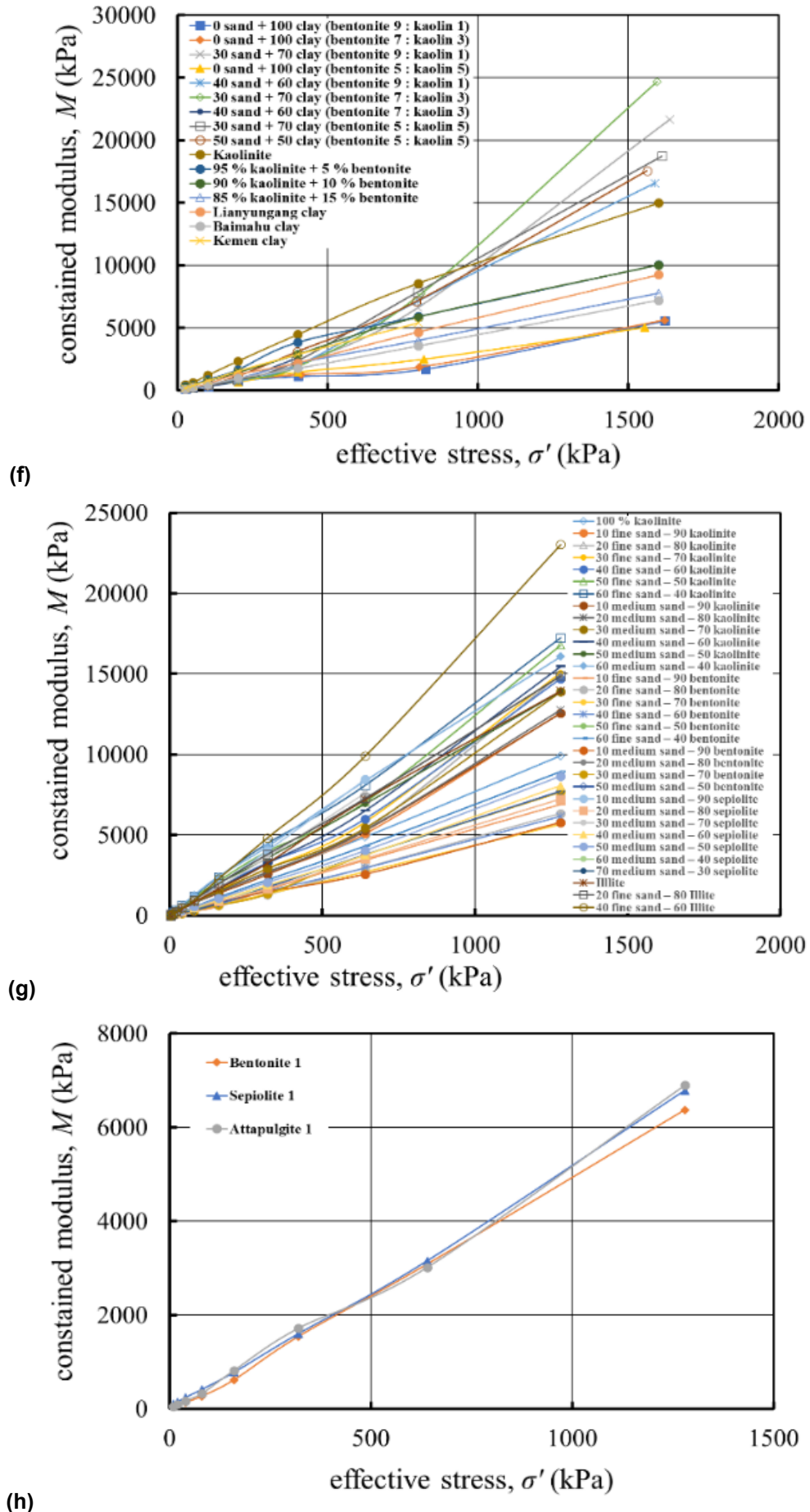

(a)

(b)

(c)

(d)

(e)

(f)

(g)

(h)
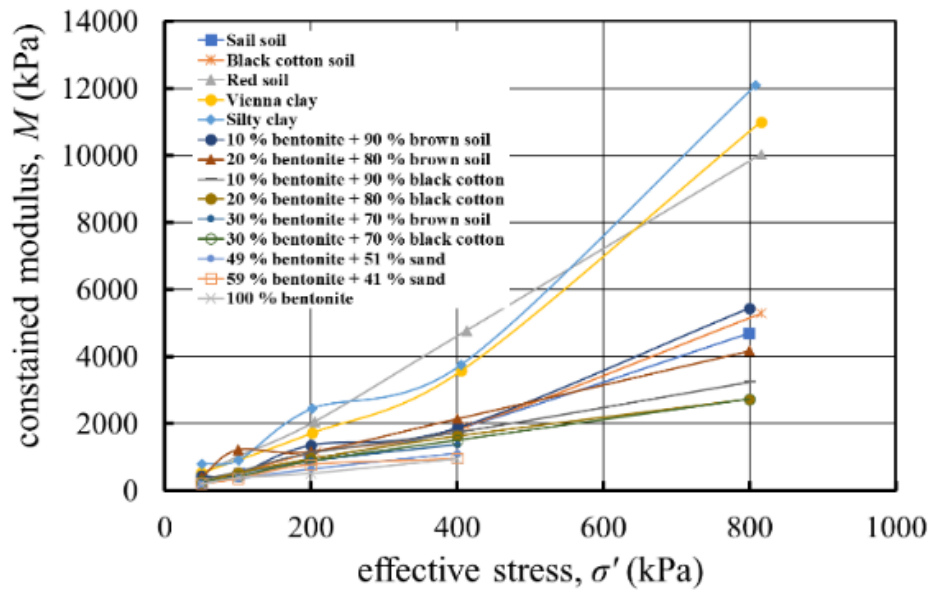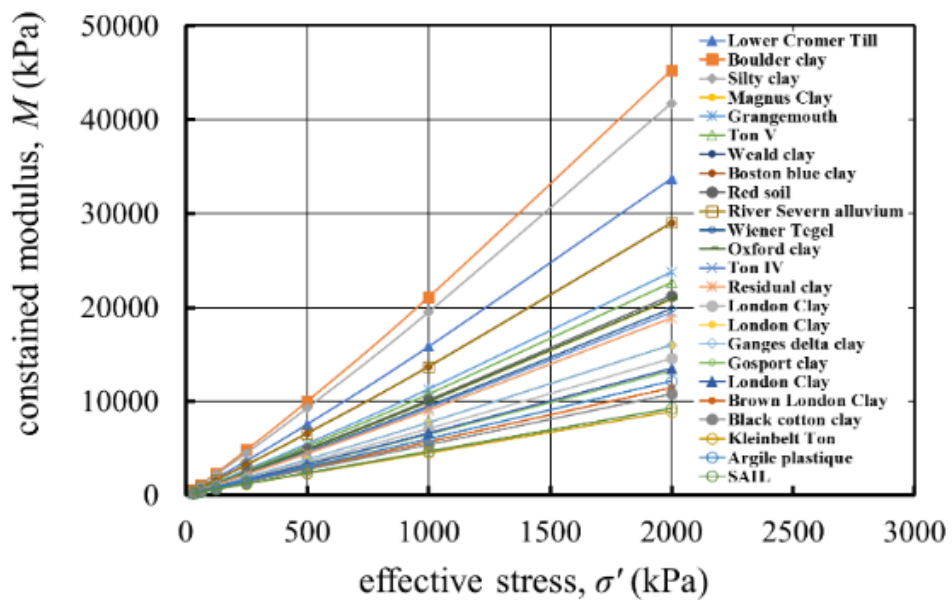
Figure 3. The relationship between the constrained modulus, M, and effective stress for soils: (a) [5] & [20]; (b) [21]; (c) [6]; (d) [22–24]; (e) [25–28]; (f) [29–30]; (g) [31]; (h) present clays.
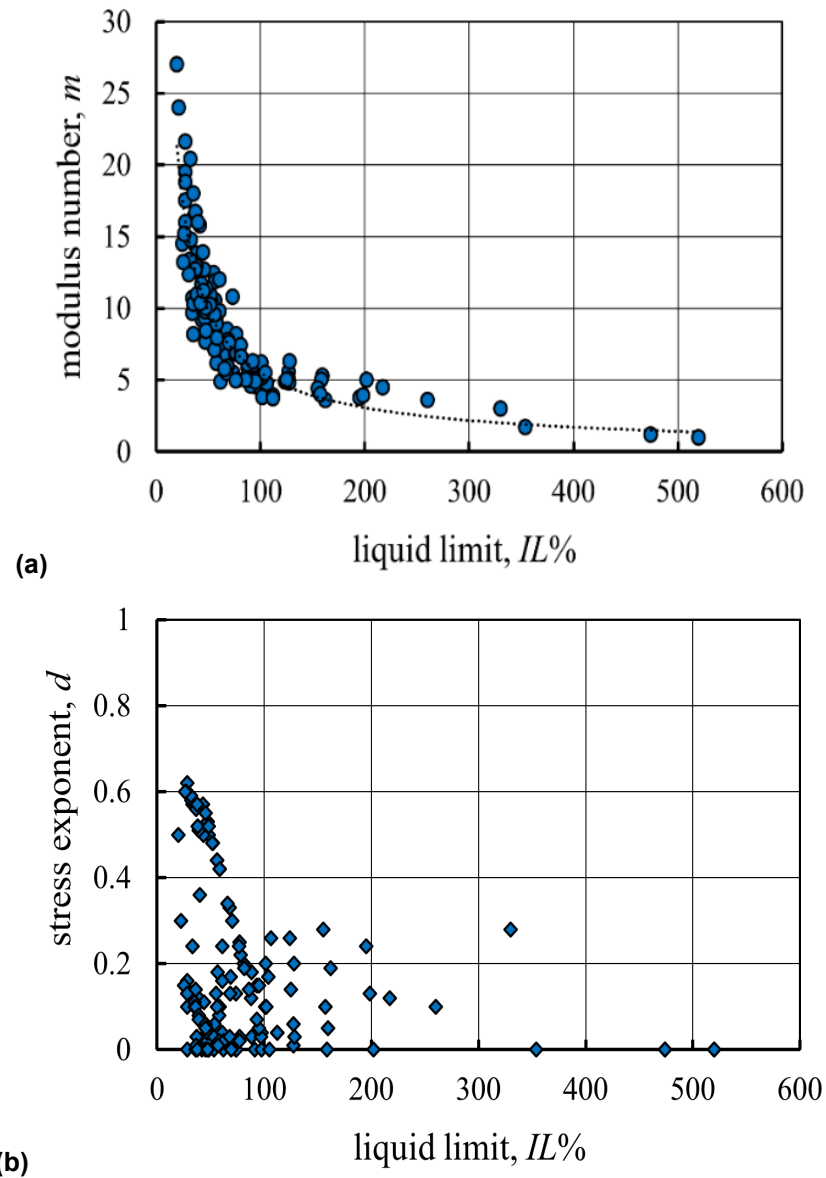
(a)

(b)

Figure 4. The relation between: (a) modulus number, m; (b) stress exponent, d, with liquid limit, IL.

4. Conclusion

This study is devoted to exploring the suitability of the constrained modulus approach for soil settlement determination. An analysis of a range of compressibility data taken from different high-quality papers along with the present experimental results on three commercial clays (bentonite, sepiolite and attapulgite) using the modulus-based approach of N. Janbu shows that:

1. The constrained modulus-based approach is a convenient approach to adequately describe the settlement phenomena of fine and intermediate transitional soils using the stress exponent (d) and the modulus number (m).

2. The results show that the stress exponent (d) in the approach depends on soil plasticity and particle size distribution and varies from 0 for clayey soils to 0.3–0.6 for silty and clayey sand soils.

3. There is a relationship between the soil modulus number (m) and the liquid limit (IL) in that an increase in the liquid limit leads to a decrease in the modulus number.

4. An empirical relationship for modulus number, m, based on the soil liquid limit, IL, was established with $R^2 = 0.83$.

References

1. Schanz, T., Vermeer, P.A. On the stiffness of sands. Pre-failure deformation behaviour of geomaterials. 1998. Pp. 383–387.

2. Nishida, Y. A brief note on compression index of soil. Journal of the Soil Mechanics and Foundations Division. 1956. 82 (3). Pp. 1–14. DOI: 10.1061/JSFEAQ.0000015

3. Cozzolino, V. Statistical forecasting of compression index. Proceedings of the fifth international conference on soil mechanics and foundation engineering. 1961. Pp. 51–53.

4. Azzouz, A.S., Krizek, R.J., Corotis, R.B. Regression analysis of soil compressibility. Soils and Foundations. 1976. 16 (2). Pp. 19–29. DOI: 10.3208/sandf1972.16.2_19

5. Nagaraj, T.S., Murthy, B.S. Rationalization of Skempton's compressibility equation. Géotechnique. 1983. 33 (4). Pp. 433–443. DOI: 10.1680/geot.1983.33.4.433

6. Sridharan, A., Nagaraj, H. Compressibility behaviour of remoulded, fine-grained soils and correlation with index properties. Canadian Geotechnical Journal. 2000. 37 (3). Pp. 712–722. DOI: 10.1139/t99-128

7. Fan, R.D., Du, Y.J., Reddy, K.R., Liu, S.Y., Yang, Y.L. Compressibility and hydraulic conductivity of clayey soil mixed with calcium bentonite for slurry wall backfill: Initial assessment. Applied Clay Science. 2014. 101. Pp. 119–127. DOI: 10.1016/j.clay.2014.07.026

8. Shimobe, S., Spagnoli, G. A general overview on the correlation of compression Index of clays with some geotechnical index properties. Geotechnical and Geological Engineering. 2022. 40 (1). Pp. 311–324. DOI: 10.1007/s10706-021-01888-8

9. Janbu, N. Soil compressibility as determined by oedometer and triaxial tests. Proceedings of European Conference on Soil Mechanics and Foundation Engineering (ECSMFE). 1963. 1. Pp. 19–25.

10. Jardine RJ, Symes MJ, Burland JB. The measurement of soil stiffness in the triaxial apparatus. Géotechnique. 1984. 34(3). Pp.323-40. DOI: 10.1680/geot.1984.34.3.323.

11. Atkinson JH. Non-linear soil stiffness in routine design. Géotechnique. 2000. 50(5). Pp. 487-508. DOI: 10.1680/geot.2000.50.5.487.

12. Sawangsuriya A, Bosscher PJ, Edil TB. Application of soil stiffness gauge in assessing small-strain stiffness of sand with different fabrics and densities. Geotechnical Testing Journal. 2006. 29(3). Pp. 207-16. DOI: 10.1520/GTJ13154.

13. Clayton CR. Stiffness at small strain: research and practice. Géotechnique. 2011. 61(1). Pp. 5-37. DOI: 10.1680/geot.2011.61.1.5.

14. Oztoprak SA, Bolton MD. Stiffness of sands through a laboratory test database. Géotechnique. 2013. 63(1):Pp. 54-70. DOI: 10.1680/geot.10.P.078.

15. Vardanega PJ, Bolton MD. Stiffness of clays and silts: Normalizing shear modulus and shear strain. Journal of Geotechnical and Geoenvironmental Engineering. 2013.139(9). Pp.1575-89. DOI: 10.1061/(ASCE)GT.1943-5606.0000887.

16. Bolton MD, Wilson JM. Soil stiffness and damping. InStructural Dynamics-Vol 1 2022. Pp. 209-216.

17. Duncan JM, Bursey A. Soil modulus correlations. InFoundation engineering in the face of uncertainty: Honoring Fred H. Kulhawy 2013. Pp. 321-336. DOI: 10.1061/9780784412763.026.

18. Fellenius, B.H. Basics of foundation design. Electronic Edition. 2016. 451 p.

19. Byington, M.L. A study of the compressibility of silty soils. Masters Theses. University of Missouri at Rolla. 1967.

20. Pandian, N.S., Nagaraj, T.S., Raju, P.N. Permeability and compressibility behavior of bentonite-sand/soil mixes. Geotechnical Testing Journal, 1995. 18 (1). Pp. 86–93. DOI: 10.1520/GTJ10124J

21. Burland, J. On the compressibility and shear strength of natural clays. Géotechnique. 1990. 40 (3). Pp. 329–378. DOI: 10.1680/geot.1990.40.3.329

22. Marcial, D., Delage, P., Cui, Y.J. On the high stress compression of bentonites. Canadian Geotechnical Journal. 2002. 39(4). Pp. 812–820. DOI: 10.1139/t02-019

23. Nocilla, A., Coop, M.R., Colleselli, F. The mechanics of an Italian silt: an example of 'transitional' behaviour. Géotechnique. 2006. 56(4). Pp. 261–271. DOI: 10.1680/geot.2006.56.4.261

24. Bharat, T.V., Sridharan, A. Prediction of compressibility data for highly plastic clays using diffuse double-layer theory. Clays and Clay Minerals. 2015. 63(1). Pp. 30–42. DOI: 10.1346/CCMN.2015.0630103

25. Cerato, A.B., Lutenegger, A.J. Determining intrinsic compressibility of fine-grained soils. Journal of Geotechnical and Geoenvironmental Engineering. 2004. 130 (8). Pp. 872–877. DOI: 10.1061/(ASCE)1090-0241(2004)130:8(872)

26. Horpibulsuk, S., Yangsukkaseam, N., Chinkulkijniwat, A., Du, Y.J. Compressibility and permeability of Bangkok clay compared with kaolinite and bentonite. Applied Clay Science. 2011. 52 (1–2). Pp. 150–159. DOI: 10.1016/j.clay.2011.02.014

27. Stewart, D.I., Studds, P.G., Cousens, T.W. The factors controlling the engineering properties of bentonite-enhanced sand. Applied Clay Science. 2003. 23 (1–4). Pp. 97–110. DOI: 10.1016/S0169-1317(03)00092-9

28. Long, M. Engineering characterization of estuarine silts. Quarterly Journal of Engineering Geology and Hydrogeology. 2007. 40(2). Pp. 147–161. DOI: 10.1144/1470-9236/05-061

29. Deng, Y., Wu, Z., Cui, Y., Liu, S., Wang, Q. Sand fraction effect on hydro-mechanical behavior of sand-clay mixture. Applied Clay Science. 2017. 135. Pp. 355–361. DOI: 10.1016/j.clay.2016.10.017

30. Hong, Z.S., Yin, J., Cui, Y.J. Compression behaviour of reconstituted soils at high initial water contents. Géotechnique. 2010. 60(9). Pp. 691–700. DOI: 10.1680/geot.09. P.059

31. Al-Moadhen, M.M., Clarke, B.G., Chen, X. The permeability of composite soils. Environmental Geotechnics. 2020. 7(7). Pp. 478–490. DOI: 10.1680/jenge.18.00030

32. ASTM D4318–17e1. Standard Test Methods for Liquid Limit, Plastic Limit, and Plasticity Index of Soils. 2018. 04.08. 20 p. DOI: 10.1520/D4318-17E01

33. ASTM D854–14. Standard Test Methods for Specific Gravity of Soil Solids by Water Pycnometer. 2014. 8 p.

34. ASTM D2487–17. Standard Practice for Classification of Soils for Engineering Purposes (Unified Soil Classification System). 2020. 04.08. 10 p. DOI: 10.1520/D2487-17

35. ASTM D2435/D2435M–11. Standard Test Methods for One-Dimensional Consolidation Properties of Soils Using Incremental Loading. 2020. 04.08. 20 p. DOI: 10.1520/D2435_D2435M-11

Information about authors:

Muataz Muayad Al-Moadhen, *PhD*
ORCID: https://orcid.org/0000-0003-2404-5724
E-mail: m.m.almoadhen@mtu.edu.iq

Murtatha M. Abdullah,
E-mail: murtathaabdullah@mtu.edu.iq

Mohammed S. Oleiwi,
E-mail: mohammadsaab3@gmail.com

Polyethylene terephthalate usage as a partial replacement for recycled fine aggregate in the subbase layer

A.A.I. Muhmood ✉

Northern Technical University / Mosul Technical Institute, Mosul, Iraq

✉ abdulbasit@ntu.edu.iq

Abstract. The best way to dispose of construction waste and plastic materials (in Mosul city in the north of Iraq) is to use them as subbase layer of the road to make them both environmentally friendly and cost-effective. Because these materials are not cohesive, a certain percentage of clay was added. The research aimed to dispose of these materials scientifically and deliberately with appropriate California Bearing Ratio (CBR) values obtained from a mixture of (clay soil + recycled concrete aggregates (RCA) + polyethylene). These values are much greater than the CBR values obtained from natural materials used in the design of the road subbase layer. Clay was added to soil in specific proportions: 10 % to type A and 20 % to type B. Various tests were carried out for the mixture to determine Maximum Dry Density (MDD) and Optimal Moisture Content (OMC), and then CBR and swelling. Tests were also carried out to determine the soil permeability (both the permeability rate in centimeters per hour (cm/h), and the coefficient of permeability k in meters per second (m/s)). Polyethylene was added in different proportions as a replacement for the remaining fine aggregate on the sieve No. 8. Multiple percentages of polyethylene terephthalate were used, ranging from 2.5 to 10 for type A (2.5, 5.0, 7.5, 10 %) and from 5 to 20 for type B (5.0, 10, 15, 20 %), in order to obtain an ideal mixture of (RCA + polyethylene + clay). The CBR was 12 %, which had been more than that of natural soil. The coefficient of permeability was more than 32 m/day, indicating that these mixes could be used for subsurface drainage purposes. This value was reasonable and no noticeable erosion was observed. The subbase would help draining and prevent settlement and channeling. Apart from the sustainable benefit, the mixture (clay soil + RCA + polyethylene) was found to be suitable for use in road pavements, according to the methodologies used in this study. Due to the encouraging results it is recommended to use these techniques to dispose of the waste and debris materials and obtain optima benefits.

1. Introduction

Despite Iraq's natural aggregate reserves, this study focuses on recycled concrete as a major road material to dispose of trash productively and safely. Crushed waste materials from demolished buildings generate a variety of particle sizes that meet the gradations criteria of Iraqi subbase course standards. Because concrete cement mix is one of the most commonly used building materials in Iraq, the demolition of existing structures under the country's current conditions has resulted in a large amount of concrete waste that must be used as useful materials to achieve environmental, economic, and social benefits.

There are three main types of construction and demolition waste aggregates: MRA (mixed recycled aggregates – also known as mixed demolition debris), RCA (recycled concrete aggregates), and RMA (recycled masonry aggregates – also known as Crushed Clay Masonry, RCM) [1, 2]. Some 60 % of the materials used in the construction of a building come with concrete (Fig. 1a), and 42 % of the wastes generated by the construction sector are concrete wastes (Fig. 1b) [3, 4].
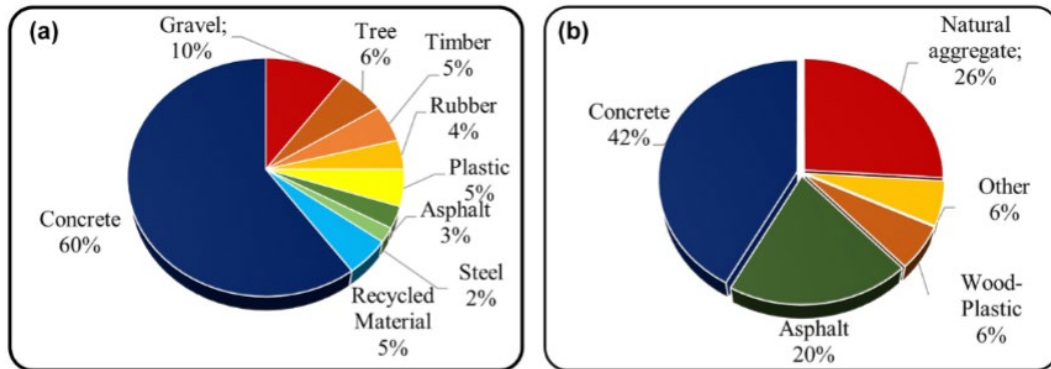

Figure 1. The proportion of materials used for the construction of a building (a) and waste rates (b) [7].

Within the specified restrictions, the researchers discovered that recycled aggregate may be used in road layers (base or subbase) [5].

The most prevalent application of RCA is in pavement (subbase, base) materials, although it has also been used in concrete and asphalt paving layers, as well as general fill and embankment material, and in a variety of other uses. We summarized the usage of RCA in paving applications in Fig. 2 [6].
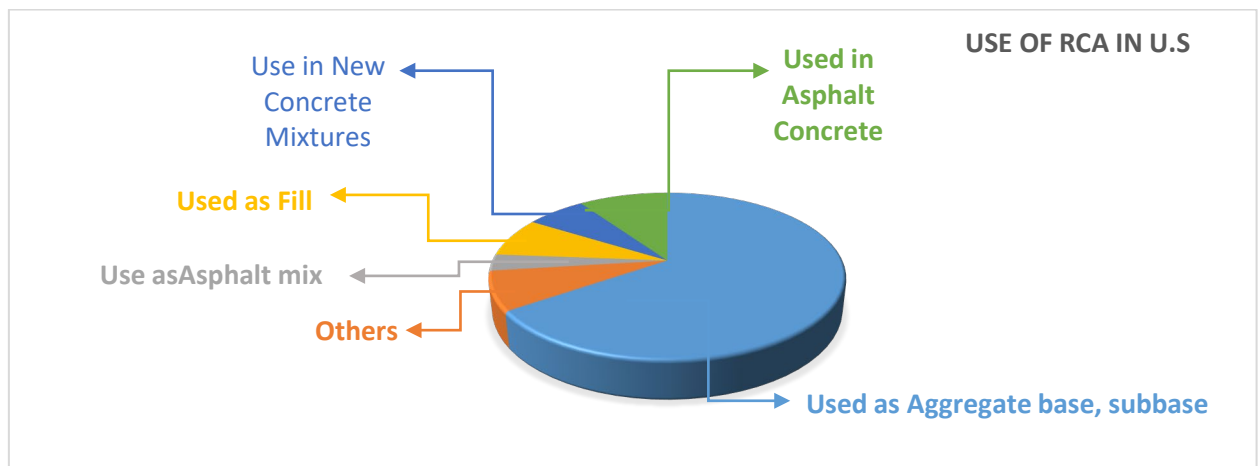

Figure. 2. An overview of RCA's utilization in paving applications.

Increasing RCA content in the mixture causes an increase in Optimum Moisture Content (OMC) and a decrease in Maximum Dry Density (MDD). Fine aggregates formed during the compaction process have a negative effect on the performance of the foundation and subbase layers, especially on the hydraulic properties. The California bearing ratio (CBR) value of RCA is equal to or higher than typical natural aggregates (NA) in relation to use in road pavement foundation and subbase layers. In addition, RCA provides the minimum specification limit required for road applications even when it has a lower CBR value than NA. CBR values vary between 67 % and 190 %. CBR values are believed to vary in such a wide range because the properties of the source concrete samples used in the studies are different from each other [7]. Compared with the crushed aggregate, the CBR values of the mixtures containing RCA were found to be between 118 % and 160 %. It was reported to be suitable for use in the base and subbase layer of RCA, as it meets the minimum 80 % CBR value specified in the Australian local state highway specification [8]. The CBR test's results suggest that CBR values obtained from recycled concrete are significantly higher than those CBR values obtained from the ordinary subbase. As a result, it is possible to conclude that recycled concrete might be used as a subbase material for highways [9]. The preceding paragraphs emphasized the advantages of RCA as compacted aggregates or stabilized mixtures. However, the application of RCA in mixtures with clay soils to improve the bearing/shear strength of the subgrade has never been investigated [10]. Due to the wide use of plastics in human daily life, the rate of plastic waste generation is increasing at an alarming rate. Every year almost 2.24 million tons of plastic waste is produced in Australia [11].

The deformation behavior of construction and demolition waste materials, such as RCA and crushed brick (CB) that were mixed with up to 7 % polyethylene terephthalate (PET) plastic waste, was investigated in [12]. It was found that increasing the PET content and stress levels increased the permanent strain of blends. It is recommended that up to 3 % PET could be mixed with RCA in base/subbase layer. [13–15] used plastic wastes for the sustainable construction of flexible pavements. In [12] it stated clearly that "the addition of plastic waste to pavement granular materials can considerably influence the strength and deformation properties of materials, which need to be fully understood prior to their wide usage for construction of pavement base/subbase layers".

The outcome of [16] illustrated that the modified subbase properties were significantly enhanced by adding the waste plastic granules and that, for best results, the optimal percentage of recycled PET granules to be added was 10 % by the volume of the subbase material. The CBR value for modified subbase, as compared with the subbase without waste plastic, increased by as much as 36 %. It has been suggested that this method could provide a potential practical use for waste plastic as well as improve the quality of subbase soil layers for flexible pavement.

The experimental results in [17] indicated that the insertion of plastic waste increased the OMC and reduced the MDD and CBR. Modified subbase layer also met the requirements of applicable standards codes. Based on these outcomes, it was suggested, that the use of plastic waste in subbase layers had been feasible for practical work [16].

Using plastic waste for soil stabilization can help to enhance pavement foundation layers [18].

Results of CBR tests in [19] revealed that inclusion of waste high density polyethylene strips in soil in suitable proportions significantly improved strength and deformation behavior of subgrade soils. The proposed technique could be beneficial in embankment/road construction.

Five types of subbases ranging from an impermeable cement stabilized material to a very permeable, uniformly graded, crushed aggregate were evaluated during a 7-year research project [20], which demonstrated that "open-graded, permeable, subbase materials could be designed to provide adequate constructability and pavement support as well as good internal drainage at a competitive cost".

Moisture enters into the pavement structure from the surface by infiltrating through cracks and joints, laterally from shoulders, and as capillary suction from bottom. One of the main reasons for the accumulation of moisture is inadequate subbase permeability. The presence of moisture within the pavement structure reduces the structural stability of the system. Therefore, it is essential to provide the subbase layer with sufficient drainage characteristics. In [21] horizontal permeability was determined using laboratory-developed horizontal permeameter under constant head mode with different hydraulic gradients. Strength characterization was also done in terms of CBR value.

The coefficient of permeability, $k,$ a unit of velocity, is a measure of the ease with which fluids can travel through a porous medium. In [22] multiple regression equation was developed by comparing maximum hydraulic conductivity with parameter affecting K values such as Voids ratio e, 75micron passing material and effective grain size material D_{10}.

Darcy's law is generally expressed as:

$$v = k * i,$$

where v is flow discharge velocity in cm/s; k is coefficient of permeability in cm/s; i is hydraulic gradient.

Using the specific sign convention, Darcy's law is expressed as:

$$Q = -KA \ dh/dl$$

where Q is rate of water flow; K is hydraulic conductivity; A is column cross section area; dh/dl indicates hydraulic gradient [28].

As per compaction test conducted and obtained MDD of 2.14 gm/cc and OMC of 3.18 % to be achieved in the field. Permeability test conducted in the field for Grade III at 2.5 %, 3.5 % and 4.0 % hydraulic gradients. At 2.5 % hydraulic gradient maximum hydraulic conductivity of 3675.66 m/day was observed [22].

During wet seasons, when the subgrade becomes saturated, cyclic loading, caused by heavy traffic, may result in the pumping of fine particles from the subgrade into the granular layers, which may lead to pumping in a concrete road. It is expected that the erosion may be less due to the presence of polyethylene. The resulting gradation from the migration of subgrade fines into the subbase also varies with the depth in

the subbase with more fines deposited in the lower section (closer to the subgrade) than in the upper section of the subbase [23].

For example, if a k of 5.000 ft/day is needed, one should be able to see openings between particles at least 1/20 inch in diameter; if 20.000 ft/day is required, visible openings should be at least 1/10 inch in diameter; and for 100.000 ft/day, at least 1/4 inch. The making of even such a crude "eye test" can help designers avoid serious mistakes in selecting types of aggregates to be use in drainage systems.

A permeable material is one that is capable of being penetrated or permeated by another substance, usually gas or liquid. Thus, dry cement is permeable to air, and an air permeability test is a useful means of obtaining an indirect measure of its fineness of grind, since the speed of flow of air through it can be related to the size of the pore spaces between the particles. Likewise, soils and aggregates and jointed, cracked, or vesicular rocks are often permeable to air and water [25].
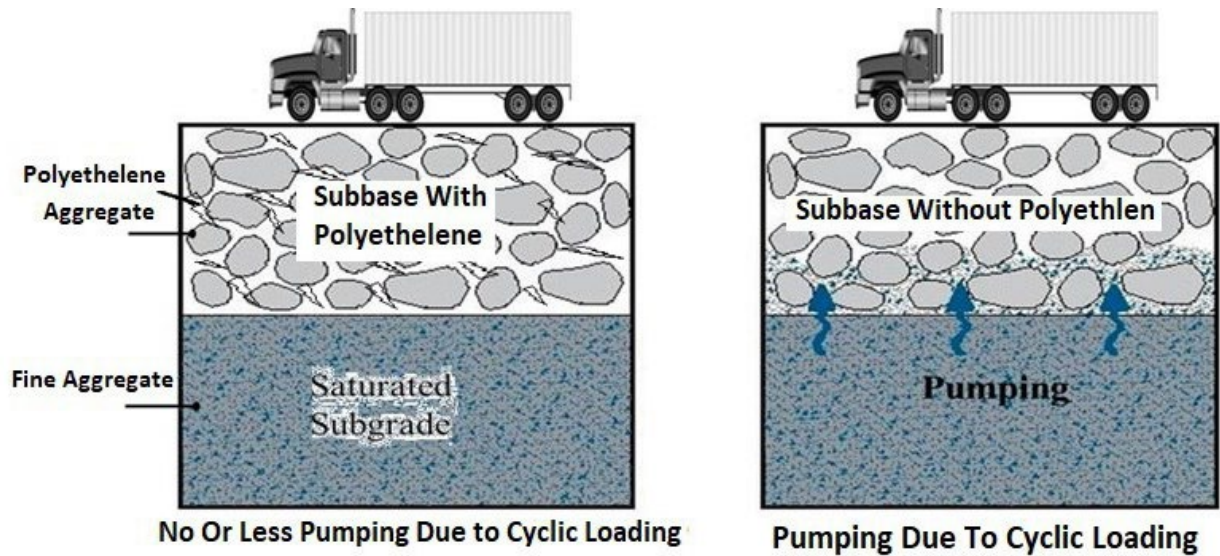

Figure. 3. Relationships between pumping through the layers with and without polyethylene.

Table 1. Some typical values of hydraulic conductivity [24].

Unconsolidated deposits	Hydraulic conductivity, m/s	Rocks	Hydraulic conductivity, m/s
Dense clay	10^{-13} ......10^{-8}	Dense sandstone	10^{-9} ......10^{-7}
Weathered clay	10^{-8} ......10^{-6}	Karstic sandstone	10^{-7} ......10^{-5}
Silt	10^{-7} ......10^{-5}	Dense limestone	10^{-9} ......10^{-7}
Alluvial deposits	10^{-5} ......10^{-3}	Karstic limestone	10^{-5} ......10^{-3}
Fine sand	10^{-5} ......10^{-4}	Dolomite	10^{-10} ......10^{-8}
Medium sand	5×10^{-4} ......5×10^{-3}	Dense crystalline rocks	10^{-13} ......10^{-12}
Coarse sand	10^{-4} ......10^{-3}	Fractured crystalline	10^{-10} ......10^{-6}
Fine gravel	10^{-3} ......5×10^{-1}	Dense basalt	10^{-13} ......10^{-10}
Medium gravel	5×10^{-2} ......10^{-1}	Fractured basalt	10^{-7} ......10^{-4}
Coarse gravel	10^{-2} ......5×10^{-1}	Claystone	10^{-13} ......10^{-9}

This research aims to dispose these debris materials scientifically and deliberately with appropriate CBR values obtained from a mixture of (clay soil + RCA + polyethylene). The study conducted various tests and reached conclusions regarding the feasibility of this study.

2. Materials and Methods

2.1. Recycled Concrete Aggregate

The recycled aggregate was obtained from the debris of destroyed houses in Mosul. The UN estimates, that there are more than ten million tons of rubble in the city of Mosul. The military actions that took place in the capital of Nineveh Governorate after the ISIS occupation of the city resulted in this significant amount of debris, since a third of the city was completely destroyed, and a half suffered

significant damage. This research was conducted to determine the suitability of these debris for road construction. The results of RCA and natural aggregate testing are shown in the Table 2.

Table 2. Results of RCA and natural aggregate testing.

Data	Value	Specification
Constant head permeability	$1.726*10^{-4}$	ASTM D2434-19
Plastic limit	NON	ASTM D4318-17e1
Liquid limit	NON	ASTM D4218-20
Shrinkage limit	NON	ASTM D4943-18
Specific gravity of fin aggregate (RCA)	2.57	ASTM C127-15, C128-15
Specific gravity of coarse aggregate (RCA)	2.45	ASTM C127-15, C128-15
Absorption of fine aggregate (RCA)	6.40 %	ASTM C127-15
Absorption of coarse aggregate (RCA)	1.70 %	ASTM C128-15
Specific gravity of natural fine aggregates	2.62	ASTM C127-15, C128-15
Specific gravity of natural coarse aggregates	2.67	ASTM C127-15, C128-15
Absorption of natural fine aggregates	2.07 %	ASTM C127-15
Absorption of natural coarse aggregates	0.73 %	ASTM C128-15
Soundness of fine aggregate (RCA) in sodium sulphate	2.7 %	ASTM C88/C88M-18
Soundness of coarse aggregate (RCA) in sodium sulphate	0.85 %	ASTM C88/C88M-18
Soundness of fine aggregate (RCA) in magnesium sulphate	2.6 %	ASTM C88/C88M-18
Soundness of coarse aggregate(RCA) in magnesium sulphate	0.6 %	ASTM C88/C88M-18
Soundness of natural fine aggregates in sodium sulphate	3.3 %	ASTM C88/C88M-18
Soundness of natural coarse aggregates in sodium sulphate	0.8 %	ASTM C88/C88M-18
Soundness of natural fine aggregates in magnesium sulphate	2.67 %	ASTM C88/C88M-18
Soundness of natural coarse aggregates in magnesium sulphate	0.65 %	ASTM C88/C88M-18
Los Angeles test (RCA)	29.6 %	ASTM C131/C131M–20

2.2. Clay

The clay samples were taken from the archeological region near the wall surrounding the ancient city of Nineveh at a depth of 1 m. According to the AASHTO Soil Classification System, the clay was pale reddish-brown, and was classified as A-2-6. According to the Unified Soil Classification System (USCS), the soil is (OH) organic clays of medium to high plasticity. The following tests were carried out:

1. Sieving of the particles through the No. 200 sieve according to ASTM D422-63(2007) to test the distribution of particle sizes in soils.

2. Calculation of specific gravity of soil solids according to ASTM D854.

3. Analysis of total soluble salts.

4. Soil organic matter chemical analysis in accordance with BS EN 1744-1:1998 and BS EN 1744-1:2009.

5. Analysis of the amount of gypsum in clay.

6. Atterberg limit test according to AASHTO T90 and ASTM D4218-20, ASTM D4318.

7. Determination of the shrinkage limit according to ASTM D4943.

2.3. Polyethylene Terephthalate

This study used recycled materials and waste to create a low-cost and environmentally friendly subbase. The waste plastic was used. Polyethylene was used as an additive to RCA at a percentage of clay soil (fine materials passing through the No. 200 sieve). It was used in following proportions: 2.5 %, 5 %, 7.5 %, and 10 % with type A and 5 %, 10 %, 15 %, and 20 % with type B – to increase the strength of the subbase layer. The polyethylene used is shown in Figure 4. It was mixed with graded recycled concrete aggregates of both A and B types.

Figure 4. The PET used in this study.

3. Results and Discussion

3.1. Clay Soil Test Results

The properties of the clay soil used with RCA as a binder for aggregates are presented in the Table 3.

Table 3. The results of the clay soil tests.

Data	L.L	P.L	P.I	SH.L	Clay size	Specific gravity	Soil organic matter	Total soluble salts	Amount of gypsum
Soil test results	38.6 %	23.9 %	14.7 %	5 %	56 %	2.577 %	7.8 %	1.2 %	10.5%

3.2. Recycle Concrete Aggregate

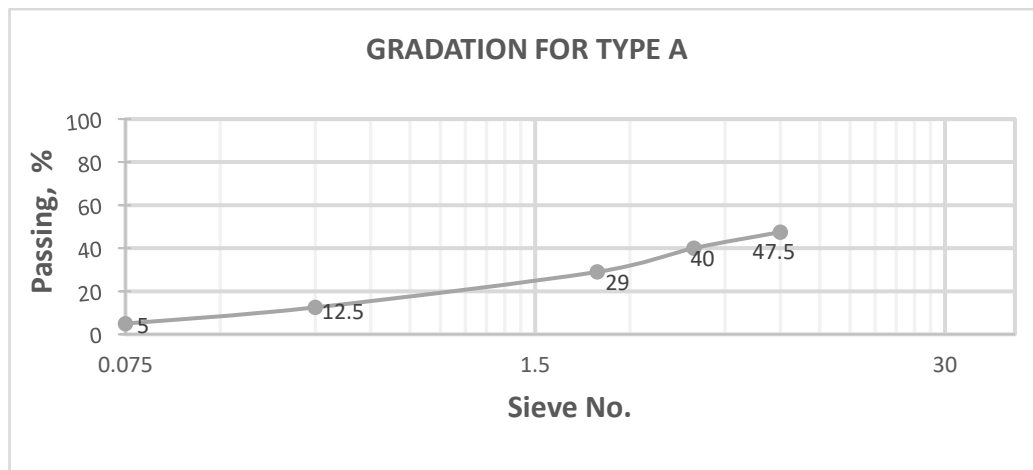Gradation, or particle size distribution, for types A and B are shown in Fig. 5 and 6 respectively.
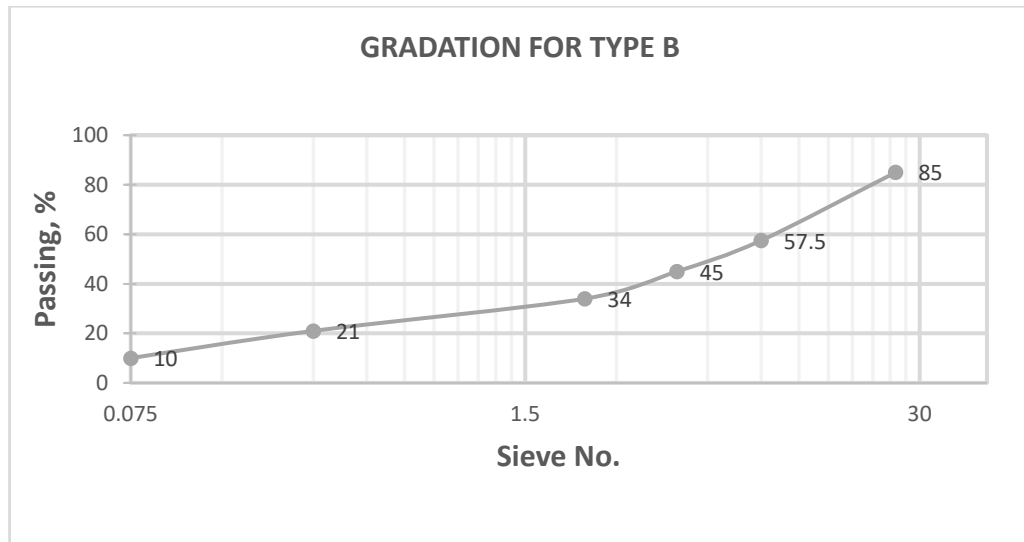

Figure. 5. Gradation for type A.

Figure. 6. Gradation for type B.

3.3.   Polyethylene Terephthalate

Table 4 shows the results of the physical tests conducted on polyethylene. Fig. 7 shows the gradation for polyethylene.

Table 4. The results of the physical tests conducted on polyethylene.

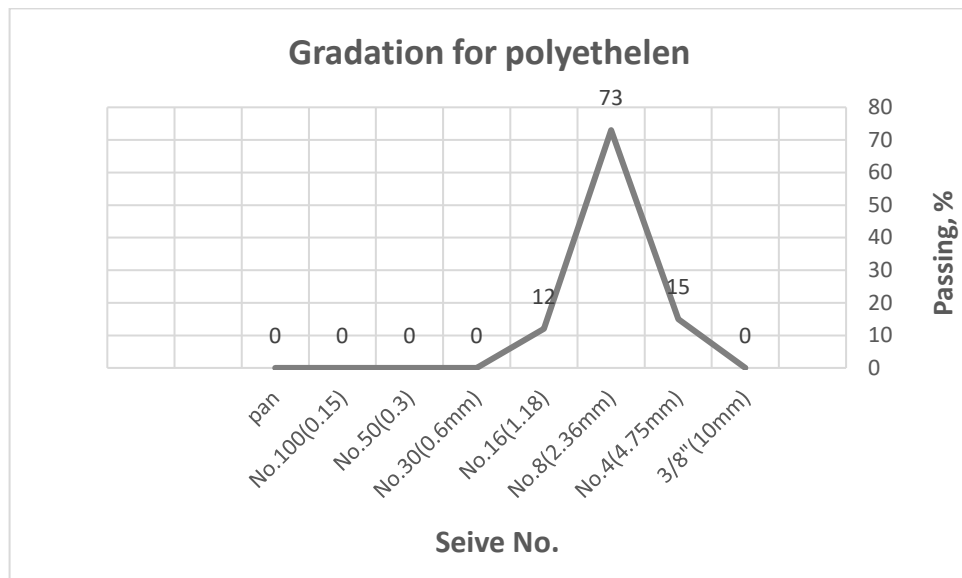| Data	Specific gravity	Absorption, %	Degree of burning	Degree of softening
Polyethylene test result	1.54	0.5	275	125

Figure. 7. Gradation for polyethylene.

3.4.   Proctor compaction test

Proctor Compaction test was conducted according to ASTM D698/AASHTO T99 and ASTM D1557/AASHTO T180. Samples were crushed to pass through sieves 1", 3/8", No. 4, No. 8, No. 50, No. 200, and pan for MDD and OMC.

Table 5. The values of MDD and OMC.

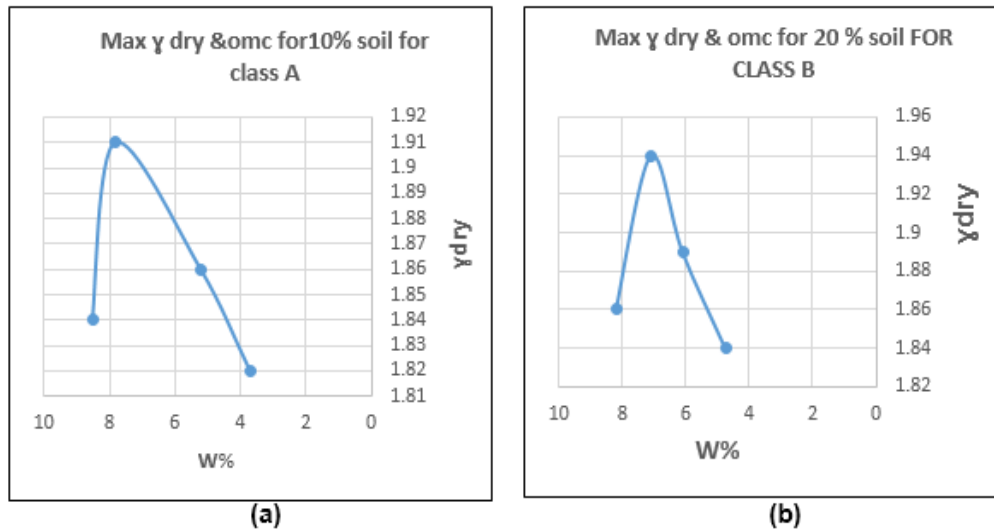| Data	Percentage of clay in soil, %	MDD for (RCA + soil), gm/cm³	OMC for (RCA + soil), %
Type A	10	1.91	7.8
Type B	20	1.94	7.1

Figure. 8. (a, b) W % and omc relationships for class A (a) and B (b).

3.5.   California Bearing Ratio (CBR) test

CBR test was conducted according to AASHTO T193 and ASTM D1883. Table 6 shows the results. And Fig. 9 and 10 show the added percentages of polyethylene and the results of CBR test values for types A and B.

Table 6. CBR test values.

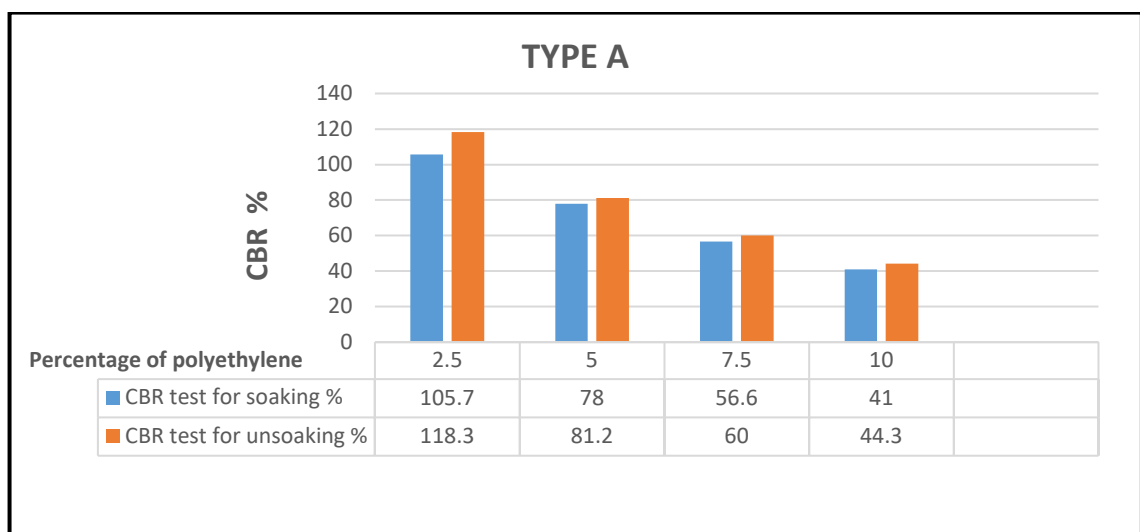| Type A					Type B				
Percentage of polyethylene with (10 % Soil + RCA), %	OMC for (RCA + soil), %	Soaked CBR test, %	Unsoaked CBR test, %	Swelling, %	Percentage of polyethylene with (20 % Soil + RCA), %	OMC for (RCA + soil), %	Soaked CBR test, %	Unsoaked CBR test, %	Swelling, %
2.5		105.7	118.3	0.12	5		121	131.4	0.19
5		78	81.2	0.22	10		75	78.2	0.27
7.5	7.6	56.6	60	0.32	15	7.0	52.1	58	0.42
10		41	44.3	0.57	20		40.4	47.1	0.55

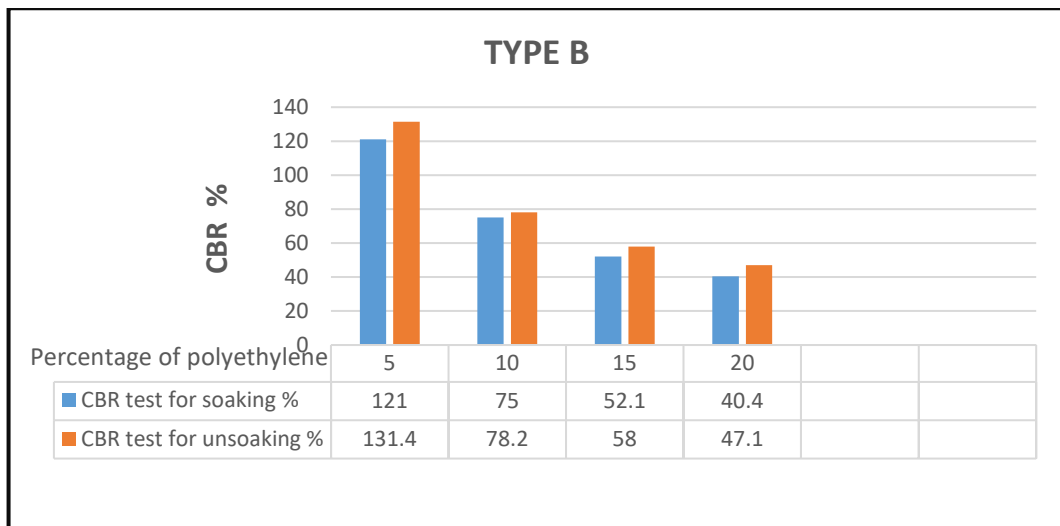**Figure. 9. Relationship between percentage of polyethylene and CBR test value for type A.**

Figure. 10. Relationship between percentage of polyethylene and CBR test value for type B.

Percentage of polyethylene	5	10	15	20		
■ CBR test for soaking %	121	75	52.1	40.4		
■ CBR test for unsoaking %	131.4	78.2	58	47.1		

Figure. 11. CBR testing.

3.6. Permeability

Permeability is the ability of water to flow through soil/sediment/rock. It is controlled by:

a) porosity;

b) grain size;

c) interconnection of the pores;

- sand/gravel: high permeability – high porosity, good interconnection of pores (k = 0.1 – 1000's m/day);

- clay: very low permeability – high porosity, moderate interconnection of the pores, very small pore size (k = <0.01 m/day) [27].

The coefficient of permeability for RCA mixes is more than 32 m/day, indicating that these mixes can be used for subsurface drainage purposes. Such a layer can also serve as a structural layer which is a lower subbase, but without desired drainage properties.

3.7. Erosion

The permeability test result, as shown in Fig. 12, was 0.032 m/s, according to Darcy's law. It could be compared with the values in Table 1 for Medium sand (0.0005–0.005 m/s). This value is reasonable and no noticeable erosion was observed.
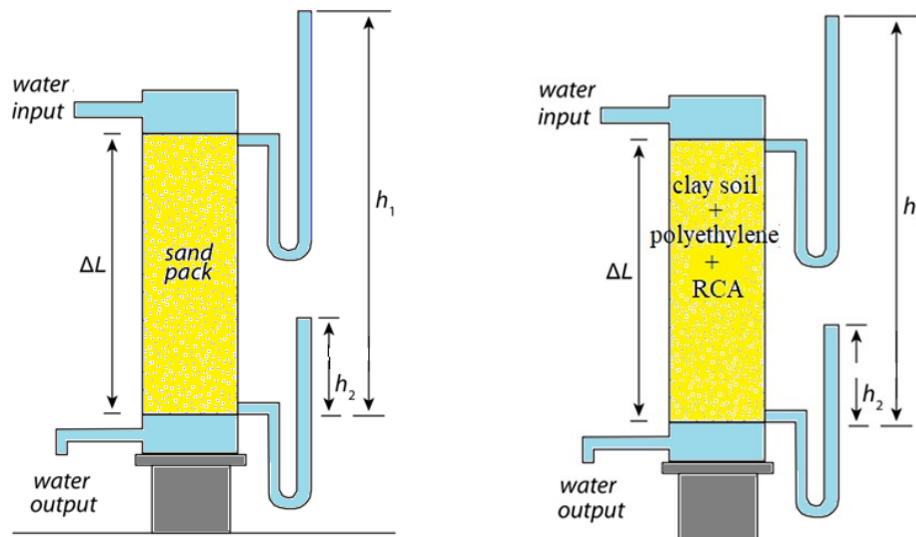
**Figure. 12. Schematic of Darcy's original experimental apparatus
(source: Maureen Feineman, Pennsylvania State University) and apparatus, used in experiment.**

4. Conclusions

This study focused on the use of waste materials such as demolition rubble and polyethylene in the design of subbase layer of the road. The impact of these wastes on CBR performance was also examined. In light of the results obtained, we were able to come to the following conclusions:

1. All tests carried out on recycled concrete were in accordance with US and Iraqi specifications in terms of Specific gravity, Absorption, Durability, L.A. Abrasion test.

2. There were two types (A, B) of granular subbase.

3. Clay soils had liquid limit 38.6 %, plastic limit 23.9 %, plasticity index 14.7 %, shrinkage limit 5 %, specific gravity 2.57, soil organic matter 7.8 %, total soluble salts 1.2 %, and amount of gypsum 10.5 %. According to the AASHTO Soil Classification System, it is classified as A-2-6. According to the Unified Soil Classification System (USCS), it is organic silty clay with low plasticity.

4. Recycled aggregates were used after the sieving test, carried out according to SORB.

5. It was concluded that the higher the percentage of polyethylene materials added, the lower the CBR value for types A and B. When adding 2.5 % of polyethylene, the CBR value was 105.7 % for the soaked sample and 118.3 % for the unsoaked sample. When adding 10 % of the polyethylene, the CBR value was 41 % for the soaked sample and 44.3 % for the unsoaked sample for type A. When adding 5 % of polyethylene, the CBR value was 121 % for the soaked sample and 131.4 % for the unsoaked sample. But when adding 20 % of the polyethylene, the CBR value was 40.4 % for the soaked sample and 47.1 % for the unsoaked sample for type B.

6. During the CBR testing, it was found that the CBR value of unsoaked samples had been higher than the CBR value of the soaked samples. Because the polyethylene pieces, when added to the mixture (RCA + clay soil) filled the spaces between the aggregate particles and made the sample cohesive. When the sample was immersed in water for 96 hours, water entered the sample and swelled the clay soil in the mixture, causing the polyethylene pieces to slide out of place, leaving empty spaces. These voids weakened the strength of the sample.

7. The use of the mixture (RCA + clay soil + polyethylene) gave satisfactory results in the tests, and the CBR value of the waste mixture exceeded the value specified in SORB for the design of the subbase layer.

8. The mixture (RCA + clay soil + polyethylene) could be used in the design of the subbase layer for the environmentally friendly roads.

References

1. Dhir, R.K., de Brito, J., Silva, R.V., Lye, C.Q. Use of Recycled Aggregates in Geotechnical Applications. Sustainable Construction Materials: Recycled Aggregates. 2019. Pp. 419–450. DOI: 10.1016/B978-0-08-100985-7.00011-X

2. Cardoso, R., Silva, R.V., de Brito, J., Dhir, R.K. Use of recycled aggregates from construction and demolition waste in geotechnical applications: A literature review. Waste Management. 2016. 49. Pp. 131–145. DOI: 10.1016/j.wasman.2015.12.021

3. Oikonomou, N.D. Recycled concrete aggregates. Cement and Concrete Composites. 2005. 27(2). Pp. 315–318. DOI: 10.1016/j.cemconcomp.2004.02.020

4. Huang, W.L., Lin, D.H., Chang, N.B., Lin, K.S. Recycling of construction and demolition waste via a mechanical sorting process. Resources, Conservation and Recycling. 2002. 37(1). Pp. 23–37. DOI: 10.1016/S0921-3449(02)00053-8

5. Sharobim, K.G., Hussein, N.A.M., Marzouk, M.H., El-Mansy, M.N. Assessment of Recycled Concrete aggregates as an Aggregate for Roads. Port Said Engineering Research Journal. 2017. 21(1). Pp. 41–48. DOI: 10.21608/pserj.2017.33438

6. Pérez, P., Agrela, F., Herrador, R., Ordoñez, J. Application of cement-treated recycled materials in the construction of a section of road in Malaga, Spain. Construction and Building Materials. 2013. 44. Pp. 593–599. DOI: 10.1016/j.conbuildmat.2013.02.034

7. Aytekin, B., Mardani-Aghabaglou, A. Sustainable Materials: A Review of Recycled Concrete Aggregate Utilization as Pavement Material. Transportation Research Record: Journal of the Transportation Research Board. 2022. 2676(3). Pp. 1–24. DOI: 10.1177/03611981211052026

8. Austroads. Guide to Pavement Technology Part 2: Pavement Structural Design. AGPT02–12. ARRB Grouted. Melbourne, Australia. 2012.

9. Hassoon, A., Al-Obaedi, J. The use of recycled concrete as a subbase layer for highways. Al-Qadisiya Journal for Engineering Sciences. 2014. 7 (3). Pp. 273–277.

10. Abbey, S.J., Ngambi, S., Coakley, E. Effect of cement and by-product material inclusion on plasticity of deep mixing improved soils. International Journal of Civil Engineering and Technology (IJCIET). 2016. 7 (5). Pp. 265–274.

11. Bajracharya, R.M., Manalo, A.C., Karunasena, W., Lau, K.T. Characterisation of recycled mixed plastic solid wastes: Coupon and full-scale investigation. Waste management. 2016. 48. Pp. 72–80. DOI: 10.1016/j.wasman.2015.11.017

12. Ghorbani, B., Arulrajah, A., Narsilio, G., Horpibulsuk, S., Bo M.W. Shakedown analysis of PET blends with demolition waste as pavement base/subbase materials using experimental and neural network methods. Transportation Geotechnics. 2021. 27. 100481. DOI: 10.1016/j.trgeo.2020.100481

13. Choudhary, A.K., Jha, J.N., Gill, K.S., Shukla S.K. Utilization of fly ash and waste recycled product reinforced with plastic wastes as construction materials in flexible pavement. Geo-Congress 2014: Geo-characterization and Modeling for Sustainability. 2014. Pp. 3890–3902. DOI: 10.1061/9780784413272.37

14. Yaghoubi, E., Arulrajah, A., Wong, Y.C., Horpibulsuk, S. Stiffness properties of recycled concrete aggregate with polyethylene plastic granules in unbound pavement applications. Journal of Materials in Civil Engineering. 2016. 29 (4). DOI: 10.1061/(ASCE)MT.1943-5533.0001821

15. Perera, S., Arulrajah, A., Wong, Y.C., Horpibulsuk, S., Maghool, F. Utilizing recycled PET blends with demolition wastes as construction materials. Construction and Building Materials. 2019. 221. Pp. 200–209. DOI: 10.1016/j.conbuildmat.2019.06.047

16. Jaber, N.H., Radhi, M.S., Alsaad, A.J. Ecological Applications of Polyethylene Terephthalate Plastic in Producing Modified Subbase Soil. IOP Conference Series: Materials Science and Engineering. 2021. 1067. 012006. DOI: 10.1088/1757-899X/1067/1/012006

17. Arulrajah, A., Yaghoubi, E., Wong, Y.C., Horpibulsuk, S. Recycled plastic granules and demolition wastes as construction materials: Resilient moduli and strength characteristics. Construction and Building Materials. 2017. 147. Pp. 639–647. DOI: 10.1016/j.conbuildmat.2017.04.178

18. Khattab, S.A., Al-Kiki, I.M., Al-Zubaydi, A.H. Effect of fibers on some engineering properties of cement and lime stabilized soils. Engineering and Technology Journal. 2011. 29 (5). Pp. 886–905.

19. Choudhary, A.K., Jha, J.N., Gill, K.S. A study on CBR behavior of waste plastic strip reinforced soil. Emirates Journal for Engineering Research. 2010. 15 (1). Pp. 51–57.

20. Highlands, K.L., Hoffman, G.L. Subbase Permeability and Pavement Performance. Transportation Research Record. 1988. 1159. Pp. 7–20.

21. Kandlavath, H.N., Chowdhury, P.S., Reddy, M.A. Evaluation of horizontal permeability characteristics of granular subbase material. Transportation Research Procedia. 2020. 48. Pp. 3725–3733. DOI: 10.1016/j.trpro.2020.08.046

22. Halyal, S., Kavitha, G., Balegar, A. Comparison of Permeability Characteristics of Granular Sub Base Layer in a Model Pavement for Different Grades as per MORT&H 5th Revision. European Journal of Applied Engineering and Scientific Research. 2017. 6 (1). Pp. 1–10.

23. Kermani, B., Xiao, M., Stoffels, S.M., Qiu, T. Measuring the migration of subgrade fine particles into subbase using scaled accelerated flexible pavement testing – a laboratory study. Road Materials and Pavement Design. 2019. 20 (1). Pp. 36–57. DOI: 10.1080/14680629.2017.1374995

24. Spitz, K., Moreno, J. A Practical Guide to Groundwater and Solute Transport Modeling. New York, 1996. 480 p.

25. Cedergren, H.R. Seepage, Drainage, and Flow Nets. New York: John Wiley & Sons, 1989. 19 p.

26. Standard specification for roads and bridges [Online]. URL: https://www.academia.edu

27. Watts, R. J. Hazardous wastes: sources, pathways, receptors. New York: John Wiley & Sons, 1998. 764 p.

28. Freeze, A., Cherry, J. Groundwater. Ch. 2. 1979. 604 p.

Information about authors:

Abdulbasit Abdulaziz Muhmood,
E-mail: *abdulbasit@ntu.edu.iq*

Anisotropy in mechanical properties of 3D-printed layered concrete

G.S. Slavcheva ✉ ⓘD , **A.V. Levchenko** ⓘD , **M.A. Shvedova** ⓘD , **D.R. Karakchi-ogly**, **D.S. Babenko**

Voronezh State Technical University, Voronezh, Russian Federation

✉ *gslavcheva@yandex.ru*

Keywords: additive manufacturing, 3D-printed concrete, mechanical properties, strength, anisotropy

Abstract. The article presents the results of studying the mechanical properties of 3D-printed layered concrete (3DPLC), including compressive, flexural, and splitting strength. To assess them, we used a compression test with a load applied perpendicular and parallel to the printed direction; a flexural test with a load applied perpendicular to the printed direction, and a splitting test to evaluate the interlayer bond strength upon the transfer of force along the boundary surface parallel to the printing direction. The mechanical properties of reference cast concrete (CC) were evaluated in accordance with the requirements of Russian standards. We established a significant anisotropy of the mechanical properties of 3DPLC along and perpendicular to the printed layers as well as a significant reduction in all strength values compared to similar values of reference CC. The printing time gap was the determining factor in the reduction of values of the mechanical properties for 3DPLC. When it increased to 20 minutes, a critical decrease in the interlayer bond strength was observed. At the same time, a threefold drop in the strength of 3DPLC compared to similar characteristics of CC could be observed in case of a decrease in humidity and a change in temperature in the range of +(10–30) °C. The impact of the curing condition on the variability of the mechanical properties of 3DPLC depended on the particle size distribution of fillers and aggregates that determined the surface roughness of the printed layer. The range of changes in the strength of sand-based printed concrete in case of varying temperature and humidity of curing (with a similar printing time gap) was 30–70 %, and for limestone-based printed concrete it was 1.5–3 times.

Citation: Slavcheva, G.S., Levchenko, A.V., Shvedova, M.A., Karakchi-ogly, D.R., Babenko, D.S. Anisotropy in mechanical properties of 3D-printed layered concrete. Magazine of Civil Engineering. 2024. 17(3). Article no. 12708. DOI: 10.34910/MCE.127.8

1. Introduction

Realizing the potential of 3D-build printing is associated not only with the possibilities of robotic construction of buildings, but also with the issues of calculation and design of hollow 3D-printed structures. Therefore, it is highly important to adequately evaluate the strength properties and standardize the classes of 3D-printed layered concrete (3DPLC).

Unlike traditional mold cast concrete (CC), strongly pronounced anisotropy of mechanical properties is typical for 3DPLC. Depending on the printing technology, constructions may have 2 types of stratification. Layering the next layer on top of the previous one creates horizontal stratification. If the next layer is layered next to the previous one on the same level, it may result in vertical and horizontal stratification. The strength

of a single-layer material $\left(R_{cc}\right)$ is greater than the strength of 3DPLC on the whole. However, upon the load action, the strength along the layers $\left(R_x\right)$ and across the layers $\left(R_y\right)$ significantly decreases.

The anisotropy in mechanical properties of 3DPLC is an object of present research.

In their review, A.U. Rehman and J.H. Kim [1] summarized and compared data from dozens of previous studies that presented relationships between the strength of 3DPLC along the layers $\left(R_x\right)$ and across the layers $\left(R_y\right)$ and the strength of the layer material $\left(R_{cc}\right)$. According to the results of different studies, these ratios varied greatly in the following range:

- compressive strength $R_{cx}/R_{cc} = 0.5 - 1.1, \ R_{cy}/R_{cc} = 0.6 - 1.1;$

- flexural strength $R_{fx}/R_{fc} = 0.3 - 0.9, \ R_{fy}/R_{fc} = 0.9 - 1.3;$

- tensile strength $R_{tx}/R_{tc} = 0.8 - 1.5, \ R_{ty}/R_{tc} = 0.3 - 0.5.$

It is obvious that the strength of 3DPLC is determined by the interlayer bond at the vertical and horizontal boundaries of layer separation. However, many studies [2–16] show that the strength of 3DPLC, compared to CC, decreased directly proportional to the printing time gap. In [3, 5, 7] it was shown that the strength and nature of destruction of layered printed samples was similar to the presented parameters of mold cast samples when layered with a printing time gap of up to 5 min. As the time interval between layering increased, the nature of the destruction changed, and cracks passed through the surface of the layer bond. Therefore, differences in the mechanical behavior of printed and cast concrete could be determined by interlayer effects that influence the path of crack development and failure patterns. As a result, the bond strength between the layers as well as compressive, flexural, and splitting strength of 3DPLC decreased. The interval of 20–30 minutes is considered critical, and exceeding this limit leads to self-destruction of the samples.

However, a more detailed analysis of the conditions of the experiments carried out in [2–15], the data of which were summarized and compared in [1], showed that in all cases the printing time gap did not exceed 1 minute [3, 8–14]. Therefore, the variability described above in data from different studies on the ratio of strength of 3DPLC and CC cannot be classified as the effect of this factor alone. In the analyzed research data, the compositions of mixtures varied significantly in their appearance and particle size distribution of fine aggregates and fillers [4, 9, 11–14] as well as printed samples curing. A number of works [16–19] used mixtures based on sand without fillers, while in [2, 20–21] they used mixtures that included various fillers (fly ash, silica fume, etc.) apart from fine aggregates. After printing, the curing state of samples also varied among different studies, mainly in the humidity of curing, which varied in the range of RH = 60–100 % [2, 13–16].

Based on this, it can be assumed that the interlayer bond strength and, correspondingly, mechanical properties of 3DPLC, apart from printing time gap, are determined by the following factors.

1. Temperature and humidity of curing. Interlayer bond strength of 3D-printed materials significantly depends on the open time, the time during which technological characteristics of fresh 3D-printable mixture (viscosity, plasticity) are preserved unchanged. In the works of A. Perrot et al. [22–24], it was proved that a decrease in the interlayer bond strength depended on the structural build-up rate: the greater the rate of curing was, the more impact the time between layering had on strength. This was due to the fact that temperature and humidity significantly affect the hydration and curing speed of cement paste.

2. Roughness of the layer surface depended on the particle size distribution of fillers and aggregates in the mixture. The roughness of the layer surface influenced the energy and the number of bonds at the interface between the layers, and therefore it can greatly affect the formation of the mechanical properties of 3DPLC.

The influence of these factors on the strength of 3DPLC has not been investigated, which determines the relevance of the research. The results presented here may have implications for use in the design of 3D-printed structure.

As a consequence, the present research aims to investigate the mechanical behavior and anisotropy properties of 3DPLC. In particular, the effects of three parameters on the properties of 3DPLC are considered as the objectives of present research:

– printing time gap;

– curing conditions – temperature and humidity;

– particle size distribution of fillers and aggregates used in mixtures.

2. Materials and methods

The studies were performed on two types of 3D-printable mixtures, the compositions of which were optimized by the authors in previous studies regarding extrudability, buildability, and strength of the layer material (Table 1):

1. sand-based mixture, patent RU 2729085 C1 [25];

2. limestone-based mixture, patent RU 2729283 C1 [26].

The initial components were used in the mixtures:
– Portland cement CEM I 42.5 R (EN 197-1:2011);
– Sika® plasticizer based on polycarboxylate ether;
– viscosity modifying admixture – metakaolin ($Al_2O_3 \cdot SiO_2$ content ~ 98 %, particle size distribution ranging from 1 to 5 μm);
– polypropylene fiber (l = 12 mm, d = 0.022–0.034 mm);
– limestone filler ($CaCO_3$ content ~ 95 %; particle size distribution ranging from 10 to 75 μm), silica sand (SiO_2 content ~ 95 %; particle size distribution ranging from 160 to 1200 μm).

Table 1. Concrete mixture design.

Mixture type	Components / mass cement (%)					W/C
	Plasticizer	Metakaolin	Polypropylene fiber	Silica sand	Limestone filler	
Sand-based	1.2	2	0.5	125	–	0.29
Limestone-based	1.2	2	0.5	–	100	0.39

To study and evaluate the mechanical properties of 3DPLC, an element ~ 50 cm long, 4 cm wide, and 16 cm high was printed on laboratory printer. The cross section of the layer was 40 × 20 mm, and the number of printed layers was 8. The following printing modes were used during the studies:

– constant print speed 20 mm/sec;

– constant distance between the nozzle and the layer 20 mm;

– variable printing time gap Δt = 0.5 min, 10 min, 30 min;

After printing, the 3D-printed samples were stored for 28 days in a different environment:

– standardized (T = 20 ± 2 °C, RH = 100 % (reference));

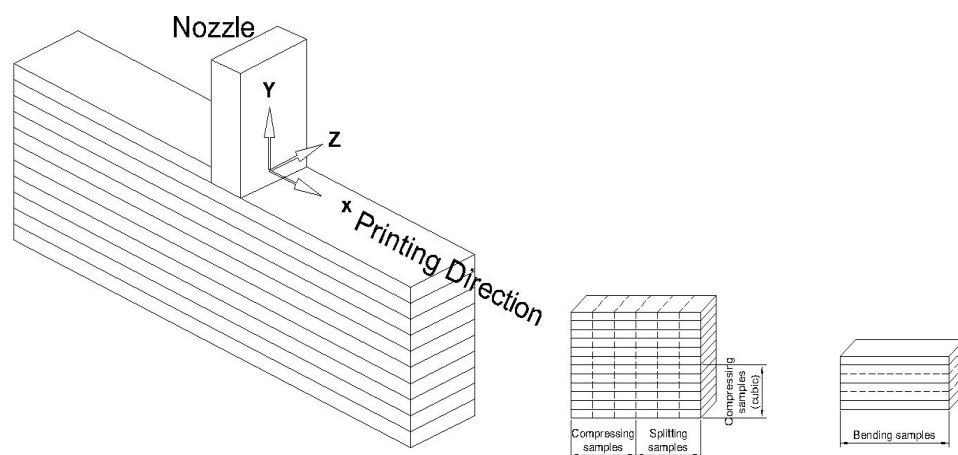– modelling (T = 10 ± 2 °C, RH = 60 %, T = 20 ± 2 °C, RH = 60 %, T = 30 ± 2 °C, RH = 60 %).

Figure 1. Scheme for preparing 3DPLC-sample for strength tests.

After curing, the model element was sawn into prism samples with the size of 40 × 40 × 160 mm.

The cutting layout of a 3D-printed model element is presented in Fig. 1.

Mechanical properties of CC were assessed as reference ones. In order to do this, reference mold samples were made from each batch of sand-based and limestone-based mixtures during the research simultaneously with the printing of model fragments. The mold samples were stored for 28 days in a standardized environment (T = 20 ± 2 °C, RH = 100 %).

3DPLC samples were tested as follows:

- compression test upon load application across the printed direction (Y-axes) – 3 prism samples in a series;
- compression test upon load application along the printed direction (X-axes) – 6 half-prism samples in a series;
- flexural test upon load application across the printed direction (Y-axes) – 3 prism samples in a series;
- splitting test to assess the interlayer bond strength with point force along the boundary surface in the sample along the printed direction (X-axes) – 3 prism samples in a series.

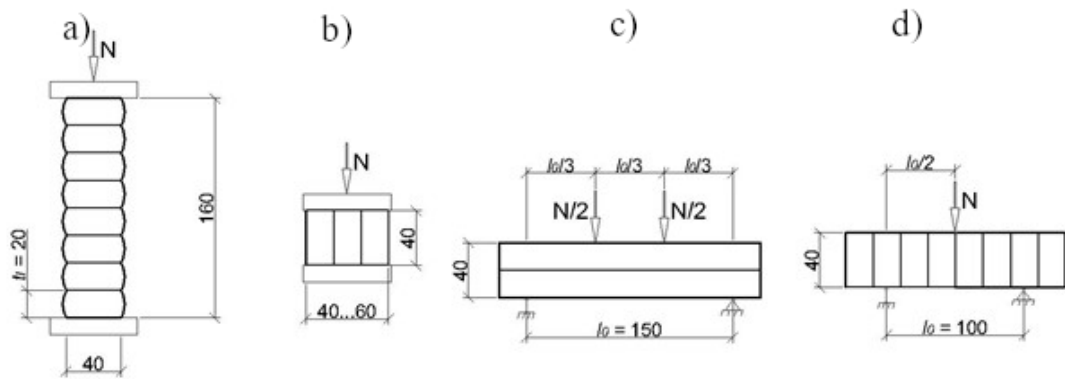Test patterns for 3DPLC samples are presented in Fig. 2.

Figure 2. Schemes for strength testing of 3DPLC-samples: (a) compressive strength test (Y-axes); (b) compressive strength test (X-axes); (c) four-point bending test (Y-axes); (d) splitting three-point bending test (X-axes).

The mold CC samples were tested according to Russian State Standard GOST 10180 "Concretes. Methods for strength determination using reference specimens".

A summary of the tests is presented in Table 2. Each set of sample is indicated by an abbreviation, where:

- CC is for the cast concrete;
- PLC is for the 3D-printed layered concrete;
- LM is for the limestone-based mixture;
- S is for the sand-based mixture.

Table 2. Test matrix.

Variables	Abbreviation			
	CC-S	CC-LM	PLC-S	PLC-LM
Printing Time Gap (min)	No	No	0, 10, 20	0, 10, 20
Samples curing (T; RH)	20 °C, 100 %	20 °C, 100 %	20 °C, 100 %; 20 °C, 60 %; 10 °C, 60 %; 30 °C, 60 %;	20 °C, 100 %; 20 °C, 60 %; 10 °C, 60 %; 30 °C, 60 %;
Load direction of compression test	According to Russian State Standard GOST 10180-2012 "Concretes. Methods for strength determination using reference specimens"		Y-axes, X-axes	Y-axes, X-axes
Load direction of flexural test			Y-axes	Y-axes
Load direction of splitting test			X-axes	X-axes

After mechanical tests were conducted, the destruction surface of the samples was examined on a desktop scanning electron microscope Thermo Scientific™ Phenom™ XL. We used the Phenom Desktop SEM software to operate the microscope as well as to obtain, process, and analyze the images. This software includes the Element Identification program, which can be used to operate the built-in EMF detector and to work with the information received from it.

3. Results and Discussion

According to the test results, we recorded a change in all mechanical properties of 3DPLC, compared to similar values of CC (Tables 3–5). The changes in the samples that were stored in a standardized environment were the following:

- prismatic strength upon axial compression and load application across the printed direction (Y-axes) decreased by 1.8 and 2.4 times for sand-based and limestone-based printed concrete, respectively;
- axial compressive strength upon load application along the printed direction (X-axes) reduced by 1.15 and 1.4 times for sand-based and limestone-based printed concrete, respectively;
- the strength at four-point load application across the printed direction (Y-axes), on the contrary, increased by 1.8 times for sand-based and limestone-based printed concrete;
- interlayer bond strength, according to splitting test, upon load application along the printed direction (X-axes) decreased by 2.1 and 1.4 times for sand-based and limestone-based printed concrete, respectively.

It is highly important that a significant anisotropy of 3DPLC properties was established. The compressive strength upon loading along and across the printed direction differed by 2–2.1 times, while the bending strength differed by 2.5–3.6 times. The loading conditions have the most significant influence on the level of anisotropy. The nature of the uniaxial compressive strength – displacement curves (Fig. 3, 4) for 3DPLC and CC differed most significantly in the tests with a load application along the printed direction (X-axes). A decrease in the slope of the ascending branch and the appearance of a long descending branch on the deformation curves are typical for 3DPLC-samples. Thus, the mechanical behavior of 3DPLC is characterized by the emergence of pseudo-plastic deformations.

Table 3. CC mechanical properties.

Mechanical properties	Mixture type	
	Sand-based	Limestone-based
Uniaxial compressive strength (prism) R_y^{cc}, MPa	49.33	46.98
Uniaxial compressive strength (cube) R_x^{cc}, MPa	3.90	2.80
Flexural strength R_{fy}^{cc}, MPa (according to four-point bending test)	3.90	2.80
Splitting strength R_{sx}^{cc}, MPa	4.04	2.97

Table 4. Sand-based 3DPLC mechanical properties.

Mechanical properties	Temperature and humidity of curing			
	T = 20 ± 2 °C, RH = 100 %	T = 10 ± 2 °C, RH = 60 %	T = 20 ± 2 °C, RH = 60 %	T = 30 ± 2 °C, RH = 60 %
Printing time gap Δt = 0.5 min				
Uniaxial compressive strength (Y-axes) R_y, MPa	27.65	19.48	24.89	16.27
Flexural strength (Y-axes) R_{fy}, MPa	6.92	5.70	6.46	6.48
Uniaxial compressive strength (X-axes) R_x, MPa	54.69	45.02	49.66	41.88

Mechanical properties	Temperature and humidity of curing			
	T = 20 ± 2 °C, RH = 100 %	T = 10 ± 2 °C, RH = 60 %	T = 20 ± 2 °C, RH = 60 %	T = 30 ± 2 °C, RH = 60 %
Interlayer bond (according to splitting test (X-axes)) R_{sx}, MPa	1.94	1.78	1.92	1.48
Printing time gap Δt = 10 min				
Uniaxial compressive strength (Y-axes) R_y, MPa	–	19.28	22.39	21.35
Flexural strength (Y-axes) R_{fy}, MPa	–	4.62	4.97	4.86
Uniaxial compressive strength (X-axes) R_x, MPa	–	49.87	51.26	45.07
Interlayer bond (according to splitting test (X-axes)) R_{sx}, MPa	–	0,82	1.53	1.57
Printing time gap Δt = 20 min				
Uniaxial compressive strength (Y-axes) R_y, MPa	–	–	–	–
Flexural strength (Y-axes) R_{fy}, MPa	–	3.10	3.60	3.89
Uniaxial compressive strength (X-axes) R_x, MPa	–	36.89	33.61	31.56
Interlayer bond (according to splitting test (X-axes)) R_{sx}, MPa	–	0.32	0.76	1.01

Table 5. Limestone-based 3DPLC mechanical properties.

| Mechanical properties	Temperature and humidity of curing			
	T = 20±2 °C, RH = 100 %	T = 10±2 °C, RH = 60 %	T = 20±2 °C, RH = 60 %	T = 30±2 °C, RH = 60 %
Printing time gap Δt = 0.5 min				
Uniaxial compressive strength (Y-axes) R_y, MPa	19.76	11.20	19.34	14.74
Flexural strength (Y-axes) R_{fy}, MPa	5.10	3.88	6.10	6.45
Uniaxial compressive strength (X-axes) R_x, MPa	41.91	37.99	41.13	36.51
Interlayer bond (according to splitting test (X-axes)) R_{sx}, MPa	2.08	0.67	2.55	2.27
Printing time gap Δt = 10 min				
Uniaxial compressive strength (Y-axes) R_y, MPa	–	–	15.89	–
Flexural strength (Y-axes) R_{fy}, MPa	–	3.95	4.74	5.52
Uniaxial compressive strength (X-axes) R_x, MPa	–	32.36	41.15	31.93
Interlayer bond (according to splitting test (X-axes)) R_{sx}, MPa	–	0.39	0.94	0.94

a)

b)
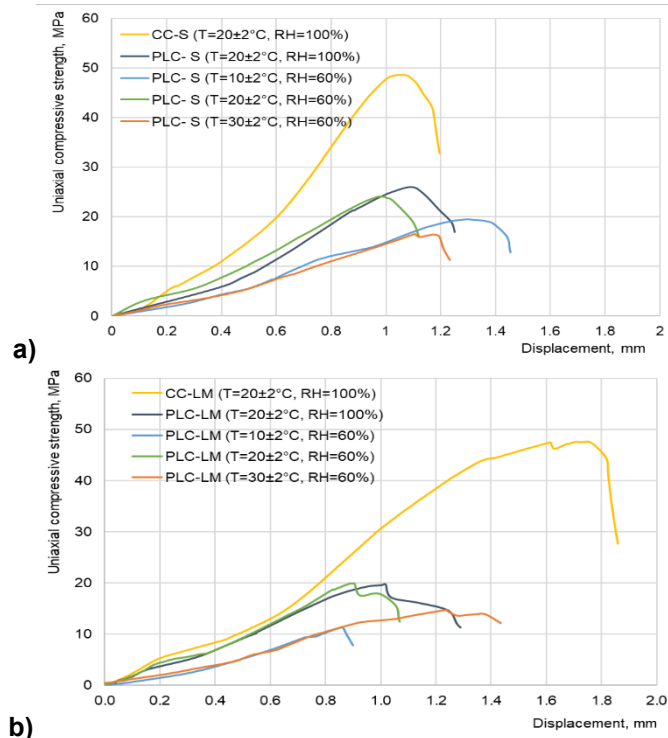
**Figure 3. Uniaxial compressive strength – displacement curves
(load across the printed direction (Y-axes)): (a) sand-based concrete;
(b) limestone-based concrete.**

Regarding the impact of technological parameters varied in experiments on the mechanical properties of 3DPLC, we established the following.
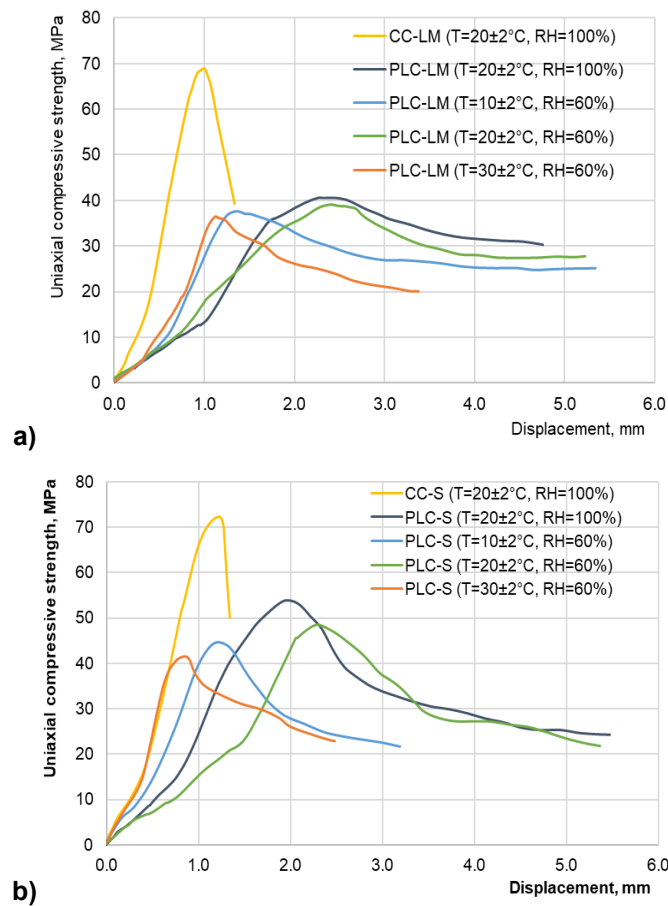

a)

b)

**Figure 4. Uniaxial compressive strength – displacement curves
(load along the printed direction (X-axes)): (a) sand-based concrete;
(b) limestone-based concrete.**

Printing time gap. Uniaxial compressive strength of 3DPLC (upon load application across the printed direction (Y-axes)), compared to CC, decreased by 1.8–3.0 times and by 2.3–4.2 times for sand-based and limestone-based printed concrete, respectively (Tables 1–3). As for the samples printed with the printing time gap Δt = 0.5 min and Δt = 10 min, the strength values with similar temperature and humidity conditions differed by less than 10–15 %. The samples printed with the Δt = 20 min split along the layer in the course of sawing, and the values of prismatic strength could not be recorded. Upon load application along the printed direction (X-axes), the compressive strength of 3DPLC decreased less significantly, compared to the compressive strength of CC. The decrease was by 1.15–1.5 times with Δt = 0.5 min and Δt = 10 min, while with Δt = 20 min it decreased by 1.7–2.0 times depending on temperature and humidity conditions of curing.

On the contrary, flexural strength of layered samples (upon a four-point bend and load application across the printed direction (Y-axes)), compared to CC, decreased by 1.2–1.8 times and by 1.4–2.3 times for sand-based and limestone-based printed concrete, respectively. The greatest increase of strength was observed for the samples with Δt = 0.5 min, which was by 1.5–2.3 times depending on temperature and humidity conditions of curing. An increase of strength for the samples with Δt = 10 min was by 1.2–1.3 times, and with Δt = 20 min the strength of 3DPLC samples was similar to its values for CC samples.

Interlayer bond strength of 3DPLC-samples, according to the splitting test (load direction along the printed direction (X-axes)), compared to the strength of CC samples with Δt = 0.5 min, decreased by 2.1–2.7 times, with Δt = 10 min – by 2.5–4.9 times, with Δt = 20 min – by 4–12 times depending on temperature and humidity conditions of curing. The samples printed with Δt = 10 min under all temperature and humidity conditions of curing had the interlayer bond strength of less than 1 MPa. The interlayer bond strength significantly decreased with Δt = 20 min, which was also confirmed by the destruction of layered samples in the course of cutting into prisms.

Temperature and humidity of curing. The humidity conditions of curing have the greatest impact on the change in strength for the entire set of mechanical properties, in all the studied cases of the time interval between the layering of layers. For all mechanical properties of 3DPLC cured at RH = 60 % and T = (10 – 30) ± 2 °C a decrease by 1.1–1.7 times was typical compared to similar samples cured under normal conditions (T = 20 ± 2 °C, RH = 100 %). The prismatic strength of the samples (Δt = 0.5 min) decreased most significantly upon curing RH = 60 % and T = 30±2 °C, by 1.7–1.8 times. Mechanical properties of 3DPLC cured at T = 10 ± 2 °C, RH = 60 %, and T = 30 ± 2 °C, RH = 60 %, were usually 10–35 % lower than the similar characteristics of the samples cured at T = 20 ± 2 °C, RH = 60 %.

With an increase in the printing time gap, the strength of limestone-based concrete decreased more, compared to sand-based concrete. At the same time, the variability of all strength characteristics of limestone-based concrete with varying temperature and humidity of curing was also higher.

According to the obtained experimental data, the range of variability of the ratios between the strength of 3DPLC along the layers $\left(R_{\mathrm{y}}\right)$ and across the layers $\left(R_{\mathrm{x}}\right)$ and the strength of the layer material $\left(R^{\mathrm{cc}}\right)$ was as follows (Fig. 5):

– compressive strength $R_{\mathrm{y}}/R_{\mathrm{y}}^{\mathrm{cc}}=0.24-0.56$; $R_{\mathrm{x}}/R_{\mathrm{x}}^{\mathrm{cc}}=0.51-0.87$,

– flexural strength $R_{\mathrm{fy}}/R_{\mathrm{fy}}^{\mathrm{cc}}=1.18-1.97$,

– splitting strength $R_{\mathrm{sx}}/R_{\mathrm{sx}}^{\mathrm{cc}}=0.13-0.86$.

The change in the mechanical properties of 3DPLC, compared to CC, was mainly determined by the specific aspects of the destruction of the layered structure upon the load action.

In case of axial compression (upon load application across the printed direction (Y-axes)), the destruction was characterized by the development of vertical cracks that crossed the layers with no changes in their crack path (Fig. 6a). Therefore, a significant decrease in the Y-axes compressive strength of 3DPLC, compared to the strength of CC, can be explained by weakening of material structure due to its layering. According to electron microscopy analysis, microdefects up to 100 μm were recorded at the boundary between the layers, which, upon load action, served as stress concentrators and contributed to the formation and development of cracks along the boundary line as well as across the layers (Fig. 7a).

The decrease in the X-axes compressive strength of 3DPLC, compared to CC, was less significant. In this case, when upon axial compression the load action was along the layers, the destruction was characterized by the development of multiple vertical cracks along the boundary surfaces as well as in the body of a single layer (Fig. 6b). This was associated with the fact that in this case of loading, the material of the layer makes a more significant contribution to the destruction resistance, which reduces the negative effect of weakening the material structure due to its layering.

In case of four-point bending, the load is applied across the layers (Y-axes), and the destruction is characterized by the development of a vertical crack that changes its path at the boundary surface (Fig. 6c) of 3DPLC-samples. Therefore, an increase in the flexural strength of 3DPLC, compared to the strength of CC, was due to the damping effect of the crack at the boundary surface.

When splitting, destruction occurs along the boundary of the adhesive bond between the layers (Fig. 6d), therefore, the roughness of the layer surface naturally affected the interlayer bond strength. According to SEM data, the destruction surface at the boundary surface for limestone-based concrete was smoother and more homogeneous (Fig. 7b), while for sand-based concrete (Fig. 7c) it was rougher due to the presence of sand grains. As a result, the decrease of splitting strength 3DPLC, compared to CC, was more significant for limestone-based concrete than for sand-based concrete.

Based on the obtained experimental data, it can be stated that the printing time gap was the determining factor in the reduction of values of the mechanical properties for 3DPLC. When it was increased to 20 minutes, we observed a critical reduction in the interlayer bond strength, which led to significant decrease in the values of all mechanical properties of 3DPLC, up to the self-destruction of the samples. This is in full agreement with the data of other researchers in [3, 5, 7, 8].

The novelty of the obtained results is that we clearly established a significant influence of the curing condition (temperature and humidity) on the variability level of the ratio between the mechanical properties of 3DPLC and CC $\left(R^{\mathrm{3DPLC}} / R^{\mathrm{CC}} \right)$. The $R^{\mathrm{3DPLC}} / R^{\mathrm{CC}}$ ratio can decrease by up to 3 times in case of changes in temperature and humidity of curing.
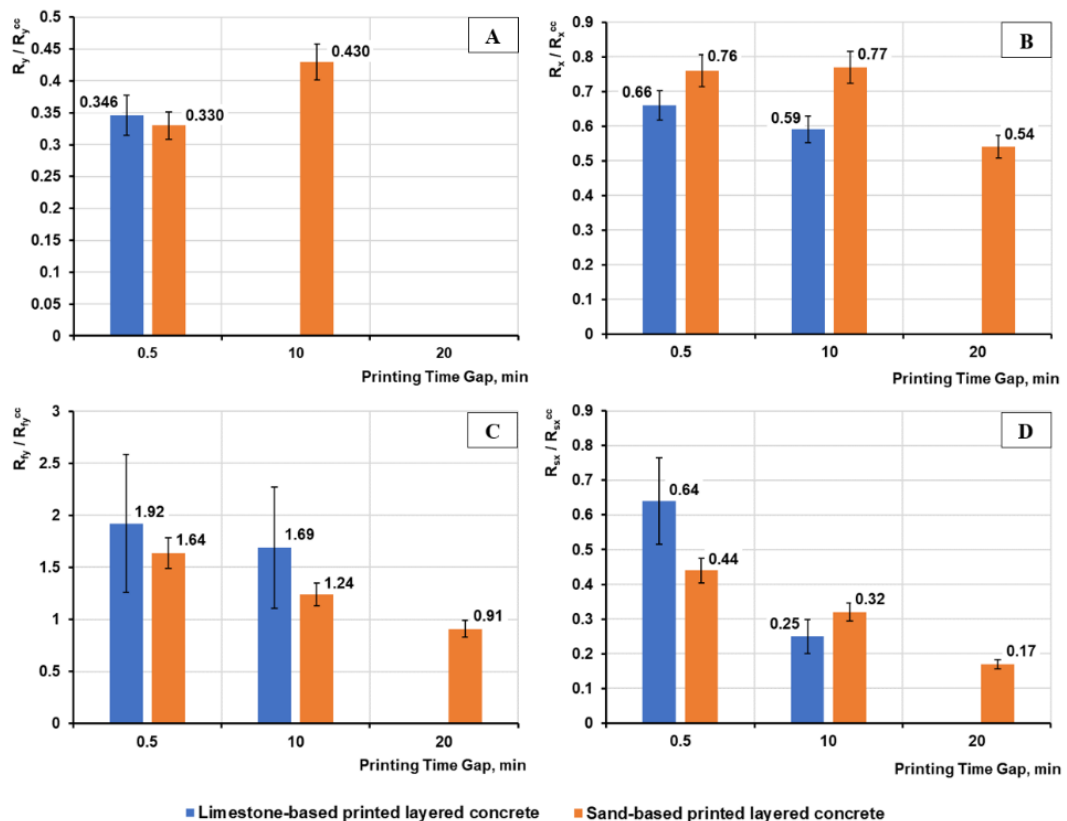

Figure 5. Anisotropy in mechanical properties of 3DPLC:
(a) uniaxial compressive strength (Y-axes); (b) uniaxial compressive strength (X-axes);
(c) flexural strength (Y-axes); (d) interlayer bond (according to splitting test (X-axes).
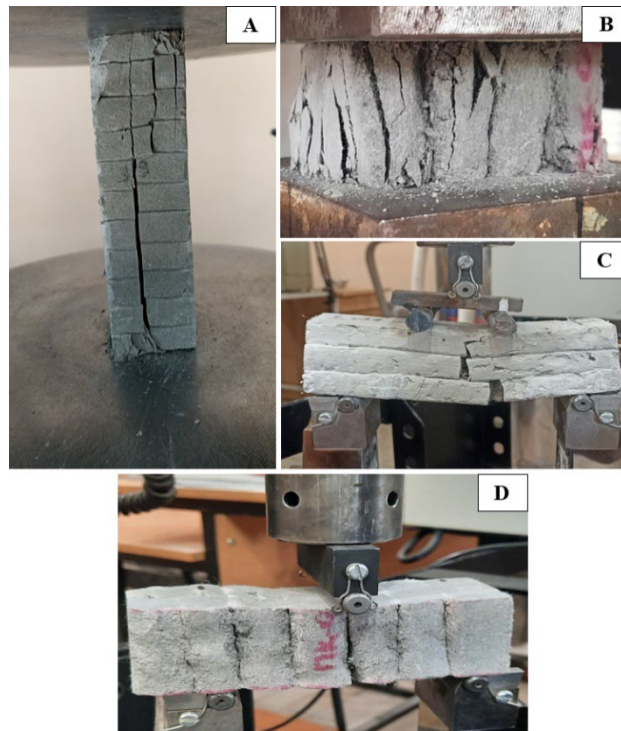
**Figure 6. Strength tests of 3DPLC-samples: (a) uniaxial compressive test (Y-axes);
(b) uniaxial compressive test (X-axes); (c) four-point bending test (Y-axes);
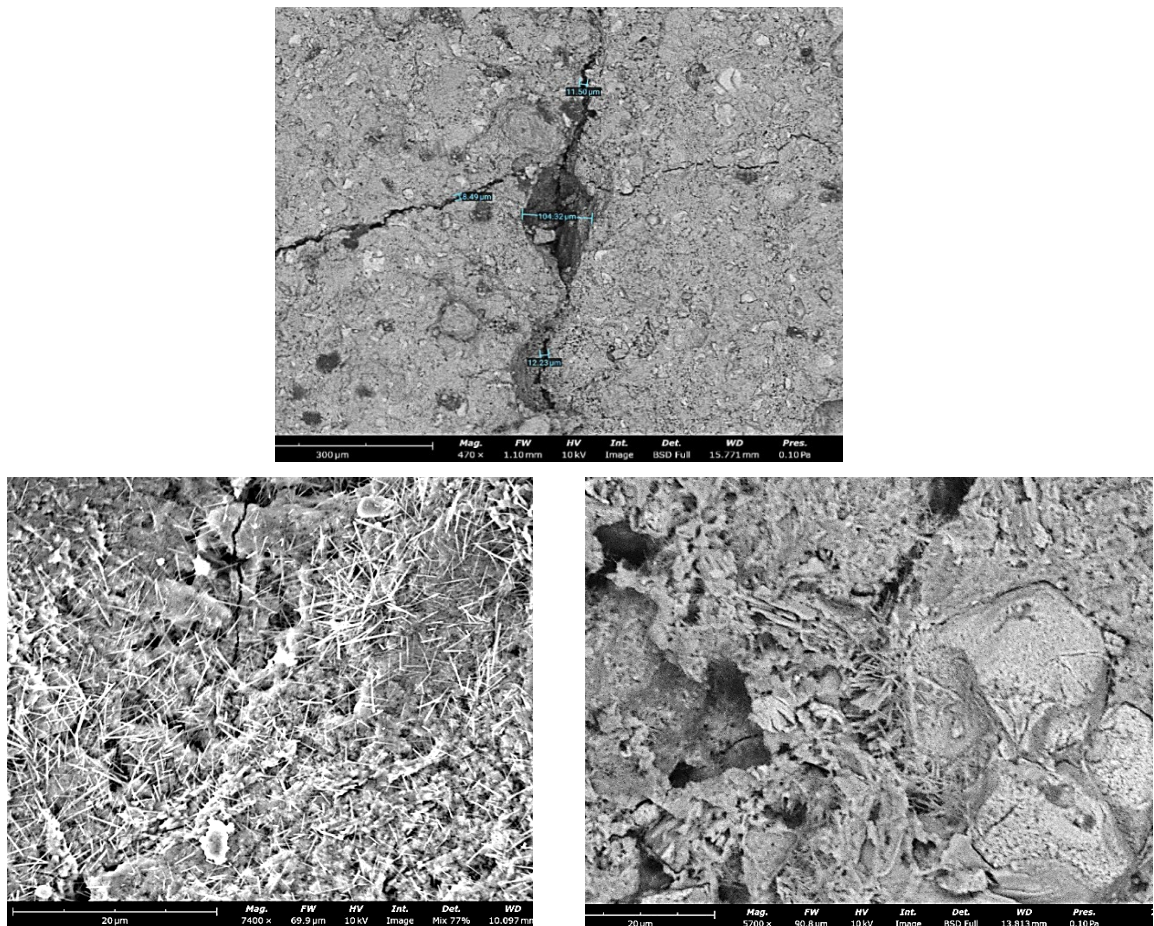(d) splitting three-point bending test (X-axes).**

**Figure 7. Micrographs of the fracture surface for 3DPLC: (a) across the printed layer;
(b) along the printed layer for limestone-based concrete; (c) along the printed layer
for sand-based concrete.**

The effect of a decrease in strength in case of reduction in temperature and humidity of curing was logically associated with a slowdown in the processes of cement hydration and corresponding decrease in the strength of the layer material. On the contrary, decrease in strength of 3DPLC related to the increasing temperature can be associated with increased setting rate and a corresponding decrease in the adhesion strength of the layers.

The extent to which curing condition influenced the variability of the mechanical properties of 3DPLC depended on the particle size distribution of fillers and aggregates. The range of changes in the mechanical properties of sand-based 3DPLC in case of varying temperature and humidity of curing (with printing time gap Δt = const) was 30–70 %, and for limestone-based 3DPLC it was 1.5–3 times. As noted above, this is explained by the factor of the layer surface roughness. When the hydration and curing conditions changed, the mechanical interlocking forces contributed more to the provision of interlayer bond strength, which could partially compensate for the physicochemical interactions at the boundary surface.

In conclusion, it is important to emphasize that at this stage of research we have not identified any clear quantitative patterns of the effect of temperature and humidity on certain types of strength values. The research must be expanded in order to obtain them.

4. Conclusions

1. A significant anisotropy of mechanical properties of 3D-printed layered concrete (3DPLC) along $\left(R_\mathrm{x}\right)$ and across $\left(R_\mathrm{y}\right)$ the printed layers was established. At the same time, a decrease in all values of strength with similar values of mold cast concrete (CC) was typical for 3DPLC. The range of variation in the ratio between the strength of 3DPLC and CC depended on the direction of load application regarding the direction of printing layers and was as follows:

   – compressive strength $R_\mathrm{y}\big/R_\mathrm{y}^\mathrm{cc} = 0.24 - 0.56; \quad R_\mathrm{x}\big/R_\mathrm{x}^\mathrm{cc} = 0.51 - 0.87;$

   – flexural strength $R_\mathrm{fy}\big/R_\mathrm{fy}^\mathrm{cc} = 1.18 - 1.97;$

   – splitting strength $R_\mathrm{sx}\big/R_\mathrm{sx}^\mathrm{cc} = 0.13 - 0.86.$

2. The printing time gap was the determining factor in the reduction of values of the mechanical properties for 3DPLC. When it was increased to 20 min, we observed a critical reduction in the interlayer bond strength, which led to significant decrease in values of all mechanical properties of 3DPLC, up to self-destruction of the samples.

3. We established a significant influence of the curing condition (temperature and humidity) on the variability level of the ratio between the strength of 3DPLC and CC $\left(R^\mathrm{3DPLC}\big/R^\mathrm{CC}\right)$. A threefold drop in the strength of 3DPLC, compared to similar characteristics of CC, could be observed in case of a decrease in humidity and a change in temperature in the range of + (10–30) °C.

4. The impact of the curing condition on the variability of the mechanical properties of 3DPLC depended on the particle size distribution of fillers and aggregates that determined the surface roughness of the printed layer. The range of changes in the strength of 3DPLC in case of varying temperature and humidity of curing (with printing time gap $\varDelta t$ = const) was 30–70 %, and for limestone-based 3DPLC it was 1.5–3 times.

References

1. Rehman, A.U., Kim, J.H. 3D concrete printing: A systematic review of rheology, mix designs, mechanical, microstructural, and durability characteristics. Materials. 2021. 14 (14). 3800. DOI: 10.3390/ma14143800

2. Le, T.T., Austin, S.A., Lim, S., Buswell, R.A., Law, R., Gibb, A.G.F., Thorpe, T. Hardened properties of high-performance printing concrete. Cement and Concrete Research. 2012. 42 (3). Pp. 558–566. DOI: 10.1016/j.cemconres.2011.12.003

3. Panda, B., Mohamed, N.A.N., Paul, S.C., Singh, G.V.P.B., Tan, M.J., Šavija, B. The effect of material fresh properties and process parameters on buildability and interlayer adhesion of 3D printed concrete. Materials. 2019. 12 (13). 2149. DOI: 10.3390/ma12132149

4. Wang, L., Jiang, H., Li, Z., Ma, G. Mechanical behaviors of 3D printed lightweight concrete structure with hollow section. Archives of Civil and Mechanical Engineering. 2020. 20. 16. DOI: 10.1007/s43452-020-00017-1

5. Chen, Y., Jansen, K., Zhang, H., Romero Rodriguez, C., Gan, Y., Çopuroğlu, O., Schlangen, E. Effect of printing parameters on interlayer bond strength of 3D printed limestone-calcined clay-based cementitious materials: An experimental and numerical study. Construction and Building Materials. 2020. 262. 120094. DOI: 10.1016/j.conbuildmat.2020.120094

6. Marchment, T., Sanjayan, J., Xia, M. Method of enhancing interlayer bond strength in construction scale 3D printing with mortar by effective bond area amplification. Materials & Design. 2019. 169. 107684. DOI: 10.1016/j.matdes.2019.107684

7. Keita, E., Bessaies-Bey, H., Zuo, W., Belin, P., Roussel, N. Weak bond strength between successive layers in extrusion-based additive manufacturing: measurement and physical origin. Cement and Concrete Research. 2019. 123. 105787. DOI: 10.1016/j.cemconres.2019.105787

8. Zareiyan, B. Khoshnevis, B. Effects of interlocking on interlayer adhesion and strength of structures in 3D printing of concrete. Automation in Construction. 2017. 83. Pp. 212–221. DOI: 10.1016/j.autcon.2017.08.019

9. Ducoulombier, N., Demont, L., Chateau, C., Bornert, M., Caron, J.F. Additive manufacturing of anisotropic concrete: A flow-based pultrusion of continuous fibers in a cementitious matrix. Procedia Manufacturing. 2020. 47. Pp. 1070–1077. DOI: 10.1016/j.promfg.2020.04.117

10. Karpova, E., Skripkiunas, G., Sedova, A., Tsimbalyuk, Y. Additive manufacturing of concrete wall structures. Proceedings of IV International Scientific Conference "Construction and Architecture: Theory and Practice of Innovative Development" (CATPID-2021 Part 1). Nalchik, 2021. DOI: 10.1051/e3sconf/202128103007

11. Dielemans, G., Briels, D., Jaugstetter, F., Henke, K., Dörfler, K. Additive Manufacturing of Thermally Enhanced Lightweight Concrete Wall Elements with Closed Cellular Structures. Journal of Facade Design and Engineering. 2021. 9 (1). Pp. 59–72. DOI: 10.7480/jfde.2021.1.5418

12. Zhu, B., Pan, J., Nematollahi, B., Zhou, Z., Zhang, Y., Sanjayan, J. Development of 3D printable engineered cementitious composites with ultra-high tensile ductility for digital construction. Materials & Design. 2019.181. 108088. DOI: 10.1016/j.matdes.2019.108088

13. Panda, B., Paul, S.C., Mohamed, N.A.N., Tay, Y.W.D., Tan, M.J. Measurement of tensile bond strength of 3D printed geopolymer mortar. Measurement. 2018. 113. Pp. 108–116. DOI: 10.1016/j.measurement.2017.08.051

14. Classen, M., Ungermann, J., Sharma, R. Additive manufacturing of reinforced concrete-development of a 3D printing technology for cementitious composites with metallic reinforcement. Applied Sciences. 2020. 10 (11). 3791. DOI: 10.3390/app10113791

15. Katzer, J., Szatkiewicz, T. Properties of concrete elements with 3D printed formworks which substitute steel reinforcement. Construction and Building Materials. 2019. 210. Pp. 157–161. DOI: 10.1016/j.conbuildmat.2019.03.204

16. Ji, G., Ding, T., Xiao, J., Du, S., Li, J., Duan, Z. A 3D printed ready-mixed concrete power distribution substation: Materials and construction technology. Materials. 2019. 12 (9). 1540. DOI: 10.3390/ma12091540

17. Lee, H., Kim, J.-H.J., Moon, J.-H., Kim, W.-W., Seo, E.-A. Evaluation of the Mechanical Properties of a 3D-Printed Mortar. Materials. 2019. 12 (24). 4104. DOI: 10.3390/ma12244104

18. Song, H., Li, X. An overview on the rheology, mechanical properties, durability, 3D printing, and microstructural performance of nanomaterials in cementitious composites. Materials. 2021. 14 (11). 2950. DOI: 10.3390/ma14112950

19. Albar, A., Chougan, M., Al- Kheetan, M.J., Swash, M.R., Ghaffar, S.H. Effective extrusion-based 3D printing system design for cementitious-based materials. Results in Engineering. 2020. 6. 100135. DOI: 10.1016/j.rineng.2020.100135

20. Wolfs, R.J.M., Bos, F.P., Salet, T.A.M. Hardened properties of 3D printed concrete: The influence of process parameters on interlayer adhesion. Cement and Concrete Research. 2019. 119. P. 132–140. DOI: 10.1016/j.cemconres.2019.02.017

21. Soltan, D.G., Li, V.C. A self-reinforced cementitious composite for building-scale 3D printing. Cement and Concrete Research. 2018. 90. Pp. 1–13. DOI: 10.1016/j.cemconcomp.2018.03.017

22. Perrot, A., Pierre, A., Nerella, V.N., Wolfs, R.J.M., Keita, E., Nair, S.A.O., Neithalath, N., Roussel, N., Mechtcherine, V. From analytical methods to numerical simulations: A process engineering toolbox for 3D concrete printing. Cement and Concrete Composites. 2021. 122. 104164. DOI: 10.1016/j.cemconcomp.2021.104164

23. Mechtcherine, V., Bos, F.P., Perrot, A., Leal da Silva, W.R., Nerella, V.N., Fataei, S., Wolfs, R.J.M., Sonebi, M., Roussel, N. Extrusion-based additive manufacturing with cement-based materials – Production steps, processes, and their underlying physics: A review. Cement and Concrete Research. 2020. 132. 106037. DOI: 10.1016/j.cemconres.2020.106037

24. Roussel, N., Bessaies-Bey, H., Kawashima, S., Marchon, D., Vasilic, K., Wolfs, R. Recent advances on yield stress and elasticity of fresh cement-based materials. Cement and Concrete Research. 2019. 124. 105798. DOI: 10.1016/j.cemconres.2019.105798

25. Slavcheva G.S., Artamonova O.V., Britvina E.A., Babenko D.S., Ibryayeva A.I. Dvukhfaznaya smes na osnove tsementa dlya kompozitov v tekhnologii stroitelnoy 3D-pechati [Two-phase mixture based on cement for composites in construction 3d printing technology]. Patent Russia No. 2729085, 2020.

26. Slavcheva G.S., Artamonova O.V., Britvina E.A., Babenko D.S., Ibryayeva A.I. Dvukhfaznaya smes na osnove tsementa dlya kompozitov v tekhnologii stroitelnoy 3D-pechati [Two-phase mixture based on cement for composites in construction 3d printing technology]. Patent Russia No. 2729283, 2020.

Contacts:

Galina Slavcheva, *Doctor of Technical Sciences*
ORCID: https://orcid.org/0000-0001-8800-2657
E-mail: gslavcheva@yandex.ru

Artem Levchenko, *PhD in Technical Sciences*
ORCID: https://orcid.org/0000-0002-6875-754X
E-mail: Alevchenko@vgasu.vrn.ru

Maria Shvedova,
ORCID: https://orcid.org/0000-0002-6484-8719
E-mail: marishwedowa@mail.ru

Davut Karakchi-ogly,
E-mail: karakchiogli.david@mail.ru

Dmitry Babenko,
E-mail: babenko.dmitrii@bk.ru

Research article

The roughness and bumping model
for cement pavement in seasonal frost regions

H.Q. Li[1], Q. Sun[2]✉, I.Z. Ideris[2], Q.Q. Zhao[3] (iD) *, R.S. Fediuk[4]* (iD) *, Y.C. Lei[5]* (iD) *, Y.Z. Yang[3]*

[1] *CHELBI Engineering Consultants Inc., Beijing, China*

[2] *Infrastructure University Kuala Lumpur, Kuala Lumpur, Malaysia*

[3] *Northeast Agricultural University, Harbin, China*

[4] *Far Eastern Federal University, Vladivostok, Russian Federation*

[5] *Central South University, Changsha, China*

✉ *465390034@qq.com*

Keywords: concrete, pavement management, numerical model, regression analysis

Abstract. The Statistical Package for Social Sciences (SPSS) Statistics software suit was used to test the model's goodness of fit and its normal distribution. Combined with the actual pavement survey data these tools were used to verify the model. The research results show that: permafrost and water-rich conditions have the same effect on pavement roughness and bumping; four key factors, including pavement riding quality index (RQI), pavement bumping index (PBI), frozen soil and water-rich environmental factors have significant impact on pavement roughness and bumping. The prediction model adjusted R^2 is 0.970, which is close to 1. The proposed model provides a high degree of fit and satisfies the assumption of normal distribution. When the PBI is from 87.5 to 95, the permafrost environmental factor is from 0.0002 to 0.0014, and the water-rich environmental factor is from 10.73 to 14.87, the prediction level of the model is the best. The model's RQI prediction value and the measured value has a degree of fit 0.987, which shows a good prediction effect. The prediction model can reasonably predict the roughness and the bumping of cement concrete pavement, which is of great significance to improve road traffic safety and to prolong the service life of cement concrete pavement in seasonal frost regions and water-rich areas.

1. Introduction

Roughness is an important pavement characteristic to evaluate the ride quality. Its value has a great impact on driving comfort and safety, damage to roads and vehicles, and is directly related to the amount of maintenance work and the durability of the road. Pavement bumping is a sudden bump of the vehicle caused by damage such as abnormal protrusion or subsidence of the road surface, which not only seriously affects the comfort of the vehicle, but also poses a serious safety hazard to the driving of the vehicle. At the same time, along with greater dynamic load of the vehicle, it causes greater damage to the road surface, decreases the road performance, and increases vehicle wear and fuel consumption. Therefore, in China's

"Highway Performance Assessment Standard" (JTG5210-2018), the pavement bumping index $\left(PBI \right)$ is given a certain weight separately, and it is used together with the pavement roughness as an index to evaluate driving comfort.

The research results in China and abroad on pavement roughness and bumping mainly focus on the factors affecting pavement roughness [1], the prediction of pavement roughness [2–4], and the detection and basic control measures of pavement bumping. There is no connection between pavement roughness and bumping, that is why mutual prediction between the two cannot be implemented. Among other studies, research on the factors influencing pavement roughness mainly focuses on the effect of moisture on pavement roughness or the effect of frozen soil environment on pavement roughness [5–9]. Most of the pavement roughness predictions are based on the international roughness index (IRI) prediction model [10–15]. Alimoradi et al. [16] improved the prediction model represented by Markov chain and realized the direct prediction of IRI. Patrick et al [17] considered the effect of different climatic conditions on the susceptibility of pavement to various types of surface distress, and established a relationship between existing surface distress and IRI. Among a few prediction models, the artificial neural network pavement roughness prediction model established by Kargah-Ostadi et al [18] is suitable for flexible pavement in wet-freeze climate, but the application scope is relatively limited. Fang et al [19] used the past roughness index values as alternative indicators of influencing factors to establish a time series pavement roughness prediction model with high accuracy. But since the time series itself is a dynamic tool, the model still needs to be modified. Nurhadiansyah et al [20] proposed to use the gray forecasting model to predict the value of toll road roughness index, and improve forecasting accuracy using Similarity Spatial Data (SSD), but it has higher requirements on the quantity and quality of the data used. At present, pavement bumping is still in the process of improvement. The foreign research on vehicle jumping mostly focuses on vehicle bumps at bridge head and the ways to mitigate these impacts [21, 22]. There are few studies on pavement bumping.

Although the above-mentioned researches are more in-depth regarding the pavement roughness and bumping, the specific relationship between pavement roughness and bumping has not been studied yet, so it is necessary to develop the model of the relationship between pavement roughness and bumping. Establishing a model of the relationship between pavement roughness and bumping in multi-factor conditions can predict them and benefit to improve road safety, driving comfort and timely pavement maintenance.

In order to achieve the goal of establishing a model of the relationship between roughness and bumping on cement pavement suitable for frozen soil and water-rich environment, this study compared the changes in pavement roughness and bumping based on actual survey data of cement roads in frozen soil and water-rich environments, and established a model of the relationship between pavement roughness and bumping, and determined applicable model conditions through experiments.

2. Methods

2.1. The influence of factors on pavement roughness and bumping

In order to explore the effect of frozen soil environment on pavement roughness, China Jing-kun Expressway (K353-K400) (A) and China Ha-zhao Highway (K50-K120) (B) were selected. In order to analyze the effect of frozen soil environment on pavement bumping, China national G214 highway (K97-K720) (C) in Qinghai Province was selected, which includes both non-frozen soil and frozen soil areas. To study the effect of water-rich environment on pavement roughness, China Jing-kun Expressway (K353-K400) (A) and Guangdong Shan-zhan Expressway Zi-jin link section (D) were selected. In order to measure the effect of water-rich environment on pavement bumping, China River Beijing-Harbin Expressway (K102-K262) (E) and Beijing-Hong Kong-Macau Expressway (K1016+000-K1310+000) (F) were selected. In the following discussion, the influence of frozen soil and water-rich conditions on pavement roughness will be divided into left and right sections for consideration. The above expressways were selected based on the location distribution of the seasonal frost regions that have been fully considered.

In order to study the effect of frozen soil environment on pavement roughness. Separate sections A and B, with the standard of separation being the corresponding station numbers every 100m, and assign station numbers 1-8. The laser profiler was used to determine the elevation of the section, and IRI value was synchronized, and the pavement riding quality index (RQI) was calculated using the equation (7.4.7) in Chinese "Highway Performance Assessment Standard" (JTG5210-2018). The result is shown in Fig. 1.

In this figure "Serial number" should be replaced with "Pile number" (as in Figure 1 in the article "Antiskid prediction model for cement pavements in seasonal frost regions").
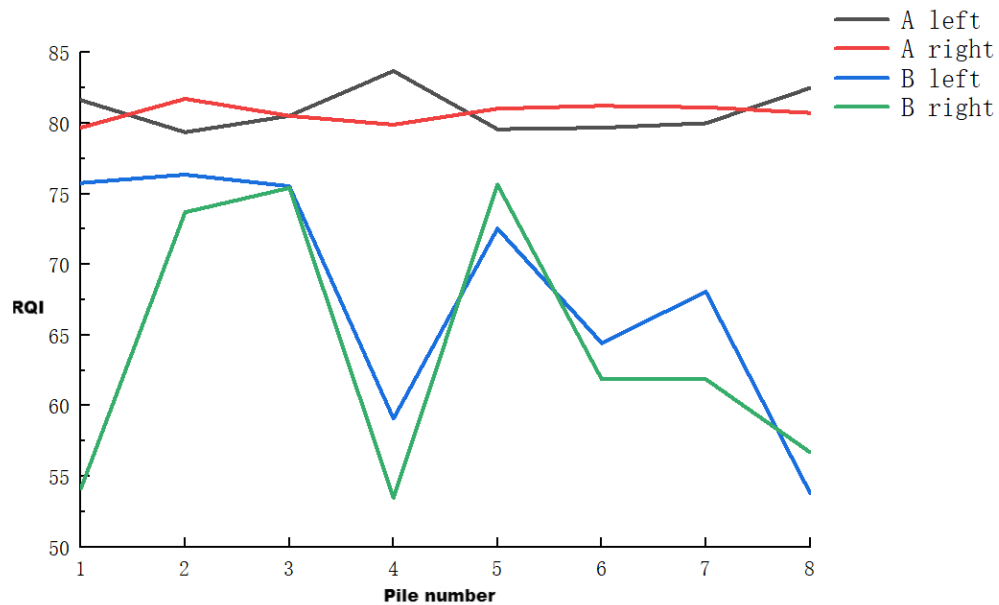
Figure 1. Distribution of pavement roughness in frozen and non-frozen soil areas.

As shown in Fig. 1, the difference between the maximum and minimum values of RQI on the left and right sections of road B in the frozen soil area can reach 20, and the variation is obvious. This is because the right side of the road is adjacent to a sand mining village. The plant uses many heavy-duty vehicles, which largely effects the pavement roughness on the right side of the road. RQI of the left and right sections of road A in the non-frozen soil area averages 82 with slight deviations, which proves that the impact of traffic load on pavement roughness is small. However, if we compare the left section of road A with the left section of road B, the right section of road A and the right section of road B, it becomes obvious that the difference in RQI between road B in the frozen soil area and road A in the non-frozen soil area can reach up to 25. On the left section of road A and the left section of road B at piles 2-3 and 5, the gap varies within 10 %. The main reason for this difference is that the low temperature in the frozen soil area causes the water in the base layer to freeze and solidify, while causing the road surface to expand and swell, at the same time, due to the inconsistent thermal conductivity of the pavement materials, the overall lateral force of the road is uneven. On the left section of road A and the right section of road B at piles 4 and 8, the difference in RQI between road B in frozen soil area and road A in non-frozen soil area is 30. The reason for this is that the water content and ice accumulation of the road sections corresponding to pile numbered 4 and 8 in the seasonal frost area differ from those corresponding to other piles, resulting in uneven frost heaving of the road surface. With the expansion of the frost heave range, the tensile force on the pavement gradually increases. When the tensile limit of the pavement material is exceeded, longitudinal cracks occur, and after the condensed ice melts, the base layer softens and turns into mud. The laitance is squeezed out of the road surface after being crushed by the load of vehicles, causing the road surface to tumble and sink, resulting in drastic changes in the pavement roughness of the road surface.

In order to analyze the impact of frozen soil environment on pavement bumping, using to the above method of dividing the road surface into sections with numbered piles, road C was divided into 44 sections with numbered piles. Moreover, 22 numbered piles were used for the non-frozen soil area and 22 numbered piles were used for the frozen soil area. In order to facilitate comparison of the number of pavement bumping in the frozen and non-frozen soil areas, the non-frozen soil and frozen soil pile numbers are numbered from 1 to 22, respectively. The multi-functional road condition rapid detection system is used to detect the elevation of the vertical section of the road, and determine the presence of bumping and the number of bumps based on the vertical section height difference. The results are shown in Fig. 2.
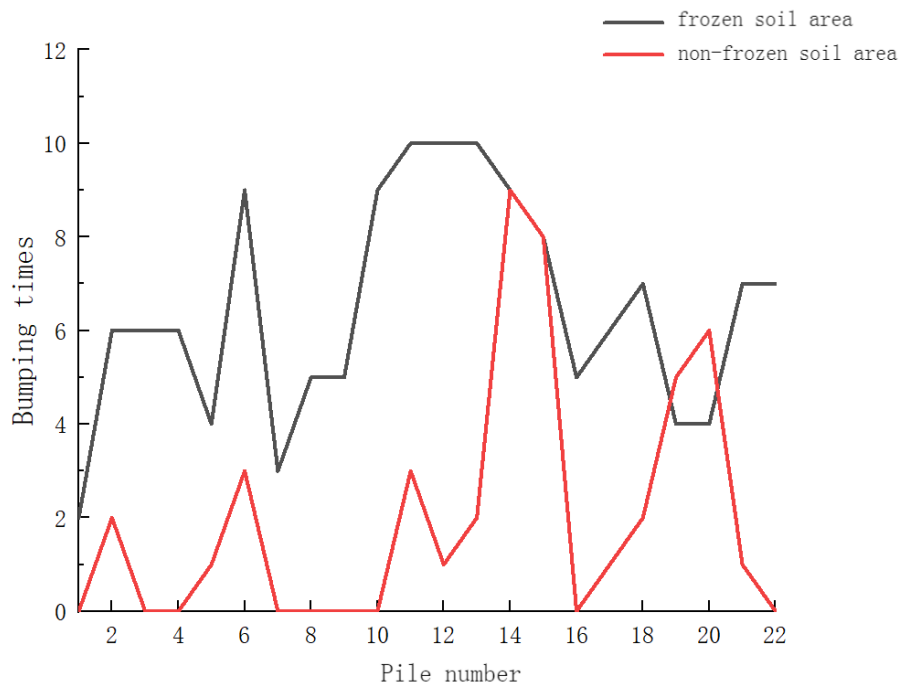
Figure 2. Distribution of pavement bumping in the frozen and non-frozen soil areas.

As shown in Fig. 2, there is a pavement bumping phenomenon in each section of the frozen soil area, and the number of pavement bumping in the frozen soil area is on average greater than that in the non-frozen soil area. Data analysis shows that the number of pavement bumping per kilometer in frozen soil area is about 2.4 times that of non-frozen soil area. The analysis of the cause is that the freezing of soil water and the thickening of ice in the frozen soil area lead to soil expansion and uneven surface uplift. At the same time, the frozen soil sinks when it melts, which eventually leads to uneven settlement of the road surface. Significant changes in road elevation have led to a significant increase in vehicle jumping onto the road while driving. Based on the analysis of Fig. 1 and 2, it is clear that climatic conditions in the seasonal frost regions will lead to the development of a tendency to deteriorate due to pavement roughness and bumping.

To study the effect of water-rich environment on pavement roughness, roads A and D were also divided into sections with piles numbered from 1 to 8. A high-precision profile meters were used to collect elevation data and pavement roughness values. RQI was calculated using the equation (7.4.7) in Chinese "Highway Performance Assessment Standard" (JTG5210-2018). The result is shown in Fig. 3.
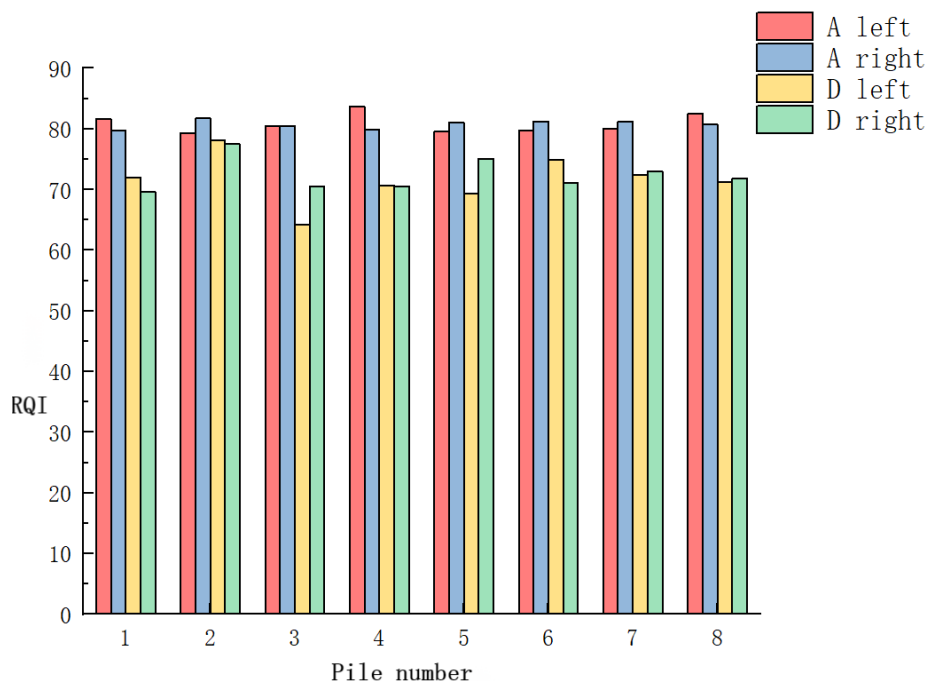

Figure 3. Distribution of pavement roughness in water-rich and non-water-rich areas.

As shown in Fig. 3, RQI of the left and right sections of road A in the non-water-rich area averages 82 with slight deviations, while RQI of the water-rich area averages 70. The reason is that there is a lot of rainfall in the water-rich areas, and the road surface joint filler fails due to rain erosion. With the frequent impact of wheels, the bending tensile stress in the slab exceeds the ultimate flexural strength of the material, resulting in cracks and fractures in the panel. Water infiltrates from the joints or cracks, and the mud in the cracks is squeezed out by the water pressure, causing rainwater to seep between the underlying and base layer. Water pressure becomes too high, and the top ash of the base layer sprays out from the cracks in the road. The base material forms a cavity, which aggravates the pavement network crack. RQI of the left section of road D has a sudden change from 78 to 65 at piles 2 and 3. The reason is that there is groundwater at this piles, and there are cavities in the roadbed soil due to groundwater erosion, which causes the roadbed to sink. At the same time rainwater will be further immersed into the roadbed, and the water content of the roadbed will increase, which will affect the compaction and bearing capacity of the soil. The uneven distribution of the water content of the roadbed soil results in uneven strength of the roadbed, causing local differential settlement of the roadbed, various slope cracks, slope settlement, etc. which lead to sudden changes in pavement roughness. The above analysis shows that water-rich environment has a serious effect on the pavement roughness, and the performance of reducing the pavement roughness is obvious.

To study the effect of water-rich environment on pavement bumping, roads E and F were also divided into sections with piles numbered from 1 to 8. A laser profiler was used to measure longitudinal elevation of the road section. PBI was calculated using the equation (7.4.9) in Chinese "Highway Performance Assessment Standard" (JTG5210-2018). The result is shown in Fig. 4.
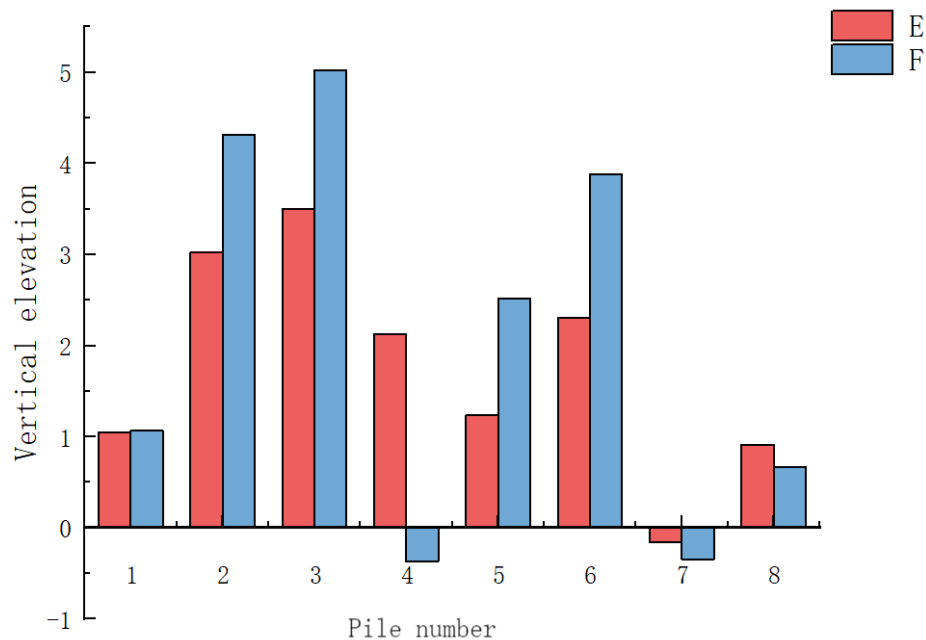

Figure 4. Distribution of pavement bumping in water-rich and non-water-rich areas.

As shown in Fig. 4, the vertical elevation of road E in the non-water-rich area is lower than that of road F in the water-rich area. The road elevation of the road F at the piles 3 and 6 drops significantly. Because the elevation zero point is chosen differently, the phenomenon of changing from positive to negative appears. The reason is that the water content of the roadbed increases due to the large amount of precipitation on road F, which affects the strength of the roadbed and causes the road surface to settle and the phenomenon of pavement bumping to appear. The greater the rainfall, the greater the water content of the roadbed, and the greater the impact on the strength of the roadbed, the greater the road subsidence, the more bumping times will appear.

Based on the analysis of Fig. 3 and 4, it can be concluded that water-rich environment will reduce the roughness of cement concrete pavement and the performance of pavement bumping.

In order to further analyze the impact of the coupling effect of frozen soil and water-rich conditions on the pavement roughness, the data in Fig. 1 and Fig. 3 were summarized, and the results are shown in Fig. 5.
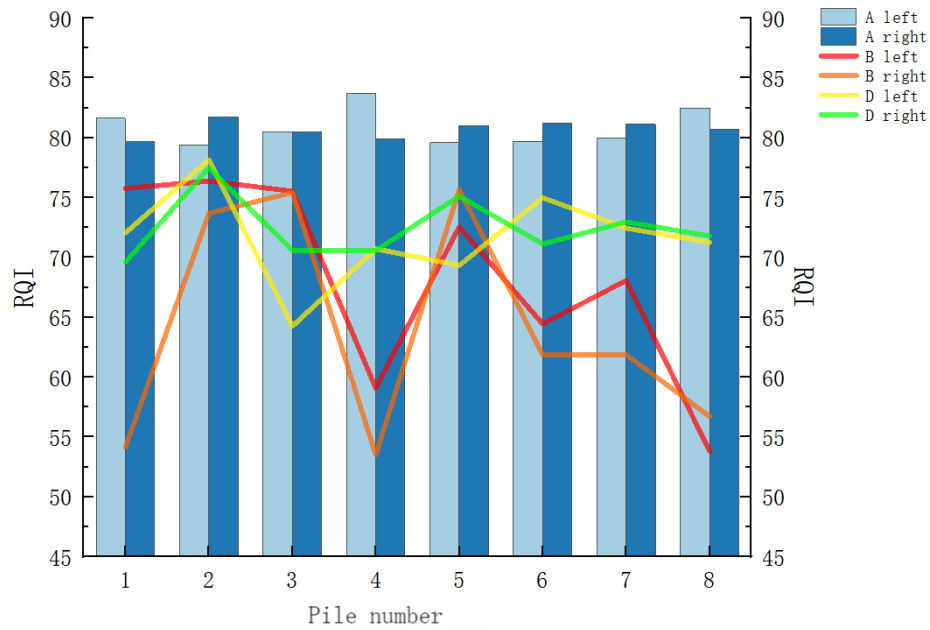
Figure 5. Distribution of road pavement roughness under coupling.

In Fig. 5 RQI of road A in the non-frozen soil and non-water-rich environment averages 80, while RQI s of road B and D in the frozen soil and water-rich environment have decrease significantly. The reason is that under the condition of a certain water content, the lower the temperature, the stronger the frost heave of the soil, the greater the change in road elevation and the smaller RQI is. Under the condition of a certain temperature, the higher the water content, the stronger the frost heave of the soil, the higher the heat resistance and thawing, the greater the change in road elevation and the smaller RQI is. The analysis shows that RQI is directly proportional to temperature and inversely proportional to water content.

In order to explore the impact of frozen soil and water-rich environment on the pavement bumping, the number of severe bumps on the road sections was collected through the road management office of each section and coded 1-8, respectively. The results are shown in Fig. 6.
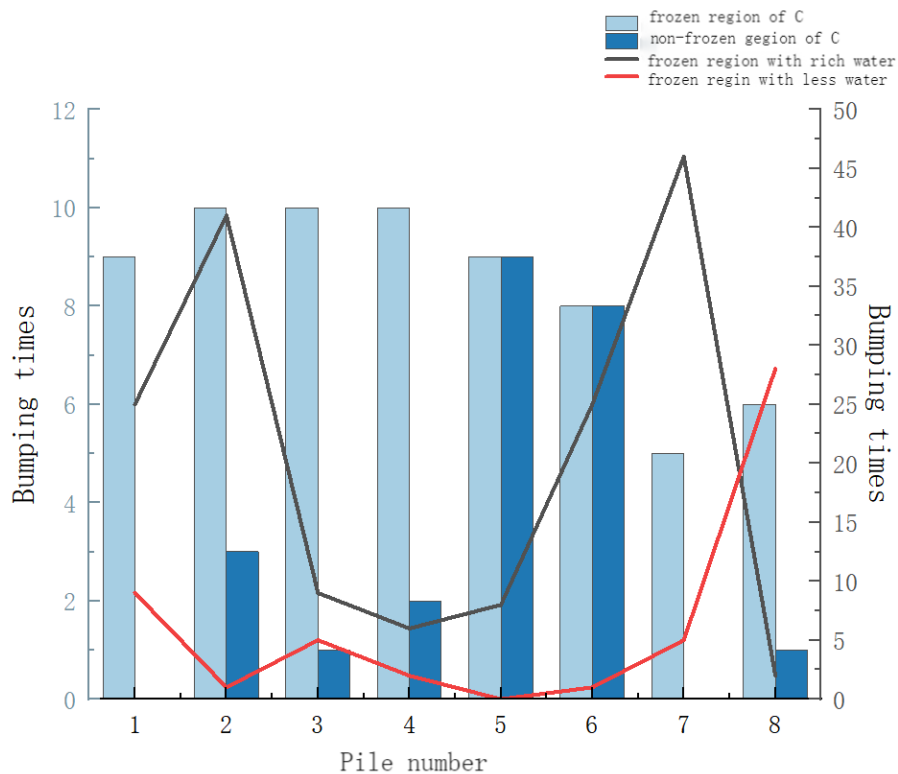

Figure 6. Distribution of pavement bumping under the coupling effect.

As shown in Fig. 6, the number of bumps on the road C and frozen soil areas in the water-rich and frozen soil environment has increased significantly. The reason is that under the condition of a certain water content, the lower the temperature, the stronger the frost heave of the soil, the greater the change in road elevation and the greater the number of bumps is. Under the condition of a certain temperature, the higher the water content, the stronger the frost heave and thaw settlement of the soil, the greater the change in road elevation and the greater the number of bumps is. The analysis shows that bumping times is inversely proportional to temperature and directly proportional to water content.

Combined with the previous analysis, the coupling effect of frozen soil environment and water-rich conditions has a significant impact on pavement roughness and bumping, and the roughness and bumping show a tendency to worsen under frozen soil environment and water-rich conditions. It shows that the roughness of cement concrete pavement has a large correlation with pavement bumping. For further verification, correlation analysis is required.

2.2. Establishment of Model Relationship

According to the above analysis, the indices needed to construct the model relationship between pavement bumping and pavement roughness should include RQI, PBI, frozen soil and water-rich environmental factors. In [23] IRI prediction revised model of cement pavement in frozen season was constructed using MEPDG and in [24] the evaluation indicator for moisture condition in the system of climatic evaluation indicators for highway was proposed. After the processing, the prediction model for pavement bumping and roughness index was established as follows:

$$RQI = K + C_1 \times PBI + C_2 \times t(1+0.5556f)(1+P_{200}) \times 10^{-6} + C_3 \times \frac{P}{PE}, \tag{1}$$

where RQI is the pavement riding quality index; PBI is the pavement bumping index; P is the precipitation; PE is the evaporation; $\frac{P}{PE}$ is the water-rich environment factor; t is the service life of the road; f is the freezing index; P_{200} is the passing rate of roadbed materials when the screen hole is 0.075 mm; $t(1+0.5556f)(1+P_{200}) \times 10^{-6}$ is the environmental factor of frozen soil; K is a constant; C_1, C_2, C_3 are the corresponding weights.

Since equation (1) is a nonlinear equation, in order to simplify the method and steps of nonlinear equation in regression analysis, the logarithmic function method is used to linearly transform the equation.

Let: $t(1+0.5556f)(1+P_{200}) \times 10^{-6} = \alpha;$ $\frac{P}{PE} = \beta.$

Then equation (1) can be converted into:

$$RQI = K + C_1 \times PBI + C_2 \times \alpha + C_3 \times \beta. \tag{2}$$

Therefore, the original nonlinear equation can be transformed into a linear equation for solving.

According to the road condition inspection evaluation and maintenance decision analysis report of the main highways in Heilongjiang Province, which involved RQI and PBI of 145 typical road sections in the seasonal freezing area and the rich water area, re-selected the field survey data of 20 highway sections such as Zhaodong, Qiqihar, Mudanjiang. Use the Statistical Package for Social Sciences (SPSS) software to perform regression analysis, combined with formula (2), set RQI measured on the spot as the dependent variable. t, f and P_{200} correspond to the transformed α. P and PE correspond to the transformed β. And the measured PBI on the spot are the independent variables, and the linearity test of the model is carried out. The Analysis Of Variance (ANOVA) of the regression model obtained is shown in Table 1.

In Table 1, the regression sum of squares of the dependent variables is 145.123, and the ratio of the squared sum of the regressions of the factors to the degrees of freedom (the mean square) is 48.374, which is much higher than the mean squared residual 0.238. The ratio of the mean regression squared to the sum of the squared mean residuals (F) is 202.986. The value is large, indicating that the change of the dependent variable is caused by the change of the independent variable rather than the experimental error, and the independent variable has a high explanatory force for the dependent variable. The significance

value is 0, less than 0.05, the model linear regression is significant. It shows that in the F test, the linear regression of the equation is obvious, and a linear model can be established between the dependent variable and the independent variable.

Table 1. Regression model of ANOVAs.

	Sum of squares	Degree of freedom	Mean square	F	Significance
Regression	145.123	3	48.374	202.986	0
Residual	3.813	16	0.238		
Total	148.936	19			

After the F test shows that a linear model can be established, it is necessary to determine whether the independent variable has a significant influence on the dependent variable, so the regression coefficients should be tested for significance. The partial regression coefficient in Table 2 represents the weight of each index. The absolute value of the standardized partial regression coefficient indicates the degree of influence of each variable on the dependent variable. The absolute value of the standardized partial regression coefficient of α is the largest among the three indicators, indicating that α corresponds to the parameters t, f and P_{200} have the greatest impact on the RQI value. The parameters P and PE correspond to β, and the relatively small impact is PBI, which is consistent with the results of the analysis of variance when determining the relations between the parameters and RQI. The absolute value of the partial regression coefficient of α is 5431.712. The reason for the analysis is that the value of the frozen soil environmental factor $t(1+0.5556f)(1+P_{200})\times10^{-6}$ is small, so the weight in the model is relatively large. The absolute value of the critical value t of the bilateral test is all-greater than the significance level, indicating that the independent variable has a significant influence on the dependent variable, and all the independent variables are retained in the model.

Table 2. Coefficient of regression modelю

Parameter	Partial regression coefficient	Partial regression coefficient standard error	Standardized partial regression coefficient	t	Significance
Constant	104.403	3.997		26.122	0
α	–5432.712	332.731	–0.931	–16.328	0
PBI	–0.070	0.038	–0.087	–1.826	0.087
β	–0.123	0.070	–0.112	–1.752	0.099

Bringing the results of the above regression analysis into equation (2), the model is expressed as:

$$RQI = 104.403 - 0.07 \times PBI - 5432.712\alpha - 0.123\beta. \qquad (3)$$

Reconverted to a nonlinear equation:

$$RQI = 104.403 - 0.07 \times PBI - 5432.712t(1+0.5556f)(1+P_{200})\times10^{-6} - 0.123\frac{P}{PE}. \qquad (4)$$

After the prediction model of the relationship between pavement bumping and pavement roughness is established, the goodness of fit between the independent variable and the dependent variable should be tested to ensure that the dependent variable can be interpreted by the model. In Table 3, R^2 is the deterministic coefficient between the dependent variable and the independent variable. Adjusted R^2 is the mean square error ratio that eliminates the influence of the number of independent variables. The closer R^2 and adjusted R^2 are to 1, the better the fitting effect of the regression equation. The adjusted R^2 of the regression equation is 0.970, which is close to 1, and the standard estimation error is 0.488, indicating that the model has a high degree of goodness of fit and the dependent variable can be explained by the model accounting for 95 %.

Table 3. Summary of regression models.

R2	Adjusted R2	Standard estimation error
0.974	0.970	0.488

In order to verify the applicability of the prediction model of the relationship between pavement bumping and pavement roughness, the normal distribution test was carried out for the model. Observing the residual histogram and the normal distribution curve in Fig. 7, we can see that the sample size is large enough and the residual distribution conforms to the normal distribution, which proves the correctness of the prediction model. Observing the residual regression P-P graph in Fig. 8, the residual distribution curve changes around the preset diagonal and diagonal directions. The two are close to coincide, and the regression model satisfies the normal distribution hypothesis. In summary, the RQI prediction model established by using PBI, t, f, P_{200}, P and PE as parameters has passed various tests, and the regression effect is significant, and the goodness of fit is high.
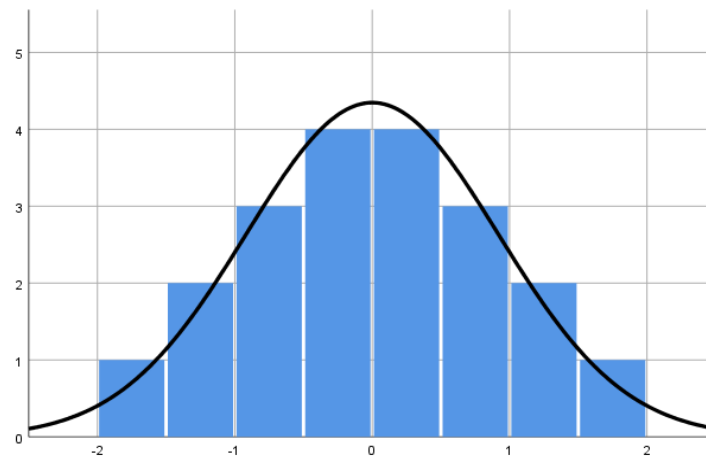
Figure 7. Residual histogram.
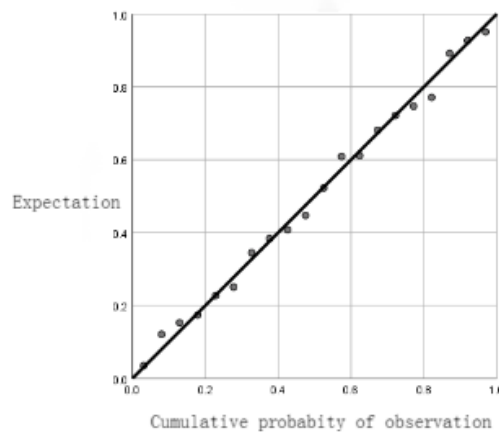

Figure 8. Residual regression P-P graph.

2.3. Analysis of the applicable conditions of the model

In order to ensure high accuracy of model evaluation, a response surface test was designed to determine the optimal prediction space for the cement concrete pavement bumping and pavement roughness prediction model under water-rich environment in the seasonal frost region. In order to facilitate the drawing of test records, the permafrost environmental factors and the water-rich environmental factors in response surface test are replaced by α and β, respectively, and the codes of PBI, α and β are A, B, and C, respectively. According to the number and range of parameters, a response surface test with 3 factors and 3 levels was selected. The coding levels and value are shown in Table 4. In order to simplify the process of drawing the response surface of PBI, α and β to RQI, the ordinate of the response surface is set as RQI value, and the abscissa is the factor value.

Table 4. Coding level table.

Code	Factor name	-1	0	1
A	PBI	87.50	93.75	100.00
B	α	0.0002	0.0010	0.0018
C	β	6.59	10.73	14.87

In the case where the coding level of PBI is 0, the response surfaces of design α and β to RQI value are as shown in Fig. 9a. When β is in the range of 6.59 to 10.73, the inclination of the response surface is smaller than the inclination of 10.73 to 14.87. The reason is that with the increase of β, the higher the moisture content of the subgrade soil, the more groundwater and the stronger the scouring effect of water on the subgrade soil. The strength of the subgrade soil is significantly lower than that of the ground moisture content, so that RQI value is significantly increased compared to the road section with low water-rich factor, so RQI is more responsive to the β range of 10.73 to 14.87.
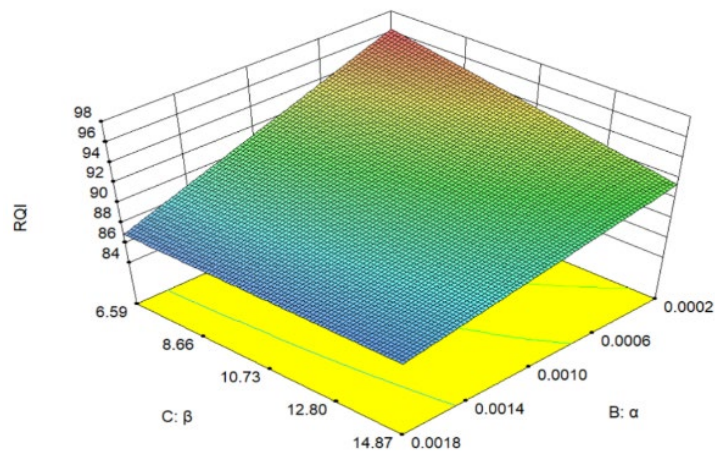
Figure 9a. Response surface of α and β to RQI value.

In the case where the coding level of α is 0, the response surfaces of PBI and β to RQI value are as shown in Fig. 9b. Observing the surface change of PBI in Fig. 9b, the inclination of the response surface increases significantly, when PBI is from 87.5 to 95 compared with that from 95 to 100. The reason is that with the decrease of PBI, the uneven settlement of the road surface becomes more and more serious. The more obvious, the more drastic the change of road elevation, so that RQI value increases significantly compared with the road sections with no obvious changes in road elevation, indicating that RQI is more responsive to PBI range of 87.5 to 95.
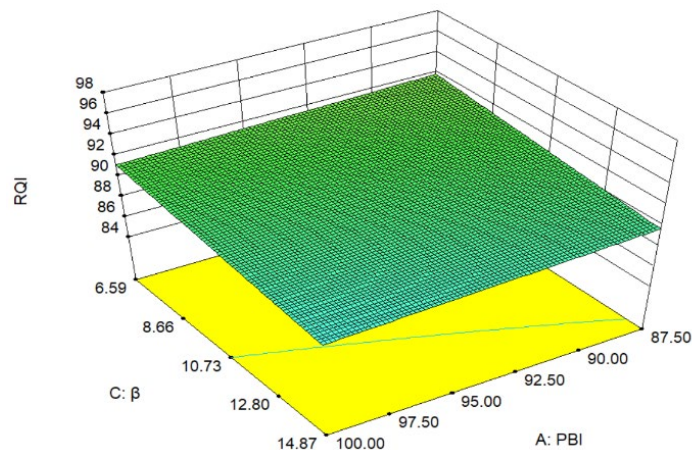
Figure 9b. Response surface of PBI and β to RQI value.

In the case where the coding level of β is 0, the response surfaces of PBI and α to RQI values are as shown in Fig. 9c. Observing the surface change of α in Fig. 9c, with the increase of α, the frost heave and thawing properties of the subgrade soil increase, and RQI value decreases accordingly. When α is from 0.0002 to 0.0014, the slope of the surface is larger than that from 0.0014 to 0.0018, and RQI value is significantly reduced. Obviously, therefore RQI has the highest responsivity to α in the range from 0.0002 to 0.0014.
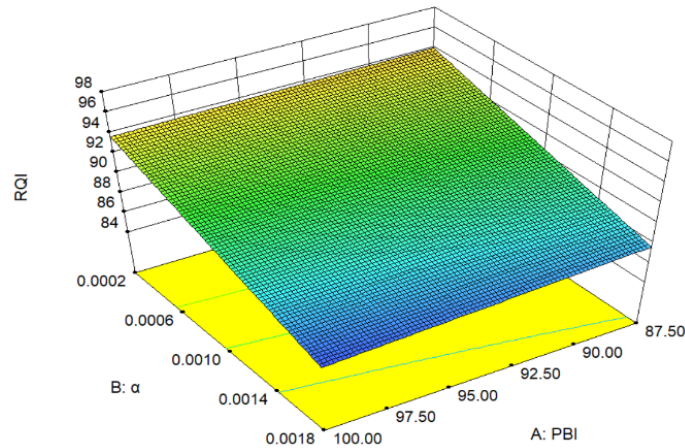

Figure 9c. Response curves of PBI **and α to** RQI **value.**

Combined with the response surface analysis above, it can be seen that the response surface tends to be flat. It means that within the range of parameters corresponding to the surface, RQI value cannot change synchronously with the parameter value, and RQI is more responsive to the parameter change. At this time, the prediction accuracy of the cement concrete pavement bumping and pavement roughness prediction model is low. If the slope of the response surface is large, RQI value changes significantly, and the corresponding parameter range is more suitable for model prediction. According to the results of the response surface analysis, the optimal prediction space of the model is the parameter value range when PBI is from 87.5 to 95, the permafrost environmental factor is from 0.0002 to 0.0014, and the water-rich environmental factor is from 10.73 to 14.87. When the optimal prediction space is selected, the prediction level of the model is the best.

3. Results and Discussion

In order to verify the practicability of the cement concrete pavement bumping and pavement roughness prediction model under the water-rich conditions in the seasonal frost region, the measured value of RQI and the predicted value of the model in 20 highway sections including Daqing and Heihe were selected for verification. The Statistical Package for Social Sciences (SPSS) Statistics software suit was used. The predicted value is matched with the measured value of RQI, as shown in Fig. 10. In Fig. 10, the abscissa is the measured value of RQI, and the ordinate is the predicted value of RQI. It can be seen from the figure that the scattered points corresponding to the measured value and the predicted value are evenly distributed on both sides of the straight line and are close to the straight line. The deterministic coefficient R^2 of the fitting between the predicted value of the prediction model RQI and the measured value is 0.987, which proves that the prediction model has a high degree of fit.
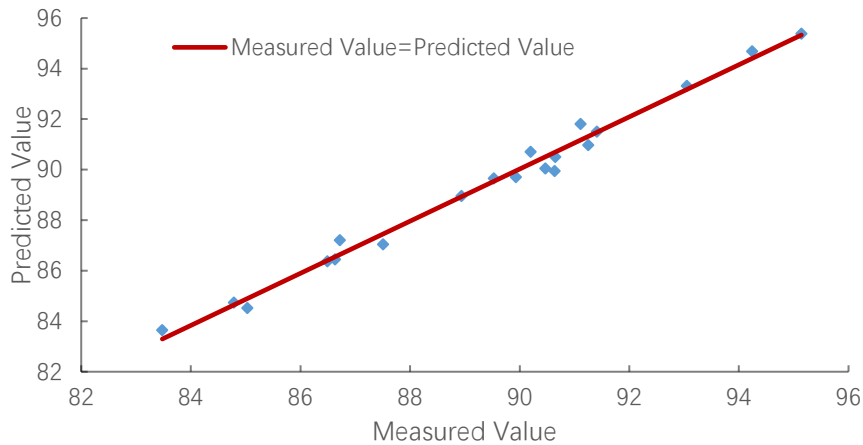
Figure 10. Correlation fitting between RQI predicted value and measured value.

In order to further reflect the fitting effect of the prediction model, separately count the prediction values of the cement concrete pavement roughness and bumping prediction model, the Backpropagation (BP) neural network prediction model [25] and the Logistic model [26–32] under the water-rich condition in the seasonal frost region. The difference between the predicted value and the actual value is shown in Fig. 11. It can be seen from Fig. 11 that the difference between the actual measured value and the predicted value of the cement concrete pavement roughness and bumping prediction model under the water-rich condition in the seasonal frost region is concentrated within ±0.5. And the BP neural network prediction model is distributed between ±0.75. The Logistic model is distributed between ±1.5. It proves that the prediction model is closer to the true value than the prediction results of the BP neural network prediction model and the Logistic model, and the prediction model has better effects and better practicability.
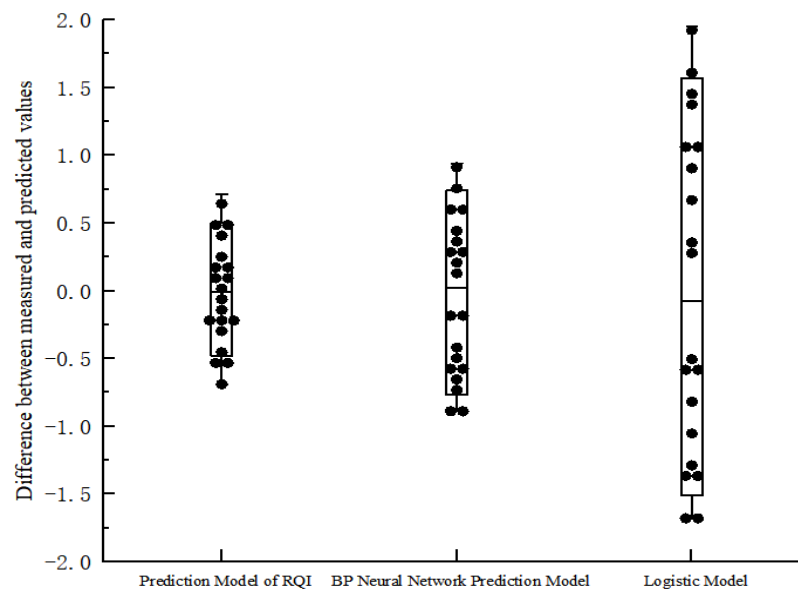

Figure 11. The prediction error of the model.

4. Conclusions

1. Frozen soil conditions and water-rich conditions will change the pavement roughness in a negative direction, and at the same time will cause the number of pavement bumping to change in a positive direction. In areas with no frozen soil and water-rich conditions, the pavement riding quality index (RQI) averages 80, while RQI in water-rich areas averages 70. In frozen soil and non-frozen soil areas the difference in RQI can reach 25. At the same time, the number of pavement bumping per kilometer in the permafrost area is 2.4 times that of the non-frozen soil area. The road elevation in the water-rich area has a sudden change from positive to negative, which is more drastic than in the non-water-rich area.

2. Frozen soil and water-rich factors are the key factors that affect the pavement roughness and pavement bumping in the water-rich conditions in seasonal frost regions. The absolute values of the standardized partial regression coefficients of frozen soil environment and water-rich environment factors are 0.931 and 0.112, respectively, indicating that the freezing index of frozen soil environment factors has the most significant effect, followed by precipitation in water-rich environment.

3. The relationship model between pavement roughness and bumping under the conditions of rich water in seasonal frost regions is proposed, using four factors, including RQI, pavement bumping index (PBI), frozen soil environmental factors and water-rich environmental factors. It can predict the pavement roughness and bumping of cement concrete pavement under water-rich conditions in seasonal frost region. The prediction model is a composite function. The deterministic coefficient R^2 of the prediction model is 0.970, and the significance level is 0. The model has a high degree of fit and significant regression. It shows that the prediction model has statistical applicability.

4. When PBI is from 87.5 to 95, the permafrost environmental factor is from 0.0002 to 0.0014, and the water-rich environmental factor is from 10.73 to 14.87, the response of RQI to parameter changes is higher than that of other parameters, which is the optimal prediction space of the model. At this time, the prediction level of the model is the best.

5. Prediction models for pavement roughness and bumping under water-rich conditions in seasonal frost regions have good accuracy. Through the verification of the prediction model in different periods of the same road section and the same period of different road sections, the R^2 of the prediction model is 0.987, and the difference between the predicted value and the measured value is within ±0.5. Compared with the BP neural network prediction model and the Logistic model, it shows a strong prediction accuracy.

References

1. Ali, A., Dhasmana, H., Hossain, K., Hussein, A. Modeling Pavement Performance Indices in Harsh Climate Regions. Journal of Transportation Engineering, Part B: Pavements. 2021. 147 (4). DOI: 10.1061/JPEODX.0000305

2. Wang, K.C.P., Li, Q., Hall, K.D., Elliot, R.P. Experimentation with gray theory for pavement smoothness prediction. Transportation Research Record: Journal of the Transportation Research Board. 2007. 1990 (1). Pp. 3–13. DOI: 10.3141/1990-01

3. Múčka, P. Current approaches to quantify the longitudinal road roughness. International Journal of Pavement Engineering. 2016. 17 (8). Pp. 659–679. DOI: 10.1080/10298436.2015.1011782

4. Soncim, S.P., de Oliveira, I.C.S., Santos, F.B., Oliveira, C.A. d. S. Development of probabilistic models for predicting roughness in asphalt pavement. Road Materials and Pavement Design. 2018. 19 (6). Pp. 1448–1457. DOI: 10.1080/14680629.2017.1304233

5. Miao, Y.-H., Wang, B.-G., Li, C., Gupta, P.K. Climate zoning for moisture damage of asphalt pavements in China. Journal of Chang'an University: Natural Science Edition. 2008. 28 (1). Pp. 26–31.

6. Byrne, M., Albrecht, D., Sanjayan, J.G., J.K. Identifying the effects of soil and climate types on seasonal variation of pavement roughness using MML inference. Journal of Computing in Civil Engineering. 2008. 22 (2). Pp. 90–99. DOI: 10.1061/(ASCE)0887-3801(2008)22:2(90)

7. Bae, A., Stoffels, S.M., Antle, C.E., Lee, S.W. Observed evidence of subgrade moisture influence on pavement longitudinal profile. Canadian Journal of Civil Engineering. 2008. 35. Pp. 1050–1063. DOI: 10.1139/L08-047

8. Sylvestre, O., Bilodeau, J.P., Doré, G. Effect of frost heave on long-term roughness deterioration of flexible pavement structures. International Journal of Pavement Engineering. 2019. 20 (6). Pp. 704–713. DOI: 10.1080/10298436.2017.1326598

9. Bo, L., Kundwa, M.J., Jiao, C.Y., Wei, Z.X. Pavement Performance Evaluation and Maintenance Decision-Making in Rwanda. 3rd GeoMEast International Congress and Exhibition on Sustainable Civil Infrastructures, GeoMEast 2019, November 10–15. Cairo, Egypt. 2020. Pp. 107–116. DOI: 10.1007/978-3-030-34196-1_8

10. Sun, L. Simulation of pavement roughness and IRI based on power spectral density. Mathematics and Computers Simulation. 2003. 61 (2). Pp. 77–88. DOI: 10.1016/S0378-4754(01)00386-X

11. Park, K., Thomas, N.E., Lee K.W. Applicability of the international roughness index as a predictor of asphalt pavement condition. Journal of Transportation Engineering. 2007. 133 (12). Pp. 706–709. DOI: 10.1061/(ASCE)0733-947X(2007)133:12(706)

12. Hossain, M.I., Gopisetti, L.S.P., Miah, M.S. Prediction of international roughness index of flexible pavements from climate and traffic data using artificial neural network modeling. International Conference on Highway Pavements and Airfield Technology 2017, August 27–30. Philadelphia, US. 2017. Pp. 256–267. DOI: 10.1061/9780784480922.023.

13. Li, W., Huyan, J., Xiao, L., Tighe, S., Pei L. International roughness index prediction based on multigranularity fuzzy time series and particle swarm optimization. Expert Systems with Applications: X. 2019. 2. 100006. DOI: 10.1016/j.eswax.2019.100006

14. Abdelaziz, N., Abd El-Hakim, R.T., El-Badawy, S.M., Hafez, A.A. International Roughness Index prediction model for flexible pavements. International Journal of Pavement Engineering. 2020. 21 (1). Pp. 88–99. DOI: 10.1080/10298436.2018.1441414

15. Zhang, L.N., He, D.P., Zhao, Q.Q. Modeling of international roughness index in seasonal frozen area. Magazine of Civil Engineering. 2021. 104 (4). 10402. DOI: 10.34910/MCE.104.2

16. Alimoradi, S., Golroo, A., Asgharzadeh S.M. Development of pavement roughness master curves using Markov Chain. International Journal of Pavement Engineering. 2020. 23 (2). Pp. 453–463. DOI: 10.1080/10298436.2020.1752917

17. Patrick, G., Soliman H. Roughness prediction models using pavement surface distresses in different Canadian climatic regions. Canadian Journal of Civil Engineering. 2019. 46 (10). Pp. 934–940. DOI: 10.1139/cjce-2018-0697

18. Kargah-Ostadi, N., Stoffels, S.M., Tabatabaee, N. Network-Level Pavement Roughness Prediction Model for Rehabilitation Recommendations. Transportation Research Record: Journal of the Transportation Research Board. 2010. 2155 (1). Pp. 124–133. DOI: 10.3141/2155-14

19. Ni, F.-J., Fang, Y., Xue, Z.-M. Prediction of pavement roughness with time series autoregression model. Journal of Southeast University: Natural Science Edition. 2006. 36 (4). Pp. 634–637.

20. Nurhadiansyah, R., Hadiana, A. Toll Road Roughness Index Forecasting with Combination Grey Forecasting Model and Similarity Spatial Data. IOP Conference Series: Materials Science and Engineering. 2019. 662. 022065. DOI: 10.1088/1757-899X/662/2/022065

21. Zhao, H., Hui, Z., Lin, J. Study on soft foundation settlement analysis and treatment of bridge-head. Advanced Materials Research. 2013. 779-780. Pp. 632–635. DOI: 10.4028/www.scientific.net/AMR.779-780.632

22. Tu, Y., Wang, X., Chai, H., Xu, J., Li, H., Yu, J. Effects of jet grouting pile composite foundation with variable stiffness treating vehicle bump at bridge head. Journal of Southeast University: Natural Science Edition. 2021. 51 (4). Pp. 588–595.

23. Zhao, Q., Cheng, P., Wei, Y., Zhou, X. IRI predictive revised model for cement pavement in seasonal frozen region using MEPDG. Journal of Harbin Institute of Technology. 2018. 50 (11). Pp. 171–177. DOI: 10.11918/j.issn.0367-6234.20170056

24. Miao, Y.-H., Wang, B.-G. Research on Climatic Evaluation Indicators for Highway. Journal of Beijing University of Technology. 2007. 33 (11). Pp. 1168–1172+1186.

25. Xu, B., Dan, H.-C., Li L. Temperature prediction model of asphalt pavement in cold regions based on an improved BP neural network. Applied Thermal Engineering. 2017. 120. Pp. 568–580. DOI: 10.1016/j.applthermaleng.2017.04.024.

26. Heidari, M.J., Najafi, A., Alavi, S. Pavement deterioration modeling for forest roads based on logistic regression and artificial neural networks. Croatian Journal of Forest Engineering. 2018. 39 (2). Pp. 271–287.

27. Tasmin, T., Wang, J., Dia, H., Richards, D., Tushar, Q. A probabilistic approach to evaluate the relationship between visual and quantified pavement distress data using logistic regression. 2020 IEEE Asia-Pacific Conference on Computer Science and Data Engineering, December 16–18. Gold Coast, Australia. 2020. Pp. 1–4. DOI: 10.1109/CSDE50874.2020.9411555

28. Kharun, M., Klyuev, S., Koroteev, D., Chiadighikaobi, P.C., Fediuk, R., Olisov, A., Vatin, N., Alfimova, N. Heat treatment of basalt fiber reinforced expanded clay concrete with increased strength for cast-in-situ construction. Fibers. 2020. 8 (11). Pp. 1–16. DOI: 10.3390/fib8110067

29. Fediuk, R., Smoliakov, A., Stoyushko, N. Increase in composite binder activity. IOP Conference Series: Materials Science and Engineering. 2016. 156. 012042. DOI: 10.1088/1757-899X/156/1/012042

30. Prakash, R., Divyah, N., Srividhya, S., Avudaiappan, S., Amran, M., Naidu Raman, S., Guindos, P., Vatin, N., Fediuk, R. Effect of Steel Fiber on the Strength and Flexural Characteristics of Coconut Shell Concrete Partially Blended with Fly Ash. Materials. 2022. 15 (12). 4272. DOI: 10.3390/ma15124272

31. Fediuk, R.S., Smoliakov, A.K., Timokhin, R.A., Batarshin, V.O., Yevdokimova, Yu.G. Using thermal power plants waste for building materials. IOP Conference Series: Earth and Environmental Science. 2018. 87. 092010. DOI: 10.1088/1755-1315/87/9/092010

32. Fediuk, R., Yushin, A. Composite binders for concrete with reduced permeability. IOP Conference Series: Materials Science and Engineering. 2016. 116. 012021. DOI: 10.1088/1757-899X/116/1/012021

33. Fediuk, R.S., Lesovik, V.S., Mochalov, A.V., Otsokov, K.A., Lashina, I.V., Timokhin, R.A. Composite binders for concrete of protective structures. Magazine of Civil Engineering. 2018. 82 (6). Pp. 208–218. DOI: 10.18720/MCE.82.19

34. Fediuk, R.S., Lesovik, V.S., Liseitsev, Yu.L., Timokhin, R.A., Bituyev, A.V., Zaiakhanov, M.Ye., Mochalov, A.V. Composite binders for concretes with improved shock resistance. Magazine of Civil Engineering. 2019. 85 (1). Pp. 28–38. DOI: 10.18720/MCE.85.3

Information about authors:

Hanqing Li,
E-mail: 79549482@qq.com

Qiao Sun,
E-mail: 465390034@qq.com

Zakaria Ideris,
E-mail: ideris753@gmail.com

Qianqian Zhao,
ORCID: https://orcid.org/0000-0002-0209-4181
E-mail: 492954791@qq.com

Roman Fediuk,
ORCID: https://orcid.org/0000-0002-2279-1240
E-mail: roman44@yandex.ru

Yuchuan Lei,
ORCID: *https://orcid.org/0000-0001-9556-2951*
E-mail: *1371904682@qq.com*

Yang Yuze,
E-mail: *18645921558@qq.com*

Three-field FEM for analysis of thin elastic shells

Yu.V. Klochkov[1] [iD] , *A.P. Nikolaev[1]* [iD] , *V.A. Pshenichkina[2]* [iD] , *O.V. Vakhnina[1]* ✉ [iD] ,

M.Yu. Klochkov[2] [iD]

[1] *Volgograd State Agrarian University, Volgograd, Russian Federation*

[2] *Volgograd State Technical University, Volgograd, Russian Federation*

✉ *ovahnina@bk.ru*

Keywords: three-field functional, finite element method, strain tensor, curvature tensor, forces, moments

Abstract. To obtain a finite element algorithm in the three-field formulation, a conditional functional was used, based on the equality of the actual work of the internal force factors (internal forces and moments) at the strains and curvatures of the middle surface. As an addition, the functional assumed the condition that the work of the residual of internal forces at the strains and curvatures of the middle surface had been equal to zero. The difference between the adopted internal forces and the internal forces represented through the strains and curvatures of the middle surface according to Hooke's law was used as the residual of internal forces. A quadrilateral fragment of the middle surface of a thin shell was used as the finite element. Kinematic quantities (displacements and their first order derivatives), strain quantities (strains and curvatures of the middle surface) and force quantities (internal forces and moments) were taken as the nodal unknowns. Approximating expressions with Hermite polynomials of third degree were used to approximate kinematic quantities. The sought strain and force quantities were approximated through the corresponding nodal unknowns by bilinear shape functions. A finite element stiffness matrix (with the dimensions 36x36) with respect to the kinematic nodal unknowns was formed through the functional minimization. Specific examples showed the efficiency of the three-field finite element algorithm in determining the displacements, strains and internal forces.

1. Introduction

Definition of the object of study. Taking into account the fairly widespread use of the theoretically based [1, 2] shell systems and objects (domes, roofs, floors, architectural forms, etc.) in various sectors of the construction industry, the development and improvement of methods of numerical analysis of the stress-strain state (SSS) of thin-walled structures made of shells and their fragments is a topical issue.

Literature review. Currently, researchers are choosing the finite element method (FEM) in various formulations as the main tool for numerical analysis of the SSS of shell structures. FEM in the formulation of the displacement method has become especially widespread. For example, when determining the SSS of shell and plate structures [3–7], when finding strength indicators of shell structures [8–13], in stability problems [14–16] as well as in composite structures [17] and in thin-walled structures with geometric imperfections [18, 19].

In recent years, for the numerical analysis of the SSS of engineering structures, the FEM in a mixed formulation has come into use for beams and plates analysis [20–23] as well as for shells analysis [24–26].

When comparing the above-mentioned FEM formulations with each other, it should be noted that the mixed FEM formulation has significant advantages, since in this case the conditions of compatibility between the finite elements are satisfied not only for displacements, but also for internal forces and moments. In addition, when solving a finite-element problem applying the mixed formulation, the researcher has an opportunity to simultaneously obtain both kinematic and force parameters of the SSS of the object under study.

Purpose and objectives of the study. When performing the numerical analysis of the SSS of thin-walled structures made of shells and their fragments, the finite element algorithm, which allows one to simultaneously study the fields of displacements, strains, internal forces and moments of the shell structure, i.e. a three-field FEM, seems to be the most preferable FEM variant.

In this paper, the above-mentioned three-field FEM is presented in a two-dimensional formulation based on the modified conditional Lagrange functional, and implemented by the example of the finite element analysis of an ellipsoidal elastic shell.

2. Materials and methods

In order to obtain a mixed finite element being a fragment of the middle surface of a shell structure, a conditional Lagrange functional is proposed, written in the following form

$$\Phi_L = \frac{1}{2} \int_F \{S_c\}^T \{\varepsilon_c\} dF - \frac{1}{2} \int_F \{U\}^T \{q\} dF - \frac{1}{2} \int_F \{\varepsilon_c\}^T \left[\{S_c\} - [h]\{\varepsilon_c^k\} \right] dF, \tag{1}$$

where $\{S_c\}_{1\times 6}^T = \left\{ N^{11} N^{22} N^{12} M^{11} M^{22} M^{12} \right\}$ is the row of internal forces and moments;

$\{\varepsilon_c\}_{1\times 6}^T = \left\{ \varepsilon_{11} \varepsilon_{22} 2\varepsilon_{12} \aleph_{11} \aleph_{22} 2\aleph_{12} \right\}$ is the row of strains and curvatures at the point M; $\{U\}_{1\times 3}^T = \{u \, v \, w\}$

are the components of the displacement vector of the point M; $\{q\}_{1\times 3}^T = \{q_1 \, q_2 \, q_3\}$ is the row of the

surface load of the shell structure.

In the functional (1), the column $\{\varepsilon_c\}$ is also represented as a matrix expression of the relation with

the column $\{S_c\}$ based on Hooke's law [2] and the expression based on Cauchy relations

$$\{S_c\}_{6\times 1} = [h]_{6\times 6} \{\varepsilon_c\}_{6\times 1}; \quad \{\varepsilon_c^k\}_{6\times 1} = [D]_{6\times 3} \{U\}_{3\times 1}, \tag{2}$$

where $[D]_{6\times 3}$ is the matrix of differential operators.

The internal forces and moments as well as the strains and curvatures included into the structure of the columns $\{S_c\}$ and $\{\varepsilon_c\}$ are expressed through their nodal values by the means of the bilinear dependences

$$N^{\alpha\beta} = \{\varphi\}_{1\times 4}^T \left\{ N^{\alpha\beta i} N^{\alpha\beta j} N^{\alpha\beta k} N^{\alpha\beta l} \right\}; \quad M^{\alpha\beta} = \{\varphi\}_{1\times 4}^T \left\{ M^{\alpha\beta i} M^{\alpha\beta j} M^{\alpha\beta k} M^{\alpha\beta l} \right\};$$

$$\varepsilon_{\alpha\beta} = \{\varphi\}_{1\times 4}^T \left\{ \varepsilon_{\alpha\beta}^i \, \varepsilon_{\alpha\beta}^j \, \varepsilon_{\alpha\beta}^k \, \varepsilon_{\alpha\beta}^l \right\}; \quad \aleph_{\alpha\beta} = \{\varphi\}_{1\times 4}^T \left\{ \aleph_{\alpha\beta}^i \, \aleph_{\alpha\beta}^j \, \aleph_{\alpha\beta}^k \, \aleph_{\alpha\beta}^l \right\}. \tag{3}$$

The components of the displacement vector of the point M of the middle surface u, v, w included

into the column $\{U\}$ are interpolated in the local coordinate system through their nodal values and their

partial first order derivatives by means of the shape functions, with the Hermite polynomials of third degree being the elements of those [25, 26]

$$u = \{\psi\}_{1\times 12}^T \{u_y^L\}_{12\times 1}; \quad v = \{\psi\}_{1\times 12}^T \{v_y^L\}_{12\times 1}; \quad w = \{\psi\}_{1\times 12}^T \{w_y^L\}_{12\times 1}. \tag{4}$$

Taking into account (3) and (4), it is possible to assemble the following interpolative matrix dependences

$$\{S_c\} = [H]\{S_y\}; \quad \{\varepsilon_c\} = [H]\{E_y\}; \quad \{U\} = [A]\{U_y^L\} = [A][P_R]\{U_y^G\}, \tag{5}$$

$$\underset{6\times1}{} \quad \underset{24\times1}{} \quad \underset{6\times1}{} \quad \underset{24\times1}{} \quad \underset{3\times1}{} \quad \underset{36\times1}{} \quad \underset{36\times36}{} \quad \underset{36\times1}{}$$

where $\underset{1\times36}{\{U_y^L\}^T} = \left\{ \underset{1\times12}{\{u_y^L\}^T} \quad \underset{1\times12}{\{v_y^L\}^T} \quad \underset{1\times12}{\{w_y^L\}^T} \right\}$ is the row of kinematic nodal unknowns in the local coordinate

system; $\{U_y^G\}$ is the column of kinematic nodal unknowns in the global coordinate system; $[P_R]$ is the

matrix dependences between the columns $\{U_y^L\}$ and $\{U_y^G\}$.

Based on the Cauchy relations [1], the column of strains and curvatures $\{\varepsilon_c^k\}$ at the point M

included into (1) can be represented in the form of the matrix product

$$\{\varepsilon_c\} = [D]\{U\} = [D][A][P_R]\{U_y^G\} = [B][P_R]\{U_y^G\}. \tag{6}$$

Taking into account (5), (6), the functional (1) can be transformed into the following form

$$\Phi_L = \frac{1}{2}\{S_y\}^T \int_F [H]^T [h]^{-1} [H] dF \{S_y\} - \frac{1}{2}\{U_y^G\}^T [P_R]^T \int_F [A]\{q\} dF -$$

$$-\frac{1}{2}\{E_y\}^T \int_F [H]^T [H] dF \{S_y\} + \frac{1}{2}\{E_y\}^T \int_F [H]^T [h][B] dF [P_R]\{U_y^G\}. \tag{7}$$

As a result of the minimization of the functional (7) in $\{S_y\}^T$, $\{E_y\}^T$ and $\{U_y^G\}^T$, the following

system of matrix equations can be obtained

$$\begin{cases} \dfrac{\partial \Phi_L}{\partial \{S_y\}^T} = [a]\{S_y\} - [b]^T \{E_y\} = 0; \\[2mm] \dfrac{\partial \Phi_L}{\partial \{E_y\}^T} = -[b]\{S_y\} + [c]\{U_y^G\} = 0; \\[2mm] \dfrac{\partial \Phi_L}{\partial \{U_y^G\}^T} = -\{f_y^G\} + [c]^T \{E_y\} = 0, \end{cases} \tag{8}$$

where $[a] = \int_F [H]^T [h]^{-1} [H] dF; \quad [b] = \int_F [H]^T [H] dF; \quad \{f_y^G\} = [PR]^T \int_F [A]^T \{q\} dF;$

$[c] = \int_F [H]^T [h][B] dF [PR].$

Based on the second matrix equation of the system (8), the column of the nodal values of the axial forces and bending moments could be expressed

$$\{S_y\} = [b]^{-1}[c]\{U_y^G\}. \tag{9}$$

Taking into account (9), the first system of equations of the system (8) results in

$$\{E_y\} = \left[[b]^T\right]^{-1}[a][b]^{-1}[c]\{U_y^G\}. \tag{10}$$

Taking into account (10), the matrix expression for the kinematic nodal unknowns can be determined from the third system of equations of the system (8)

$$[c]^T\left[[b]^T\right]^{-1}[a][b]^{-1}[c]\left\{U_y^G\right\}=\left\{f_y^G\right\} \tag{11}$$

or in a more compact form

$$\left[K^G\right]\left\{U_y^G\right\}=\left\{f_y^G\right\}, \tag{12}$$

where $\left[K^G\right]=[c]^T\left[[b]^T\right]^{-1}[a][b]^{-1}[c]$ is the stiffness matrix of a four-node element of discretization.

The stiffness matrix and the column of the nodal internal forces of the shell structure are assembled from the stiffness matrices of four-node elements of discretization $\left[K^G\right]$ and the columns of the nodal internal forces $\left\{f_y^G\right\}$ of individual finite elements by means of an index matrix in a standard manner for FEM [9].

The sought kinematic quantities, determined by solving a system of equations for the entire structure using equations (9) and (10), make it possible to determine the nodal values of the axial forces and bending moments $\left\{S_y\right\}$ and $\left\{E_y\right\}$ for all of the elements, the set of which was used to model the thin-walled shell structure.

The stress fields in the suggested three-field FEM variant can be obtained in two independent ways. The first method is to use the internal force factors obtained through the finite element solution in the formula

$$\sigma^{\alpha\beta}=\frac{N^{\alpha\beta}}{F}+\frac{\xi M^{\alpha\beta}}{I}, \tag{13}$$

where F, I are the area and the moment of inertia of the cross section (as applied to a thin-walled shell structure $F=t$; $I=t^3/12$); ξ is the vertical distance from the middle surface point to the cross-section point under consideration.

The second method is to use the calculated strains and curvatures of the matrix $\left\{E_y\right\}$ by first passing to the strains at an arbitrary cross-section point located at the distance $\xi\cdot\varepsilon_{\alpha\beta}^{\xi}=\varepsilon_{\alpha\beta}+\xi\aleph_{\alpha\beta}$ from the corresponding point of the middle surface and then using the elasticity matrix $[d]$

$$\underset{3\times1}{\left\{\sigma^{\alpha\beta}\right\}}=\underset{3\times3}{[d]}\underset{3\times1}{\left\{\varepsilon_{\alpha\beta}^{\xi}\right\}}, \tag{14}$$

assembled using of the relations of continuum mechanics [2]

$$\sigma^{\alpha\beta}=\lambda I_1\left(\varepsilon\right)g^{\alpha\beta}+2\mu g^{\alpha\rho}g^{\beta\gamma}\varepsilon_{\rho\gamma}^{\xi}, \tag{15}$$

where λ, μ are Lamé parameters; $I_1\left(\varepsilon\right)=g^{\alpha\beta}\varepsilon_{\alpha\beta}^{\xi}$, is the first invariant of the strain tensor; $g^{\alpha\beta}$ are the contravariant components of the metric tensor determined at an arbitrary cross-section point of the shell structure.

The correctness and high accuracy of the calculations of the required parameters of the SSS of shell structures applying the developed three-field FEM variant are shown through the examples of solving a number of test problems.

3. Results and Discussion

Example 1. A fragment of an elliptical cylinder with a rigidly fixed left generatrix and a free right generatrix loaded with internal pressure with intensity of $q=0.1$ N/cm² was analyzed (Fig. 1). The

numerical values of the geometric and physical quantities in the example 1 are taken as follows: $b = 0.5$ m; $c = 0.4$ m; $h = 0.01$ m; $L = 0.01$ m; $E = 2 \cdot 10^5$ MPa; the transverse strain coefficient $\nu = 0.3$.
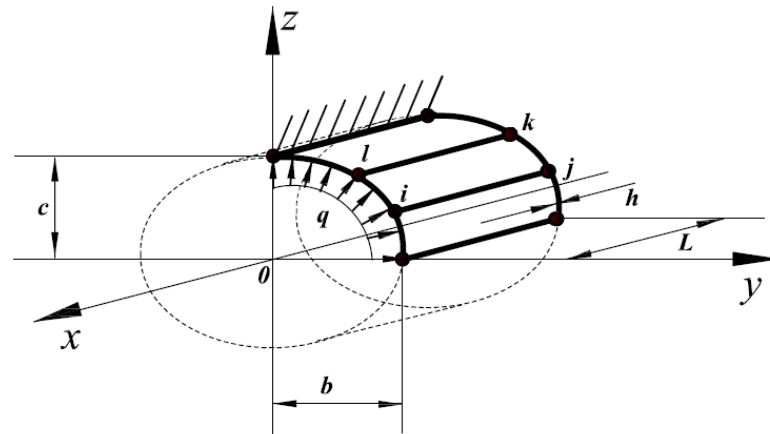
Figure 1. Analytical scheme of an elliptical cylinder loaded with internal pressure.

The chosen analytical scheme allows to analytically determine the value of the physical bending moment M_f^{22} at arbitrary point of the elliptical cylinder, having previously resolved the internal pressure into the vertical and horizontal components q_v and q_g. Thus, at an arbitrary point K (Fig. 2) the value of the physical bending moment M_f^{22} will be determined by the formula

$$M_f^{22} = q_v z^2 \big/ 2 + q_g (b - y)^2 \big/ 2. \tag{16}$$

Figure 2. Analytical scheme of the elliptical cylinder section.

Table 1 gives the values of the "physical" moments M_f^{22} and normal stresses in points P, K, T of the elliptical cylinder (Fig. 2).

Table 1. Values of the SSS parameters under control.

Discretization mesh

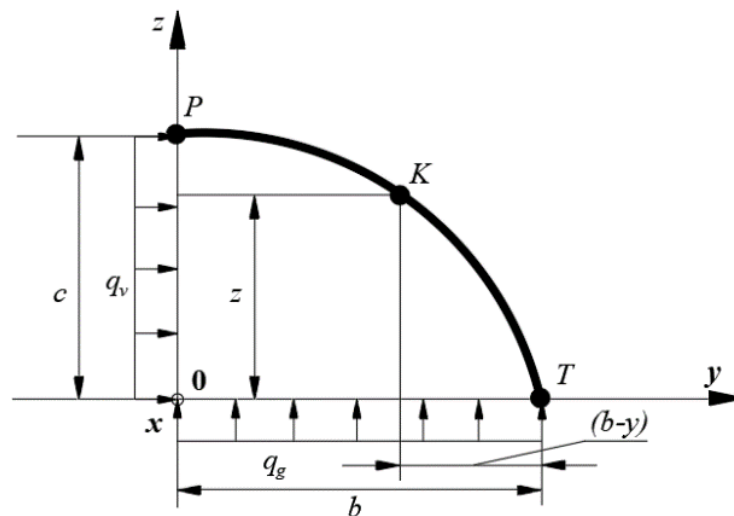| Coordinates of the points, y; t	Moments M_f^{22}, N·m, stresses σ, MPa	31×2	61×2	91×2	121×2	Analytical solution M_f^{22}, N·m, $\sigma_{tt} = M_f^{22}/W$
Rigid fixing, $y = 0$, $t = 0$	M_f^{22}	2.0495	2.0499	2.0499	2.04997	2.050
	σ_{tt}^{in}	12.44	12.44	12.44	12.44	12.3
	σ_{tt}^{out}	-12.16	-12.16	-12.16	-12.16	
Point K, $y = b/\sqrt{2}$, $t = \pi/4$	M_f^{22}	0.50705	0.5072	0.50721	0.50722	0.50723
	σ_{tt}^{in}	3.084	3.09	3.09	3.09	3.043
	σ_{tt}^{out}	-2.993	-3.00	-3.00	-3.00	
Point T, $y = b$, $t = \pi/2$	M_f^{22}	0.00036	0.00009	0.00004	0.00002	0.000
	σ_{tt}^{in}	0.00215	-0.0006	-0.00025	-0.00014	0.000
	σ_{tt}^{out}	0.0005	0.0005	0.00024	0.00013	

The normal stresses values were calculated using the formula (14), i.e. using the previously obtained values of strains and curvatures $\{E_y\}$. The rightmost column shows the values of the bending moment M_f^{22} calculated using the formula (16) and the values of the normal stresses calculated using the formula $\sigma_{tt} = M_f^{22}/W$ (W is the moment of resistance of the cross section). Analysis of the data in Table 1 shows a stable convergence of the calculating process as the discretization mesh becomes finer, and there is an almost complete coincidence of the values of the moments calculated according to the developed algorithm with the values obtained analytically through the formula (16). The calculation error for M_f^{22} is 0.005 %.
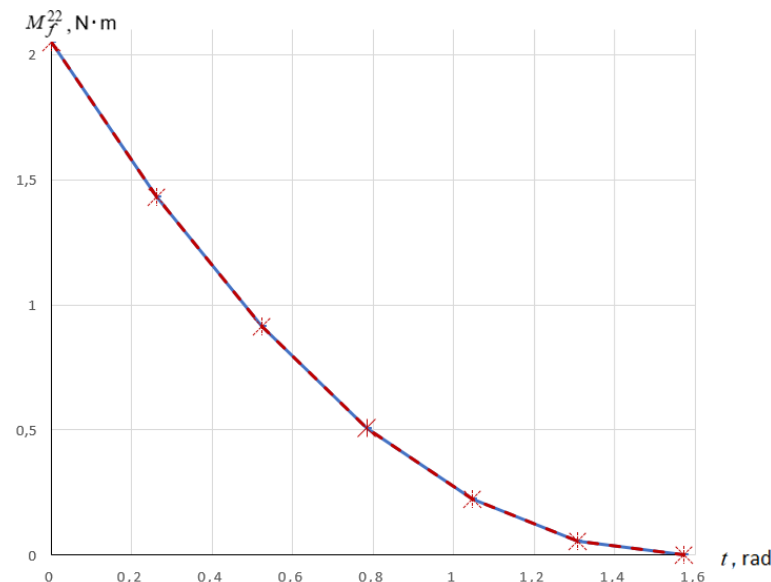

Figure 3. Curve of the dependence of the bending moment M_f^{22} on the parameter t.

Figure 3 shows the curve of the dependence of the bending moment M_f^{22} on the parameter t. The value $t = 0$ corresponds to the rigid fixing (point P in Fig. 2), and the value $t = \pi/2$ corresponds to the

free edge (point T in Fig. 2). The marks in the shape of asterisks on the curve indicate the values of M_f^{22} calculated with the formula (16) based on the static equilibrium condition. The graph shows that the numerical and analytical values of M_f^{22} completely coincide.

Example 2. An analysis of the elliptical ring, the analytical scheme of which is shown in Fig. 4, was carried out. Due to the symmetry of the ring, only a quarter of it was used in the analysis. The numerical values of the geometric and physical quantities of the shell were taken as follows: $q = 10$ N/m; $E = 2 \cdot 10^5$ MPa; $\nu = 0.3$; $b = 0.5$ m; $c = 0.2$ m; $h = 0.001$ m; $L = 0.01$ m.
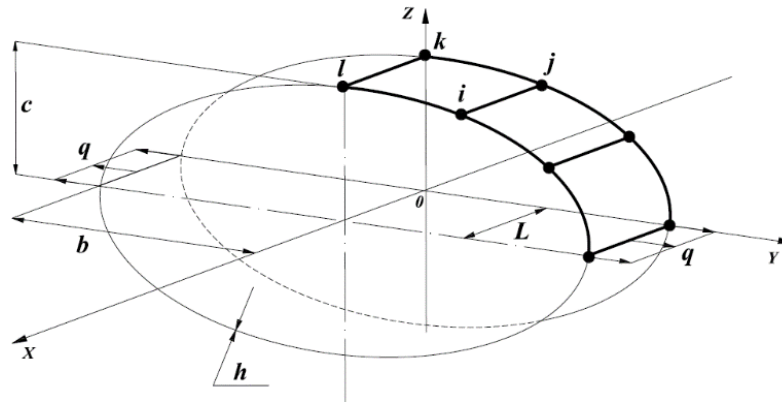

Figure 4. Analytical scheme of the elliptical ring.

Table 2 gives the values of the bending moments M_f^{22}, the internal forces N_f^{22} and the normal stresses at the points of the analytical scheme (Fig. 4) marked with the coordinates y, t.

Table 2. Values of the controlled SSS parameters.

Coordinates of the points, y; t	Moments M_f^{22}, N·m, axial force N, N, stresses σ_{xx}, σ_{tt}, 10^{-2} MPa	Discretization mesh				Values M_f^{22} and σ_{tt} calculated with the formulas of the strength of materials [27]
		31×2	61×2	91×2	121×2	
$y = 0,$ $t = 0$	M_f^{22}	-0.55334	-0.55316	-0.55312	-0.55311	-
	N_f^{22}	0.10437	0.10441	0.10442	0.10442	0.100
	σ_{tt}^{in}	333.39	333.09	333.04	333.02	-
	σ_{tt}^{out}	-331.13	-330.83	-330.77	-330.75	-
	σ_{xx}^{in}	100.01	99.93	99.91	99.91	-
	σ_{xx}^{out}	-99.34	-99.25	-99.23	-99.23	-
$y = b,$ $t = \pi/2$	M_f^{22}	1.450	1.448	1.447	1.447	1.450
	σ_{tt}^{in}	-871.61	-873.03	-873.30	-873.40	870.0
	σ_{tt}^{out}	860.81	862.19	862.46	862.56	
	σ_{xx}^{in}	-261.16	-261.89	-261.99	-262.02	-
	σ_{xx}^{out}	258.54	258.68	258.74	258.77	-

The rightmost column of Table 2 gives the values of the bending moment at the points of application of the load, taken from [27]. The normal stresses in the right column are determined through the bending moment using the formula of the strength of materials.

The analysis of the data in Table 2 shows a stable convergence of the calculation process sought parameters and a coincidence in the values of the compared quantities of the bending moments. The calculation error for the bending moment was 0.14 %. Based on the static equilibrium condition $\left(\sum N_x = 0\right)$ the value of the axial force N_f^{22} at the leftmost point of the analyzed quarter of the ring should be equal to $N_f^{22} = q_v \cdot L = 0.1$ N. The obtained value of the axial force differs from the exact value by 4 %. However, it should be noted here that a larger value of the calculation error in the axial force as compared to the small error in the bending moment is explained by the fact that the axial force value is much smaller than the bending moment value, the contribution of which to the normal stress value is determining.

Example 3. A problem of determination of the SSS of a fragment of an elliptical cylinder was solved with the same support conditions as in example 1, which is loaded with a combined external load in the form of internal pressure with intensity of $q = 0.1$ N/cm² and a linearly distributed load with intensity of $q_w = q_v = 1$ N/cm (Fig. 5).
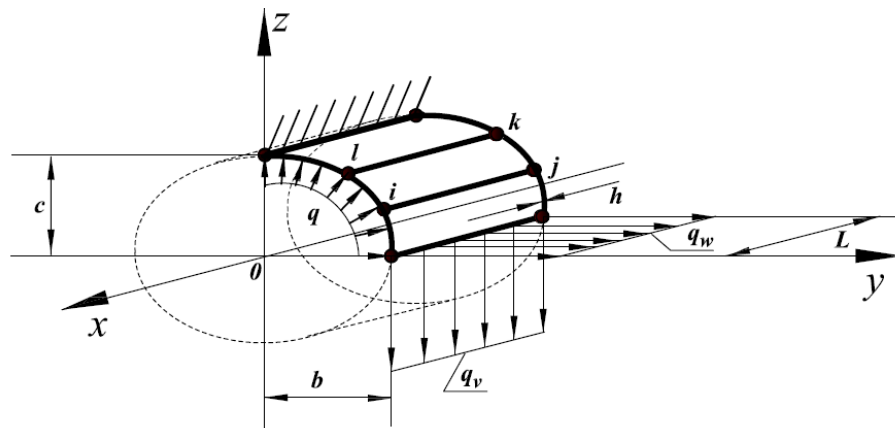

Figure 5. Analytical scheme of an elliptical cylinder loaded with a combined external load.

The values of the parameters of the cross-sectional ellipse were taken equal to $b = 0.5$ m; $c = 0.1$ m; with the wall thickness of $h = 0.01$ m; $L = 0.01$ m; $E = 2 \cdot 10^5$ MPa; $\nu = 0.3$.

The analysis of the adopted shell was carried out based on FEM in two formulations:

- based on displacement method formulation [13];
- based on three-field formulation presented in this article.

The results of the analysis are given in Table 3, where the values of the normal stresses σ_{tt}, σ_{xx} and the bending moments at the points of the analytical scheme (Fig. 5) are given depending on the dimension of the discretization mesh. The rightmost column shows the values of M_f^{22}, N_f^{22}, σ_{tt}, σ_{xx} analytically from the static equilibrium condition, for example, the bending moment in a rigid fixing is determined by the formula

$$M_f^{22} = q\left(c^2/2 + b^2/2\right) = q_v \cdot L \cdot b + q_w \cdot L \cdot c =$$

$$= 0.1\left(10^2/2 + 50^2/2\right) - 1.0 \cdot 1.0 \cdot 50 + 1.0 \cdot 1.0 \cdot 10 = 90.0 \cdot \text{N} \cdot \text{cm}.$$

At the free edge of the shell, the values of the N_f^{22} and normal stress are equal

$$N_f^{22} = q_v \cdot L = 1.0 \cdot 1.0 = 1 \,\text{N};$$

$$\sigma_{22}^{midl} = N_f^{22}/F = 1H/1.0 \cdot 1.0 \,\text{cm}^2 = 1 \,\text{N}/\text{cm}^2,$$

and the value of the M_f^{22} should be equal to zero $\left(M_f^{22} = 0.000\right)$.

Table 3. Values of the controlled SSS parameters.

Coordinates of the points, y; t	Moments M_f^{22}, 10^{-2} N·m, internal force N_f^{22}, N, Stresses σ_{22}, 10^{-2} MPa	Three-field FEM Mesh of nodes				Displacement method Mesh of nodes					Analytical solution M_f^{22}, 10^{-2} N·m, N_f^{22}, N, $\sigma_{11}=\nu\sigma_{22}$, $\sigma_{22}= =M_f^{22}\big/W$, 10^{-2} MPa
		71×2	91×2	121×2	151×2	71×2	91×2	121×2	151×2	181×2	
Point P, $y=0$, $t=0$	M_f^{22}	89.87	89.90	89.93	89.94	87.89	89.18	89.70	89.85	89.91	90.0
	σ_{22}^{in}	539.4	539.6	539.8	539.9	530.4	538.1	541.3	542.2	542.5	540.0
	σ_{22}^{out}	-539.0	-539.2	-539.4	-539.5	-524.3	-532.0	-535.1	-536.0	-536.4	
	σ_{xx}^{in}	162.3	162.3	162.4	162.4	159.1	161.4	162.4	162.7	162.8	162.00
	σ_{xx}^{out}	-161.3	-161.3	-161.4	-161.4	-157.3	-159.6	-160.5	-160.8	-160.9	
Point T, $y=b$, $t=\pi/2$	M_f^{22}	0.0022	0.0013	0.0007	0.0004	64.69	36.0	18.34	10.96	7.25	0.000
	N_f^{22}	1.006	1.0034	1.0018	1.0011	157.0	84.27	40.55	23.10	14.78	1.000
	σ_{22}^{in}	0.57	0.57	0.57	0.57	-411.0	-234.2	-123.5	-75.78	-51.07	-
	σ_{22}^{out}	1.55	1.56	1.56	1.56	348.9	192.2	96.38	56.85	37.30	-
	σ_{22}^{midl}	1.006	1.0034	1.0018	1.0011	157.0	84.27	40.55	23.10	14.78	1.000
	σ_{xx}^{in}	0.810	0.378	0.228	0.192	-123.3	-70.27	-37.06	-22.73	-15.32	-
	σ_{xx}^{out}	0.186	0.355	0.415	0.430	104.7	57.66	28.91	17.06	11.19	-
	σ_{xx}^{midl}	0.498	0.367	0.322	0.311	47.1	25.28	12.16	6.93	4.43	0.300

Analysis of the data in Table 3 shows, that when using three-field FEM a rapid convergence of the calculation process in determining the sought quantities is observed, and there is a practical coincidence of the controlled SSS parameters obtained by using the developed algorithm with the results of the analytical solution at a coarse discretization mesh. In the second variant, a slow rate of convergence of the calculation process could be observed even at a significant refinement of the discretization mesh. If the results of the finite element solutions could be considered satisfactory in the section of support, in which the curvature of the middle surface is insignificant, then at the free edge of the shell, at which the curvature increases significantly, the calculation error remains considerable despite a serious refinement of the discretization mesh.

Based on the above-mentioned comparative evaluation of the FEM analyses of the elliptical cylinder with a significant curvature of the middle surface, we can conclude that it is preferable to use the developed three-field FEM variant rather than the most common FEM variant in the displacement method formulation.

Example 4. The developed three-field FEM variant (1) ... (15) demonstrates a significantly greater calculation efficiency as compared to the FEM variant in the form of the displacement method [13] and when solving the problems concerning a concentrated load. To confirm this fact, we can consider a problem of determining the SSS of a cylindrical shell loaded with a concentrated force $P = 226.8$ N in the middle, which has a hinged support at the diametrically opposite edge, preventing it from vertical movement (Fig. 6).
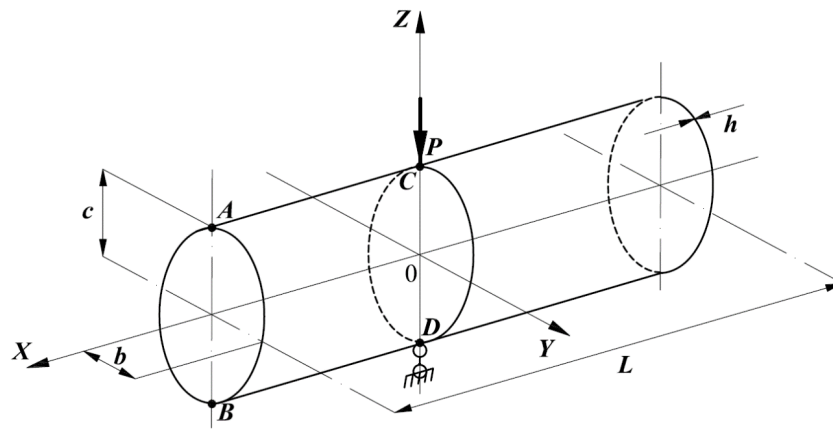
Figure 6. Analytical scheme of the cylinder loaded with concentrated force P.

Taking into account the symmetry of the analytical scheme, only one quarter of the shell was analyzed. The initial data values were as follows: $L = 26.3$ cm; $h = 0.24$ cm; $E = 7.38 \cdot 10^4$ MPa; $v = 0.3125$. First, a circular cylinder with the radius of $R = 12.6$ cm was analyzed in order to compare the deflection value under the action of the force P with the existing solution presented in [28]. The analysis was performed in two variants: in the first one the three-field FEM variant was used; in the second variant, FEM in the form of the displacement method was used [13]. The results of the analysis are presented in Table 4, which shows the deflection values under the action of the force P and normal stresses σ_{tt} at the point A (Fig. 6) at the end of the cylinder during successive refinement of the finite element mesh.

Table 4. Values of the deflection and normal stresses for the circular cylinder.

Deflection v, cm; stresses σ_{tt}, MPa	Variants of the analysis						Existing solution [28]
	The first variant			The second variant			
	Discretization mesh						
	21×21	31×31	41×41	21×21	31×31	41×41	
v	-0.28781	-0.28792	-0.28798	-0.28748	-0.28766	-0.28773	0.2889 (Bogner, Fox, Schmitt)
σ_{tt}^{in}	21.3224	21.0245	20.9017	22.0884	21.7066	21.5818	0.2865 (Cantin, Klauf)
σ_{tt}^{out}	-30.5207	-30.4651	-30.4669	-30.5221	-30.4683	-30.4869	0.2888 (Ashvel, Sabir)

Analysis of the data in Table 4 shows, that the values of the deflection and stresses turned out to be quite similar in both variants of the analysis. In addition, the deflection values coincide with the existing solutions [28].

However, if an elliptical cylinder replaces the circular one, the calculation results become significantly different. Thus, when the ratio of the semi-axes of the cross-sectional ellipse b/c is equal to four, a large calculation error is observed in the second variant of the analysis. This fact is confirmed by the analysis of the data in Table 5, which gives the values of the deflection under the action of the force P and the values of the stresses σ_{tt} at the points A and B (Fig. 6), which should coincide.

Table 5. Values of the deflection and normal stresses for the elliptical cylinder.

Coordinates of the points, $x; t$	Deflection v, cm; stresses σ_{tt}, MPa	Variants of the analysis						
		The first variant			The second variant			
		Discretization mesh						
		21×21	31×31	41×41	21×21	31×31	41×41	51×51
Point $C(0;0)$	v	-0.202355	-0.203385	-0.203568	-0.071653	-0.117069	-0.163220	-0.186131
Point $A(26.3;0)$	σ_{tt}^{in}	17.5780	17.3591	17.2583	11.0566	13.4309	15.5899	16.6424
	σ_{tt}^{out}	-20.5413	-20.4789	-20.4380	-12.5950	-15.5502	-18.1924	-19.4827
Point $B(26.3;\pi)$	σ_{tt}^{in}	17.5541	17.3662	17.2619	1.7814	6.9961	12.6244	15.3878
	σ_{tt}^{out}	-20.5711	-20.4877	-20.4427	-2.2496	-8.3036	-14.8404	-18.0619

In the first variant of the analysis, it is possible to observe a fast convergence of the calculating process both in terms of the value of the deflection under the action of the force P and in terms of the values of the σ_{tt}. In addition, the values of the σ_{tt} at the points A and B in the first variant turned out to be almost equal to each other even at a coarse (21 × 21) mesh of the discretization elements. In the first variant, the values of the deflection under the action of the force P differ from each other by only 0.6 % at the nodes mesh coarseness of 21 × 21 and 41 × 41. In addition, on the contrary, in the second variant of the analysis, it is possible to observe a rather slow convergence of the calculating process in both the deflection and the stresses as compared to the first variant of the analysis. Thus, the deflection values at the nodes mesh coarseness of 21 × 21 and 51 × 51 differ from each other by a factor of 2.6. The values of σ_{tt} at the points A and B significantly differ from each other as well, although they should completely coincide based on the symmetry of the analytical scheme.

The stresses at the points C and D (Fig. 6) should also be equal. Fig. 7 and 8 show the changes in the coefficients k^{in}, k^{out} (for each variant), which are the ratios of the stress values at the points C and D of the shell

$$k^{in} = \left(\sigma_{tt}^{in}\right)_C \Big/ \left(\sigma_{tt}^{in}\right)_D \quad \text{and} \quad k^{out} = \left(\sigma_{tt}^{out}\right)_C \Big/ \left(\sigma_{tt}^{out}\right)_D$$

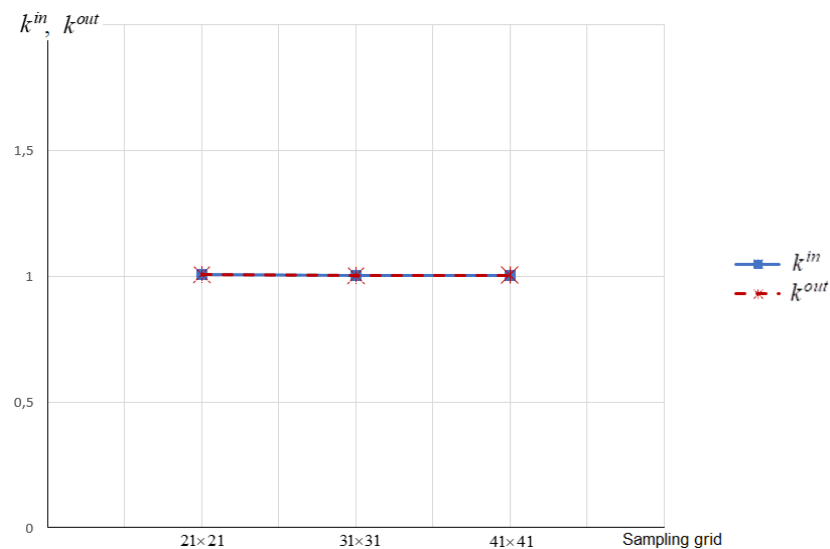depending on the refinement of the discretization mesh.

Figure 7. Graphs of the changes in the coefficients k^{in} and k^{out} in the first variant of the analysis.
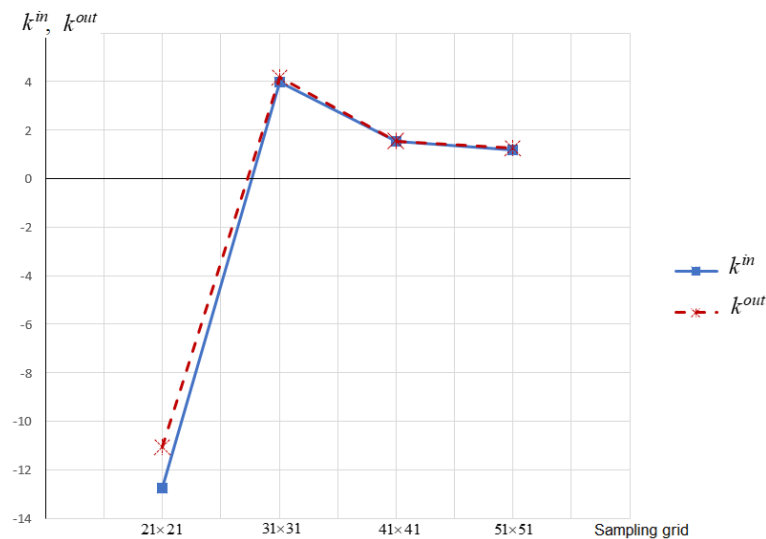
Figure 8. Graphs of the changes in the coefficients k^{in} and k^{out} in the second variant of the analysis.

Fig. 7 shows that, when the developed three-field FEM is used, the values of the coefficients k^{in} and k^{out} are equal to one both at a coarse finite element mesh and in case of its refining, just the way it should be due to the symmetry of the analytical scheme (Fig. 6). When FEM in the form of the displacement method is used, the values of the coefficients k^{in} and k^{out} reach unacceptably large values at a coarse finite element mesh. The coefficients can approach the value of one, if there is a significant refinement of the finite element mesh, which increases the computer time expenditures and enlarges the calculation error being proportional to the total number of the sought unknowns.

Thus, we can conclude that the calculations of the required strength parameters of shells are correct and highly accurate when implementing the developed three-field variant of the FEM.

4.   Conclusions

Based on the foregoing, the following conclusions can be formulated:

1. The developed three-dimensional FEM variant was implemented using the example of the analysis of a thin-walled shell structure. It allows to simultaneously obtain the fields of displacements, internal force factors and strains of the middle surface of a shell, which significantly expands the capabilities of a detailed numerical analysis of the stress-strain state of such type of structures.

2. The correctness and high accuracy of the calculations of the controlled strength parameters of the SSS of thin-walled shell structures has been proven by solving test problems on the analysis of elliptical cylinders loaded with internal pressure and a linearly distributed load.

3. The calculation error for the values of bending moments was 0.14 %, and it was 4 % for the axial forces values. However, it should be noted here that the normal stress value is mainly determined by the value of the bending moment, while the contribution of the axial force to the value of the stress is minimal.

4. The comparison of two variants of the analyses of an elliptical cylinder with a significant curvature of the middle surface showed substantial advantages of the developed three-field FEM variant. It could be compared to the FEM variant in the displacement method formulation in terms of much higher accuracy of finite element solutions at relatively coarse discretization meshes of the shell.

5. The developed three-field version of FEM has fundamental advantages over the FEM variant in the form of the displacement method, such as indifference to the geometry of the middle surface of the shell and the types of external load.

References

1. Novozhilov, V.V. Teoriya tonkikh obolochek [Theory of thin shells]. St. Petersburg: St. Petersburg University Publ., 2010. 378 p. (rus)

2. Sedov, L.I. Mekhanika sploshnoy sredy [Mechanics of a continuous medium]. V. 1. Moscow: Nauka, 1976. 536 p. (rus)

3. Lalin, V., Rybakov, V., Sergey, A. The finite elements for design of frame of thin-walled beams. Applied Mechanics and Materials. 2014. 578–579. Pp. 858–863. DOI: 10.4028/www.scientific.net/amm.578-579.858

4. Kirichevsky, R.V., Skrynnykova, A.V. Vliyaniye Approksimiruyushchikh Funktsiy pri Postroyenii Matritsy Zhestkosti Konechnogo Elementa na Skorost' Skhodimosti Metoda Konechnykh Elementov [The effect of approximating functions in the construction of the stiffness matrix of the finite element on the convergence rate of the finite element method]. Tomsk State University Journal of Mathematics and Mechanics. 2019. 57. P. 26. DOI: 10.17223/19988621/57/2 (rus)

5. Tyukalov, Yu.Ya. Quadrilateral Finite Element for Thin and Thick Plates. Construction of Unique Buildings and Structures. 2021. 5 (98). 9802. DOI: 10.4123/CUBS.98.2

6. Agapov, V., Golovanov, R. Comparative analysis of the simplest finite elements of plates in bending. Advances in Intelligent Systems and Computing. 2018. 692. 1009. DOI: 10.1007/978-3-319-70987-1_109

7. Dmitriev, A.N., Lalin, V.V., Novozhilov, Iu.V., Mikhaliuk, D.S. Simulation of Concrete Plate Perforation by Coupled Finite Element and Smooth Particle Hydrodynamics Methods. Construction of Unique Buildings and Structures. 2020. 7 (92). 9207. DOI: 10.18720/CUBS.92.7

8. Rickards, R.B. Metod konechnykh elementov v teorii obolochek i plastin [Finite element method in the theory of shells and plates]. Riga: Zinatne, 1988. 284 p. (rus)

9. Postnov, V.A., Kharkhurim, I.Ya. Metod konechnykh elementov v raschetakh sudovykh konstruktsiy [Finite element method in calculations of ship structures]. Leningrad: Sudostroienie, 1974. 342 p. (rus)

10. Jeon, H.-M., Lee, P.-S., Bathe, K.-J. The MITC3 shell finite element enriched by interpolation covers. Computers & Structures. 2014. 134. Pp. 128–142. DOI: 10.1016/j.compstruc.2013.12.003

11. Ko, Y., Lee P.-S., Bathe, K.-J. A new 4-node MITC element for analysis of two-dimensional solids and its formulation in a shell element. Computers & Structures. 2017. 192. Pp. 34–49. DOI: 10.1016/j.compstruc.2017.07.003

12. Schöllhammer, D., Fries, T.-P. A Higher-order Trace Finite Element Method for Shells. Numerical methods in Engineering. 2021. 122 (5). Pp. 1217–1238. DOI: 10.1002/nme.6558

13. Klochkov, Yu.V., Nikolaev, A.P., Sobolevskaya, T.A., Vakhnina, O.V., Klochkov, M.Yu. The calculation of the ellipsoidal shell based FEM with vector interpolation of displacements when the variable parameterisation of the middle surface. Lobachevskii Journal of Mathematics. 2020. 41 (3). Pp. 373–381. DOI: 10.1134/S1995080220030117

14. Maslennikov, A.M., Kobelev, E.A., Maslennikov, N.A. Solution of sustainability tasks by finite element method. Bulletin of Civil Engineers. 2020. 2 (79). Pp. 68-74. DOI: 10.23968/1999-5571-2020-17-2-68-74

15. Lalin, V.V., Yavarov, A.V., Orlova, E.S., Gulov A.R. Application of the finite element method for the solution of stability problems of the Timoshenko beam with exact shape functions. Power Technology and Engineering. 2019. 4 (53). Pp. 449–454. DOI: 10.1007/s10749-019-01098-6

16. Agapov, V.P., Aidemirov, K.R. Designing of the blades of aircraft propellers by the finite element method, taking into account the strength of structure. RUDN Journal of Engineering Researches. 2021. 1 (22). Pp. 65–71. DOI: 10.22363/2312-8143-2021-22-1-65-71

17. Agapov, V. The Family of Multilayered Finite Elements for the Analysis of Plates and Shells of Variable Thickness. E3S Web of Conferences. 2018 Topical Problems of Architecture. Civil Engineering and Environmental Economics. TPACEE 2018. 2019. Pp. 02013. DOI: 10.1051/e3sconf/20199102013

18. Yakupov, S.N., Kiyamov, H.G., Yakupov, N.M. Modeling a Synthesized Element of Complex Geometry Based Upon Three-Dimensional and Two-Dimensional Finite Elements. Lobachevskii Journal of Mathematics. 2021. 42 (9). Pp. 2263–2271. DOI: 10.1134/S1995080221090316

19. Jiapeng, T., Ping, X., Baoyuan, Z., Bifu, H., A finite element parametric modeling technique of aircraft wing structures. Chinese Journal of Aeronautics. 26 (5). 2013. Pp. 1202–1210. DOI: 10.1016/j.cja.2013.07.019

20. Lalin, V.V., Rybakov, V.A., Ivanov, S.S., Azarov, A.A. Mixed finite-element method in V.I. Slivker's semi-shear thin-walled bar theory. Magazine of Civil Engineering. 2019. 5 (89). Pp. 79–93. DOI: 10.18720/MCE.89.7

21. Tyukalov, Yu.Ya. Finite element model of reisner's plates in stresses. Civil Engineering Journal. 2019. 5 (89). Pp. 61–78. DOI: 10.18720/MCE.89.6

22. Magisano, D., Liang, K., Garcea, G., Leonetti, L., Ruess, M. An efficient mixed variational reduced-order model formulation for nonlinear analyses of elastic shells. International Journal for Numerical Methods in Engineering. 2018. 113 (4). Pp. 634–655. DOI: 10.1002/nme.5629

23. Chernysheva, N.V., Rozin, L.A. Algorithm of Combined Method of 3D Analysis for the Boundary Problems in Infinite Medium. Materials Physics and Mechanics. 2017. 31 (1–2). Pp. 82–85.

24. Gureeva, N.A. Calculation Plainly Loaded Geometrically Nonlinear Designs on the Basis of Mixed FEM with Tenzorno-Vector Approximation Requires Sizes. Izvestiya of Saratov University. MATHEMATICS. MECHANICS. INFORMATICS. 2012. 3 (12). Pp. 56–62. DOI: 10.18500/1816-9791-2012-12-3-56-62. (rus)

25. Klochkov, Yu., Pshenichkina, V., Nikolaev A., Vakhnina, O., Klochkov, M. Stress-strain state of elastic shell based on mixed finite element. Magazine of Civil Engineering. 2023. 4 (120). 12003. DOI: 10.34910/MCE.120.3

26. Klochkov, Yu.V., Pshenichkina, V.A., Nikolaev, A.P., Vakhnina, O.V., Klochkov, M.Yu. Quadrilateral element in mixed FEM for analysis of thin shells of revolution. Structural mechanics of engineering constructions and buildings. 2023. 1 (19). Pp. 64–72. DOI: 10.22363/1815-5235-2023-19-1-64-72

27. Ruditsyn, M.N., Artemov, P.Ya., Lyuboshits, M.I. Spravochnoye posobiye po soprotivleniyu materialov [Reference book on strength of materials]. Minsk: Vysheishaia Shkola Publ., 1970. 630 p. (rus)

28. Sekulovich, M. Metod konechnykh elementov [Finite element method]. Moscow: Stroyizdat, 1993. 664 p. (rus)

Contacts:

Yuri Klochkov, *Doctor of Technical Sciences*
ORCID: *https://orcid.org/0000-0002-1027-1811*
E-mail: *klotchkov@bk.ru*

Anatoly Nikolaev, *Doctor of Technical Sciences*
ORCID: https://orcid.org/0000-0002-7098-5998
E-mail: anpetr40@yandex.ru

Valeria Pshenichkina, *Doctor of Technical Sciences*
ORCID: https://orcid.org/0000-0001-9148-2815
E-mail: vap_hm@list.ru

Olga Vakhnina, *PhD in Technical Sciences*
ORCID: https://orcid.org/0000-0001-9234-7287
E-mail: ovahnina@bk.ru

Mikhail Klochkov,
ORCID: https://orcid.org/0000-0001-6751-4629
E-mail: m.klo4koff@yandex.ru